Universidad Autónoma de Madrid

In-beam γ-ray spectroscopic studies near the doubly-magic nuclei ^{56}Ni and ^{208}Pb

Memoria presentada para la obtención del título de Doctor en Ciencias Físicas por:

Álvaro Fernández Martínez

Universidad Autónoma de Madrid
Instituto de Estructura de la Materia (IEM-CSIC)

Tesis dirigida por:

Dr. Andrea Jungclaus

Instituto de Estructura de la Materia (IEM-CSIC)

Departamento de Física Teórica
Facultad de Ciencias
Universidad Autónoma de Madrid

Madrid, Julio de 2021

Grupo de Física Nuclear Experimental

CSIC
Consejo Superior de Investigaciones Científicas

Resumen

En esta tesis se presentan los resultados de dos experimentos de física nuclear llevados a en regiones próximas a los núcleos doblemente mágicos ^{208}Pb y ^{56}Ni. Estos proyectos abordan, respectivamente, la cuestión de la existencia de estados excitados de naturaleza α-core a lo largo de toda la carta de núcleos, así como el estudio de la simetría de isospín en regiones próximas a la línea de goteo de protones.

Parte I – Estados α-core en núcleos pesados: el caso del ^{212}Po.

El experimento de esta parte de la tesis se llevó a cabo en el laboratorio de GANIL (Caen, Francia). El núcleo ^{212}Po tiene dos protones y dos neutrones fuera de capas cerradas y constituye el único caso hasta la fecha, más allá del ^{56}Ni, en el que se ha propuesto la existencia de estados excitados α-core puros.

El núcleo ^{212}Po se pobló en este experimento mediante la reacción de transferencia en cinemática inversa ^{12}C(^{208}Pb,^{212}Po)^{8}Be. Durante la primera parte del experimento, se hizo incidir el haz de ^{208}Pb sobre un blanco compuesto por una única capa de diamante con un espesor de 0.51 mg/cm^2. En la última parte del experimento se empleó un blanco compuesto por una capa de grafito con un espesor de 0.49 mg/cm^2 y una capa de frenado de Au con espesor de 13.50 mg/cm^2 para la medida de vidas medias nucleares mediante la técnica de atenuación del efecto Doppler (conocida como DSAM). Los rayos γ emitidos por el ^{212}Po se observaron en el espectrómetro γ AGATA (Advanced GAmma-ray Tracking Array), un conjunto de detectores de Ge con gran resolución espacial que permiten corregir con una alta precisión el efecto Doppler en la radiación emitida en vuelo y reconstruir las interacciones de los fotones dentro de los detectores, recuperando su energía total y dirección inicial empleando algoritmos de tracking. Las dos partículas α procedentes de la desintegración del ^{8}Be se observaron en un detector de silicio circular segmentado por ambas caras (DSSSD). La fuerte correlación espacial presente entre ambas partículas proporcionó una condición experimental clara para identificar y seleccionar aquellos eventos con un núcleo ^{212}Po en el canal de salida. Las posiciones de impacto en el DSSSD se emplearon para reconstruir la cinemática de la reacción evento por evento, maximizando así la precisión de la corrección Doppler. Los eventos correspondientes a los núcleos ^{212}Po producidos en el experimento se seleccionaron examinando las multiplicidades de partículas y las energías depositadas en el DSSSD.

Se determinó un esquema de niveles del ^{212}Po mediante espectros de coincidencia γ–γ, incluyéndose 14 nuevos estados excitados a los ya conocidos. Se realizaron asignaciones tentativas de espín y paridad a tres estados excitados con la ayuda de las energías y las probabilidades de decaimiento de los estados calculados según el modelo de capas. En este trabajo se han establecido además cotas superiores a la vida media para cuatro estados excitados.

Se examinó el esquema de niveles a la luz de los modelos propuestos en la literatura para describir la colectividad octupolar y la existencia de dobletes con grandes correlaciones de α-clustering que decaen mediante transiciones E1 muy colectivas hacia la banda del estado fundamental. A pesar de la selectividad del mecanismo de reacción y del dispositivo experimental, no se ha encontrado evidencia de la existencia de ninguno de los estados excitados predichos en todos los modelos con espín igual o inferior a 3. Los estados excitados de paridad negativa a más baja energía se han interpretado como mezclas entre configuraciones del tipo $^{212}Po(0^+,2^+,4^+,6^+,8^+)\otimes^{208}Pb(3^-)$ y el multiplete $\pi(h_{9/2}^2)_0$ $n(g_{9/2}j_{15/2})_{I^-}$, de manera similar a lo que ocurre con otros núcleos en la vecindad del ^{208}Pb.

Se ha efectuado además un estudio de la polarización de la radiación emitida empleando la buena resolución espacial de AGATA. A partir de este estudio se realizó la primera asignación directa de la paridad al estado con espín 6 y a una energía de 1788 keV (uno de los denominados "dobletes α-cluster"), encontrándose que dicho estado es de paridad positiva. De acuerdo con los cálculos del modelo de capas efectuados en este trabajo, se han identificado los dobletes como el segundo y el tercer estado excitado de cada momento angular par. La energía de excitación de los estados, su única rama de decaimiento hacia el estado con el mismo espín de la banda fundamental, así como la elevada probabilidad de transición B(M1) de dicha rama se reproducen en los cálculos. Todo ello lleva a cuestionar la interpretación de los dobletes como estados de naturaleza α-core llevada a cabo en la literatura.

Parte II: Espectroscopía γ del núcleo ^{56}Zn: simetría de isospín hacia la línea de goteo de protones.

En la segunda parte de la tesis se presenta el primer estudio de espectroscopía γ del núcleo ^{56}Zn. Este núcleo se pobló en un experimento con un haz radioactivo mediante reacciones de separación de un único neutrón. Los rayos γ detectados en el espectrómetro DALI2+ se correlacionaron temporalmente con los núcleos del haz radioactivo incidente identificados en el separador BigRIPS y con los productos de las reacciones en el blanco secundario de Be registrados en el separador ZeroDegree. Se han observado tres transiciones del ^{56}Zn, cuyo esquema de niveles se ha construido empleando coincidencias temporales e intensidades de dichas transiciones. La comparación con el núcleo espejo ^{56}Fe permitió la asignación del espín y la paridad a los estados excitados del ^{56}Zn.

El ^{56}Zn es ahora el núcleo más pesado con $T_z = -2$ en el cual se conocen estados excitados. En contraste con la abundante información experimental disponible para los núcleos de la capa $f_{7/2}$ y aquellos con masas por encima de A=60, los datos experimentales de diferencias de energía entre núcleos espejo (MED) son escasos en las cercanías del núcleo ^{56}Ni. Con esta motivación se llevó a cabo el análisis de las MEDs en el par ^{56}Fe/ ^{56}Zn, validándose dicho análisis con los datos del par $T_z = -1$ ^{58}Zn/^{58}Ni. La fuerte ocupación de los orbitales del espacio pf por encima del

$f_{7/2}$ amplifican los efectos de ruptura de la simetría de isospín en los orbitales p y $f_{5/2}$ y proporcionaron evidencia acerca de la presencia de la interacción multipolar V_B que rompe la simetría de isospín, diferente de la coulombiana, en todo el espacio de valencia. Esta conclusión concuerda con un trabajo previo en los pares $T_Z = \pm 1$ con masas A=66 y A=70.

Además, se encontró que las MEDs son muy sensibles al término monopolar radial de la interacción, relacionado con la ocupación de los orbitales p. Se encontró que es posible reproducir las MEDs experimentales extrapolando la prescripción para el término radial propuesta originalmente para describir las MEDs en la capa $f_{7/2}$. Según esta descripción, la ocupación de los orbitales p cambia significativamente la energía de Coulomb como resultado de la mayor extensión espacial de la función de onda en los orbitales p que en los f.

Contrariamente a las interpretaciones previas en las que se ha relacionado el término radial en esta región con el desplazamiento de Thomas-Ehrman, este trabajo proporciona evidencia a favor de su interpretación como una medida de la ocupación de los orbitales p independientemente del grado de deformación nuclear. Se relacionaron estos resultados con los de trabajos previos con núcleos de masas próximas a A=48, en los que se ha sugerido que el orbital $p_{3/2}$ juega un papel crucial en los radios nucleares mediante una extensión excepcionalmente grande de la función de onda del nucleón en este orbital.

Contents

List of Figures

List of Tables

Chapter 1

Basic principles

The first atomic model consisting on a massive nucleus and orbiting electrons was proposed over a century ago and yet the atomic nucleus still constitutes a contemporary field of research. Advances in its understanding are linked with fundamental questions such as the origin and proportion of the elements in the cosmos.

The fundamental ingredients for the modern nuclear science were established in the 30's of the past century with the discovery of the neutron by J. Chadwick and the pioneering work of H. Yukawa treating the nucleon-nucleon interaction as a field theory based on one pion exchange. At a fundamental level, the nucleus is viewed nowadays as a low-energy QCD field theory, with nucleons and mesons as the degrees of freedom instead of quarks and gluons[1]. The nucleon-nucleon interaction is regarded as a residual interaction similar to the Van der Waals forces among neutral molecules. A derivation of the nucleon-nucleon potential from field theory, however, still resists the physicists because of the non-perturbative character of QCD at low energies. Lattice QCD calculations[2] are focused on this goal, but they are under a continuous improvement and only very limited results have been reported.

1.1 The nuclear shell model

Instead of starting from first principles, nuclear structure is usually tackled from phenomenological approaches. It is well established from nucleon-nucleon scattering data that the nucleon-nucleon potential is almost infinitely repulsive at short distances. This, combined with the Pauli exclusion principle and the short range of the nuclear force, is able to explain the gross features of a vast amount of nuclear data[3] and, in particular, the saturation of the binding energy per nucleon at $\sim 8\,\mathrm{MeV}$. It is known as well that the nuclear density is low and that the constituent nucleons to a large extent interact only with their closest neighbors.

A limiting model exploiting this idea is the so-called independent particle model. This theory regards the nucleus as composed of independent particles moving in an average central potential, called the mean field, caused by the other nucleons. The mean field is usually parametrized by isotropic Woods-Saxon or harmonic -oscillator potentials, whose analytical solutions makes them a handy choice for qualitative analyses. These solutions result in degenerate levels characterized by a quantum number $N = 2(n-1) + l$, in terms of which the level energies ϵ_N and their degeneracies $D(N)$ are given by

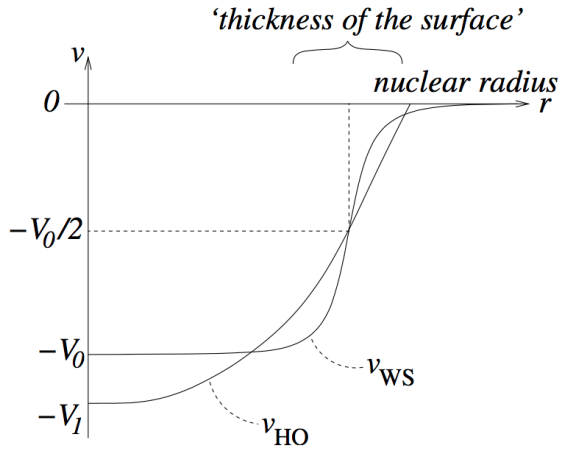

Figure 1.1: Illustration of harmonic oscillator and Wood-Saxon single-particle potentials. Adapted from [4].

$$\epsilon_N = \hbar\omega\left(N + \frac{3}{2}\right) \tag{1.1}$$

$$D(N) = \frac{1}{2}(N+1)(N+2) \tag{1.2}$$

The isospin quantum number $\tau = 1/2$ and its projections $m_\tau = \pm\frac{1}{2}$ are introduced to distinguish between protons and neutrons. Thus the set of quantum numbers characterizing the nucleons in this model are $nls\tau m_l m_s m_\tau$, where the usual convention is to take $m_\tau = +\frac{1}{2}$ for neutrons and $m_\tau = -\frac{1}{2}$ for protons. According to the exclusion principle, protons and neutrons fill the so-called oscillator shells each one with a different set of quantum numbers.

One of the most compelling experimental evidences of the existence of nuclear shells and therefore the importance of single-particle motion in nuclear structure is the observation of magic numbers[5], specific numbers of protons and neutrons that provide additional stability to the nucleus. These are 2, 8, 20, 28, 50, 82 and 126, where the first three are already predicted so far by the schematic harmonic oscillator model previously introduced. Regarding the remaining ones, it was realized[6, 7] that they result from a spin-orbit coupling term in the central potential,

$$V_{s-o} = f(r)\,\vec{s}\cdot\vec{l} \tag{1.3}$$

Although its origin is still not clear, a spin-orbit term was already predicted in the field theory of Yukawa. The eigenvalues of the independent-particle hamiltonian are now characterized by the total angular momentum $j = l + s$ of the nucleon and

its projection m_j, where the original m_s degeneracy is now removed. The spin-orbit splitting is proportional to $2l+1$, that is, the larger the orbital angular momentum the larger the spin-orbit splitting. As a result, the complete set of magic numbers known from stable nuclei is now well reproduced with the attractive spin orbit interaction[1], responsible for the presence of the $l + \frac{1}{2}$ intruder state, the one having a distinctive parity within a major oscillator shell. The total wave function of the $A = N + Z$ nucleon system must obey the antisymmetrization principle for identical fermions, thus it is constructed as the factorized product of a Slater determinant for proton and neutron states.

The enormous success of the independent-particle model has put it on the grounds of a number of modern many-body approaches to nuclear structure and it is the simplest shell model theory of the nucleus. These models presume the existence of the mean field which is used as the starting point, and then construct an effective hamiltonian containing the two-body interactions, called residual interactions, that are not accounted for within that mean field. This corresponds to re-writing the nuclear hamiltonian, composed of a kinetic energy term plus nucleon-nucleon two-body interactions, into a mean-field term (one-body operator) plus two-body interactions by introducing a one-body potential U acting on each nucleon,

$$\begin{aligned} H = T + V &= (T + U) + (V - U) \\ &= H_0 + H_{\text{res}} \end{aligned} \tag{1.4}$$

Other approaches to nuclear structure, on the other hand, do not presume the mean field. Among them, ab initio methods start from parametrizations of the nucleon-nucleon potential whose parameters are adjusted to reproduce experimental nucleon-nucleon scattering data; a variety of techniques such as the reaction matrix in the nuclear medium (G-matrix), correlation functions and coupled cluster methods allowed calculations with realistic potentials having the strong repulsive interaction at short inter-nucleon distances[9]. As another example, self consistent mean field theories[10] use phenomenological effective potentials whose parameters are fitted to reproduce ground-state data throughout the nuclear chart. Collective models with built-in deformed mean field features have been developed as well[11] for describing deformed nuclei occurring between closed shells.

Only the shell-model approach has been used in the calculations performed in this work and the next section briefly introduces the usual approaches for the construction of the residual interactions and the diagonalization of shell-model hamiltonians.

[1] An additional term proportional to l^2 is introduced in more detailed treatments so that the remaining degeneracies with n and l are also removed[8].

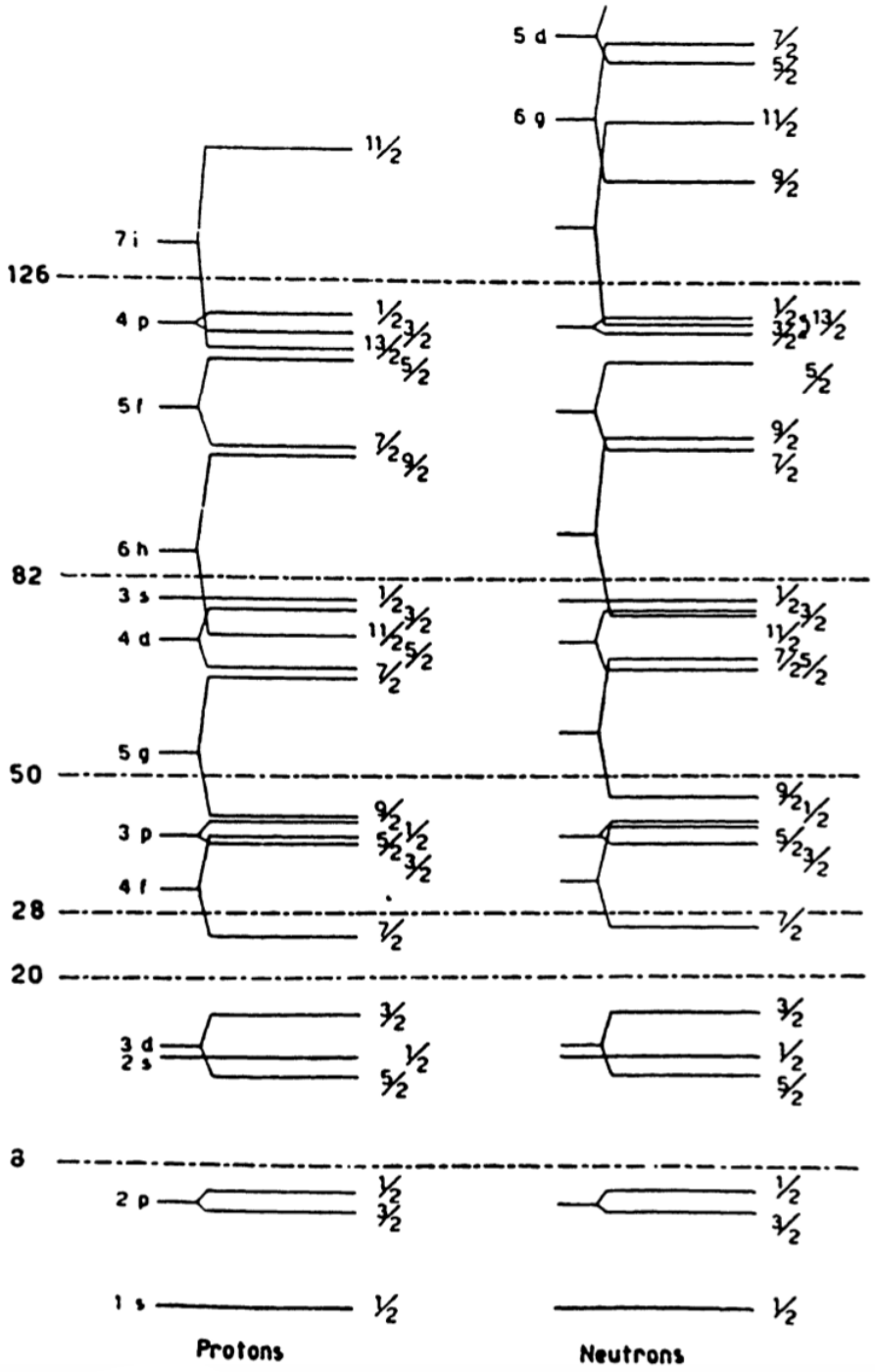

Figure 1.2: Illustration of the spin-orbit splitting of single-particle levels for protons and neutrons in an harmonic-oscillator potential. Magic numbers are indicated by the dot-dashed lines. The figure was taken from [8].

1.1.1 Shell model hamiltonians

Finite-sized, computationally tractable hamiltonian matrices are constructed in shell model calculations by distinguishing three model spaces: an inert core, the valence space and the external space. The valence space is a truncated one meaning that no configuration mixing by the residual interaction occurs in the external space. The residual interactions are therefore effective in the sense that they are only suited for the specific valence space for which they were obtained. Once the effective hamiltonian is given by its matrix elements in a certain basis, one proceeds to diagonalize the hamiltonian in the model space. Spherical symmetry of the hamiltonian guarantees that the eigenstates will be of defined total angular momentum J. Two bases are usually chosen in the calculations[12], the coupled (referred to as J-scheme) and the uncoupled one (m-scheme). In the uncoupled basis, only $M = \sum_i m_i$ and $T_z = \sum_i t_{z,i}$ are good quantum numbers because the basis is constructed out of pure Slater determinants. On the other hand, J is a good quantum number in the coupled basis. In an m-scheme calculation, the matrix elements are readily obtained up to a phase, where additional angular momentum algebra in the matrix elements is required for working in the J-scheme. The choice of the basis mostly depends on the application one is interested in. As an example, in an m-scheme calculation all $M = 0$ states will be computed, thus resulting in larger matrix sizes. On the other hand, significantly smaller matrices are dealt with in the J-scheme if, among the $M = 0$ states, one is only interested in those with $J = 0$. Specific codes such as ANTOINE[12, 13] (m-scheme) and NuShellX[14, 15] (J-scheme) are available for calculations.

Following the usual classification of residual interactions[8, 16], they can be of three types:

- **Empirical interactions**. The two-body matrix elements are obtained either by χ^2 fitting procedures to experimentally known low-lying excited states as a function of the matrix elements or from binding energies assuming pure two-particle configurations, where only the diagonal elements of the interaction are extracted in the latter case. As an example of this procedure, properties of low-energy 2^+ states in ^{212}Po are calculated in ref. [17] by assuming pure $h^2_{9/2}$ and $g^2_{9/2}$ configurations for protons and neutrons, where the matrix elements of the residual pp, nn and pn interactions are extracted from the yrast seniority spectra of ^{210}Po, ^{210}Pb and ^{210}Bi whereas single-particle energies can be taken from the spectra of ^{209}Bi and ^{209}Pb.

- **Schematic interactions**. A handy functional form for the radial part of the interaction is chosen, enabling analytical calculations and mimicking its

short range character. Examples include delta, gaussian or a Yukawa-type potentials, where symmetry arguments can be used to restrict the analytical form of the two-body interaction[3]. The free constants are adjusted to reproduce experimental spectra.

- **Realistic interactions**. In the pioneering works of Kuo et al.[18–20], shell-model effective interactions were derived starting from the Hamada-Johnston potential describing free nucleon - nucleon scattering. The effects of the nuclear medium that cure the hard core emerge from the G-matrix, the equivalent to the scattering matrix for the nuclear medium. An effective interaction $V' = G$ is then formally used to turn the original eigenvalue problem into a new eigenvalue problem in terms of a finite sum of oscillator functions in the valence space. Perturbative expansions such as that of the folded-diagram method[21] are used to compute the G-matrix by retaining the lowest orders as corrections to the bare nucleon-nucleon potential.

The calculations in this work have been performed with the Kuo-Herling[22] and KB3G[23] interactions.

Kuo-Herling

This is a realistic interaction which is intended for calculations around $A = 208$. The inert core is that of the doubly-magic ^{208}Pb. The matrix elements of the hamiltonian were derived from the Hamada-Johnston potential. Corrections to the bare matrix elements originally included a 1p-1h core polarization correction plus a second-order term due to 2p-2h excitations. Single-particle energies for protons and neutrons are extracted from ^{209}Bi and ^{209}Pb. The harmonic oscillator wave functions are used for the calculation of the radial integrals, with $\hbar\omega \approx 41\, A^{-1/3}\,\mathrm{MeV} = 7\,\mathrm{MeV}$. The valence space includes the $0h_{9/2}$, $1f_{7/2}$, $0i_{13/2}$, $1f_{5/2}$, $2p_{3/2}$, $2p_{1/2}$ proton shells and the $1g_{9/2}$, $0i_{11/2}$, $0j_{15/2}$, $2d_{5/2}$, $3s_{1/2}$, $1g_{7/2}$, $2d_{3/2}$ neutron shells. The original interaction was later on modified in ref. [24], where the 2p-2h term was dropped and a scaling K_{ph} of the 1p-1h term was introduced instead for better agreement with experiment. The values of K_{ph} used in the calculations of this work are 0.92, 1.07 and 0.90 for the pp, nn and pn interactions (the same values of ref. [24]).

KB3G

This interaction is a modified one from the original interaction obtained by Kuo and Brown in [20] for nuclei in the fp shell using the Hamada-Johnston potential with

a single 1p-1h correction to the bare interaction. The monopole part of the residual interaction, responsible for the evolution of single-particle energies across shells, has been adjusted so as to reproduce properties of near-closed shell nuclei, such as binding energies and single-particle gaps of ^{48}Ca and ^{56}Ni as well as excitation energies in ^{49}Sc, ^{49}Ca and ^{57}Ni.

1.2 Nuclear reactions

Nuclear reactions are often classified in direct or compound nucleus reactions[25]. In the latter, the reaction time is long enough to prevent the reacting system from "remembering" its initial identity. Then, the compound nucleus decays by particle evaporation and γ-ray emission. Direct reactions, on the other hand, depend on the entrance channel, and the contact time between the reacting nuclei is shorter so as to prevent thermalization and a significant inter-nuclear flow of mass.

The following sections introduce two types of direct reactions, nucleon removal and transfer reactions, that were used for populating the nuclei of interest in this work.

1.2.1 Nucleon removal

The content of this section is mainly based on the review of Hansen and Tostevin[26]. The use of nucleon removal reactions -also referred to as knockout reactions in a wider sense- as a tool to populate nuclear excited states and as a highly selective probe in itself of the single-particle degree of freedom has been traditionally linked with the use of fast radioactive ion beams (RIB). Energies above 100 $^{\mathrm{MeV}}/_{\mathrm{u}}$ are typically required to produce short-lived exotic beams, transport them towards secondary reaction targets and identify the exotic reaction products. Whereas transfer reactions dominate in non-relativistic regimes, nucleon knockout is a selective reaction mechanism (from the spectroscopic point of view) at intermediate to high beam energies. In a knockout reaction such as the one represented in figure 1.3, one or more nucleons are removed from the projectile by interaction with the target nucleus. For a single-nucleon removal from a projectile with A nucleons, the incoming momentum $\vec{p}_A$ of the projectile relates to that of the ejected nucleon ($\vec{p}_N$), the target ($\vec{p}_T$) and the residue $\vec{p}_{A-1}$ as

$$\vec{p}_A = \vec{p}_{A-1} + \vec{p}_T + \vec{p}_N \tag{1.5}$$

where, in usual applications involving light targets, the residual $A-1$ nucleus keeps moving after the reaction with virtually the same velocity of the projectile and scattering angles close to 0°. The link of this reaction with nuclear structure is given by the

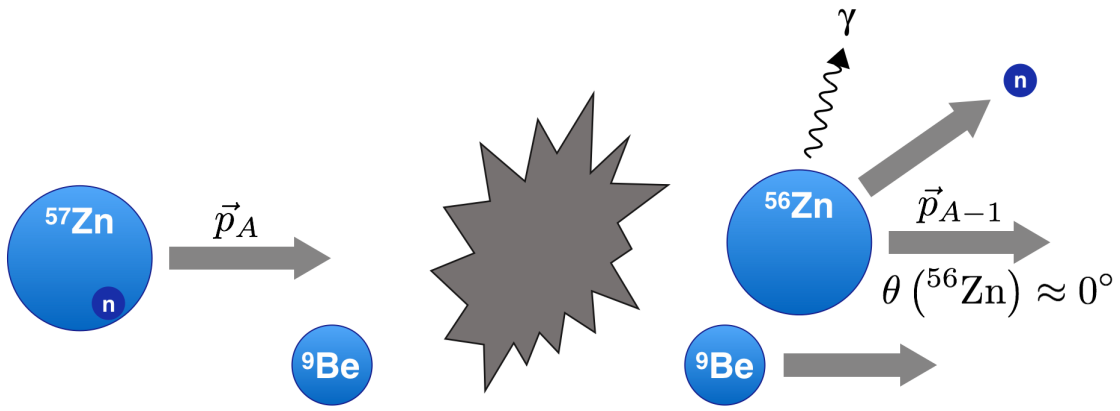

Figure 1.3: Diagram of a typical setup for nucleon removal reactions with a radioactive beam. The reaction occurs in inverse kinematics in the laboratory, where a ^{57}Zn ion impinges on a ^{9}Be target acting as a "black disk". The reaction results in the emission of a γ ray following the removal of a loosely bound neutron of the projectile.

partial cross section for the removal of a nucleon from a single-particle configuration j^{π}, leaving the residue with excitation energy E_x in a final state c. This cross section is factorized as the product of a single-particle cross section σ_{sp}, calculated from reaction theory as described hereafter, and the spectroscopic factor $C^2S(c, nlj)$,

$$\sigma_{\mathrm{th}}(c) = \left(\frac{A}{A-1}\right)^N \sum_j C^2S(c, nlj)\sigma_{\mathrm{sp}}(nlj) \tag{1.6}$$

where N is the oscillator shell of the removed nucleon. The spectroscopic factors are defined by the overlaps between the A and $A-1$ nuclei and are thus related to the occupancy probabilities in the parent nucleus. They can be theoretically calculated using the shell model. The quantity σ_{sp} is the result of three contributions and is written as

$$\sigma_{\mathrm{sp}} = \sigma_{\mathrm{str}} + \sigma_{\mathrm{diff}} + \sigma_{\mathrm{C}} \tag{1.7}$$

The first contribution in the above equation stems from stripping or inelastic breakup processes and represents the interaction of the removed nucleon with the target, from which it is finally ejected at small angles or absorbed, with possible excitations of the target. The diffractive one refers to the elastic dispersion of the target and the removed nucleon. The last term in eq. (1.7) is the Coulomb dissociation term and corresponds to electromagnetic elastic breakup processes. This term and its interference with the diffraction processes is often neglected in applications involving light targets. σ_{sp} is usually evaluated under two approximations: the adiabatic or sudden approximation, in which the nucleons are considered as "frozen" in the reaction process, and the eikonal approximation. The latter is justified for the small scattering angles of the projectile,

whereas the former is applicable as long as the collision time is short enough, which is often the case with relativistic beams. The adiabatic approximation enables to calculate the cross section as a function of the impact parameter alone according to the following equations:

$$\sigma_{\text{str}} = \frac{1}{2j+1} \int \mathrm{d}\vec{b} \sum_{m} \langle \psi_{jm} | \left(1 - |S_n^2|\right) |S_c|^2 | \psi_{jm} \rangle \tag{1.8}$$

$$\sigma_{\text{diff}} = \frac{1}{2j+1} \int \mathrm{d}\vec{b} \sum_{m,m'} \langle \psi_{jm} | \, |1 - S_c S_n|^2 \, | \psi_{jm} \rangle \, \delta_{m,m'} - | \, \langle \psi_{jm'} | \left(1 - S_c S_n\right) | \psi_{jm} \rangle \, |^2 \tag{1.9}$$

where S_c and S_n are the elastic S-matrices that can be calculated from a variety of approaches such as using empirical potentials.

In a typical RIB experiment where this kind of reaction is exploited (see for instance [27]) the projectile residue is identified in an spectrometer in coincidence with its deexciting γ rays, thus enabling the experimental determination of the so-called exclusive cross-sections corresponding to nearly direct population of the excited states. The exclusive cross sections can be compared with calculated cross sections using the formalism previously presented and using spectroscopic factors from the shell model. Knockout experiments with both stable and radioactive nuclei, however, revealed systematic underestimations, in the range of 10%-90%, of the experimental cross sections by the calculated ones. A strong isospin correlation was pointed out by A. Gade et al.[28] in the deviations, with smaller (larger) deviations for more weakly (strongly) bound nucleons. The origin of this deviation is not fully understood and deficiencies of the effective interaction and/or the approximations used in knockout calculations have been proposed. Therefore, an empirical reduction factor $R_S = \frac{\sigma_{\text{exp}}}{\sigma_{\text{th}}}$ is defined for comparisons with theoretical cross sections, where the partial cross sections defining R_S refer to the sum of cross sections to all states that lie below the corresponding nucleon-separation threshold. The trend of experimental R_S factors as a function of the asymmetry in proton-neutron separation energies is represented in fig. 1.4.

1.2.2 Transfer

Transfer reactions are classified in stripping reactions, when one or more nucleons are transferred from the projectile to the target, pickup reactions when the target is the donor and the projectile is the receptor of the transferred nucleons, and exchange reactions, when the target and projectile act simultaneously as donor and receptor. Heavy-ion transfer reactions are highly peripheral ones, meaning that only single-particle

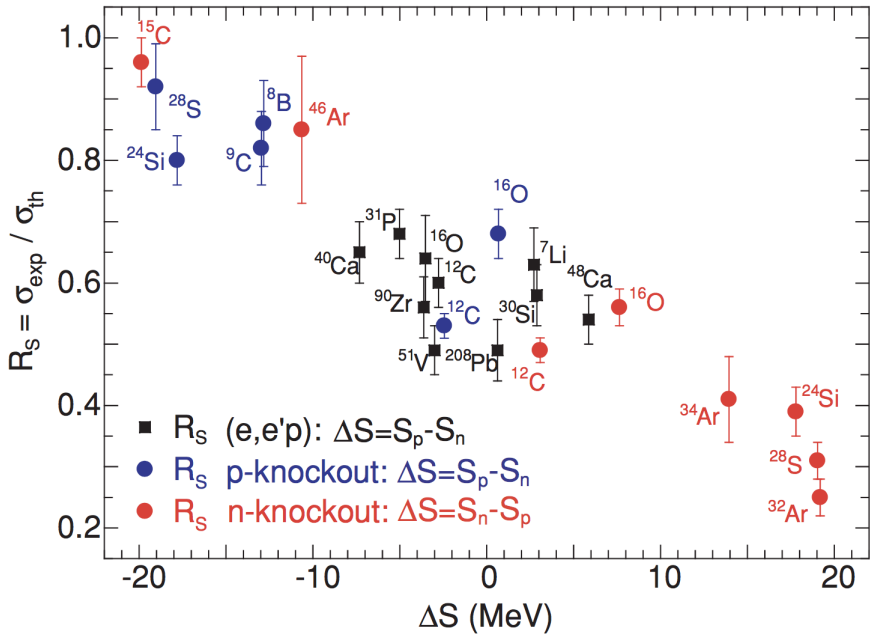

Figure 1.4: Quenching factors of experimental knockout cross sections relative to theoretical ones as a function of the asymmetry in proton-neutron separation energies. From [28].

excitations around the Fermi level and surface vibrations are probed. Usually, the reduced wavelength is much smaller than the interaction region given by the sum of the two nuclear radii so that the application of the semiclassical approximation is valid. The semiclassical formalism of transfer reactions closely follows that of Winther and Alder for Coulomb excitation reactions[29, 30]. In this description, the total time-dependent wavefunction of the system, $|\Psi(t)\rangle$, is expanded in terms of channel wavefunctions $|\psi_\beta\rangle$,

$$|\Psi(t)\rangle = \sum_\beta c_\beta(t)\,|\psi_\beta\rangle\, e^{-i(E_\beta t + \delta_\beta(t))/\hbar} \tag{1.10}$$

with the phase $\delta_\beta(t)$ given by

$$\delta_\beta(t) = \int_{-\infty}^{t} \mathrm{d}t\, \mathcal{L}_\beta(t) \tag{1.11}$$

being $\mathcal{L}_\beta(t)$ the Lagrangian of the relative motion in channel β. The time-dependent Schrödinger equation yields the following system of differential equations for c_β:

$$\dot{c}_\beta(t) = \frac{i}{\hbar} \sum_\gamma c_\gamma(t)\,\langle\omega_\beta|\,(V_\gamma - U_\gamma)\,|\psi_\gamma\rangle\, e^{-i[(E_\gamma - E_\beta)t - (\delta_\gamma(t) - \delta_\beta(t))]/\hbar} \tag{1.12}$$

where the state vectors $|\omega_\beta\rangle$ constitute a dual base constructed from the overlaps $\langle\psi_\gamma\,|\,\psi_\beta\rangle$. The above system is solved with the condition that the system is initially

prepared in the entrance channel. One of the main ingredients of eq. (1.12) are the transfer form factors modulating the channel probabilities,

$$f_{\beta\gamma}(\vec{k}, \vec{r}) = \langle \omega_\beta | \left(V_\gamma - U_\gamma \right) | \psi_\gamma \rangle \tag{1.13}$$

where $\vec{k}$ is the transferred momentum and $\vec{r} = \frac{1}{2}(\vec{r}_\beta + \vec{r}_\gamma)$. Form factors for inelastic excitations are usually calculated as the product of an empirical deformation parameter measuring the collectivity of the state and the radial derivative of the average potential in the entrance and exit channels. Approximate parametrizations of form factors for single-particle transfers have been derived by Sørensen and Broglia[31] and by Quesada et al.[32] in the low-energy limit, using average and phenomenological parametrizations of single-particle densities, potentials and wave functions around the Fermi surface that are at the basis of more complex multinucleon transfers. Although the role of multistep sequential transfer has been emphasized for the latter since the failure of the DWBA in reproducing absolute cross sections[33], multinucleon transfer reactions pose, however, a more complex scenario as significant enhancements are observed in the transfer probability of 2 nucleons with respect to the expectation from a sequential transfer[34].

Since the reaction mechanism is not fully understood, it is often resorted to some well established results for a qualitative understanding of the data. One of them is the strong dependence of the cross section on the Q-value, stemming from the existence of a Q-value window. The amplitude c_β is given in first-order perturbation theory as[35]

$$c_\beta(t \to \infty) = \frac{1}{i\hbar} F_\beta(r_0, Q_\beta) \sqrt{\frac{2\pi}{\alpha \ddot{r}_0}} \exp\left[-\frac{(Q_\beta - Q_{\text{opt}})^2}{2\hbar^2 \alpha \ddot{r}_0} \right] \tag{1.14}$$

where $\ddot{r}_0$ is the acceleration at the distance of closest approach and Q_{opt} is the optimum Q-value, for which an expression can be obtained by matching the classical trajectories in the entrance and exit channels[36],

$$Q_{\text{optimum}} = Q_{\text{gg}} - E^*_{\text{optimum}} = \frac{Z_3 Z_4 - Z_1 Z_2}{Z_3 Z_4} K_{\text{CM}} \tag{1.15}$$

Here, the subscripts $1, 2$ refer to the target and the projectile whereas $3, 4$ correspond to the target-like and the beam-like nucleus. The predictions of eq. (1.15) have been benchmarked against the experimental Q-value distributions obtained at different center of mass energies in many cases, such as in the ^{208}Pb+^{16}O reaction[34] where a smooth increase of the excitation energy with the CM energy is measured in all transfer channels with at least one transferred proton. Furthermore, isotopic yields after transfer, such as those shown in figure 1.5, generally show an exponential dependence on the ground state to ground state Q-value within an isotopic chain. The important

role in the reaction mechanism of the change in Coulomb energy between the entrance and exit channel is also apparent in the figure when comparing different isotopic chains, whose curves present different offsets. Therefore an effective Q value corrected for the change in Coulomb energy is often found in qualitative discussions,

$$Q_{\text{eff}} = Q - \frac{Z_3 Z_4 - Z_1 Z_2}{R} e^2 \tag{1.16}$$

Other dependencies of Q_{eff} have been captured as well, in particular with the number of transferred nucleons. A linear dependence on ΔN is predicted from the semiclassical model imposing the velocity-matching condition. Alternatively, the energy dissipation was modeled by Karp et al.[38] by assuming a phenomenological frictional force proportional to the velocity, in which case the formula relating the Q-value and the number of transferred nucleons depends on a single free parameter and was found to satisfactorily reproduce the data.

It is also a well established empirical feature that, in general, the partition of the excitation energy in transfer reactions tends to be governed by the flow of the transferred nucleons[39]. In fact, qualitative agreement with experiment can be achieved

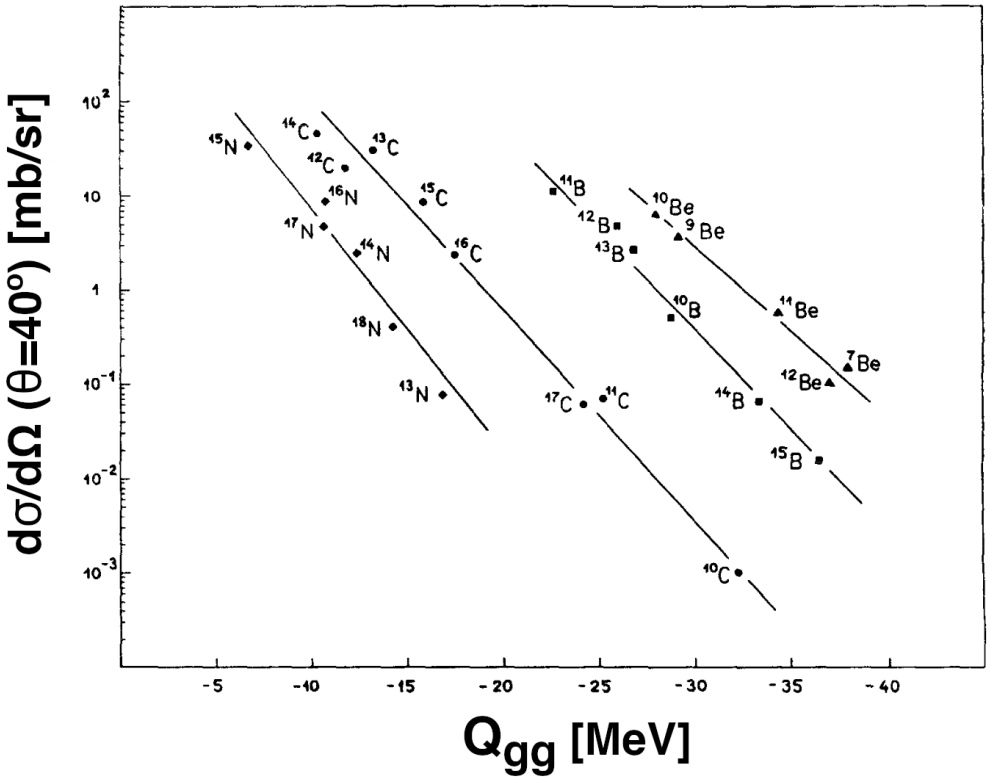

Figure 1.5: Dependence of the differential cross section for multinucleon transfer on the ground-state-to-ground-state Q-value for the projectile-like products observed in the ^{232}Th + ^{12}C reaction. The figure was adapted from [37].

by simple semiclassical models of the reaction dynamics[36, 40], in which the receptor nucleus absorbs the incoming momentum of the transferred nucleon or cluster. The mass asymmetry between the receptor and the donor seems also to play a role, specially at low excitation energies as observed from few nucleon transfers in normal kinematics with Li projectiles[41] and also in inverse kinematics with a ^{238}U beam[42], with little or no excitation of the light reaction product in all cases, in contrast with the results shown in ref. [43] for the more symmetric case of the single-neutron pickup reactions ^{161}Dy(^{58,61}Ni, ^{59,62}Ni)^{160}Dy in which the residual ^{59,62}Ni nuclei share a significant amount of the excitation energy.

An even simpler evaluation of the first-order transfer amplitude was performed by Brink[44]. Only the transfer of a spinless cluster with mass m from a structureless projectile to a structureless target was initially considered. The projectile impinges on the target nucleus with velocity v, and the cluster is initially orbiting with angular momentum ℓ_1 in the reaction plane around the core. After the transfer, the cluster is orbiting around the target with angular momentum ℓ_2 in that plane. The momentum of the cluster before the transfer is $p_i = mv - \hbar\lambda_1/R_1$ whereas after the transfer it becomes $p_f = \hbar\lambda_2/R_2$. Here, $R_{1,2}$ are the radii of the stripped donor and the receptor. The scheme of the transfer process and the choice of the reference frame for the analysis of the reaction kinematics is given in figure 1.6.

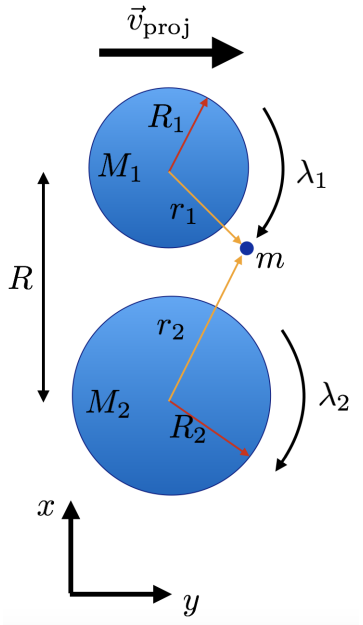

Figure 1.6: Sketch of the transfer reaction and the reference frame used for obtaining Brink's kinematical matching conditions.

The transfer probability is maximum in this model when the cluster is as close as possible to both nuclei during the grazing collision. It is written as

$$P = P_0(R) \left| Y_{\ell_1\lambda_1}\left(\frac{\pi}{2}, 0\right) Y_{\ell_2\lambda_2}\left(\frac{\pi}{2}, 0\right) \right|^2 \exp\left[-\left(\frac{R\Delta k}{\sigma_1}\right)^2 - \left(\frac{\Delta\ell}{\sigma_2}\right)^2 \right] \tag{1.17}$$

The above equation implies the existence of kinematical matching conditions, namely conservation of linear ($\Delta k = 0$) and angular momentum ($\Delta\ell = 0$) that maximize the

transfer probability. The effect of the uncertainty principle is present in the smearing introduced by σ_1 and σ_2. The quantities $\Delta\ell$ and Δk are given in this model by

$$\Delta k = \frac{mv}{\hbar} - \frac{\lambda_1}{R_1} - \frac{\lambda_2}{R_2} \approx 0 \tag{1.18}$$

$$\Delta\ell = \lambda_2 - \lambda_1 + \frac{1}{2}\frac{mv}{\hbar}(R_1 - R_2) + \frac{RQ_{\text{eff}}}{\hbar v} \approx 0 \tag{1.19}$$

All the above means that there is a selectivity, of kinematical origin, in the angular momentum of the states populated in the reaction. For a stripping reaction, large negative Q_{eff} values foster large positive $\lambda_2 - \lambda_1$ values and also large $\lambda_2 + \lambda_1$ ones. Charge transfer, on the other hand, will enlarge Q_{eff} thus favoring a smaller angular momentum transfer over a larger one, specially in reactions involving heavier nuclei such as ^{208}Pb. The population of stretched two-neutron configurations and high-spin states in ^{210}Pb by means of the ^{208}Pb(α,^{2}He)^{210}Pb reaction[45, 46], in contrast to the well-known preferential population of low-spin states in (t, p) reactions, is an example of this selectivity.

Anyas-Weiss et al.[47] extended the model by incorporating structure effects, with the main ingredients being the transition amplitudes evaluated as in eq. (1.17) and spectroscopic amplitudes for the breakups of the donor and the receptor in a core plus a transferred cluster. Their formulae explicitly demonstrate that even with a high level of approximation, the population of final states in the two residual nuclei will in general be correlated.

1.3 γ-ray spectroscopy

The study of γ rays from excited nuclei following a nuclear reaction is a qualified tool to provide valuable information regarding the nature of the nuclear excited states. The power of this technique is based on the knowledge of the electromagnetic interaction mediating the deexcitation process and the availability of sensitive instrumentation involving either larger detection efficiencies, as in scintillator arrays, or the larger energy and position resolutions achieved with modern HPGe arrays. Not only excitation energies and level schemes can be constructed in γ-ray spectroscopy experiments by means of temporal coincidences and γ-ray intensities, but also the angular momentum and parity of the excited states can be accessed by means of γ-ray directional correlations as long as the reaction mechanism leaves the nucleus in an oriented state (which is the case in e.g. Coulomb excitation and heavy-ion fusion-evaporation reactions), or otherwise $\gamma - \gamma$ correlations, the latter typically used in experiments in which prompt γ rays following β decays are detected. Moreover, specific techniques have

been developed that enable a direct determination of nuclear lifetimes in the same γ-ray spectroscopy experiment. These topics are briefly introduced in the following sections. The first of them is a general introduction following the book of Hamilton[48]. The determination of angular momentum and parity of excited states from the angular distribution and the linear polarization is introduced in section 1.3.2. The reviews of K. P. Lieb[49], Alexander and Forster[50] and Nolan[51] are followed in the last section describing the DSAM.

1.3.1 Transitions between nuclear excited states

The width of an excited state is inversely proportional to its lifetime, $\Gamma = \frac{\hbar}{\tau}$, and stems from the contribution of all the deexcitation paths available to the state. They generally include particle and γ-ray emission of all the allowed multipolarities, the latter related to the angular momentum carried off by the photon. The partial widths of all these processes add up to yield the total width,

$$\Gamma = \sum_n \Gamma_n = \sum_n \frac{\hbar}{\tau_n} \tag{1.20}$$

We use the above equation for calculating the partial lifetimes from the branching ratios and competing particle-emission channels, given the lifetime τ of the level and provided that all the decay paths are known.

Electromagnetic transitions can be of electric or magnetic type depending on the electromagnetic operator $\mathfrak{M}$ mediating the transition. The partial widths for γ decay can be expressed in terms of these operators as

$$\Gamma_L = \frac{8\pi(L+1)}{L[(2L+1)!!]^2}\left(\frac{E_\gamma}{\hbar c}\right)^{2L+1} \mathrm{B}(\pi L,\, J_f \to J_i) \tag{1.21}$$

with $\mathrm{B}(\pi L,\, i \to f)$ being the reduced transition probability of π type and multipolarity L,

$$\mathrm{B}(\pi L,\, f \to i) = \frac{1}{2J_i+1}\,|\langle f \|\, \mathfrak{M}(\pi L)\, \| i\rangle|^2 \tag{1.22}$$

The above equations illustrate the usefulness of the γ decay as a probe to nuclear structure, since the lifetime of a transition is sensitive to the wave function of the initial and final states. Hence, reduced transition probabilities can be extracted from experiment and compared with model predictions. Experimental results refer to either the reduced transition probability for excitation, $\mathrm{B}(\pi L)\uparrow$, or for decay, $\mathrm{B}(\pi L)\downarrow$. The relationship between both is

$$\mathrm{B}(\pi L)\uparrow = \frac{2J_i+1}{2J_f+1}\mathrm{B}(\pi L)\downarrow \tag{1.23}$$

Blatt et al. extracted estimates for single-particle transitions[52]. They are known as "Weisskopf units" (W.u.) and give an immediate idea of the collectivity of the transition. Table 1.1 gives the relationship between the lifetime and the reduced transition probability in W.u., e^2fm^{2L} for electric transitions and in $\mu_N^2 fm^{2L-2}$ for the magnetic ones. The multipolarity of the transition is restricted by the angular momentum selection rules to a limited set of values that depends on the initial and final angular momenta,

$$|J_i - J_f| \leqslant L \leqslant |J_i + J_f| \tag{1.24}$$

Furthermore, electric transitions with odd (even) multipolarity link levels with opposite (same) parity, whereas only the inverse is true for magnetic transitions. Typically, only a couple of multipoles contribute to the sum in eq. (1.20) so that an electromagnetic multipole mixing ratio δ for transitions between an initial state i and a final state f is defined as

$$\delta^2(\pi L/\pi' L') = \frac{\Gamma(\pi L,\, i \to f)}{\Gamma(\pi' L',\, i \to f)} \tag{1.25}$$

and can be experimentally extracted from the γ-ray angular distribution and/or $\gamma - \gamma$ correlation measurements. Specialized methods, such as the Coulex multipolarimetry one[53, 54] in Coulomb excitation experiments, have been proposed for the direct experimental determination of specific mixing ratios. In those cases where only the lowest two multipoles, L and $L+1$, contribute to the transition probability (that is, $\Gamma = \Gamma_L + \Gamma_{L+1}$), the decay width is written in terms of the mixing ratio as

$$\Gamma_L = \frac{1}{1+\delta^2}\Gamma \tag{1.26}$$

$$\Gamma_{L+1} = \frac{\delta^2}{1+\delta^2}\Gamma \tag{1.27}$$

One of the most common cases found in the practice is E2/M1 mixing. The B(E2) and B(M1) values can be extracted in such a case from the lifetime of the transition

L	B(EL)↓ [e^2fm^{2L}]	B(EL)↓ [W.u.]	B(ML)↓ [$\mu_N^2 fm^{2L-2}$]	B(ML)↓ [W.u.]
1	$\frac{6.287\times10^{-16}}{\tau E_\gamma^3}$	$\frac{9.754\times10^{-15}}{\tau E_\gamma^3 A^{2/3}}$	$\frac{5.697\times10^{-14}}{\tau E_\gamma^3}$	$\frac{3.182\times10^{-14}}{\tau E_\gamma^3}$
2	$\frac{8.156\times10^{-10}}{\tau E_\gamma^5}$	$\frac{1.373\times10^{-8}}{\tau E_\gamma^5 A^{4/3}}$	$\frac{7.391\times10^{-8}}{\tau E_\gamma^5}$	$\frac{4.479\times10^{-8}}{\tau E_\gamma^5 A^{2/3}}$
3	$\frac{1.751\times10^{-3}}{\tau E_\gamma^7}$	$\frac{2.948\times10^{-2}}{\tau E_\gamma^7 A^2}$	$\frac{1.586\times10^{-1}}{\tau E_\gamma^7}$	$\frac{9.612\times10^{-2}}{\tau E_\gamma^7 A^{4/3}}$

Table 1.1: Expressions relating the lifetime of a transition and the reduced transition probability, for the lowest 3 multipoles. τ is in seconds, E_γ in MeV. $A = Z + N$ is the mass number.

as long as the mixing ratio is known. Under the phase convention of [48], the E2/M1 mixing ratio is given by

$$\delta(\mathrm{E2/M1},\, i \to f) = \frac{\sqrt{3}}{10}\frac{E_\gamma}{\hbar c}\frac{\langle f \| \, \mathfrak{M}(\mathrm{E2}) \, \| i\rangle}{\langle f \| \, \mathfrak{M}(\mathrm{M1}) \, \| i\rangle} \tag{1.28}$$

One of the decay paths that will compete with the emission of γ radiation in depopulating a certain level is internal conversion. In this process, the nucleus transfers the energy of the transition to a nearby electron resulting in the ejection of the electron, now in an unbound state, plus an X ray following the rearrangement of the remaining atomic electrons. The transition probability between the initial and the final state is the result of at least the probability for γ ray emission and internal conversion,

$$\Gamma(i \to f) = \Gamma(\gamma) + \Gamma(K) + \Gamma(L_{\mathrm{I,II,III}}) + \ldots \tag{1.29}$$

where, depending on the atomic shell involved, one speaks of K, $L_{\mathrm{I,II,III}}$, M_{I}, etc. conversion. The effect of internal conversion has to be taken into account when comparing with theoretical transition probabilities. This is done by means of a total conversion coefficient α_T, defined as the ratio between the probability of internal conversion relative to γ emission,

$$\alpha_T = \frac{\sum_n \Gamma(e^-, n)}{\Gamma(\gamma)} \tag{1.30}$$

The lifetime of the transition is now written in terms of the lifetime of the γ decay and the conversion coefficient as

$$\tau_{\mathrm{transition}} = \frac{1}{1+\alpha_T}\tau_\gamma \tag{1.31}$$

The conversion electrons are not measured in any of the experimental cases presented in this thesis. Instead, γ ray intensities and transition probabilities are corrected for internal conversion when relevant using calculated conversion coefficients from BrIcc[55].

1.3.2 γ-ray emission from aligned states

Certain reaction mechanisms, such as fusion-evaporation, result in an anisotropic population of magnetic substates in the initial state with respect to a quantization axis in the laboratory. When the oriented initial state with angular momentum J_i deexcites towards a final state via γ-ray emission, the angular distribution of the radiation, $W(\theta)$, depends on the angular momenta of the excited states, the multipolarity of the radiation and the relative population parameters $P(m)$ of the

$2J_i + 1$ initial magnetic substates. Oriented distributions of angular momenta are referred to either as *polarized* or *aligned* depending on whether there is a preferred sense along the quantization axis for populating the substates that results in an asymmetric distribution of population parameters, $P(m) \neq P(-m)$. Practical applications in this work involve axial symmetry, $P(-m) = P(m)$, hence the discussion will be restricted to γ-ray emission from *aligned* states.

The degree of alignment depends on the details of the reaction mechanism. It is known that heavy ion fusion-evaporation reactions result in *oblate* alignment, in which the angular momentum is perpendicular to the beam axis, i.e. $m = 0$ substates are preferentially populated. If, on the other hand, the population is maximum for parallel or antiparallel substates, $m = \pm J_i$, the alignment is said to be *prolate*. Fragmentation reactions are known to induce some degree of prolate alignment[56].

The statistical tensor is used in order to specify the degree of orientation. It is defined as

$$\rho_k(J_i) = \sqrt{2J_i + 1} \sum_m (-1)^{J_i - m} \langle J_i \, m \, J_i \, -m | k \, 0 \rangle \, P(m) \tag{1.32}$$

where the statistical tensor for the complete alignment is often denoted as B_k,

$$B_k = \sqrt{2J_i + 1} (-1)^{J_i - m_0} \langle J_i \, m_0 \, J_i \, -m_0 | k \, 0 \rangle \tag{1.33}$$

with $m_0 = 0$ for integral spins and $m_0 = \frac{1}{2}$ for half-integral spins.

It is noticed upon inspection of the above equations that the odd-k entries of the statistical tensor vanish in aligned states. The angular distribution is written in this case for multipolarities equal to or lower than 2 as

$$W(\theta) = 1 + \underbrace{\rho_2 A_2}_{a_2} P_2(\cos\theta) + \underbrace{\rho_4 A_4}_{a_4} P_4(\cos\theta) \tag{1.34}$$

where $P_{2,4}$ are the ordinary Legendre polynomials. For a transition with mixed multipolarities L_1, L_2 and a mixing ratio $\delta_{L2/L1}$, the A_k coefficients are given by

$$A_k = \frac{1}{1 + \delta^2} \left[F_k(J_f L_1 L_1 J_i) + 2\delta F_k(J_f L_1 L_2 J_i) + \delta^2 F_k(J_f L_2 L_2 J_i) \right] \tag{1.35}$$

where the F_k coefficients are calculated in terms of Racah's $\mathcal{W}$ symbol as

$$\begin{aligned} F_k = (-1)^{J_f - J_i - 1} \sqrt{(2L_1 + 1)(2L_2 + 1)(2J_i + 1)} \times \\ \times \langle L_1 \, 1 \, L_2 \, -1 | k \, 0 \rangle \, \mathcal{W}(J_i \, J_i \, L_1 \, L_2 \, ; \, k \, J_f) \end{aligned} \tag{1.36}$$

A number of tabulations of the a_k coefficients as a function of J_i and J_f exists such as the tables of Yamazaki[57] for full oblate alignment. The degree of orientation induced by the reaction mechanism is usually a priori unknown in most practical situations and

sthus treated as a free parameter that may be estimated from other known transitions. In this case, an attenuation factor α_k is defined which relates the partially aligned case with the ideal case of full alignment,

$$\alpha_k = \frac{\rho_k(J_i)}{B_k(J_i)} \tag{1.37}$$

Furthermore, since the distribution of population parameters can be well approximated by a gaussian function in terms of a single parameter σ[56, 57],

$$P(m) = \frac{\exp -\frac{m^2}{2\sigma^2}}{\sum_{m'=-J}^{J} \exp -\frac{m'^2}{2\sigma^2}} \tag{1.38}$$

the $a_{2,4}$ coefficients are automatically determined for a given attenuation factor.

Compton polarimetry

For linearly polarized radiation, the angular correlation function $W(\theta)$ introduced above has been integrated over all the angles ϵ specifying the orientation of the polarization vector with respect to the so-called polarization plane, defined by the beam direction and the momentum vector of the γ ray (see figure 1.7). If the direction of the polarization vector is measured, an additional correlation is introduced and the angular distribution for multipoles equal to or lower than 2 takes the form[58]

$$W(\epsilon, \theta) = 1 + a_2 P_2(\cos\theta) + a_4 P_4(\cos\theta) + f(\epsilon, \theta) \tag{1.39}$$

with

$$f(\epsilon, \theta) = (\pm)_{L_2=2} \frac{1}{2} \cos 2\epsilon \left[H_2(L_1 L_2) a_2 P_2^2(\cos\theta) + H_4(L_1 L_2) a_4 P_4^2(\cos\theta) \right] \tag{1.40}$$

where P_2^2 and P_4^2 are the associated Legendre polynomials. The phase factor $(\pm)_{L_2=2}$ depends on the character of the mixed multipolarities L_1 and L_2: if the $L_2 = 2$ transition is electric, then $(\pm)_{L_2} = +1$, whereas for a $L_2 = 2$ magnetic transition it is $(\pm)_{L_2=2} = -1$.

Furthermore, if the linearly polarized γ ray undergoes Compton scattering, there will be an anisotropy not only in the polar angle θ_c of the Compton-scattered γ ray but also in the azimuth angle ϕ_c of the electric vector. This dependence is given by the Klein-Nishina differential cross section,

$$\frac{\mathrm{d}\sigma}{\mathrm{d}\Omega} = \frac{r_e^2}{2} \left(\frac{E'_\gamma}{E_\gamma} \right) \left(\frac{E'_\gamma}{E_\gamma} + \frac{E_\gamma}{E'_\gamma} - 2 \sin^2\theta_c \cos^2\phi_c \right) \tag{1.41}$$

Hence choosing $\epsilon = 0°$ and $\epsilon = 90°$, there will be a dependence of the intensity as a function of both θ and ϕ, where the latter is the angle of the Compton-scattered γ ray

with respect to the polarization plane defined in figure 1.7. It then follows that for linearly polarized radiation the intensity as a function of θ and ϕ is given by

$$N(\theta,\phi) = \text{const} \times [\mathrm{d}\sigma(\phi_c = \phi)W(\epsilon = 0°,\theta) + \\ + \mathrm{d}\sigma(\phi_c = 90° - \phi)W(\epsilon = 90°,\theta)] \tag{1.42}$$

The anisotropy in the azimuth angle of the Compton-scattered γ ray can be studied using a Compton polarimetry setup wuth a twofold purpose. Firstly, the combined measurement of the a_2 and a_4 coefficients with the anisotropy in the Compton scattering as a function of ϕ can be used to deduce the multipole mixing ratio of the transition in a model-independent way, that is, without neither knowing the attenuation factor nor the individual population parameters $P(m)$: this is the goal behind the tabulation of H_2 coefficients as a function of $\delta_{L=1/L=2}$ in e.g. [58]. Secondly, for transitions with unmixed multipolarity it can be used for a direct determination of the character of the transition which is given by the phase $(\pm)_{L=2}$.

The sensitivity to the anisotropy in ϕ depends on the Compton scattering angle θ_c, the γ-ray energy and its polar angle θ. The analyzing power Σ is a way of quantifying

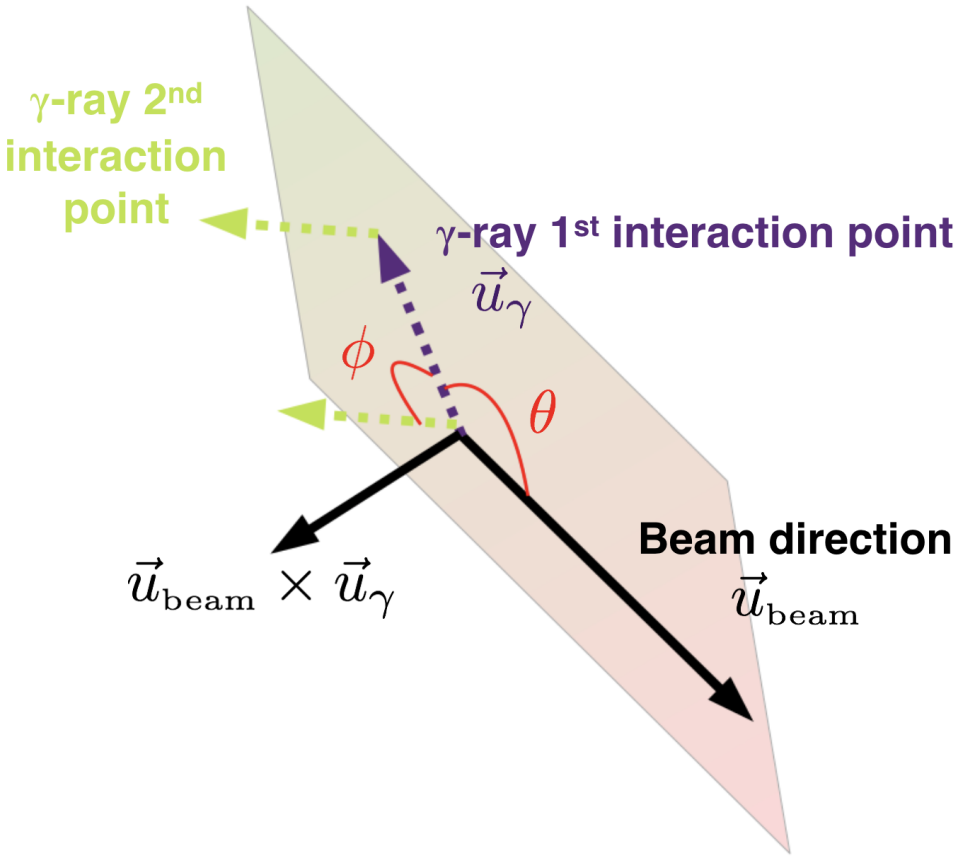

Figure 1.7: Illustration of the polarization plane and the (θ,ϕ) angles used for Compton polarimetry studies in this work.

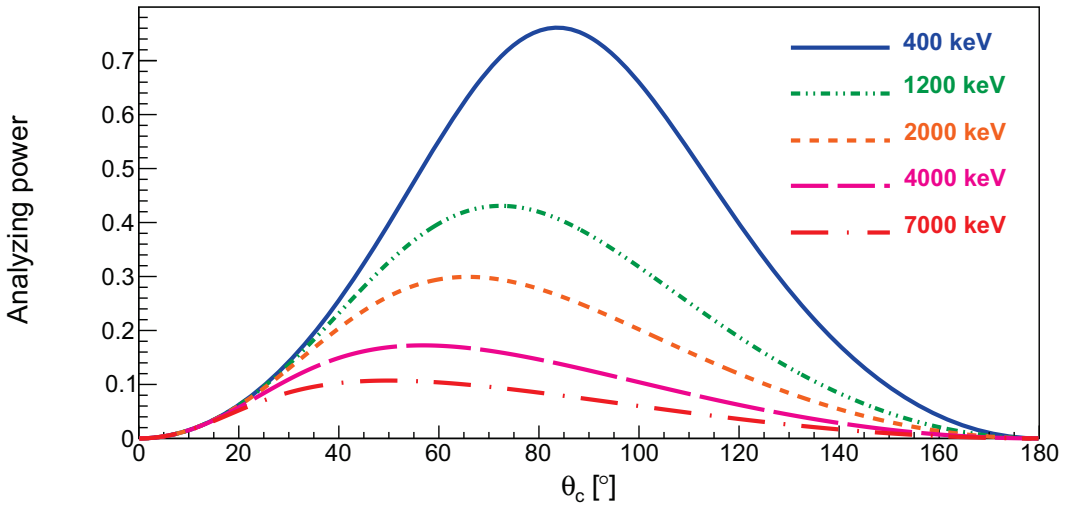

Figure 1.8: Analyzing power of a Compton polarimeter in terms of the Compton scattering angle. The curves are given for several γ-ray energies.

this sensitivity as a function of θ_c and E_γ. It is defined as

$$\Sigma = \frac{\frac{\mathrm{d}\sigma}{\mathrm{d}\Omega}(\theta_c, \phi_c = 90°) - \frac{\mathrm{d}\sigma}{\mathrm{d}\Omega}(\theta_c, \phi_c = 0°)}{\frac{\mathrm{d}\sigma}{\mathrm{d}\Omega}(\theta_c, \phi_c = 90°) + \frac{\mathrm{d}\sigma}{\mathrm{d}\Omega}(\theta_c, \phi_c = 0°)} = \frac{\sin^2\theta_c}{\frac{E'_\gamma}{E_\gamma} + \frac{E_\gamma}{E'_\gamma} - \sin^2\theta_c} \tag{1.43}$$

Calculated analyzing powers are shown in figure 1.8 in terms of θ_c for several γ-ray energies. The sensitivity of the polarimeter will be higher for low-energy γ rays scattered at θ_c angles close to 90°. The analyzing power drops steadily as the γ-ray energy increases, thus rendering this technique applicable in practice only for energies below few MeV.

The degree of linear polarization is the quantity which is often reported in Compton polarimetry analyses. It is defined as

$$P(\theta) = \frac{W(\epsilon = 0°, \theta) - W(\epsilon = 90°, \theta)}{W(\epsilon = 0°, \theta) + W(\epsilon = 90°, \theta)} = \frac{1}{Q_0}\frac{N(\theta, \phi = 90°) - N(\theta, \phi = 0°)}{N(\theta, \phi = 90°) + N(\theta, \phi = 0°)} \tag{1.44}$$

with

$$Q_0 = \frac{1 + \left(\frac{E_\gamma}{m_e c^2}\right)}{1 + \left(\frac{E_\gamma}{m_e c^2}\right) + \left(\frac{E_\gamma}{m_e c^2}\right)^2} \tag{1.45}$$

For $\theta = 90°$ the polarization is expressed in terms of a_2 and a_4 as

$$P(\theta = 90°) = (\pm)_{L_2=2}\frac{3H_2(L_1 = 1, L_2 = 2)a_2 + 1.25a_4}{2 - a_2 + 0.75a_4} \tag{1.46}$$

1.3.3 The Doppler Shift Attenuation Method (DSAM)

The frequency of the electromagnetic radiation changes between reference frames. For a γ ray emitted from a moving source with relative velocity β, its energy in the laboratory depends on β and the angle θ_L between the momentum of the γ-ray and the nucleus,

$$\frac{E_\gamma}{E_\gamma^0} = \frac{\sqrt{1-\beta^2}}{1-\beta\cos\theta_L} \approx 1+\beta\cos\theta_L \tag{1.47}$$

where E_γ^0 is the γ-ray energy in the nucleus rest frame. A direct lifetime determination is possible for lifetimes in the range between 10^{-11}-10^{-13} s exploiting the Doppler effect described by the above equation. This is at the grounds of the family of Doppler-shift methods for lifetime determination, based on the response of the Doppler-shifted energies to changes in the velocity of the emitting nucleus within time scales comparable to the lifetime. This change in the velocity can be introduced gradually in comparison with that lifetime by using a certain stopper material so that the Doppler-shift histories are "recorded" in the γ-ray spectrum, or it can be introduced in a sudden way by using a plunger device that fully stops the ion. The latter is called the Recoil Distance Doppler Shift method (RDDS) and the lifetime is extracted by a comparison of the intensity of the shifted and unshifted peaks in the spectrum. The former is referred to as the Doppler Shift Attenuation Method (DSAM) which is the subject of this section. Both methods are illustrated in figure 1.9.

The main ingredients entering in a typical DSAM experiment involve 1) the accurate description of the stopping process 2) the knowledge and precise treatment of the feeding pattern of the excited state, 3) the proper characterization of the reaction kinematics and 4) a well-characterized instrumental response and target profile. Perhaps the simplest variant of the DSA is the "centroid shift method", which is applicable in those cases where the Doppler shift is smaller than the instrumental energy resolution. Although this method is the oldest one for instrumental reasons, it is still in use and specially well suited for inelastic scattering reactions such as (p, p'γ)[59] inducing a low velocity to the recoils. Furthermore, the detection of the light charged particle enables an accurate kinematical reconstruction thus minimizing the uncertainty in θ_L as well as a controlled feeding pattern of the level based on an event-by-event Q-value selection. Having control over these factors, γ-ray spectra corresponding to different angles are sorted and the centroid of the peak is determined in each angular slice. The observed Doppler shift corresponds to γ-ray emissions at an average velocity $\bar{\beta}$, corresponding to a fraction $F[\tau]$ of the initial velocity,

$$E_\gamma = E_0(1+F[\tau]\beta_0\cos\theta_L) \tag{1.48}$$

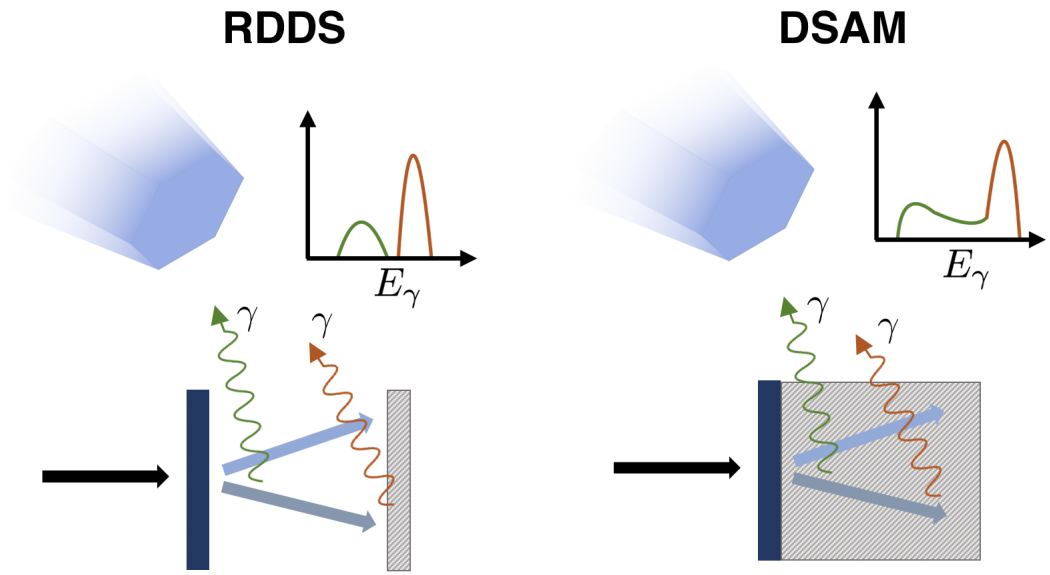

Figure 1.9: Illustration of the DSA and the RDDS techniques for lifetime determination. Elements colored in green are referred to in-flight γ-ray emissions, whereas the orange color refers to γ-ray emissions at rest.

It is clear from this example that the main ingredient for the lifetime determination is a model of the stopping process of the heavy ion in the target material, from which a curve of the attenuation factor F as a function of the lifetime is calculated and used to extract the experimental lifetime. A measurement of the peak centroid in at least two different angular slices is required for applying this technique.

As the projectile energy or the energy resolution increases, it is possible to observe a lineshape resulting from deexcitations at different velocities within the target. They are modulated by a probability distribution $P(\beta, t)$, called the stopping matrix, that depends on the lifetime and the details of the stopping process,

$$N[E_\gamma(\beta)] = \int_0^\infty \mathrm{d}t \, \frac{1}{\tau} \, P(\beta, t) \, n(t) \tag{1.49}$$

Theoretical lineshapes can be calculated given a model of the stopping process and compared with the experimental one. Moreover, a measurement at a single angular slice can be used to extract the lifetime, since the sensitivity to the lifetime is now given by the deceleration process itself. Nevertheless, the modern approach of APCAD[60], which is specially well suited for position-sensitive detectors, makes use of both the lineshape and its dependence with the polar angle in order to maximize the sensitivity to the lifetime by performing a two-dimensional fit. Figure 1.10 shows sample lineshapes calculated with APCAD.

Although the stopping power is an essential ingredient in any DSAM analysis, the available experimental stopping powers in wide energy ranges are rather scarce so that

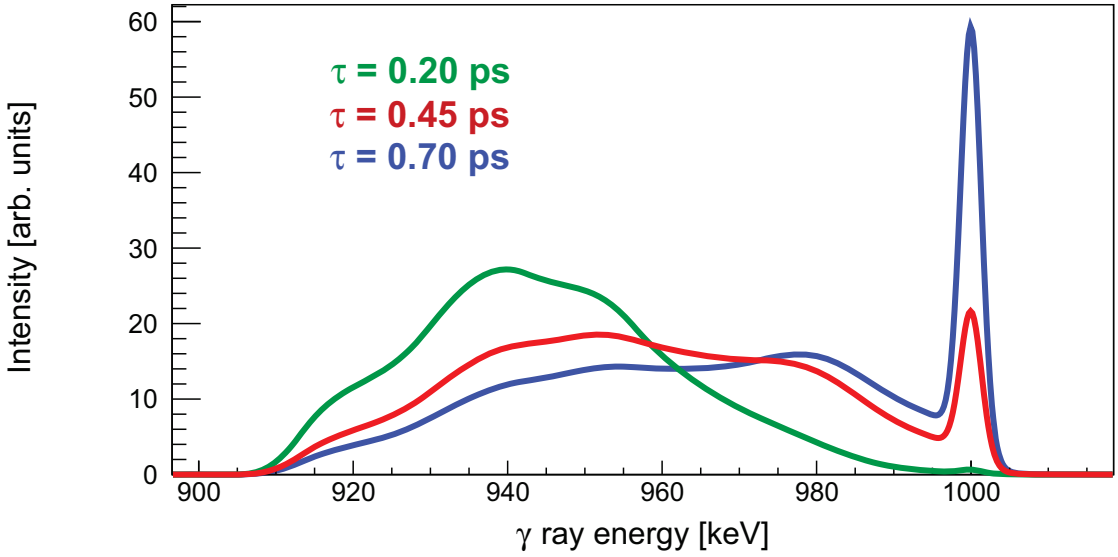

Figure 1.10: Illustration of the DSAM sensitivity to subpicosecond lifetimes. The spectra show integrated lineshapes in the entire range of particle scattering angles with a selection on particle-γ angles between 120° and 160°. The lineshapes correspond to a ficticious 1-MeV transition in ^{212}Po produced in the α transfer reaction ^{12}C(^{208}Pb,^{8}Be)^{212}Po at a CM energy of 64.7 MeV. The stopper material is a 20-µm thick Au backing.

it is usually resorted to pre-calculated tables obtained under several approximations. The energy loss of a heavy ion along its path in the material is the result of two contributions: energy release to the surrounding electrons (electronic stopping) which does not change the ion trajectory to a significant extent, and scattering by the atoms of the stopper material (nuclear stopping) that deviates the ion from its original direction of motion,

$$\frac{\mathrm{d}E}{\mathrm{d}x} = \left(\frac{\mathrm{d}E}{\mathrm{d}x}\right)_{\mathrm{el}} + \left(\frac{\mathrm{d}E}{\mathrm{d}x}\right)_{\mathrm{nuc}} \tag{1.50}$$

The effect of the nuclear stopping power was often treated in the past using the approximate formulae of Blaugrund[61]. Since then it has become feasible to determine its effect by means of a Monte Carlo simulation so that they have become the usual approach for modelling the nuclear stopping. For beam energies of a few $^{\mathrm{MeV}}/_{\mathrm{u}}$, the nuclear stopping power represents only a few percent of the total stopping power save in rare exceptions.

Let us introduce below the most common stopping power theories used in DSAM analyses.

- **Lindhard-Scharff-Schiøtt (LSS)**[62]: these stopping powers are obtained from the Thomas-Fermi model of the atom and are written in terms of dimensionless

energy and range parameters,

$$\varepsilon = E\frac{aM_2}{Z_1Z_2e^2(M_1+M_2)} \quad , \qquad \rho = RNM_2 4\pi a^2 \frac{M_1}{(M_1+M_2)^2} \tag{1.51}$$

where the subscript 1 refers to the projectile, 2 refers to the stopping medium and $a = a_0 0.8853(Z_1^{2/3}+Z_2^{2/3})^{-1/2}$ with a_0 the Bohr radius. Using the LSS variables the electronic stopping power is found to be proportional to $\sqrt{\varepsilon}$,

$$\frac{d\varepsilon}{d\rho} = \kappa(Z_1,Z_2,A_1,A_2)\sqrt{\varepsilon} \quad \text{with} \quad \kappa \cong Z_1^{1/6}\frac{0.0793Z_1^{1/2}Z_2^{1/2}(A_1+A_2)^{3/2}}{(Z_1^{2/3}+Z_2^{2/3})^{3/4}A_1^{3/2}A_2^{1/2}} \tag{1.52}$$

and a universal curve for the nuclear stopping power $(\mathrm{d}\varepsilon/\mathrm{d}\rho)_{\mathrm{nuc}}$ is found. The scaling factor of the LSS electronic stopping power multiplying $\sqrt{E}$ is not used for practical purposes since pronounced oscillations in the experimental stopping powers in terms of Z_1 and Z_2 due to atomic structure have been observed and are not reproduced within the theory. The nuclear stopping power, on the other hand, is widely used but it is scaled down by 30% in order to account for ion channeling[63]. A tabulation of the $(\mathrm{d}\varepsilon/\mathrm{d}\rho)_{\mathrm{nuc}}$ function up to $\varepsilon = 600$ is given in [64].

- **Semiempirical Northcliffe-Schilling tables**[65]: these tables of electronic stopping power have been constructed from the stopping curves in Al of various heavy ions using the concept of effective heavy-ion charge. The fundamental assumption is that the relative stopping powers in different materials at a given velocity are independent of the beam identity. The stopping power is often scaled by a 10%-30% factor in real aplications.

- **SRIM**[66]: the electronic stopping powers and the parameters of the screened Coulomb interatomic potential used in the quantum mechanical calculations have been adjusted to a vast amount of experimental data. SRIM stopping powers for beam energies above $1\,^{\mathrm{MeV}}/_{\mathrm{u}}$ are accurate within 10% in most cases[63]. Figure 1.11 shows calculated stopping powers for ^{212}Po ions in Au according to the model of SRIM.

The reaction mechanism used for populating the states of interest should be carefully chosen in DSAM experiments. Heavy-ion fusion-evaporation reactions are characterized by intense side-feeding proceeding via fast statistical γ rays from the continuum. Side feeding times are dependent on the projectile-target combination and range from tens of picosecond to few picoseconds. Influence of side-feeding times on the observed transition lifetimes are usually characterized by gating on discrete feeders as well

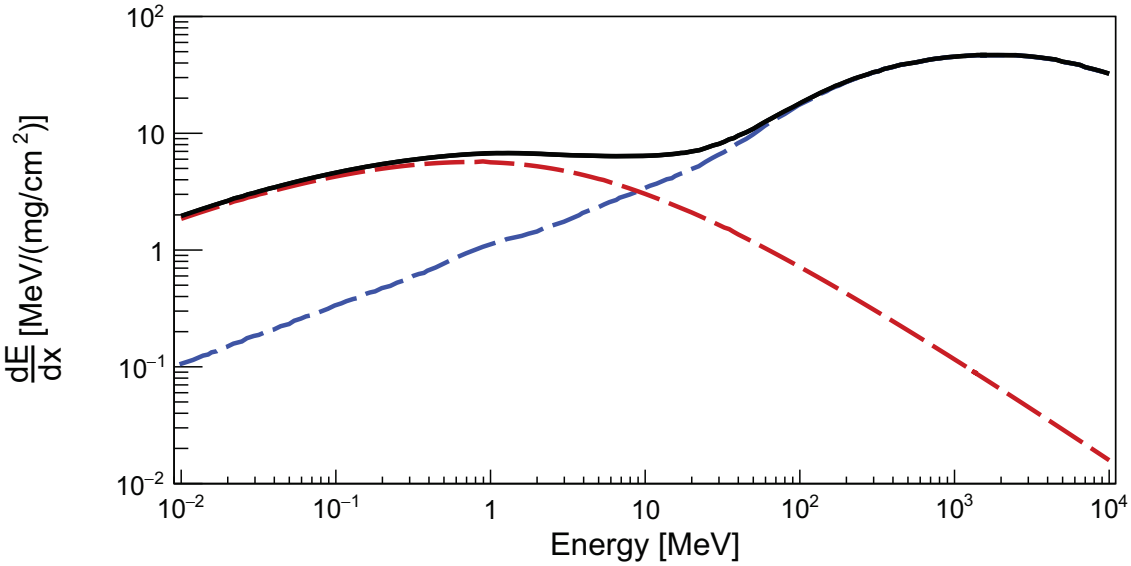

Figure 1.11: SRIM stopping power of ^{212}Po ions in Au as a function of the ion energy. The nuclear and electronic components of the total stopping power are represented by the red and blue dashed lines, respectively.

as transitions below in the cascade. This usually implies the necessity for joint lifetime analysis in the cascade which is not always possible, so that fusion-evaporation reactions are not very well suited for the DSAM in general. Transfer reactions, on the other hand, have been widely used for DSAM analyses, and it is assumed that as a consequence of the selectivity of the reaction, from both the Q-value and angular momentum points of view, the side feeding is negligible. Moreover, similarly as in inelastic scattering, transfer reactions in which the light transfer partner is detected permit a minimization of unwanted feeding in the level of interest by performing a full kinematical reconstruction, hence enabling lineshape analyses also in singles spectra.

1.4 Structure of the thesis

This thesis work is divided in two parts each one corresponding to a different research topic. The analysis and results of an experiment aimed at researching α clustering in ^{212}Po is presented in the first part. The second part addresses the topic of mirror-energy differences in the fp shell through the first γ-ray spectroscopy of the proton-rich nucleus ^{56}Zn. The data from the latter experiment is shared with Sara Pigliapoco from the University of Padova who is in charge of the analysis of nuclei other than ^{56}Zn. The ^{56}Zn data have been analyzed in the latest stage of my PhD.

The tools and techniques common to both parts that are used for obtaining the results of this work have been introduced in this chapter. Each part starts with an

introductory chapter presenting the experimental case within the framework of the current research on the topic and the motivation of the experiment. The data analysis and conclusions are explained in separate chapters after introducing the relevant information regarding the experimental setup.

Part I

α clustering in heavy nuclei: the case of ^{212}Po

Chapter 2

Introduction

2.1 Clustering in nuclei

2.1.1 α clusters in light nuclei

The concept of the α particle as the building block of the nucleus has been present since the earliest models of the nucleus[67]. These early models were based on the additional binding energy found in light $N = Z$ nuclei and the great stability of the α particle that would prevent its dissolution in a mean field structure with the protons and neutrons of the parent nucleus. In this picture, all proton-proton, neutron-neutron and proton-neutron correlations would contribute to the additional binding energy. Even before, in a seminal work of Gamow[68], the α decay was described as a process in which a preformed α particle tunnels through the potential barrier in the parent nucleus. The success of this model was one of the earliest triumphs of quantum mechanics.

Although the idea of the α particle as a fundamental building block of the nucleus was eventually replaced by the shell model which is based on the degrees of freedom of the individual nucleons, several experimental findings in light conjugate nuclei revealed the existence of extremely deformed nuclear shapes, called nuclear molecules. These were explained by the clusterization of α particles inside the nucleus and among their experimental fingerprints is the presence of rotational behavior with moments of inertia compatible with such cluster structures in combination with large α decay widths comparable to the Wigner limit[1][69, 70]. Moreover, it was noticed by Ikeda, based on the available experimental information for ^{12}C, ^{16}O and ^{20}Ne, that the lowest-lying cluster states are located near the energy threshold for the breakup into their components[71]. This prompted the so-called Ikeda diagram for the light $N = Z$

[1]This quantity is an estimate of the decay width for a fully preformed α particle within the parent nucleus.

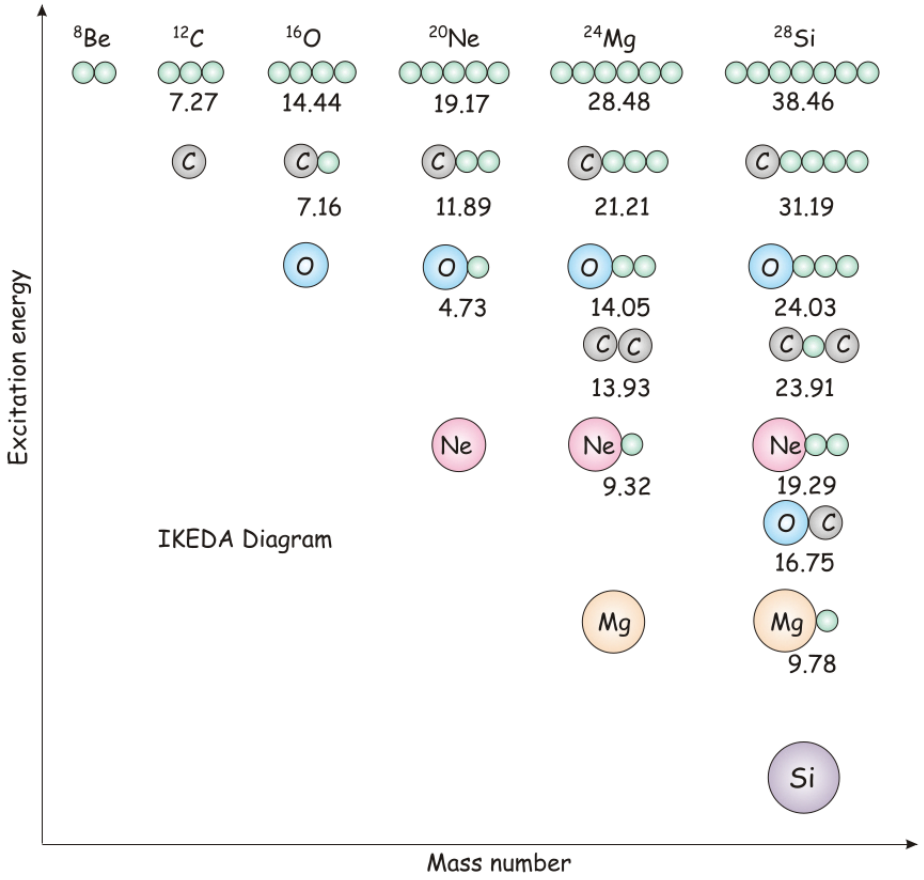

Figure 2.1: Ikeda diagram. Structures involving the arrangement of one or multiple α particles around an $N = Z$ core are predicted to occur near the separation energy of the structure into its constituents. Figure taken from [72].

nuclei that gives an estimate of the excitation energy required for the formation of cluster states. The diagram is represented in figure 2.1.

All these findings pointed to clustering as a well established feature, like the existence of the mean field itself, of the nuclear quantum many-body system, for light and medium-mass nuclei up to ^{56}Ni. The ^{8}Be, ^{12}C, ^{16}O and ^{20}Ne nuclei have been the topic of a vast number of studies and showcase the salient features of α clustering in light nuclei. Some of the evidence for the occurrence of α cluster structures in light nuclei is briefly introduced in the next sections.

^{8}Be

A 2^+ state at 3.03 MeV and a 4^+ at 11.35 MeV are the first two excited states of ^{8}Be. The ratio of their excitation energies is 3.7, close to a value of 3.3 expected from a rigid rotor and, furthermore, they lie above the α-decay threshold which makes them likely candidates for α cluster states according to the Ikeda diagram. The

rotational character of its first excited states has been proposed from the ab initio calculations of Wiringa[73] that predicted a dumbbell-like shape for the 2_1^+ and 4_1^+ state as well as for the ground state, being the rotation of the $\alpha - \alpha$ system around its center of mass responsible for its moment of inertia, $\hbar^2/2\mathcal{I} = 0.51$. Electromagnetic transition probabilities within the ground-state band represent a testing ground for such calculations, however its measurement is a challenge from the experimental point of view due to the extremely small branching ratio ($< 10^{-7}$) of γ ray emission against α decay, the predominant decay mode in ^{8}Be($0_1^+, 2_1^+, 4_1^+$). The B(E2, $4_1^+ \longrightarrow 2_1^+$) has been measured twice by Datar[74, 75] in dedicated experiments using the radiative capture reaction ^{4}He+^{4}He. The B(E2) was found in good agreement with the predictions of the ab initio calculations.

^{12}C

The excitation energies of the 2_1^+ and 4_1^+ state in this nucleus, 4.4 MeV and 14.1 MeV, clearly resemble the position of the corresponding states in ^{8}Be. In the algebraic cluster model proposed by Bijker[76], which is based on a 3α arrangement, these are identified as members of a rotational band having $K^\pi = 0^+$ as the head band and comprising rotations around a symmetry axis within the plane containing the α particles, with a moment of inertia given by the rotations of the $\alpha - \alpha$ system in ^{8}Be. Rotations around an axis perpendicular to the 3α plane would give to a series of negative parity states having $K^\pi = 3^-$ as band head. Simple expressions for transition probabilities and excitation energies are deduced from the model. They suggest the 3^- state at 9.6 MeV as the band head, an assertion supported by its large α decay width. Furthermore, a 4^- state at 13.4 MeV and a 5^- at 22.5 MeV are likely candidates for higher lying 3α states[78]. Moreover, the predicted B(E2, $2_1^+ \longrightarrow 0_1^+$) of 8.4 e^2fm^4 is in very good agreement with the experimental value of 7.6(4) e^2fm^4. A more complicated puzzle is the 0_2^+ state, called the Hoyle state, whose existence was conjectured in the 50's as a mechanism for explaining the stellar nucleosynthesis of ^{12}C and experimentally confirmed soon after[79, 80]. From the experimental point of

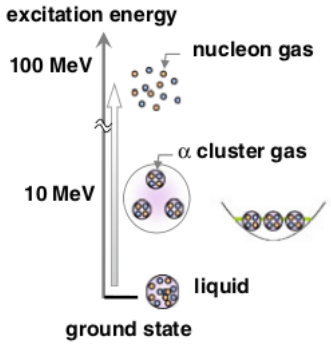

Figure 2.2: Illustration of the excitation energies of the α gas and the nucleon gas in ^{12}C. Figure taken from [77].

view, its cluster structure is well established based on its much larger radius than in ^{12}C(GS), its α decay properties and in particular its ^{8}Be+α decay reproduced in 3α cluster models and the failure of state-of-the-art shell model calculations in reproducing its low excitation energy[81–84]. Interpretations of this state as an α gas or a loosely bound α orbiting around an ^{8}Be have been proposed[85, 86].

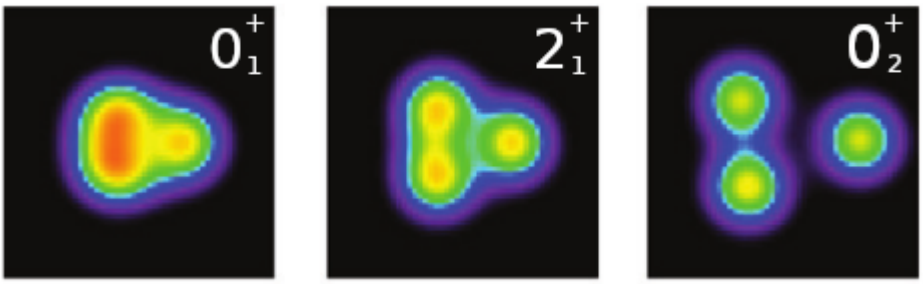

Figure 2.3: ^{12}C density distributions for the ground state and the first two excited states calculated by AMD-VAP. Figure adapted from [87].

^{16}O and ^{20}Ne

^{16}O is a doubly magic nucleus and its ground state is described as an $N = Z = 8$ closed shell for both neutrons and protons. Its first excited state, a 0^+ at 6.05 MeV, lies at an exceptionally low excitation energy given the estimated separation of $\hbar\omega \approx$ 15 MeV between the p and the sd shells. It is now well established that this state is deformed and involves a 2 particle-hole excitation $[(p)^{-2}(sd)^2]$, being such deformation responsible for the reduced gap between the p and sd orbits. Positive parity states $2^+, 4^+, 6^+$ on top of the 0^+_2 were experimentally observed, as well as negative parity states $3^-, 5^-, 7^-$ above a 1^- state at 9.59 MeV pointing to rotational behavior. The latter ones had large α decay widths and the large moments of inertia of the negative and positive parity bands were almost identical. Based on these facts, it was suggested by Horiuchi[88] that the two bands are inversion parity doublets of a ^{12}C+α molecular structure. Tunneling through a potential barrier would enable passing from one configuration to another, therefore a superposition of two ^{12}C+α structures, one being the mirror image of the other, is made and projected onto good parity. The gap between the negative and positive parity states would arise in this picture as a consequence of such tunneling effect. A similar scheme was proposed for ^{20}Ne based on the similarity of the level scheme with ^{16}O, in this case based on a ^{16}O+α rotating structure. A weak coupling between the 4 particles and the four holes establishes a link between the ^{12}C+α pure cluster picture and the deformed mean field model, being this configuration equivalent to a core+α rotating structure[77]. The algebraic cluster

model of Bijker has also been recently applied to ^{16}O[89], providing evidence for a tetrahedral arrangement of four α particles in this nucleus based on the comparison of excitation energies and transition probabilities for decays from the $3^-_1, 4^+_1$ and 6^+_1 states.

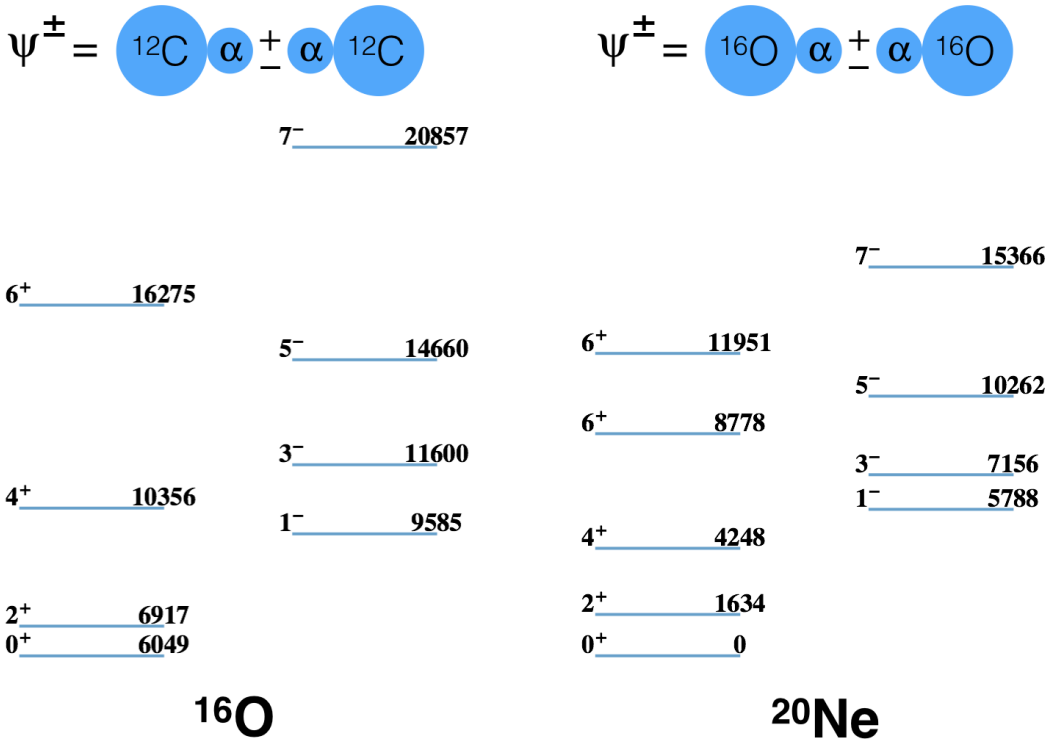

Figure 2.4: Inversion doublet rotational bands in ^{16}O and ^{20}Ne. Energies of the excited states are given in keV and were taken from [90].

2.1.2 Persistence of α clustering in heavier mass regions

In contrast to the situation in light and medium mass nuclei, the direct experimental evidence for the persistence of α clustering into heavier mass regions of the nuclear chart is scarce. Although one may think of the α-decay process itself as a fingerprint of an α cluster structure, a shell model description of the α-decay process having as ingrendients the mean field, either deformed or spherical, and like-nucleon pairing is suggested, in view of previous calculations[91, 92], to correctly reproduce the decay widths as long as a significantly expanded shell-model basis is used. Moreover, it is usually considered that the presence of a strong spin-orbit coupling combined with the short-range pairing curbs the formation of clusters as the Fermi levels of protons and neutrons separate.

A recent highlight on this topic[93] links the occurrence of clustering with the spatial localization of the single-nucleon wave functions. Clustering is viewed in this approach as a phase of the fermionic system in between a crystalline and a quantum liquid phase, which is destroyed by the spatial spread of the nucleon density distributions. Such a spread, quantified by the parameter $\alpha = (\hbar R)^{1/2}(2mV_0)^{-1/4}r_0^{-1}$ being V_0 the depth of the potential, R the radius of the system, and m the mass of the nucleon, is favored in heavy nuclei by the increasing nuclear radius R.

The analysis of binding energies near closed shell nuclei, shell effects observed in α-transfer reactions and theoretical calculations of α-preformation probabilities for α decays (although in a model-dependent way) are long-standing arguments supporting the presence of the necessary conditions for the occurrence of clustering in heavier nuclei. The importance of 2n2p α-like correlations for $N > Z$ nuclei beyond the "doubly magic" ^{90}Zr has been suggested in ref. [94] on the basis of their binding energies corrected for the mean-field energy and Coulomb interaction, showing much larger amounts of correlation energy than expected from like-nucleon pairing vibrations. A similar study has been conducted in ref. [95] for the region beyond the $Z = 82$, $N = 126$ shell closure. In this latter case, the α correlation energy was isolated from the long-range correlation and the paring energy by a three-point formula, obtaining significant values of the α correlation energy with a maximum in ^{212}Po. Such an alpha-like correlation would be connected to the shell and blocking effects observed in (d, ^{6}Li) transfers[96, 97], and the idea that was pushed forward in a schematic calculation aimed at qualitatively explaining these effects in α and nucleon pair transfer reactions simultaneously[98]. The cross-shell excitations of correlated nucleon pairs considered in this model would be required for the formation of α clusters in heavy nuclei.

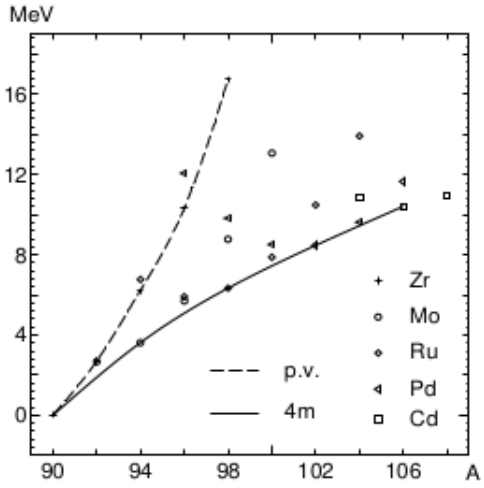

Figure 2.5: Calculated correlation energy of valence nucleons outside a ^{90}Zr core. The dashed line connects Zr isotopes and the solid line connects the ^{94}Mo, ^{98}Ru, ^{102}Pd and ^{106}Cd nuclei which have a multiple of 2n2p valence nucleons. Image taken from [94].

It is well known that the $N = 126$ shell closure has a strong effect of the α

decay widths, in such a way that different sets of coefficients have to be used in the Geiger-Nuttall law for $N < 126$ and $N > 126$. Surprisingly, the corresponding effect of the $Z = 82$ shell closure is much slighter and direct evidence of its effect has not been obtained until recently[99]. This has triggered a number of theoretical studies of the α decay process around $N = 126$. For instance, Delion[100] calculated preformation probabilities using a mean field plus pairing approach. It was found that, whereas the model accounted well for the decay widths of the neutron defficient isotopes below $N = 126$, this mean field plus pairing approach underestimated those widths for the neutron rich ones which could only be reproduced by introducing an ad hoc cluster factor amplifying the preformation probability. This was considered as an evidence of α clustering in heavy nuclei. Other calculations such as those of Ahmed[101] illustrate the trend of the preformation probabilities around the $N = 126$ shell for the Po, Rn, Ra and Th isotopes. According to these calculations, the preformation probability regularly decreases as the neutron number approaches the shell closure. There is a steep increase of this quantity beyond $N = 126$, with a maximum for the $N = 128$ isotones that reach preformation probabilities close to 30%. This is followed by a regular decrease of the preformation factor in the isotopic chain when moving away

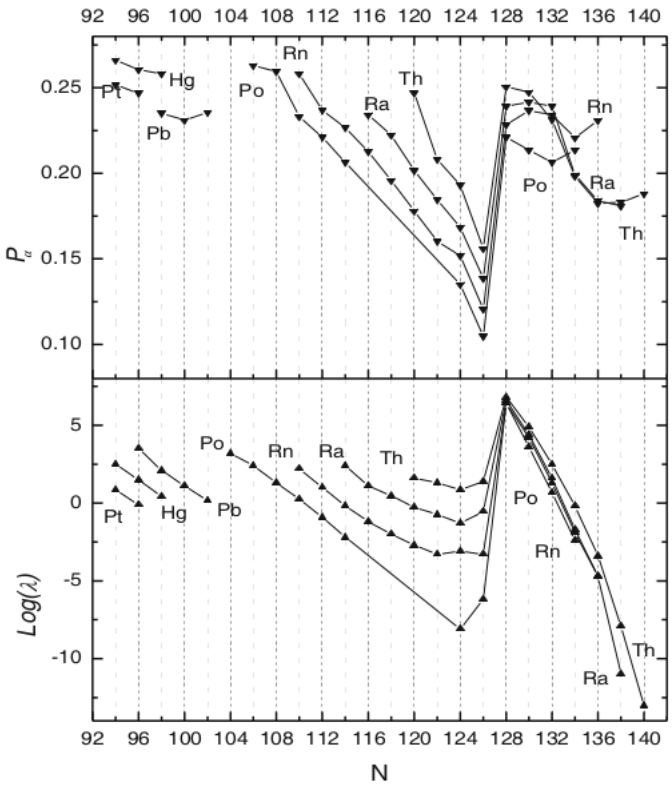

Figure 2.6: Comparison between experimental α decay constants and the calculated preformation probabilities of ref. [101]. Image taken from the same reference.

from the shell closure. Recent works[102] have correlated the pairing gaps with this behavior of the preformation factors beyond $N = 126$.

The neutron-rich region beyond $N = 126$ is therefore the suggested place to look for novel experimental fingerprints of α clustering. More specifically, the ^{212}Po nucleus is the only known case so far for which coexistence of mean field and α clustering correlations has been claimed for long time and it is presented in the following section.

2.1.3 The case of ^{212}Po

Several shell model calculations of the α decay width have been made for ^{212}Po[103–105]. Those early calculations demonstrated that the monopole pairing acting among identical particles in combination with large degrees of configuration mixing greatly enhances the calculated width. Those calculations, however, still underestimated by an order of magnitude the experimental half life of 300 µs. The multi-step shell-model approach of Dodig-Crnković[106] was an attempt to remedy this issue by including all two-body correlations, including the proton-neutron pairing, in the calculation. This approach failed as well to provide the right order of magnitude. It was finally demonstrated by Varga[107] that treating shell-model and clustering correlations on equal footing using a wave function of the form

$$\Psi(^{212}\mathrm{Po}) = \Psi_{\text{shell model}} + \Psi_{\text{cluster}} \tag{2.1}$$

the precise value of the α-decay width of the ground state in this nucleus can be reproduced. The obtained amplitude of the cluster part was 30%, a value which matches the preformation probability calculated by Ahmed using the cluster formation model[101].

The excitation energies in the yrast band of ^{212}Po have been successfully reproduced by the shell model. In this description, the two valence neutrons and the two valence protons outside the doubly-magic ^{208}Pb core occupy the single particle states $\nu g_{9/2}$ and $\pi h_{9/2}$, respectively. The excitation of the neutron pair is mostly responsible of the yrast sequence in a seniority-like pattern. The existence of the well-known 45 s isomer, a $J^\pi = 18^+$ state at 2922 keV that decays via α emission only, was also explained by invoking shell-model configurations. Its particular deexcitation property is now understood as the result of a spin gap, namely the absence of states with comparable spin at similar excitation energies makes difficult its depopulation by electromagnetic transitions of low multipolarity. In spite of this early successes, a lifetime measurement of the 10^+_1, 8^+_1 and 6^+_1 states revealed considerable disagreement between the experimental and the calculated B(E2) values[108]. Although the intensities

of the α-decay branches of the yrast states were revised in[109], this discrepancy still persists. Calculated and experimental B(E2) values for these transitions are compared in table 2.1. Given the success of the SM+cluster model of Varga, the presence of

J^π	$E_{\text{lev}}^{\text{exp}}$ [keV]	$T_{1/2}^{\text{exp}}$ [ns]	b_α [%]	$B(E2)^{\text{exp}}$ [$e^2\text{fm}^4$]	$B(E2)^{\text{th}}$ [$e^2\text{fm}^4$]
6^+	1355	0.76(21)*	∼3(1)*	1006(302)	301†
8^+	1476	14.6(3)*	∼3(1)*	342(5)	103†
10^+	1834	0.55(14)‡	∼0@	164(42)	0.17‡

* From [109].
† From [110].
‡ From [108].
@ From [111].

Table 2.1: Comparson between experimental and shell model B(E2) values for the transitions depopulating the 6^+, 8^+ and 10^+ yrast states. Internal conversion coefficients for the experimental B(E2) were calculated using BrIcc[55]

the additional α clustering correlations were proposed as well for the states of the yrast band as an explanation for the unusually large collectivity in these states and their α decay branchings[111, 112], finding a much better agreement with the reported lifetimes in this approach. Surprisingly, a recent determination of the lifetime of the 2_1^+ state for the first time[110] does not indicate an unusual degree of collectivity, the fingerprint of clustering correlations in its structure, but rather the contrary, its collectivity is much lower than expected. Hence the ground state band of ^{212}Po still lacks a unified description.

Although the contribution of α-clustering correlations in the yrast structure of ^{212}Po is accepted nowadays, the observation of excited states of an α-core nature, similar to those observed in light nuclei, is still doubtful. A significant extension of the level scheme to non-yrast states was performed by Astier[109, 113] and an α-core nature for some of them identified as collective was proposed. The ^{212}Po was populated using the α-transfer reaction ^{208}Pb(^{18}O, ^{14}C)^{212}Po and only γ rays were detected. Only events with 3 γ rays in coincidence were stored and analyzed. Among the populated states, two bands of nearly degenerate doublets were observed. According to refs. [109, 113], the band at lowest energy is composed of states with even angular momentum and negative parity. They decay via E1 transitions to the yrast state having the same spin. States with odd angular momentum and positive parity form an additional band near 3 MeV decaying by E1 transitions as well. Since lifetimes in the range of 0.3-0.5 ps were extracted in the negative parity band using the DSAM, these states are highly

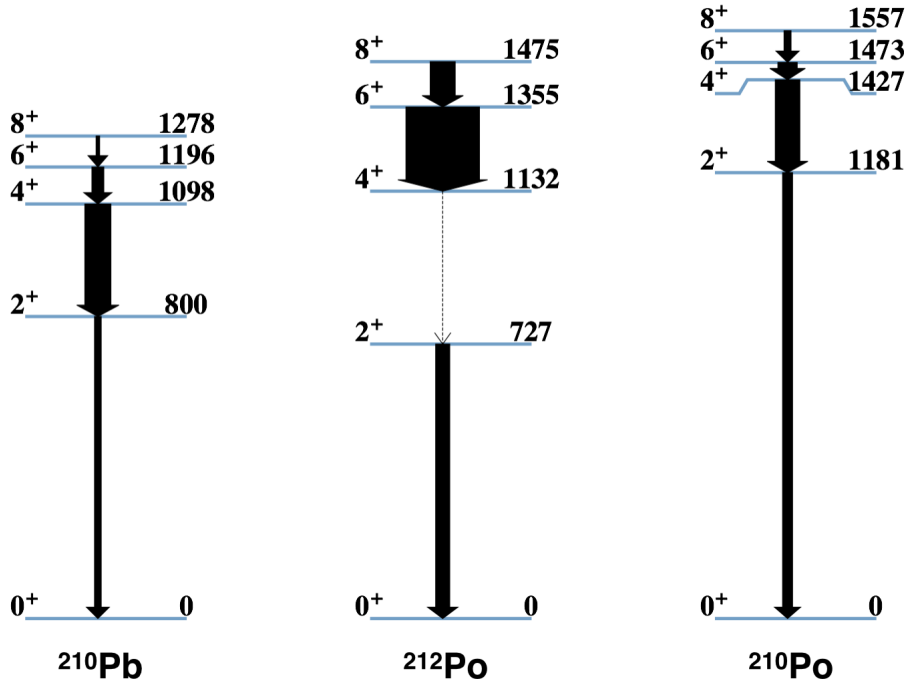

Figure 2.7: Comparison between experimental excitation energies in ^{210}Pb, ^{210}Po and ^{212}Po. The width of the arrows is proportional to the measured B(E2). Dashed lines indicate unknown B(E2) values. The experimental data for the $A = 210$ nuclei is from [90] and the data for ^{212}Po is from table 2.1.

collective. Furthermore, for the positive parity band, upper limits were established with the exception of the 7^+ state, for which a lifetime of 0.12(6) ps was determined.

According to [109], these states are peculiar in the sense that their excitation energy is much lower than the predictions of the shell model for the first negative parity states. Whereas the trend and the energy of natural parity states with odd spin, interpreted as octupole vibrations coupled to two-neutron yrast states, compare favorably with the situation in other nuclei regarded as similar to ^{212}Po, such as the ^{148}Gd nucleus, the similar structure of doublets has not been observed yet. Therefore, based on their large B(E1) values, comparable with the transition probabilities in the α-core light rotational nuclei, they were interpreted as the first evidence of pure α-core excited states in heavier nuclei.

According to this interpretation, the α-core separation would give rise to a large dipole moment in the intrinsic frame, which would be responsible for the large E1 transition probabilities. Given that the α-^{208}Pb system can be considered essentially as spherical, collective rotations are forbidden so that the collectivity is the result of an α-^{208}Pb oscillatory motion. Similar to the inversion doublets in ^{16}O and ^{20}Ne, tunneling through a potential barrier and projection onto good parity would give rise

to the two parities and the shift towards larger energies of the positive parity doublets.

This picture of a pure α-core oscillatory motion was disregarded in a couple of theoretical works[114, 115] trying to simultaneously reproduce the doublets and the subset of states identified by Astier and collaborators as octupole vibrations. Since only natural parity states would be allowed in an oscillatory motion α-^{208}Pb(GS), another mechanism has to be responsible the collective doublets. Among the alternative descriptions, an oscillatory motion of the α particle, this time against a ^{208}Pb core in its 3^- excited state, was proposed as well as a coupling of two-neutron, seniority-excited states to the octupole mode in ^{208}Pb. The proposed descriptions manage to reproduce well the enhanced B(E2) within the ground-state band, the B(E1) values of the decays depopulating the doublets as well as their excitation energy. Therefore, additional experimental information in terms of new lifetime measurements, particularly in the

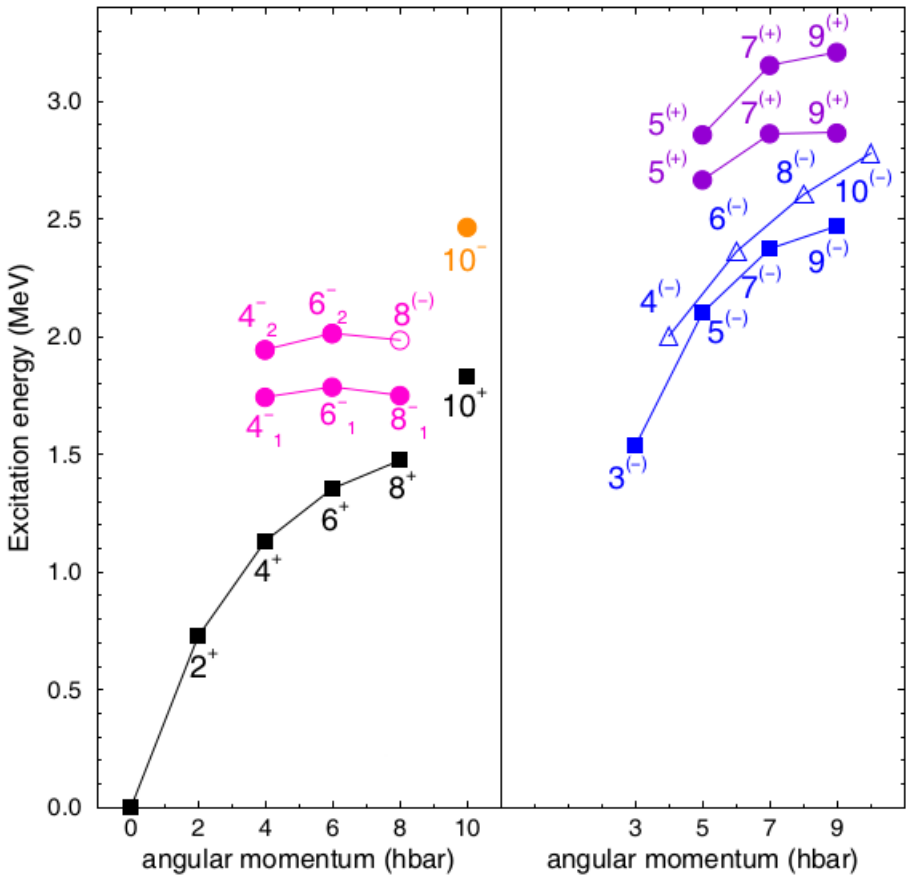

Figure 2.8: Excitation energy as a function of the angular momentum in the ^{212}Po yrast band (black squares) and the collective states observed in ref. [109]. Pink and purple markers indicate the states decaying by enhanced E1 and blue markers indicate those other states regarded as a coupling of the octupole phonon to two-neutron excitations and with unknown lifetimes. Adapted from [109].

positive parity band, as well as new spectroscopical information, is required to benchmark the theories.

2.2 Goals of the experiment

The focus of this work is the analysis of a dedicated γ-ray spectroscopy experiment to enlarge the available experimental information about the ^{212}Po nucleus. The experiment was originally proposed with the following goals:

- To observe a missing 2^- doublet that is predicted in all the models, as well as a missing 10^- state which, together with the 10^- state at 2465 keV observed by Astier, would constitute the 10^- doublet
- To perform lifetime measurements via DSAM of transitions depopulating the positive-parity doublets. No quantitative theoretical description or interpretation has been made for them, being the focus of the previous theoretical works on the negative-parity doublets.
- The observation of an even-parity sequence at higher excitation energy predicted by the oscillatory model of Astier.
- A new lifetime measurement of the transitions depopulating the negative-parity doublets under more sensitive conditions. In particular, the reduced sensitivity stemming from DSAM lifetime measurements in normal kinematics, the use of a thick, unbacked ^{208}Pb target and the measurement with a position-insensitive γ-ray spectrometer are overcome by proper choices for the experimental setup as described in the next chapter.

Chapter 3

Experiment and setup

The experiment E693 was conducted in the laboratory of GANIL[116] in Caen (France) and provided the data for this part of the thesis. The aim of the experiment was to extend the spectroscopical information of ^{212}Po via in-flight γ-ray spectroscopy and nuclear lifetime determination using the DSAM. The E693 setup and targets were optimized to overcome the limiting sensitivities of the most recent experiments populating ^{212}Po and provide complementary results. Ultimately, the new experimental information would be used as input in order to test the variety of proposed theories for collectivity and α-clustering in ^{212}Po. Achieving a precise Doppler correction and at the same time measuring with a large detection efficiency allowing the accumulation of statistics under reasonable measurement times were key to the goals of the experiment. Thus the E693 setup consisted of the AGATA γ-ray spectrometer in combination with a charged-particle detector, and the ^{212}Po nucleus was populated by means of the α-transfer reaction in inverse kinematics ^{12}C(^{208}Pb, ^{212}Po)^{8}Be. The aim of this chapter is to provide an overview of the experimental technique used to populate ^{212}Po excited states.

3.1 The GANIL facility

The stable ^{208}Pb beam was delivered by the GANIL cyclotrons. The accelerator complex is a long-standing facility that became operational in 1982. It is one of the two largest in Europe along with GSI in Darmstadt (Germany) allowing research in various fields such as nuclear physics, material science, astrophysics and radiobiology. GANIL is well known for providing stable heavy-ion beams ranging from Carbon to Uranium as well as radioactive ion beams (RIB) through its ISOL facility SPIRAL or by means of the in-flight separator LISE in combination with SISSI. Up to 3-4 experiments can be run simultaneously in the experimental halls in which the complex

is divided. They host a variety of instrumentation that can be used according to the purposes of the corresponding research. The E693 experiment took place in hall G1 where AGATA was installed.

The trip of the ^{208}Pb ions starts in the ECR ion source, where an electron gas ionizes the beam. Then the ions are extracted and injected into the C0 cyclotron, emerging with energies of 0.25-1 MeV. They traverse a charge stripper before they are injected into the CSS1 cyclotron, where they finally reach the desired beam energy of 5.7 $^{\mathrm{MeV}}/_{\mathrm{u}}$. Then the ^{208}Pb beam is directed to hall G1. A layout of the accelerator complex is presented in figure 3.1.

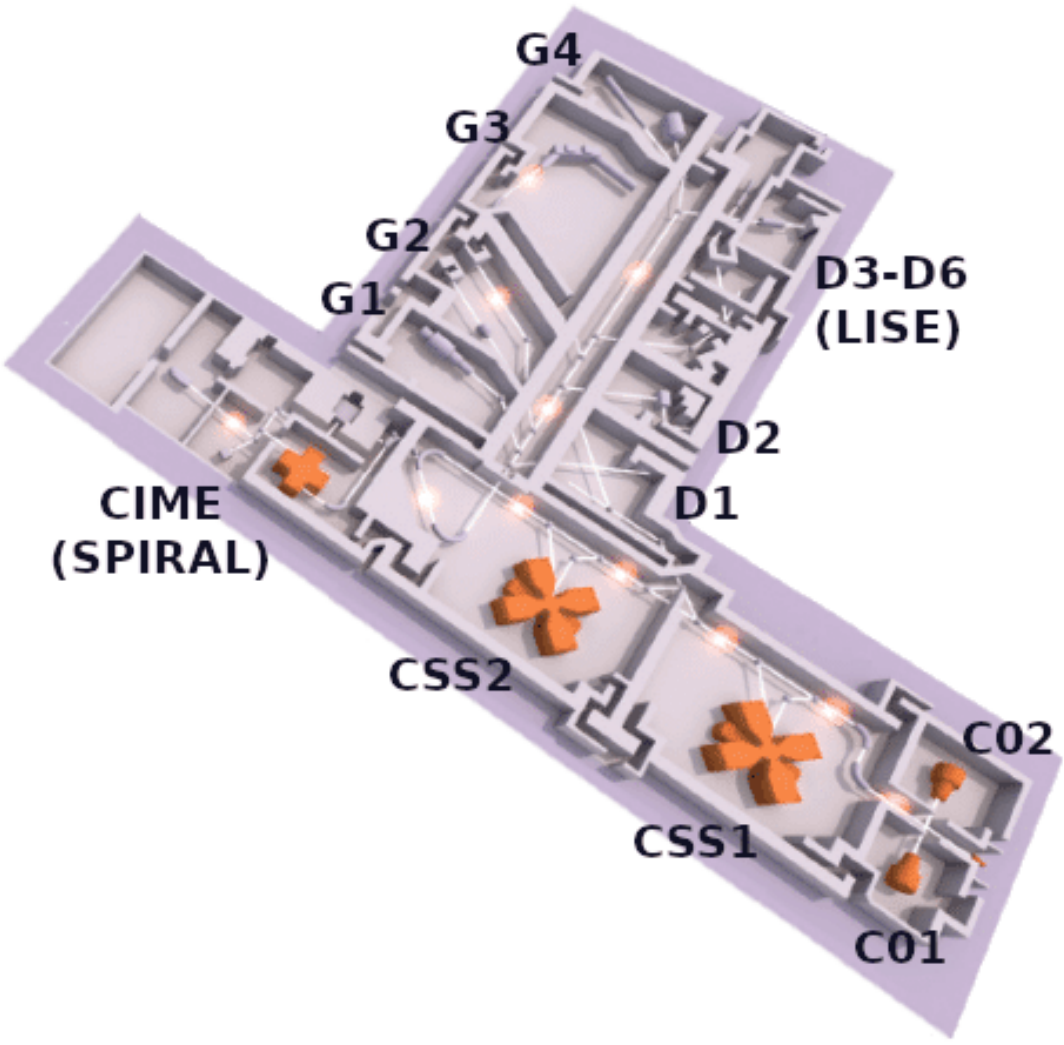

Figure 3.1: Overview of the GANIL accelerator complex. The figure was adapted from [116].

3.2 DSSSD and charge-particle detection

A double-sided Silicon strip detector (DSSSD) was placed behind the target in order to detect light charged particles from reactions in the target. This detector is segmented into 32 concentric segments (referred to as *rings*) in the n side and 64 consecutive segments in the p side providing spatial sensitivity over the entire range of azimuthal angles ϕ, which are refered to as *sectors* in this work. The inner and outer diameters of the active area are 32 mm and 85 mm. Each of the segments is isolated from its neighbours by a 110 µm wide interstrip area. The 310 µm Silicon wafer was mounted in a PCB whose inner and outer diameters are 28 mm and 120 mm. The PCB readout is sent to the analogue acquisition chain of the DSSSD. A photograph of the model DSSSD used in the experiment is shown in figure 3.2.

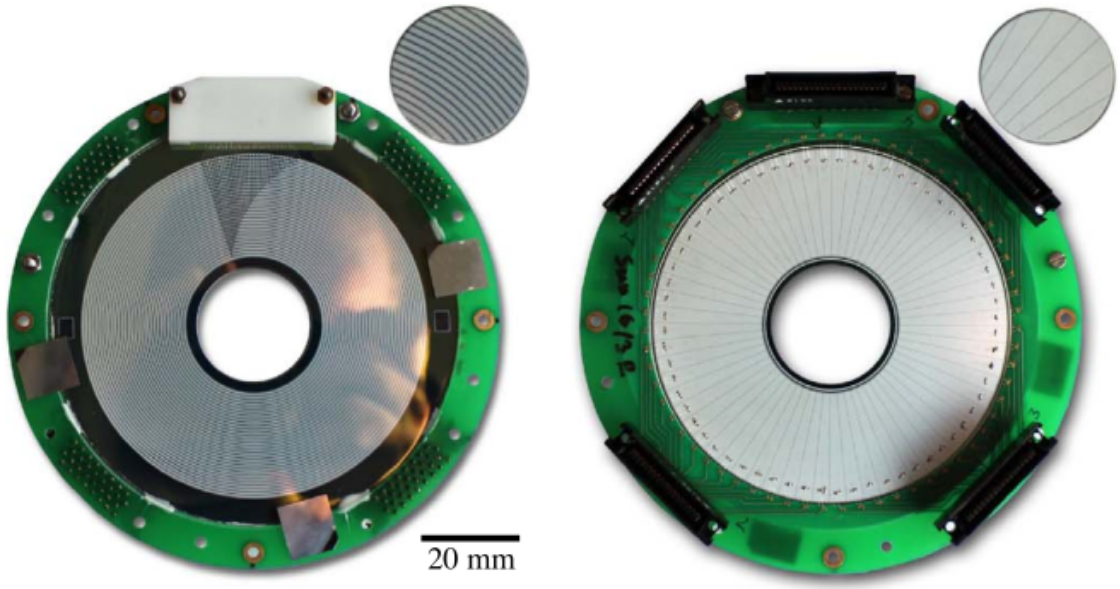

Figure 3.2: Picture of the model DSSSD used in the experiment as viewed from the front (left picture) and back side (right picture). The figure was adapted from [117].

The high granularity of the detector is not only essential for a precise Doppler correction, but also for preserving the selectivity of the setup to the α-transfer channel in the presence of the Tantalum shield installed in front of the detector. This passive element prevented the elastically scattered ^{12}C ions from reaching the DSSSD. Further optimizations regarding the DSSSD positioning and the design of the Tantalum shield were studied before the experiment in order to maximize the yield of detected α particles originating from the transfer reaction. They are described in the following sections.

3.2.1 Reaction kinematics and ^{8}Be decay

The ^{8}Be produced after the α-transfer reaction decays into two α particles. Since the lifetime for decays from its ground state is 0.1 fs[118], the breakup is assumed to occur at the reaction vertex when performing the kinematical reconstruction using the DSSSD segmentation. The available energy for a breakup from the ground state is 91.8 keV, which is transformed into kinetic energy of the two alphas emitted in opposite directions in the ^{8}Be rest frame. In the laboratory frame, the two particles are focused within a cone whose maximum angle of aperture Ψ is

$$\Psi = 2\sin^{-1}\sqrt{\frac{91.8\text{ keV} + E_x}{K}} \tag{3.1}$$

where K is the ^{8}Be kinetic energy and E_x is its excitation energy. The maximum opening angle between both particles occurs when they are emitted in the plane defined by the momentum direction of the ^{8}Be. The DSSSD covered the angular range from 26° to 52° (see next section), corresponding to maximum opening angles between 3° and 4° for the chosen beam energy of 1187 MeV and resulting in a maximum spatial separation of 2-5 mm between the α particles as they impinge on the DSSSD surface. This strong spatial correlation between them is the signature of the α-transfer channel and opens the possibility of generating very clean singles γ-ray spectra. Hence the advantage of using the ^{12}C(^{208}Pb, ^{212}Po)^{8}Be reaction in combination with charged-particle detection is twofold: limiting the data acquisition to reactions involving light charged particles in the exit channel reduces the load of the acquisition system and enables the replacement of a multiple γ trigger by the much more efficient particle+γ(+γ) trigger while profiting from the channel sensitivity provided by the segmentation.

The kinematics of the α transfer reaction is illustrated in figure 3.3(a) and it is compared in figure 3.3(b) with the same reaction at the same CM energy (63.7 MeV) in normal kinematics. In inverse kinematics the projectile-like nucleus ^{212}Po has a maximum polar angle of around 2°, and the DSSSD covers polar angles of the target-like recoils corresponding to a window around the maximum polar angle of ^{212}Po. The β(^{212}Po) is around 0.1, thus the larger velocity of the ejectile in inverse kinematics results in Doppler-shifted lineshapes extended over a wider range of γ-ray energies. Consequently, a larger sensitivity for lifetime measurements using the DSAM is achieved in inverse kinematics. Moreover, the larger kinetic energy of the ^{8}Be results in a stronger kinematical focusing of the two α particles, so that a larger geometrical efficiency for their simultaneous detection is achieved in inverse kinematics.

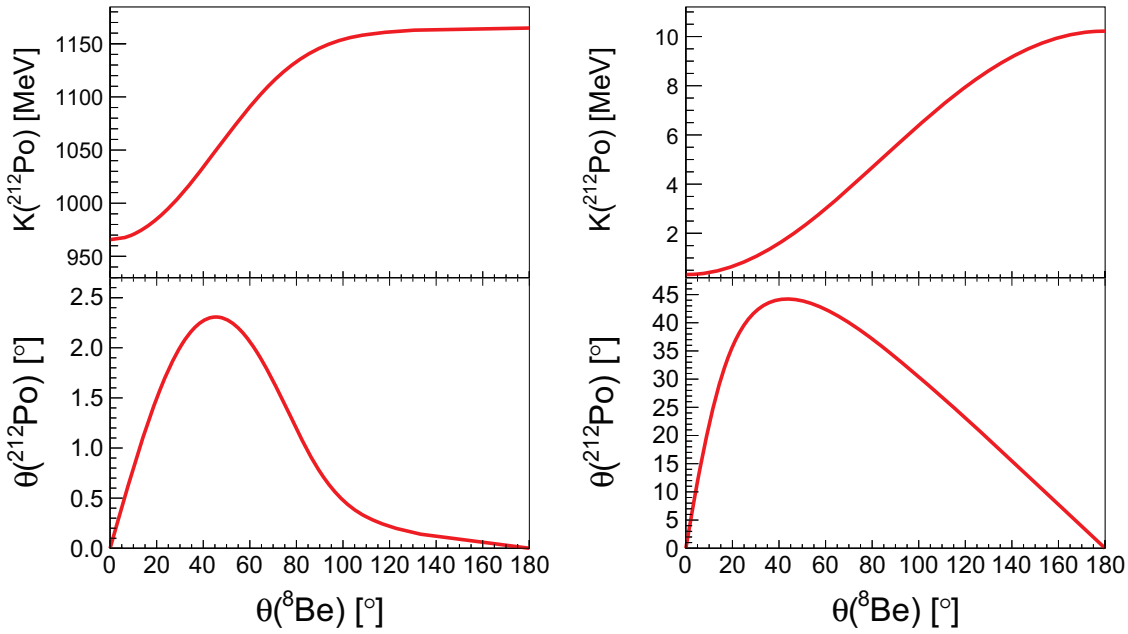

(a) Inverse kinematics **(b)** Normal kinematics

Figure 3.3: Kinematical curves illustrating the dependence of the kinetic energy and the polar angle of the ^{212}Po nucleus on the polar angle of the residual ^{8}Be after the α-transfer reaction. The curves were calculated for reactions at a center of mass energy of 63.7 MeV.

3.2.2 The projectile energy

The integrated cross section for multinucleon transfer reactions is peaked for center of mass (CM) energies around the Coulomb barrier, thus the projectile energy is an important parameter in the preparation of any experiment using this kind of reaction. The criterion used in this work for defining the Coulomb barrier is that of Bass[119], from which $B_{\mathrm{CB}} = 58.9\,\mathrm{MeV}$ is calculated for the ^{12}C+^{208}Pb system, a value that is close to the maximum at 57 MeV of the experimentally measured barrier distribution[120].

As explained in section 1.2.2, the analysis of multinucleon transfer reactions is greatly simplified by using the semiclassical approximation. The tunneling probability for the transferred cluster decreases when the distance of closest approach in Coulomb trajectories is large, so that head-on collisions dominate in transfer reactions at energies well below the barrier. This results in differential cross sections peaked at backward angles in the CM system. On the other hand, nuclear absorption as well as complete and incomplete fusion reactions dominate in the range of impact parameters smaller than the nuclear interaction radius[121], thus forward-peaked differential cross sections corresponding to larger impact parameters are observed at increasing energy above the

barrier.

Besides the above considerations regarding the integrated transfer cross section, the optimum[1] transfer distance resulting in an optimum dispersion angle Θ in the CM frame plays as well an important role for transfer reactions around the barrier if detection of the transfer products is intended. This angle is referred to as the *grazing angle*, corresponding to impact parameters that result in a grazing collision between the two nuclei. The grazing angle is usually estimated using the following formula relating the distance of closest approach R and the scattering angle Θ,

$$R = \frac{\alpha\hbar c\, Z_1 Z_2}{2K_{\mathrm{CM}}}\left(1 + \frac{1}{\sin\frac{\Theta}{2}}\right) \tag{3.2}$$

where R is calculated as $1.27(A_1^{1/3} + A_2^{1/3})$ for a grazing collision. Another criterion for the grazing distance in reactions above the Coulomb barrier is the position of the Coulomb barrier itself ([122] and references therein). Using this criterion, eq. (3.2) yields

$$\sin\frac{\Theta_{\mathrm{gr}}}{2} = \frac{B_{\mathrm{CB}}}{2K_{\mathrm{CM}} - B_{\mathrm{CB}}} \tag{3.3}$$

Figure 3.4 shows experimental transfer cross sections measured in normal kinematics by Biswas et. al.[123] for the ^{12}C + ^{232}Th reaction and by Videbæk et. al.[124] for the ^{16}O+^{208}Pb reaction.

Monte Carlo simulations of the transfer reaction at different energies around the barrier have been performed using the StopSim code[125] and are shown in figure 3.5. The experimental cross sections measured by Biswas were parametrized by gaussian functions and used in the simulation. It was assumed that the shape of the cross section and its maximum, according to eq. (3.3), is the same at the equivalent CM energy above the barrier. For transfer reactions in inverse kinematics, the maximum of the cross section is focused towards smaller angles with increasing beam energy. Moreover, the width of the differential cross section for the target-like product is narrowed by a factor ~ 2 in the laboratory, thus illustrating the need of a precise DSSSD positioning. The DSSSD was finally placed 34 mm behind the target and an incident energy 10% above the barrier was chosen after consideration of the mechanical constraints related to the geometry of the reaction chamber, the angular aperture of the fission fragments (described in section 3.2.4), the behavior of the grazing angle with the projectile energy and the need for stopping all the elastically scattered ^{12}C ions (see section 3.2.3). Indeed, according to the simulations shown in figure 3.5, a distribution of α particles spatially centered in the DSSSD is only possible by measuring at energies slightly above the barrier if the detector is located 30-34 mm behind the target.

[1] Optimum means here that maximizes the cross section.

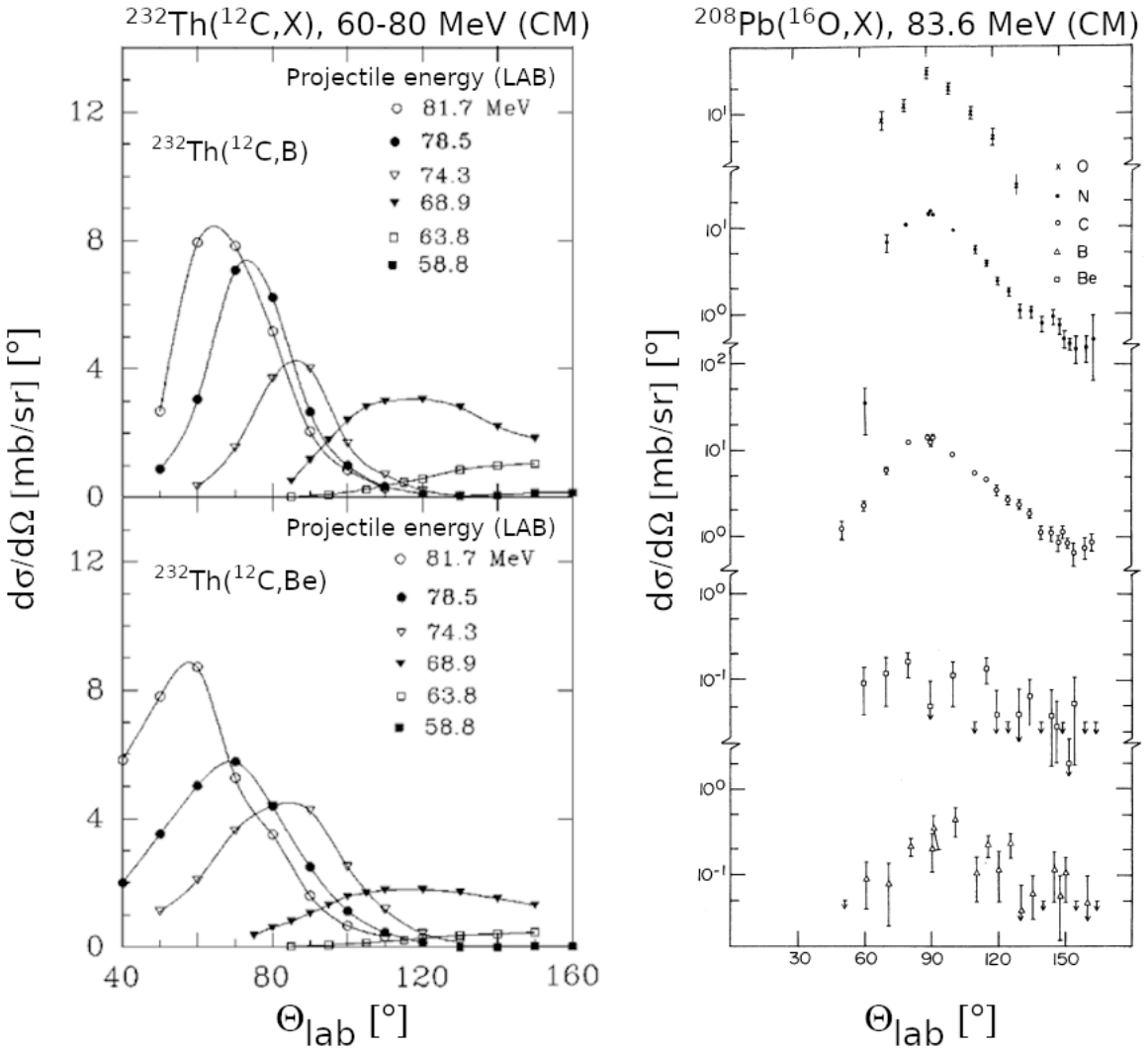

Figure 3.4: Differential cross sections for transfer channels following the ^{12}C + ^{232}Th and ^{16}O + ^{208}Pb reactions. The figures were adapted from [123] and [124].

Considerations regarding the excitation energy reached in the reaction should also be accounted for according to the semiclassical formula for the optimum Q-value. Higher beam energies would populate states at higher excitation energy than measured in a previous ^{212}Po study using the same α-transfer reaction in normal kinematics and covering the energy range up to the Coulomb barrier[17]. From the γ-ray spectroscopist point of view, the projectile energy should be kept as low as possible for two main reasons: 1) reaching ^{212}Po excitation energies above 6 MeV, the ^{212}Po neutron-separation energy[126], will result in neutron evaporation instead of ^{212}Po deexcitation via γ ray emission and 2) the strong fragmentation of the intensity from low spin states at higher excitation energies that deexcite towards the yrast band. For the α-transfer reaction at CM energies 5-10% above the barrier, the predicted excitation energy available for

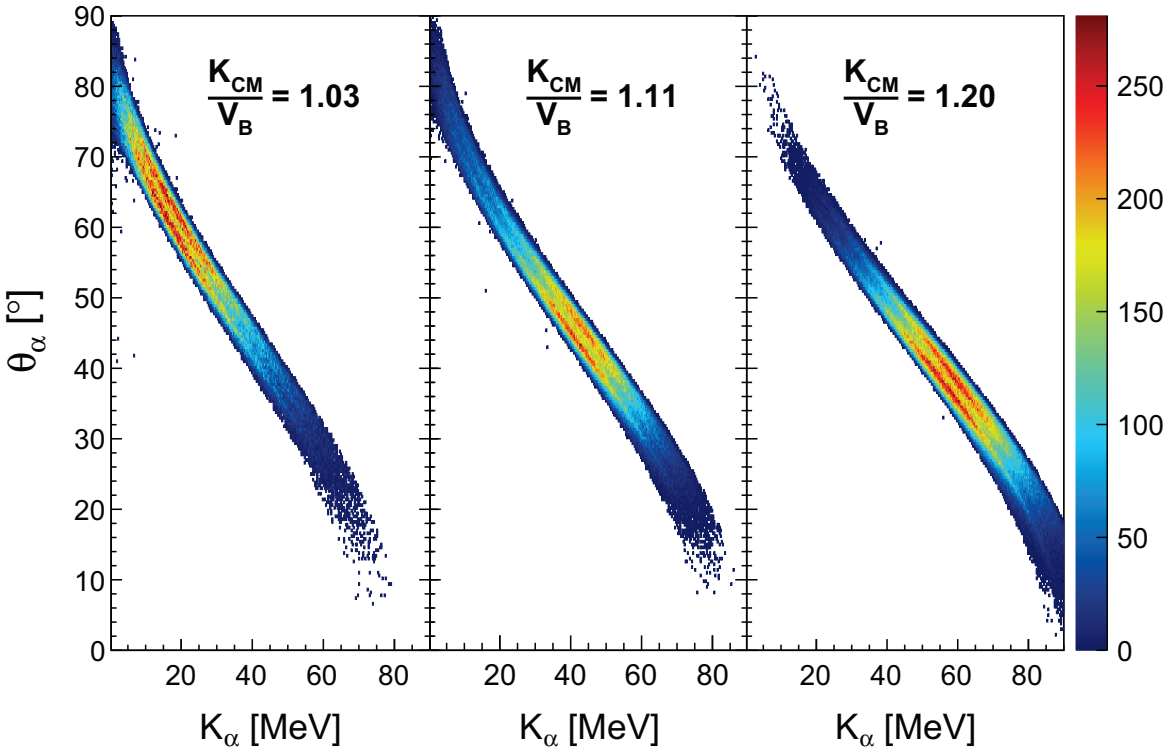

Figure 3.5: Monte Carlo simulations of the α-transfer reaction ^{12}C(^{208}Pb,^{212}Po)^{8}Be at three different energies above the Coulomb barrier. The plots show energies and polar angles of the outgoing α particles behind the target. The simulations were performed for a 0.5 $^{mg}/_{cm^2}$ thick diamond target.

both the projectile and target-like nuclei is 3-4 MeV according to eq. (1.15).

3.2.3 Design of the Tantalum shield

Silicon detectors, and particulary n-type ones, are sensitive to radiation damage by heavy ion bombardment[127]. Elastic scattering yields the largest number of charged particles following the reaction ^{12}C+^{208}Pb, and doses of 3×10^6 ^{12}C ions per mm^2 have been demonstrated to cause severe issues on the DSSSD performance[117]. The rate of elastically scattered ^{12}C ions was estimated using the Rutherford formula and the experimental cross sections of elastic scattering measured in ref. [120] for the ^{12}C+^{208}Pb reaction. For reasons that will become clear at the end of this section, the DSSSD must be positioned around 34 mm behind the target, thus covering polar scattering angles from 26° to 52°. The Rutherford cross section can be integrated in the solid angle Ω_L subtended by the DSSSD in the laboratory frame. In terms of the polar scattering angle ψ of the ^{12}C ion in the laboratory in inverse kinematics, the

integral gives in the non-relativistic approximation

$$\sigma_{\text{Ruth}} = \int \mathrm{d}\Omega_L \left(\frac{\mathrm{d}\sigma}{\mathrm{d}\Omega_L}\right)_{\text{Ruth}} = \left(\frac{Z_1 Z_2\, \alpha\, \hbar c}{4K_{\text{CM}}}\right)^2 \times 4\pi \left(\frac{1}{\cos^2 \psi_{\max}} - \frac{1}{\cos^2 \psi_{\min}}\right) \tag{3.4}$$

with $\psi_{\max}$, $\psi_{\min}$ the maximum and minimum ^{12}C scattering angles covered by the DSSSD. As shown in figure 3.6, the cross sections for the elastic scattering are essentially given by the Rutherford cross section for energies up to 12% above the barrier and CM scattering angles above 100°, that is, below 50° in inverse kinematics for the scattered ^{12}C. The targets used in experiment E693 have either graphite or diamond reaction layers with a thickness of 0.5 $^{\text{mg}}/_{\text{cm}^2}$, representing a balance between the reaction cross sections and the smearing of the γ-ray energies as a consequence of deexcitations at different velocities within the foil. Using this target thickness, a rate of 213 kHz of ^{12}C ions in the detector is calculated at a beam intensity of 1 pnA[2] resulting in a dose of 3.8×10^6 ^{12}C ions per mm^2 after a day of measurement[3]. Hence, all ^{12}C were stopped by installing a Tantalum shield in front of the detector. The ranges in Tantalum of the elastically scattered ^{12}C ions and α particles from the ^{8}Be breakup after the

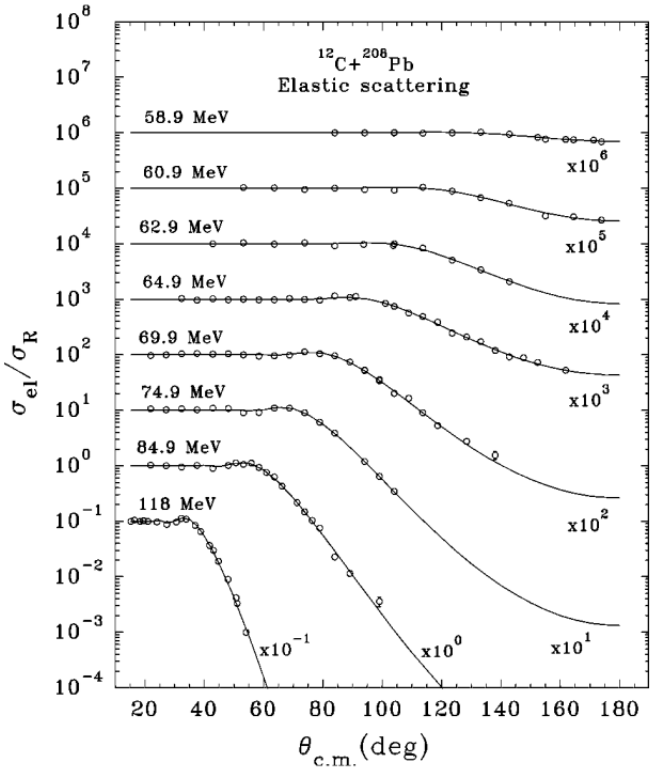

Figure 3.6: Elastic cross section normalized to the Rutherford cross section, for the ^{12}C + ^{208}Pb reaction. The figure was taken from [120].

[2] 1 pnA = 6.241×10^9 pps

[3] The experiment was planned to run for 6 days.

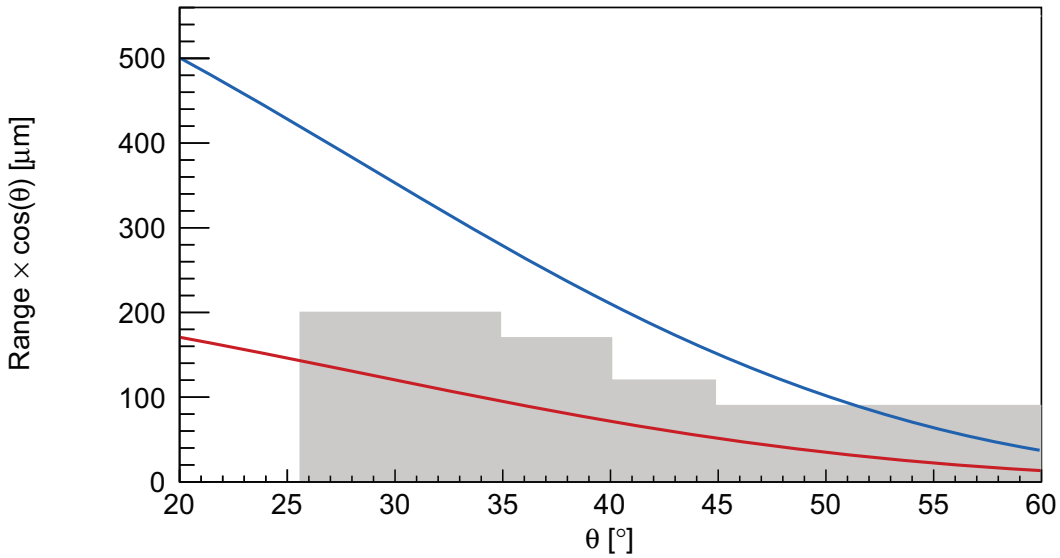

Figure 3.7: Ranges in Tantalum of elastically scattered ^{12}C ions (red) and α particles (blue) following the ^{8}Be breakup after the α-transfer reaction, as a function of the polar angle of the ^{12}C ion and the original ^{8}Be nucleus, respectively. The range has been multiplied by $\cos\theta$ in order to account for the angle of incidence. The net Tantalum thickness used for stopping all the ^{12}C nuclei is represented in grey.

α-transfer reaction were calculated using SRIM[66] and are given in figure 3.7. It can be noticed that by using a single foil it is not possible to stop all the ^{12}C ions without stopping all the α particles above 35°-40°. Therefore, the absorber was built by stacking 4 Tantalum disks in order to modulate the net thickness of the stopper as a function of the polar angle. As a result, the range of the elastically scattered ^{12}C ions is below the effective thickness of the shield whereas the range of the α particles is above the distance they travel into it. For polar angles above 50°-55° it becomes increasingly difficult to stop the ^{12}C ions and at the same time allow the α particles to reach the DSSSD following that this detector must be placed more than 30-34 mm behind the target. Table 3.1 gives the radii and thicknesses of the Tantalum disks used in the experiment.

Layer number	1	2	3	4
Radius [mm]	18.0	21.5	25.5	60.0
Thickness [µm]	30	50	30	90

Table 3.1: Radii and thicknesses of the Tantalum disks used for constructing the absorber. Layer 4 was replaced by a thinner foil with a thickness of 12.5 µm during the thick target runs.

3.2.4 Fission fragments

A 16% of fusion reactions leading to ^{220}Ra will undergo fission according to PACE4 calculations[128]. The fission fragments will be confined within a cone whose aperture essentially depends on the available kinetic energy in the CM frame as well as on the mass asymmetry of the fragments and on the projectile energy. Because of the large cross section for fusion-fission reactions, it is better to let the fission fragments leave the chamber in order to get rid of their activity. By adjusting the distance between the DSSSD and the target, the fission cone should be covered by the central hole of the DSSSD. In order to estimate the aperture of the cone, the available kinetic energy Q for the fragments in the CM is estimated as[129, 122]

$$Q = \frac{Z_1 Z_2 \, \alpha \, \hbar c}{1.2(1 + \frac{2}{3}\beta_1)A_1^{1/3} + 1.2(1 + \frac{2}{3}\beta_2)A_2^{1/3} + 1.4\,\mathrm{fm}} \tag{3.5}$$

with β_1, β_2 deformation parameters at the scission point whose value was approximated as 0.6. Energy conservation in the CM frame can be straightforwardly applied to obtain the partition of the above kinetic energy which is determined by the ratio of the masses.

Banerjee et. al.[130] measured the isotopic yield after fission using the reaction ^{18}O+^{208}Pb. The most asymmetric fragments detected were ^{78}Se and ^{78}Ru whose yield is approximately 100 times lower than the maximum observed yield, the latter corresponding to the more symmetric fission leading to ^{110}Ru. The polar angles of the fission fragments are expected from kinematics and eq. (3.5) to be larger in cases involving a larger mass asymmetry, with the largest polar angle corresponding to the lightest fragment and with little dependence on the proton number of the fragments. In particular, for a fission following the ^{208}Pb+^{12}C reaction at 63.6 MeV in CM and leading to ^{78}Se and ^{142}Xe fragments, the maximum polar angle[4] is 25° for ^{78}Se and 15° for ^{142}Xe, hence the DSSSD was conveniently positioned covering polar angles above 25°.

3.3 AGATA

The Advanced Gamma Ray Tracking Array (AGATA)[131] is a state-of-the art γ-ray spectrometer. It uses segmented HPGe detectors as well as the Pulse Shape Analysis (PSA) technique in combination with γ-ray tracking to achieve unprecedented levels of cleanliness in γ ray spectra, full energy peak efficiency and Doppler correction capabilities. The precise tracking of the γ ray path inside the array is achieved

[4]Neglecting the recoil imprinted by nucleon evaporation.

by means of its position resolution, higher than the geometrical one given by the segmentation itself. This technique allows a significant gain in detection efficiency by enlarging the solid angle covered by the array after removing the anti-Compton shields used in the previous generation of γ-ray spectrometers. Therefore the array represents a new generation of instrumentation for γ ray spectroscopy, where a significant upgrade has been performed with respect to the Ge arrays used in the past such as EUROBALL or GAMMASPHERE[132, 133]. These enhancements provided by AGATA are indeed specially desirable for RIB experiments with low beam intensities, of the existing facilities and the future ones under construction where the spectrometer is to be hosted[5]. The AGATA array is an ongoing project which is foreseen to end with the completion of a spectrometer with almost full solid angle coverage, AGATA 4π. In its final form, the array will be composed of 180 closely-packed crystals with a solid angle coverage of 82%[135] and a γ-ray detection efficiency of 44(25)% at $M_\gamma = 1(30)$ for γ-ray energies of 1 MeV[131].

The crystals composing the array are n-type, 36-fold electrically segmented HPGe detectors arranged in triple (ATC) or double clusters[6], each of them sharing the same cryostat. The crystals in every ATC have three different asymmetric shapes that are used for tiling a sphere into irregular hexagons. They are labelled as A, B and C according to their shape. The crystals have a length of 9 cm, a diameter of 8 mm at the rear and they are tapered on the front with an angle of 8°. They are encapsulated in a thin, 0.8 mm aluminum canister. The only limiting factor for the solid angle coverage within an ATC is the distance between the canister and the crystal faces, ranging from 0.4 mm to 0.7 mm. Each crystal has a coaxial geometry with a central (anode) and outer contact (cathode). Both longitudinal and transversal segmentations are applied in the outer contact that result in six rings labelled with a number and 6 sectors per ring labelled with the letters a-f. Therefore each crystal provides a total of 36 + 2 spectroscopic channels, the latter ones corresponding to the central contact at two different gains. Figure 3.8 illustrates the 3 different crystal shapes as well as the segmentation pattern with the standard labelling of the segments.

The 36 segments and the core have individual preamplifiers. Their signals are digitally processed in order to apply the PSA algorithms. A snapshot of segment and core waveforms is recorded and stored on disk. Consequently, the amount of information written to disk is much bigger than in experiments with unsegmented Ge crystals. The amount of information written as waveforms was around 15 TB for this

[5] A recent review of the physics cases which will be well suited to explore in combination with this γ-ray spectrometer is given in [134].

[6] AGATA 4π will have 60 ATC.

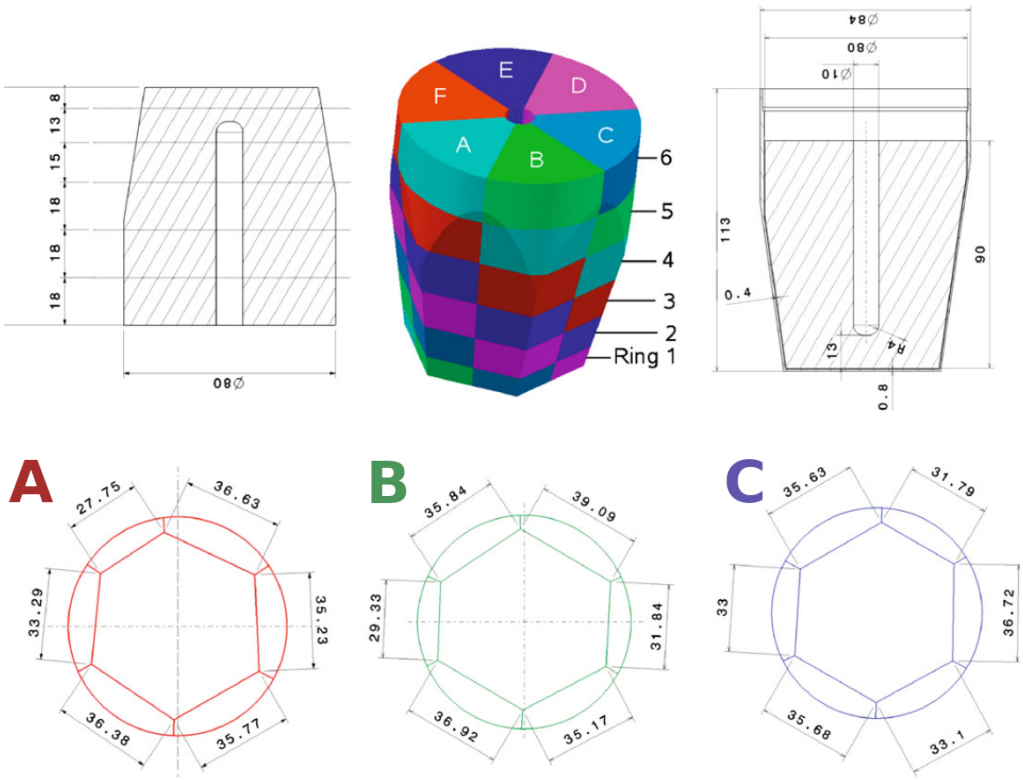

Figure 3.8: Geometry and dimensions (in mm) of the three types of AGATA crystals. The segmentation of the crystal into 36 segments is illustrated with the standard labelling of numbers 1-6 in the longitudinal dimension and letters A-F in the transversal plane. The figures were adapted from [135].

experiment.

At the time of the experiment, the array was composed of 35 crystals arranged into 11 ATC plus a single double cluster. The spectrometer was placed in nominal position at a distance of 23.5 cm from the target, covering backward polar angles from 120°-130° to 160°-170°. The solid angle coverage was nearly 1π, with 10 additional crystals missing for full 1π solid angle coverage. A picture of the arrangement of AGATA with respect to the reaction chamber is displayed in figure 3.9. The following sections briefly introduce how the distinctive outputs of AGATA, 3-dimensional positions and reconstructed interactions of the γ rays in the array, are produced.

3.3.1 Pulse Shape Analysis

The concept of Pulse Shape Analysis for position determination is based on the dependence of the collected charge, as a function of time, on the interaction position within the Ge volume. An example of how the radial coordinate of the interaction

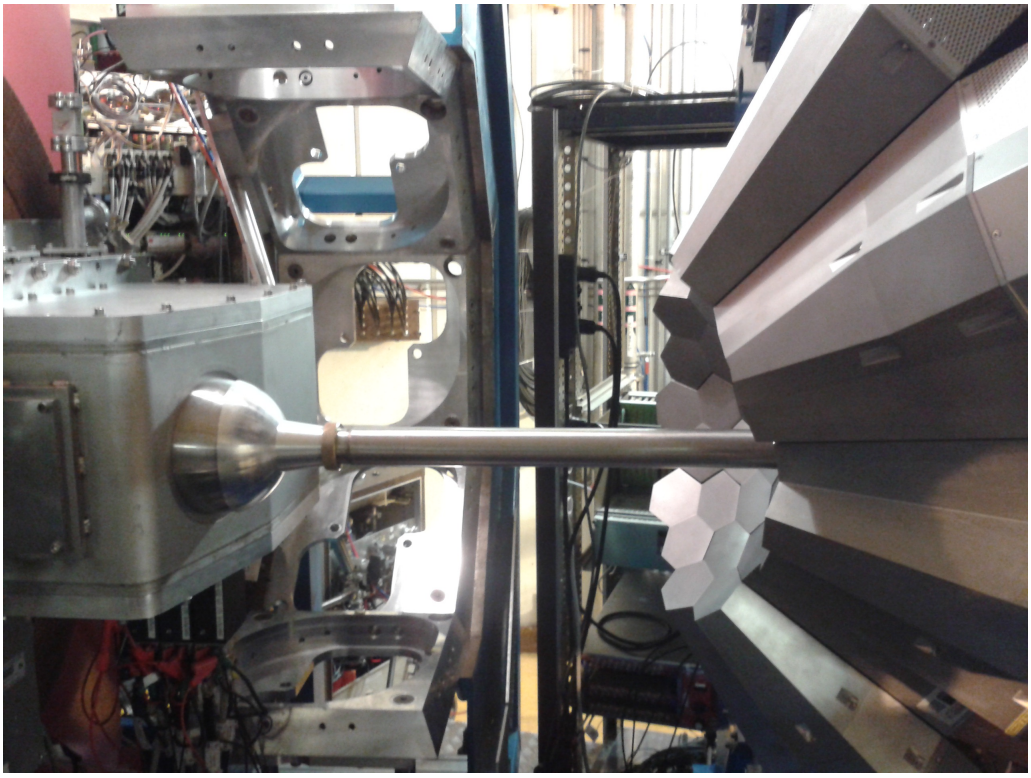

Figure 3.9: Picture of AGATA, the reaction chamber (on the left side) and the beam pipe. The beam comes from the right.

in cyllindrical coordinates can be obtained in an unsegmented, coaxial detector can be found in [137]. This sensitivity on how close/far to the cathode the interaction occurred is given by the different drifting times of electrons and holes.

The γ ray interaction releases a net charge in the segment where this interaction took place and this net charge is collected in the electrodes. The net charge induces mirror charges also in the surrounding electrodes (called transient signals), with the particularity that they integrate to 0 after the collection of the net charge finishes. The amplitude and sign of those mirror charges in a particular moment depends on how far the charge carriers were with respect to the electrode at that time. As an example, if an interaction is located near the central contact, a positive mirror charge is induced in it and a negative mirror charge is induced in the adjacent segments as the positive charge carriers approach the cathode. Therefore the shape and amplitudes of the charge collection signals in all the segments are related to the position of the interaction. The latter is graphically exemplified in figure 3.10, where an interaction takes place in segment "c". Since segments "b" and "d" are adjacent to "c", transient signals are clearly visible in them, and, moreover, the amplitude of the transient signal in segment "b" is slightly larger than in "d", indicating that the interaction is closer to

"b" than to "d".

The above means that, in practice, a set of reference signals at different positions in the crystal is needed for extracting the position from a comparison between the reference and the experimental signal. Such reference sets can be produced by two means, experimentally or from a calculation. A variety of scanning systems have been developed for determining experimental PSA bases[138–140], and they usually imply the use of collimator systems in order to detect coincident Compton scattering events in an AGATA crystal and the surrounding detectors belonging to the scanning setup. The stringent geometrical and energetic conditions that are imposed as well as the large number of signals needed in the bases makes this procedure time consuming so that a PSA basis composed of calculated signals is normally used, such as a PSA basis from the Agata Detector Library[141] (used in this work). Although the observed position resolution depends on the energy, with a better spatial resolution at higher energies, typical values of this resolution are around 5 mm FWHM[142].

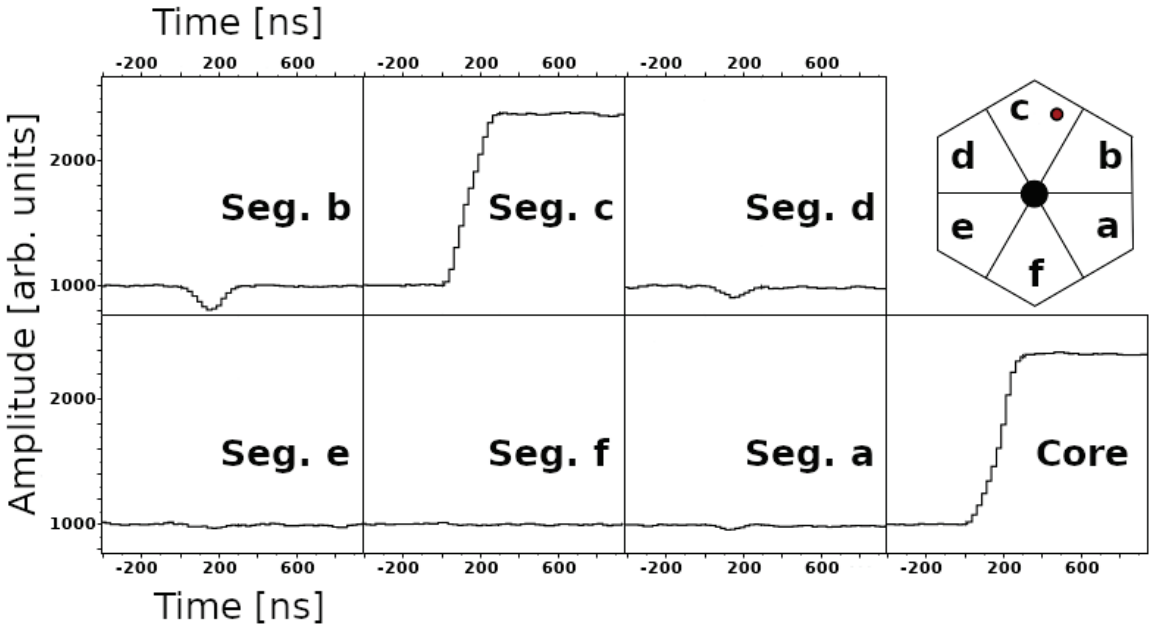

Figure 3.10: Signals measured in a 6-fold segmented detector following an interaction in segment "c" at the position marked in red. Transient signals are observed in segments "b" and "d" that are used by PSA algorithms to infer the actual position of the interaction. The figure was originally taken from [136] and modified.

3.3.2 γ-ray tracking

Starting from the individual interaction positions (*hits*) that were assigned a 3D spatial coordinate by the PSA, the tracking algorithm identifies the most likely γ ray interaction(s) that produced those hits. Ultimately, the energies of the original γ rays that impinged on the array as well as their initial directions[7] are determined, thus enabling a precise Doppler correction. Two tracking algorithms were implemented at the time of this work, the Mars Gamma Tracking (MGT)[143] and the Orsay Forward Tracking (OFT) algorithm[144], the latter used in this work.

In the energy range of interest for this experiment (100 keV-2 MeV), the dominant interaction processes of the γ rays with the Ge array are photoelectric absorption and Compton scattering. Elastic γ ray scattering, known as Raleigh scattering, becomes important only for energies smaller than 100-200 keV, whereas for energies larger than 10 MeV pair production is the most likely mechanism of interaction (see figure 3.11). Separating the hits belonging to Compton scattering processes from direct photoelectric absorptions, and, more importantly[8], refining the position of the first interaction point in those cases in which it does not correspond to the interaction point with the largest energy deposition, are the main improvements expected from the tracking itself in this work over other techniques such as an add-back based solely on the relative distance between hits.

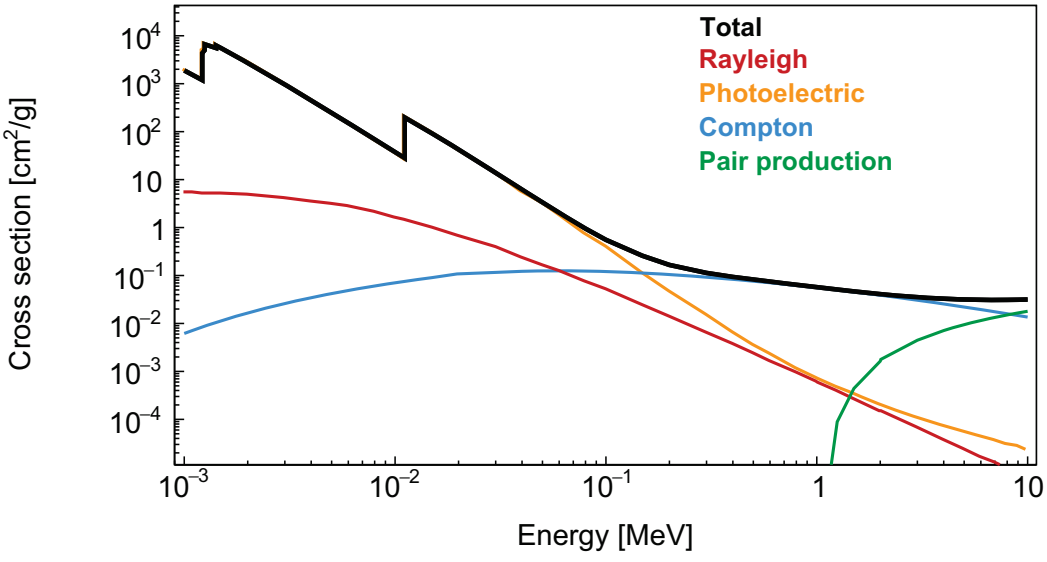

Figure 3.11: Cross sections of the main interaction processes of photons in Germanium as a function of the photon energy.

[7] Assuming emission from the target.

[8] Given the low absolute efficiency of the array at the time of the experiment and the low rate per crystal.

The main ingredients used for the OFT algorithm are the specific kinematical features of the interation processes and their absolute cross sections that determine interation probabilities according to the Beer-Lambert law. This information is used by the algorithm in order to guess whether a certain physical process is likely to occur for a certain γ ray energy at a given depth in the detector. As an example, the energy depositions coming from a sequence of Compton scatterings must satisfy the following formula relating the scattering angle of the γ ray and its energy E'_γ after the scattering,

$$E'_\gamma = \frac{E_\gamma}{1 + (E_\gamma / m_e c^2)(1 - \cos\theta)} \tag{3.6}$$

where $\cos\theta$ can be calculated using the individual positions of the interactions. On the other hand, having a 200 keV γ ray interacting by photelectric effect at a depth of 8-9 cm is highly unlikely, a fact that can be used by the algorithm to reject unphysical isolated hits in the back side of the crystal (see for instance [145]) thus resulting in a cleaner spectrum.

An approach consisting of taking the list of hit energies and positions and evaluating all possible processes giving rise to that list becomes rapidly prohibitive as the number of hits in the event is increased. Alternatively, the OFT algorithm groups the hits in clusters according to their opening angle in the unit sphere. Multiple opening angles, from a certain minimum one up to a maximum one depending on the number of hits, are tried and the corresponding clusters are formed. For clusters with multiple interactions points the algorithm tries the different possible orderings of the interactions in the cluster, assigning them a Figure Of Merit (FOM) quantifying the likelihood for a certain combination to occur. Uncertainties stemming from the finite position resolution are accounted for in the FOM by "softening" its value as a function of e.g. the difference between the expected energy deposition according to the Compton formula from eq. (3.6) and the measured one, a mismatch originating from the finite position resolution. The combination with the best FOM is finally accepted as long as it is above the cutoff probability defined by the experimentalist, or otherwise rejected.

3.4 Electronics of the acquisition

Three preamplifiers of 32 channels each were used, two of them for the sectors and the remaining one for the rings. The preamplifiers of the sectors were applied a bias voltage of -60 V on the p side to fully deplete the detector. The preamplifier signal was shaped by 6 Mesytec amplifiers of 16 channels each, four of them MSCF-16 and two STM-16+. The latter ones were used for the rings and the MSCF-16 for the

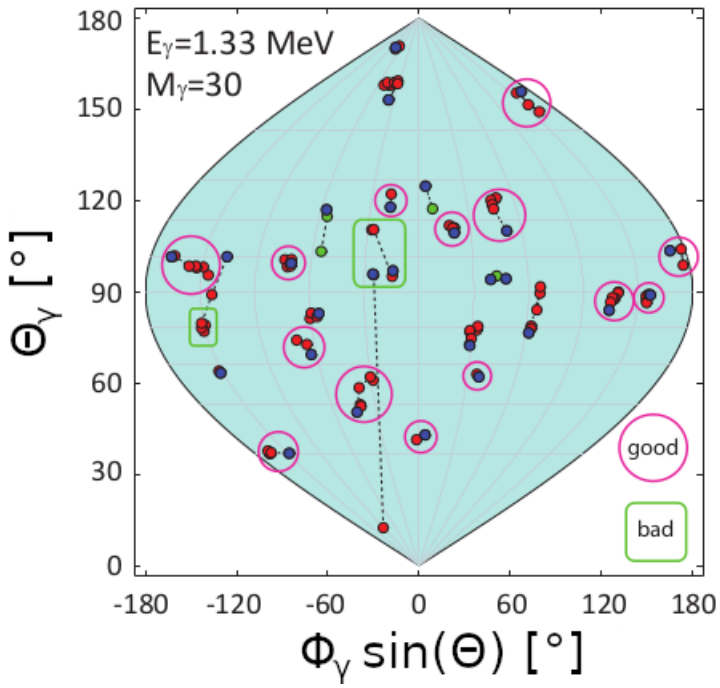

Figure 3.12: Hit map on the unit sphere of the individual interaction points in a 4π Ge sphere from a simulated cascade of 30 γ rays with energies of 1.3 MeV. Adapted from [146].

sectors. They have 16 outputs for the amplitude of the signal and 16 logic outputs. An additional CFD output in the modules provides a logic signal every time there was an energy deposition above the thresholds on one of the 16 channels. The particle trigger was constructed as an OR of the latter signal as coming from the 4 MSCF-16 modules. The shaped signal was digitized by means of 3 GANIL VXI 14-bits ADC modules with 32 channel inputs/outputs each. The logic outputs of the amplifiers were locally timestamped in 3 GANIL VXI TDC modules. A GAMER VXI trigger module was used a master trigger centralizing all the signals.

The AGATA array was equipped with two types of digitizer: version 1 (V1) which produces a CFD logic signal output from the onboard digital processing and version 2 (V2) which emits a bipolar signal, for each detected gamma ray. In total 11 crystals were connected to the V2 digitizers. The signals of both the V1 and V2 digitizers were converted to NIM signals, widened to 300 ns and aligned in time by means of gate and delay generators. The aligned signals were fed into two 32 channel LeCroy 380A multiplicity logic units. These modules allow a given crystal multiplicity to be selected. They produce a $n \times (-50)$ mV signal, where n is the number of coincident signals. The signals of the two multiplicity logic units were summed and sent to a CAEN N417 low-threshold discriminator which allowed the event multiplicity to be

selected (e.g. a threshold set on -40 mV selects multiplicity 1 and greater, -70 mV selects multiplicity 2 and greater etc.). Coincidences with the DSSSD were obtained within a 1 µs wide coincidence time window using a LeCroy coincidence module. Here the width of the AGATA multiplicity signal remained 300 ns wide and was delayed (using a gate+delay unit) so as to arrive in the center of this 1 µs wide window. During the experiment, crystal multiplicities of 1 and 2 were selected.

The trigger processor of the Global Trigger and Synchronization (GTS) system was ultimately responsible for enabling the event processing by validating the AGATA event and checking that the acquisition was not in dead time.

A sketch of the acquisition chain is represented in figure 3.13.

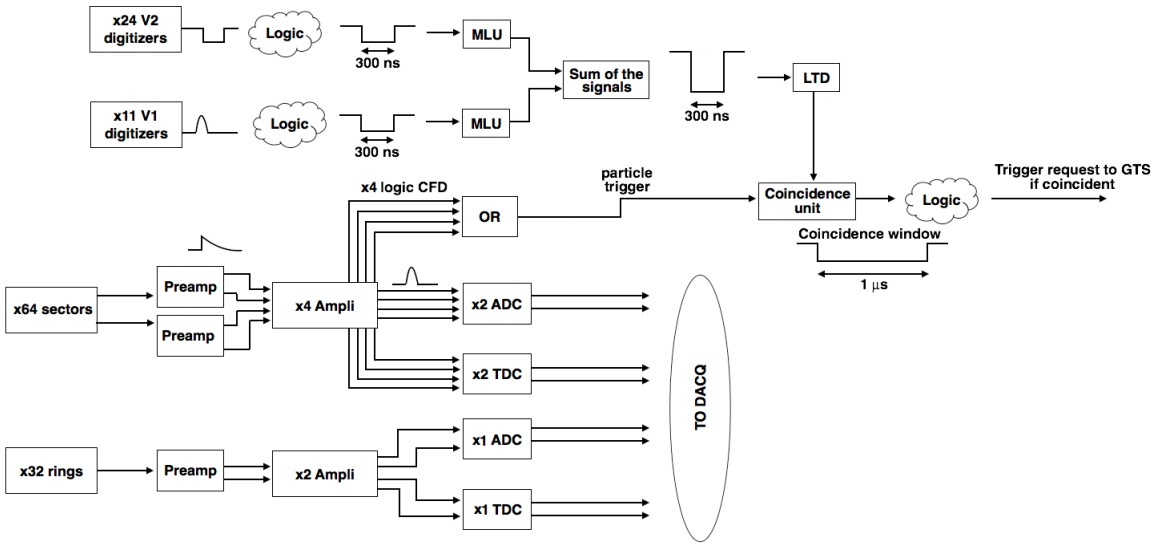

Figure 3.13: Sketch of the electronic acquisition chain and the formation of the particle+γ(+γ) trigger.

3.5 Measurement conditions

The experiment run for 6 days and comprised measurements with DSAM and self supporting targets whose thicknesses and compositions are given in table 3.2. The thicknesses of the DSAM targets were optimized for measuring lifetimes around 0.3 ps. For this lifetime there would be a balanced probability of γ-ray emission inside and outside the target. APCAD[60] simulations are shown in appendix A and illustrate the sensitivities to different lifetimes by comparing the effect of fully stopping the ^{212}Po nuclei in the backing versus letting the ions exit the target.

The self-supporting 0.56 $^{mg}/_{cm^2}$-thick diamond target was used during the first 2.5 days of data taking at a beam intensity of 2 pnA. A particle+γ trigger was used

Reaction layer	Backing
0.56 $^{mg}/_{cm^2}$ diamond	-
0.51 $^{mg}/_{cm^2}$ diamond behind 1.05 $^{mg}/_{cm^2}$ Au degrader	-
0.56 $^{mg}/_{cm^2}$ diamond	13.92 $^{mg}/_{cm^2}$ W
1.00 $^{mg}/_{cm^2}$ diamond	13.55 $^{mg}/_{cm^2}$ W
0.49 $^{mg}/_{cm^2}$ graphite	13.50 $^{mg}/_{cm^2}$ Au

Table 3.2: Composition and thicknesses of the targets used in the experiment.

within a small fraction of this data set (13 h) and the rest of the time a particle+γ+γ trigger was used. The aim of this measurement was to determine level schemes and intensities without the presence of broad lineshapes. A brief measurement of 1.5 h with a 1.05 $^{mg}/_{cm^2}$-thick Au degrader in front of a 0.51 $^{mg}/_{cm^2}$ diamond target was conducted in order to decrease the beam energy and perform a short measurement around the Coulomb barrier.

In the second part of the experiment the focus was on acquiring data for lifetime determination. A lead shield was placed around the reaction chamber at this point in order to suppress the high rates of X rays in AGATA from the electrons in the dense Au/W backings. The backed diamond targets were broken after few hours of exposure to beam intensities around 1 pnA-2 pnA. Finally, the backed graphite taget was used during the remaining beam time (2.5 days). The beam intensity was progressively increased from 0.3 pnA to 1 pnA in this last measurement.

Chapter 4

Data analysis

This chapter presents the data treatment performed for optimizing the γ-ray energy resolution and the selection of the different reaction channels. The resulting γ-ray spectra are used for constructing the ^{212}Po level scheme, for determining exclusive cross sections and for extracting lifetime information from the DSAM data as described in the following chapters. The data analysis starts with the processing of the recorded signals in AGATA and the DSSSD which are introduced in sections 4.1 and 4.2. The selection of coincident events among detectors was important for cleansing the data and is described in section 4.3. Precise conditions linking detector geometry, measured energy and particle multiplicity are required for improving the sensitivity to the α-transfer channel: these are the subject of sections 4.4, 4.5 and 4.8. This information is also necessary for identifying the reaction channels in section 4.7 and performing the accurate Doppler correction explained in section 4.6. This experiment is the first attempt of DSAM lifetime determination in inverse kinematics assisted by charge particle detection and using a projectile as heavy as ^{208}Pb. Thus the overall performance of the setup is assessed in section 4.9 based on the data analysis and with the purpose of optimizing future experiments using the similar technique.

4.1 AGATA calibrations

In γ-ray spectroscopy experiments with AGATA, the observables on which the analysis is built on, namely γ-ray energy depositions, interaction positions within the crystals and accurate absolute times of detection are extracted from the digitized waveforms or traces consisting of the electrical signals at a crystal level. The latter means that for every event validated by the GTS, the signals measured by the core and all the segments are written to disk in samples of 10 ns (according to the clock frequency of the digitizers, 100 MHz [131]), 40 samples before the triggering time and 60 samples after.

Pulse-height spectra are produced by means of the MWD algorithm and subsequently calibrated. Then, the interaction positions within the crystal are obtained from the PSA algorithm.

All the γ-ray interactions in AGATA are timestamped by the GTS. Eventually, their precise timing[1] is obtained from the fit of the experimental traces performed by the PSA. Once crystal energies and positions are determined, they are grouped into "events" spanning a certain time interval that was fixed to 600 ns in this work. Then the paths of the γ rays in the array are reconstructed on an event basis using the tracking algorithm. The output of each data processing stage is structured in the ADF format[147] and dumped to disk, including the information from the ancillary detector which is also timestamped by the GTS and merged with the AGATA events using a 1 µs coincidence window.

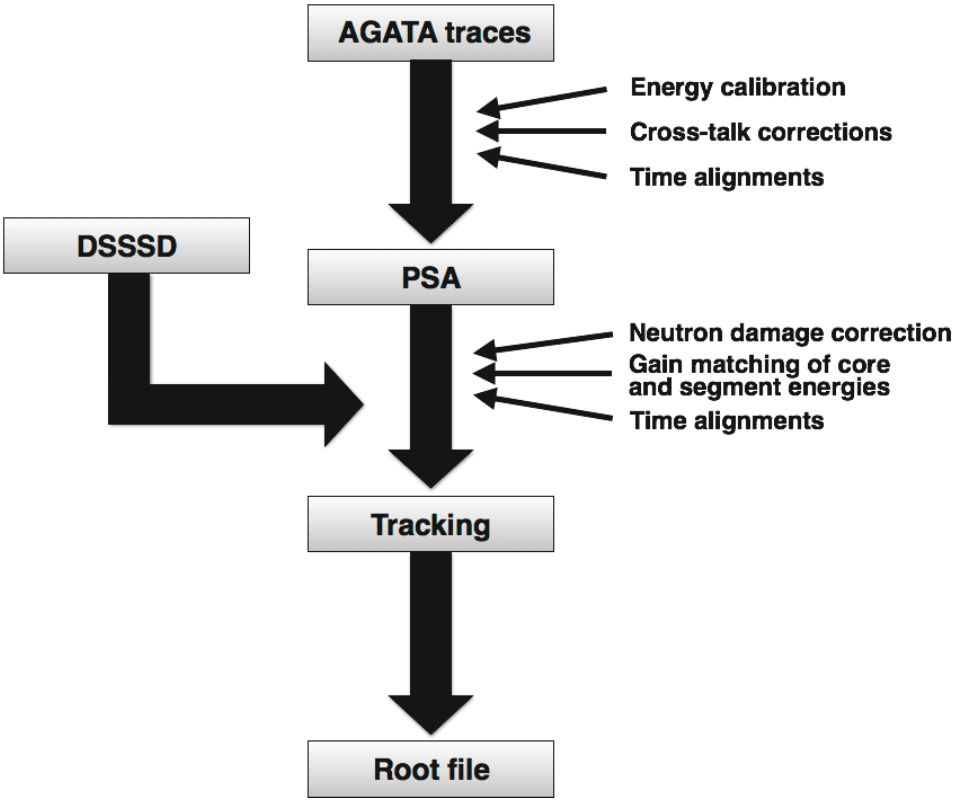

Figure 4.1: Illustration of the data processing flow starting from the AGATA traces and the DSSSD data.

The overall procedure is is divided in two parts which are sketched in figure 4.1. The first one aims to optimize the performance of the PSA and the second one is intended to maximize the performance of the tracking. Further refinements involving the energy resolution, such as an empirical correction for trapping of the charge carriers in the

[1] With a precision below 10 ns.

Ge lattice, a time alignment among all crystals and a gain matching between core and calorimetric energy of the segments in the crystal are customarily introduced in this latter stage. The DSSSD and AGATA data are also merged at this point. In the end, a ROOT file is written and analyzed using the ROOT framework[148]. An emulator of the AGATA DAQ software NARVAL[149] is available for the optimization of the procedure in offline analyses and provides a complete suite of tools that automate the extraction of calibration coefficients and correction parameters. The details of the AGATA data processing are thoroughly covered in previous works [146, 150] thus this section focuses on the specifics of this work.

4.1.1 Energy calibrations

Energy calibrations were performed using the energies of the 10 most intense transitions of a ^{152}Eu radioactive source. Only a linear function of the trace amplitude is required to properly calibrate core and segment spectra. Each crystal provides 38 channels which are assigned their individual calibration slope: they correspond to the 36 segments and the core at low and high gain. Only core energies from the high-gain spectrum were used given the low-energy range of interest in this experiment. The initial calibration is done before the PSA in order to feed the scaled traces to the PSA algorithm that fits to simulated waveforms. There was a lapse of 4 days between the initial ^{152}Eu calibration and the first in-beam data set, hence some of the channels already displayed

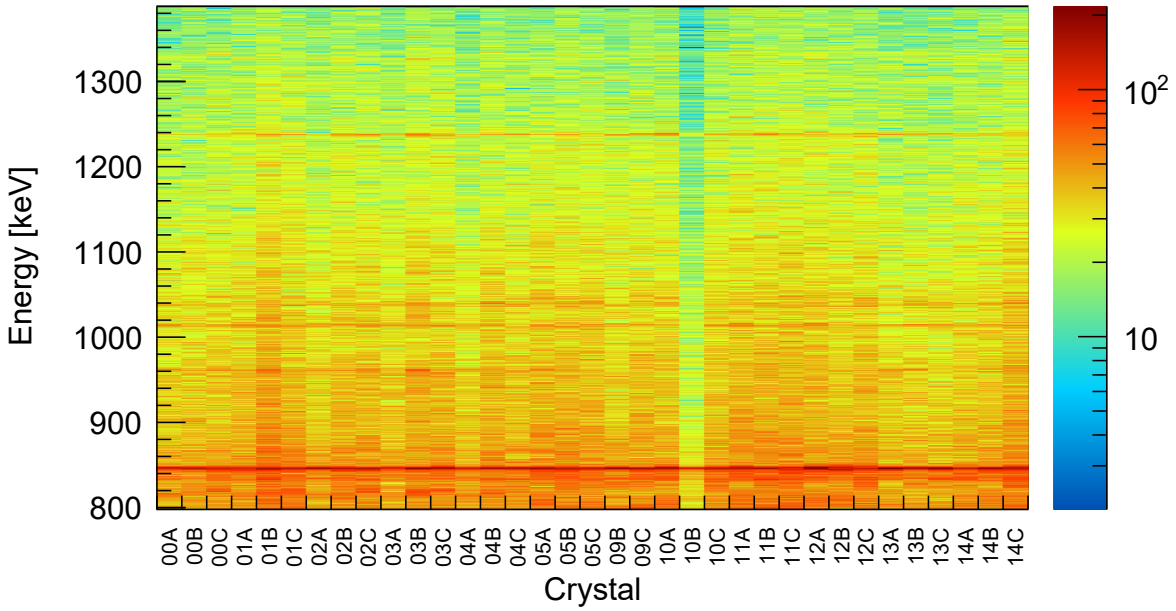

Figure 4.2: Calibrated spectrum of the cores from the in-beam data. The spectrum was constructed using events with full energy deposition in a single crystal.

large energy shifts and a source measurement taken at the end of the experiment was used for improving the initial calibration. Since the outermost segments of the crystal are to a large extent shielded by the innermost ones, the condition of full energy release in a single segment was imposed when sorting uncalibrated spectra in order to reduce the Compton background to a minimum and extract the slopes of all channels. Figure 4.2 shows a matrix of calibrated γ-ray spectra generated from the in-beam data, used for validating the calibration of the cores on inspection of the ^{56}Fe γ-rays with energies of 846.8 keV and 1238.3 keV. They are emitted at rest and stem from the activation of the surroundings.

4.1.2 Time alignments

Fine tuning of the timing occurs across multiple stages of the replay. Before the PSA, the traces of the segments must be aligned in time with the trace of the core in order to perform a reliable PSA comparison with the ADL simulated waveforms that presuppose the same interaction time. The proper offsets are extracted from time distributions calculated by software. The real interaction time of the γ ray does not directly correspond to neither the triggering time of the net charge segment neither the core due to their different shapes, but it is in between. A T_0 offset is returned by the PSA which allows to construct the precise absolute time of detection.

Lastly, a global time alignment of all crystals is performed after the PSA in which the timing of every crystal is offset in order to remove the artificial delays caused by the different electronic modules and cable lengths. The offsets are obtained as the solution of a linear optimization problem where the quantity that is minimized is the sum of squared differences of shifted times for all pairs of crystals.

4.1.3 Cross talk corrections

The calorimetric energy of the segments shows an unphysical correlation with the segment fold. This dependence is observed as a deficit on the tracked energy that increases with the fold and corresponds to cross-talk among the AGATA segments that is corrected using the empirical model described in ref. [151]. The linear correction is extracted from the baseline shift induced in all segments when the full γ-ray energy is released in a single segment. A ^{60}Co source with a large activity was used for extracting the coefficients of the linear correction, which are then applied to all E693 data sets. Moreover, the extracted matrix with the correction coefficients is inverted and folded with the "calibrated" PSA basis, hence the specifics of the instrumental response is accounted for in the PSA.

Signals in segment 13 of crystal 11B were not recorded during the experiment and therefore treated as *missing*. In contrast with a broken or faulty segment whose charge is split between the adjacent ones, in a missing segment the charge is collected in the electrodes but the information is not present in the data flow. The missing amount of energy in the segment is recovered from the energy difference between the central contact and the calorimetric energy of the segments using the cross-talk matrix. Segments 6 and 10 of the respective crystals 04C and 14A displayed exceptionally large energy shifts of 6 keV and 8 keV at 779 keV. Hence their calibration coefficient was fixed to 0 and they were treated as missing as well. Missing segments were flagged so that they do not participate in the determination of the position during the PSA.

4.1.4 Pulse Shape Analysis

The Full Grid Search PSA algorithm was applied during the offline sorting of the data. The experimental traces are benchmarked against the whole PSA basis to make the decision on the position when using this algorithm, thus it is guaranteed that the global minimum of the PSA figure of merit is always returned. On the contrary, the less time-consuming Adaptive Grid Search (AGS)[152] algorithm is typically performed in online analyses and proceeds by progressively localizing a minimum starting from a coarse lattice.

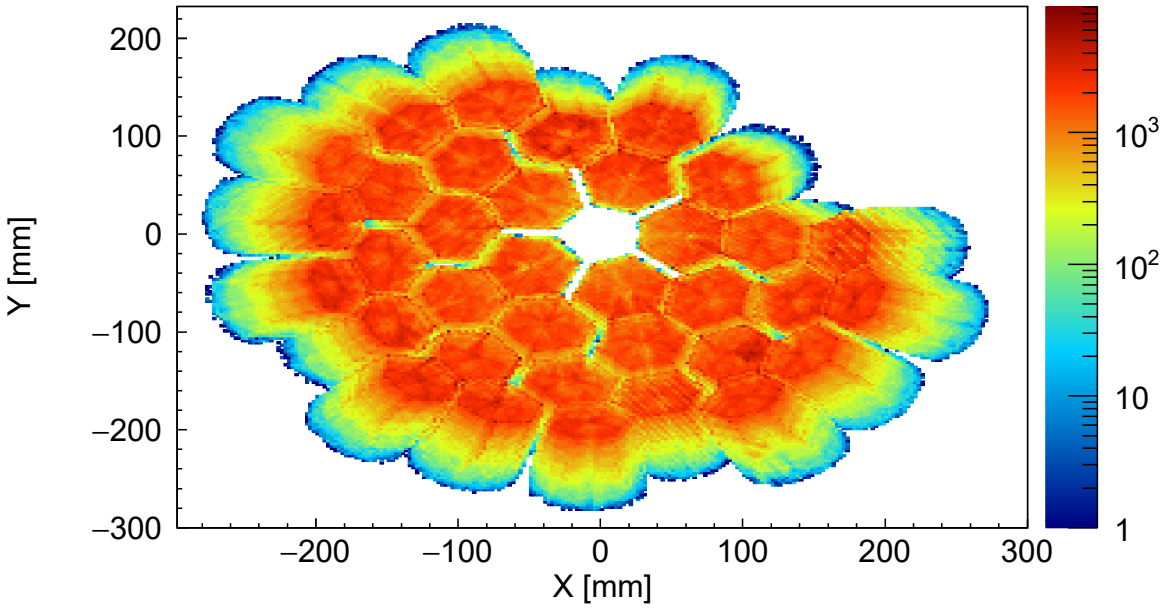

Figure 4.3: Hit pattern of AGATA constructed from the positions obtained in the PSA. Distances are relative to the nominal target position.

The fundamental assumption in both techniques is that there is a single Compton scattering per segment, otherwise the PSA result is interpreted as the barycentre of the interaction points[152]. A variant of the AGS algorithm considering the possibility of two hits within a single segment is implemented but it was not used in this work since in its current version there is an important probability of having "false positives"[153], that is, the best fit of the traces is erroneously given in many cases by a superposition of two hits within a segment when only a single interaction actually occured.

The hit map of AGATA constructed from the PSA positions is represented in figure 4.3.

4.1.5 Neutron damage correction

Exposures to fast neutrons causes lattice defects in HPGe crystals that reduce the efficiency of the charge collection process[154]. Charge trapping in the crystal is manifested in γ-ray spectra with asymmetric peak shapes with a tail on the left. Holes are more sensitive to trapping than electrons so that the energy measured by the segments will be more affected by neutron damage than the energy measured by the central contact. Given the low absolute efficiency of the array, it is possible to use only the energies measured by the core for constructing γ-ray spectra as long as the rate per crystal is low enough, thus avoiding the effects of neutron damage in the spectra. Additionally, in order to profit from the ability of the tracking algorithm in reconstructing the first interaction point using the segment energies, a gain matching between the core energy and the calorimetric energy of the segments can be performed instead. Most of the AGATA crystals displayed signs of neutron damage at the time

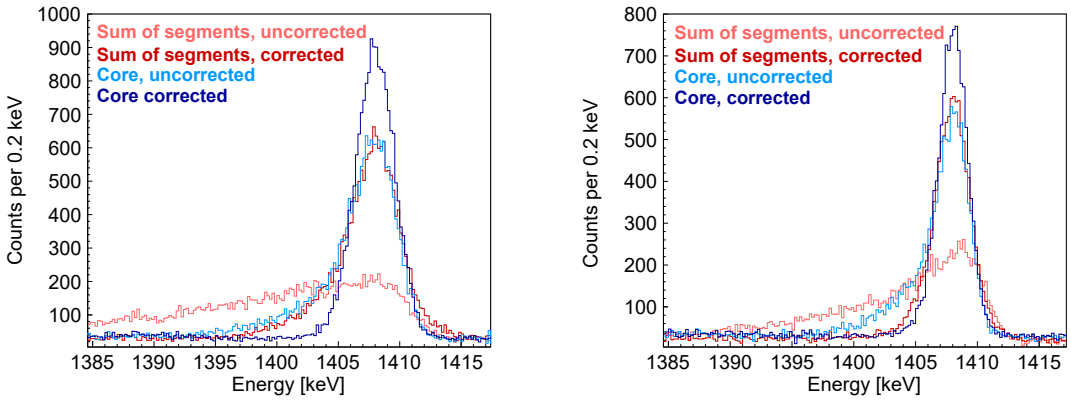

(a) Crystal 12A **(b)** Crystal 13A

Figure 4.4: Illustration of the effect of the charge trapping correction in the shape of the 1408 keV transition measured with the ^{152}Eu source.

of experiment E693 which were also evident in the energies measured by the core. Therefore, the empirical correction described in [155] was applied to both core and segment energies. A decision on whether to analyze the data using segment or core energies was eventually made based on a comparison of their performance as described in the next section. The neutron-damage correction employs the positions deduced in the PSA by introducing a correction for the loss in collection efficiency in terms of the interaction position within the crystal. Figure 4.4 shows the improvement in the shape of the 1408 keV line measured with the ^{152}Eu source before and after the correction for two different crystals.

4.1.6 Gain matching condition

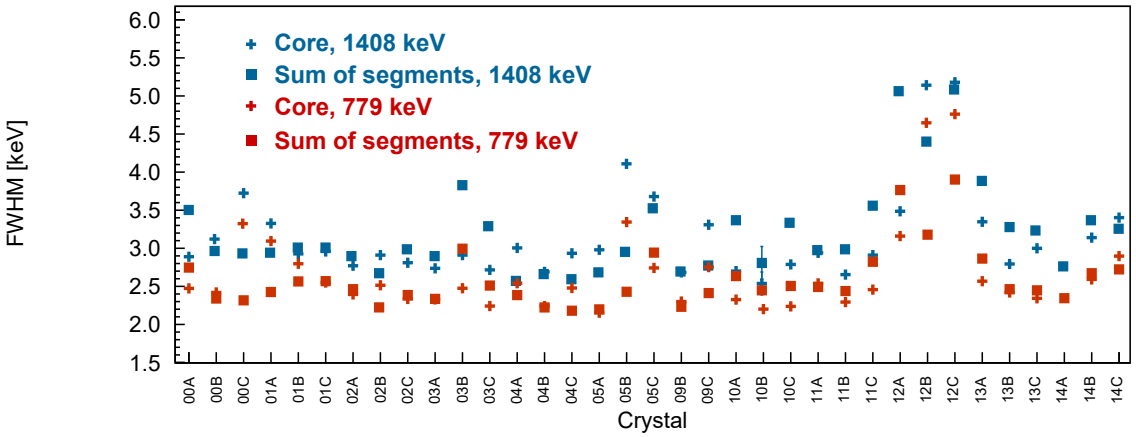

Figure 4.5: Comparison between the energy resolution of calorimetric segment energy spectra and core energy spectra.

Figure 4.5 shows a comparison of the energy resolution from the cores and the sum of segment energies after introducing the corrections. The summed γ spectra from the segments and the cores are compared in figure 4.6 for a selection of events with full energy deposition in a single AGATA crystal. Although the dependency of the peak position with the segment fold is removed after the cross-talk correction, there is a certain degree of non-linearity in the spectrum from the segments for folds larger than 1 that gives rise to the tails on the left side of the peaks in figure 4.6. The tails could be removed by setting a diagonal cut in the core versus sum of segments matrix but the profit of using the segments instead of the core energy (in terms of energy resolution) is negligible. Moreover, the smearing towards lower energies is expected to impact the performance of the tracking in general, therefore the energies of the segments within a crystal were renormalized to the core energy on an event basis. For the measurement conditions in experiment E693 at a low rate per crystal, this means that tracking and

add-back algorithms will recover the γ-ray energy by adding its energy depositions, as measured by the central contacts, in the cluster of fired crystals along its path in the spectrometer. The renormalization was not applied to crystal at position 14A because of its poor energy resolution of 13 keV at 1408 keV.

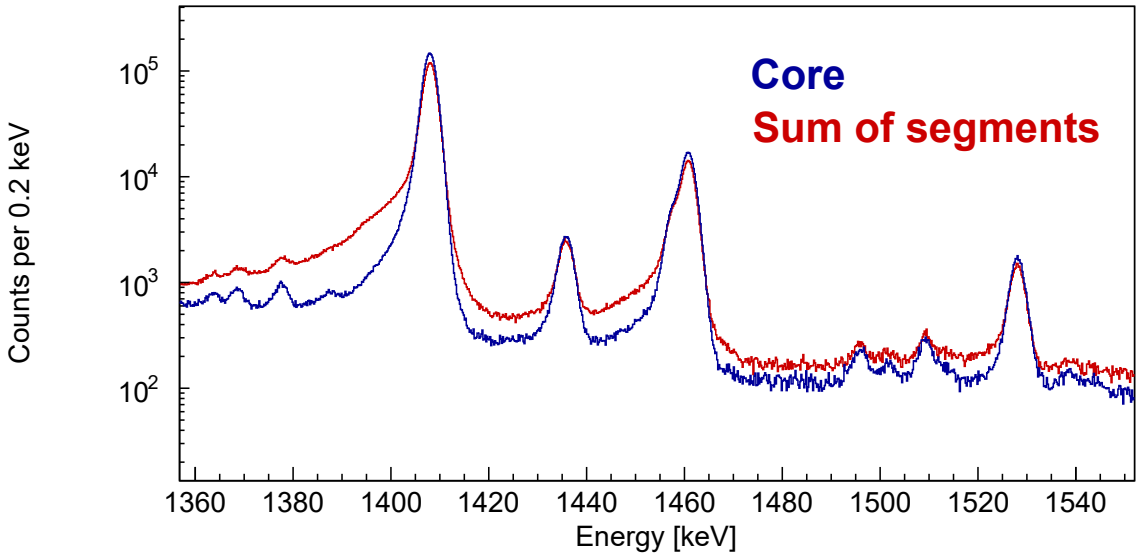

Figure 4.6: Comparison of γ ray spectra constructed using core and segment energies. Full energy deposition in one AGATA crystal was imposed for sorting the spectra.

4.1.7 Tracking

There are three adjustable parameters in the OFT algorithm that can be fine-tuned for the particular measurement conditions and the energy range of interest. Two of them define cutoff probabilities, one for accepting an isolated hit as a photoelectric interaction based on the interaction depth within the crystal and the other one for accepting a set of interaction points belonging to a cluster as depositions from the same γ ray. If a certain interaction does not belong to a cluster of multiple interaction points, an attempt is made to treat it as photoelectric interaction. It is finally rejected if the probability for the latter is below the threshold. The last parameter accounts for the uncertainty in the position of the interaction point in the figure of merit when considering the specifics of the physical process, for instance the dependence of the energy deposition with the scattering angle for Compton events. The set of values used in this work are given in table 4.1 and are suitable for γ-ray energies of a few MeV: they result in a balanced compromise between P/T and tracking efficiency as demonstrated in other works[156].

MinProbTrack [%]	MinProbSing [%]	SigmaTheta [mm]
5	2	0.8

Table 4.1: Parameters used with the OFT algorithm.

4.1.8 Efficiency calibration

The relative efficiency of the AGATA array after tracking was determined using the ^{152}Eu calibration source. The smooth function used for parametrizing the efficiency has the form[157]:

$$\varepsilon(E_\gamma) = \exp\left\{\left(\left[A + Bx + Cx^2\right]^{-G} + \left[D + Ey + Fy^2\right]^{-G}\right)^{-1/G}\right\} \tag{4.1}$$

where $x = \ln \frac{E_\gamma}{100\,\mathrm{keV}}$, $y = \ln \frac{E_\gamma}{1000\,\mathrm{keV}}$ and A, B, C, D, E, F, G are adjustable parameters. The parameter C was fixed to 0.

There are systematic uncertainties that result in small deviations, typically below 4%, between the model efficiency as given by eq. (4.1) and the actual efficiency. Therefore, the remaining adjustable coefficients in eq. (4.1) were obtained by a least squares fit.

Unfortunately, the efficiency curve has to be extrapolated towards higher energies than those covered by the ^{152}Eu source in order to extract the intensity of many transitions. It is apparent, however, that extrapolating a curve that was fitted to data points having a certain dispersion can result in a significant departure of the optimum efficiency curve at higher energies that would invalidate the assumption of e.g. 4% of systematic uncertainty in the extrapolated energy range. This issue is easily circumvented by an additional, on-site source measurement providing transitions at higher energies, using for instance a ^{56}Co source that provides γ rays with energies up to $\sim 3\,\mathrm{MeV}$. Since such a measurement was not performed in experiment E693, the additional uncertainty stemming from the extrapolation is estimated instead. The assumptions underlying the estimate are 1) that the functional form of the efficiency given by eq. (4.1) can be used to parametrize the efficiency of the array in the entire energy range and 2) that the probability of having a certain relative deviation, of systematic origin, with respect to the model curve providing the best fit in the entire energy range is the same regardless of the energy and is approximately given by a normal distribution. These assumptions are supported by previous experimental studies of the efficiency of AGATA using both ^{152}Eu and ^{56}Co sources in which the parametrization of eq. (4.1) was successfully used for energies up to 3 MeV [158]. Then, it is easy to imagine that including the transitions from a ^{56}Co measurement

in the current determination of the efficiency would only slightly modify the shape of the curve at energies below 1.4 MeV whereas significantly different values may be evaluated from eq. (4.1) at higher energies. Given the latter and the assumption for the deviations of the data points, a Monte Carlo method was used for estimating the uncertainty in the extrapolation. The procedure consisted in sampling from the fitted curve the 9 intensities used in the fit, and then refitting to eq. (4.1) the new set of 9 points. The deviation of the fitted efficiency at higher energies from the actual efficiency used for sampling can be inspected on each simulated data set. An energy-dependent uncertainty was finally extracted after performing 10000 simulations from the standard deviation of the data points at every energy. The standard deviation amounts to 6% (14%) at 1800 keV (2500 keV), therefore extrapolation to this energy range with reasonable uncertainties is possible.

The final systematic uncertainty in the efficiency was calculated as

$$\sigma(\varepsilon[E_\gamma]) = \sqrt{\sigma^2_{\text{experiment-parametrization}} + \sigma^2_{\text{extrapolation}}(E_\gamma)} \tag{4.2}$$

where 4% was adopted for $\sigma_{\text{experiment-parametrization}}$. The term $\sigma_{\text{extrapolation}}$ was added in the entire energy range for convenience, nevertheless $\sigma(\varepsilon[E_\gamma])$ is essentially identical to $\sigma_{\text{experiment-parametrization}}$ at energies between 0.2 MeV and 1.4 MeV.

Figure 4.7 shows the obtained relative efficiency curve as well as the adopted systematic uncertainty as a function of the energy, depicted by the colored band

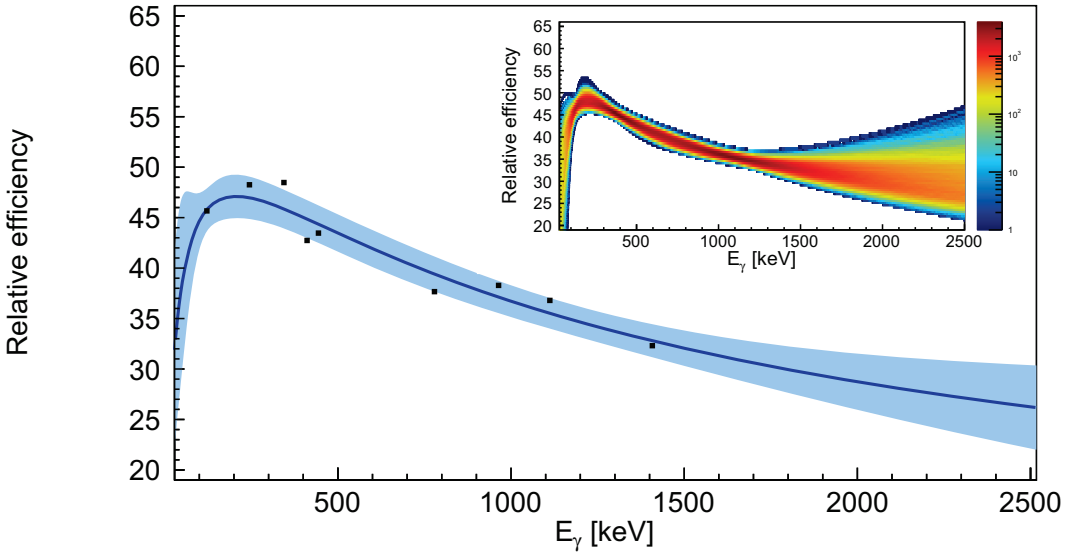

Figure 4.7: Parametrization of the relative efficiency of AGATA, represented by the solid line, deduced with the ^{152}Eu source. The uncertainty in the relative efficiency is depicted by the blue band. The inset shows the result of the Montearlo simulations used for determining the uncertainty (see text).

around the curve. The relative efficiencies obtained from the Monte Carlo simulations are shown in the 2D histogram of the inset.

Unless otherwise specified, the γ-ray intensities were extracted from coincidence spectra using all the statistics from the unbacked target data. The coincidence spectrum was corrected for the efficiency on an event-by-event basis, by both the efficiency at the energy of the gating transition and the efficiency evaluated at the energy of the coincident γ ray. The intensities of only a few γ rays were extracted from singles spectra, using the reduced data set comprising measurements with a particle-γ trigger (cf. section 3.5). A scaling factor stemming from the absolute detection efficiency and the difference in statistics between both data sets, namely the restricted and the unrestricted ones, was deduced for this purpose. The procedure was validated by extracting the intensities of prominent transitions with both techniques and comparing the results, obtaining virtually identical values in both cases.

4.2 DSSSD calibrations

4.2.1 Energy calibration

The energy calibration of the 96 DSSSD segments was performed using a 3α source. The α-particle energies emitted from the source and the branching ratios of the transitions are given in table 4.2. The ADC spectrum of every electronic channel was fitted to three gaussian functions. Then, calibrated spectra were produced by applying a first order calibration with slope and offset. These parameters were extracted from the position of the peaks using the energies of the most intense decay branches from table 4.2. Notice that the aim of this energy calibration is not to provide absolute energies but to achieve a sufficiently good alignment among all channels in their

Isotope	E_α [keV]	I_α [%]
^{239}Pu	5156.6	70.8
	5144.3	17.1
	5105.5	11.9
^{241}Am	5485.6	84.8
	5442.8	13.1
	5388.0	1.7
^{244}Cm	5804.8	76.9
	5762.6	23.1

Table 4.2: Energies and intensities of the emitted α particles from the 3α source used for calibration. The values were taken from [159–161].

calibrated spectra. Such alignment between all channels was also validated in the in-beam data by inspecting the correlation between calibrated ring and sector energies represented in figure 4.8.

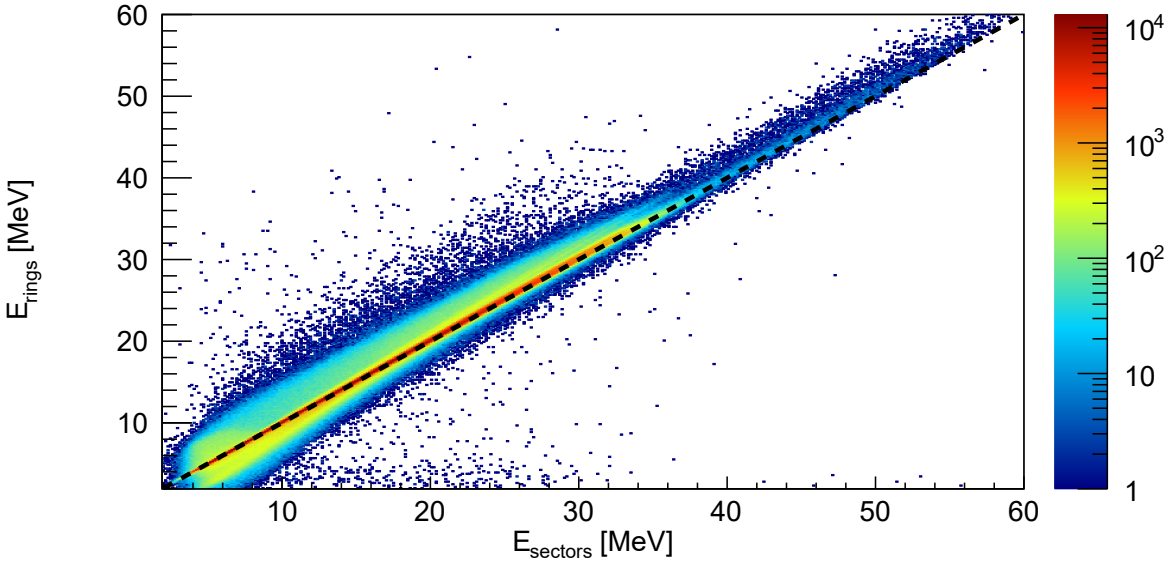

Figure 4.8: Two-dimensional matrix constructed using the in-beam data showing the correlation between the energy in the DSSSD rings and the sectors. The dashed, black line marks the events with $E_{\text{rings}} = E_{\text{sectors}}$. A selection on events firing a single pixel was applied.

4.2.2 TDC alignment

The TDC gives the difference between the timing of the sectors and the validated trigger signal. The prompt peak in the TDC spectrum of the sectors was aligned to the same value using an offset parameter extracted for each individual sector. Figure

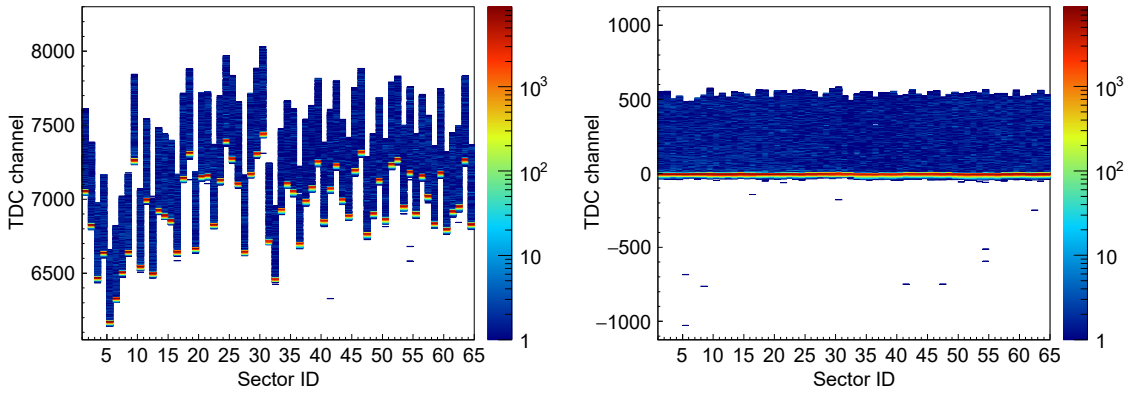

(a) Before alignment **(b)** After alignment

Figure 4.9: TDC spectra of the 64 DSSSD sectors before and after the common alignment.

4.9 shows the TDC spectrum of the sectors before and after offsetting the TDC values.

4.3 Timing and background-reducing conditions

The timestamp difference between the tracked γ ray and the detected particle was constructed and employed in order to select only those AGATA events in prompt coincidence with a particle event in the DSSSD. The spectrum of particle-γ time differences is shown in figure 4.10(a) in terms of the measured energy in the DSSSD. A dependence of the triggering time on the particle energy is observed which is most likely the result of the implantation at different depths in the detector. This effect was corrected empirically by introducing a smooth polynomial function extacted from the position of the prompt peak as a function of the energy. The removal of this dependence after the correction is shown in figure 4.10(b). The time resolution considering gamma energies higher than 500 keV and energy depositions larger than 20 MeV is 28 ns after the data processing. A number of additional peaks within the 1 µs-wide data acquisition window, separated by 120 ns, are observed on either sides of the prompt peak due to the pulsed structure of the beam. Such uncorrelated particle-γ events observed with the unbacked target mainly arise from xn fusion evaporation with large cross sections, such as the 3n one leading to ^{217}Ra. Characteristic Au γ rays emitted at rest after Coulomb excitation reactions in the backing are, on the other hand, responsible for the much larger rate in the backed target data. A comparison between the time distributions sorted in terms of γ ray energies is shown for the two targets in figures 4.11(a) and 4.11(b). Uncorrelated γ rays were removed to a large extent by selecting only those events within the prompt peak. However, γ-rays

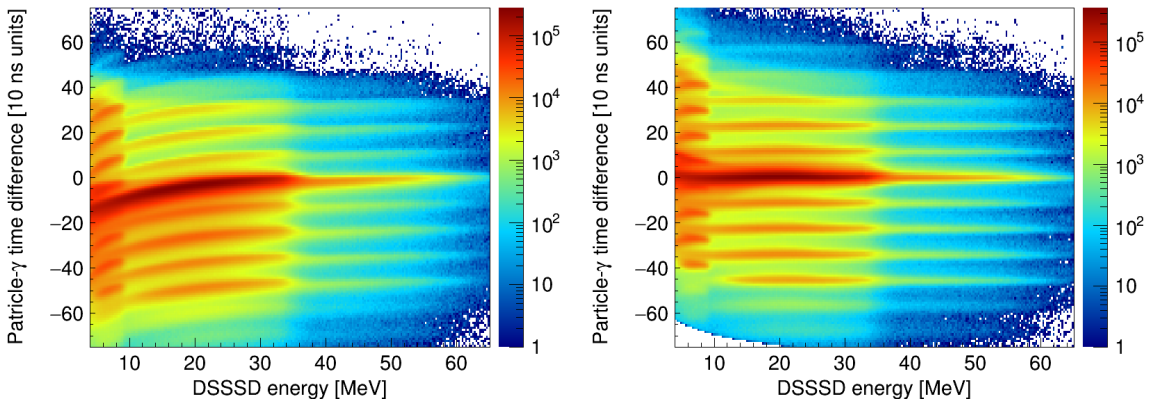

(a) Not corrected. **(b)** Corrected.

Figure 4.10: Distributions of particle-γ time differences before and after the time walk correction.

uncorrelated with the particles are also included when selecting prompt coincidences, hence a sample γ-ray spectrum from uncorrelated particle-γ events was obtained and subtracted from the prompt spectrum. The final statistical uncertainty in the bins was the result of quadratically propagating the uncertainties in the background and prompt γ-ray spectra.

Protons arriving at the DSSSD with energies between 5 and 10 MeV are responsible for the additional structures observed at low energy in figure 4.10. The timing difference between the proton events and the α particles can not be explained by time-of-flight

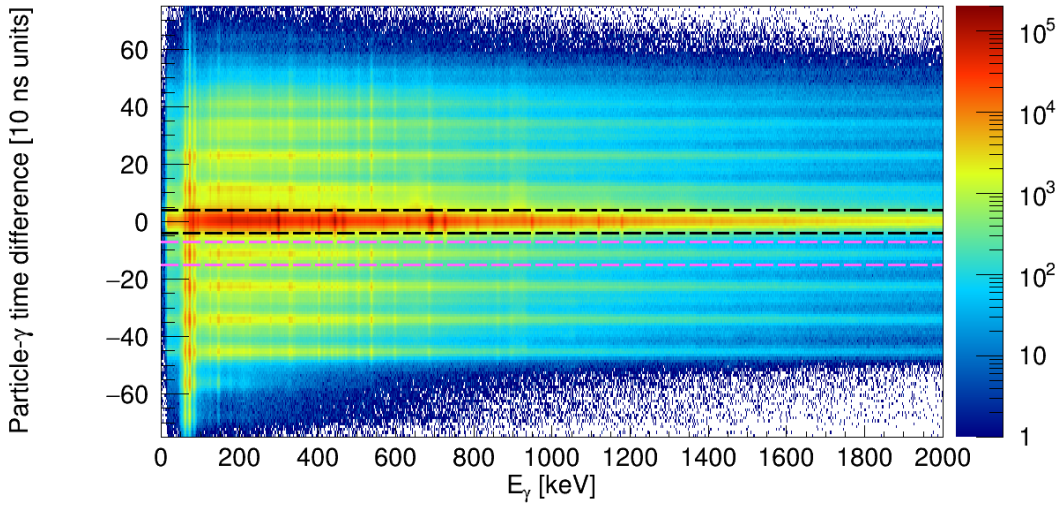

(a) Self-supporting target.

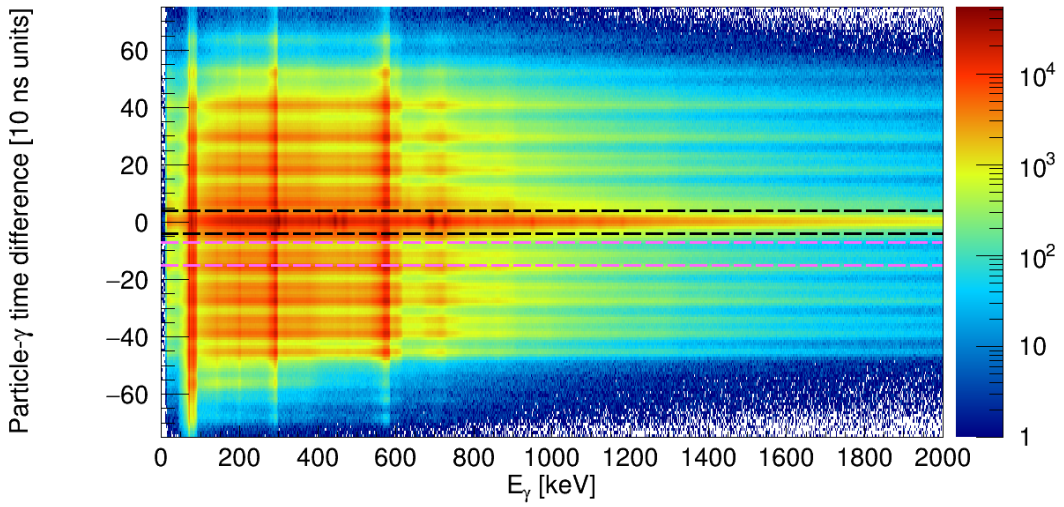

(b) Backed target.

Figure 4.11: Illustration of background-reducing conditions using the timing information. Selected events are enclosed by the black, dashed lines. The time window in the particle-γ time difference used for background subtraction is enclosed by the pink, dashed lines. Doppler correction has been performed for all γ rays.

arguments. It is due to the different timing properties of 5 MeV protons, depositing most of their energy towards the end of the detector, and 5 MeV α particles that are stopped after traversing few microns in the ohmic side. Indeed, ^{217}Fr peaks from the $1p2n$ fusion evaporation channel (see section 4.7) were only observed after selecting time differences comprised between 60 and 110 ns in the spectrum of figure 4.10(b). Additionally, only those events within the prompt peak in the TDC spectrum of the DSSSD sectors were selected in the analysis. The summed TDC spectrum of all sectors is represented in figure 4.12.

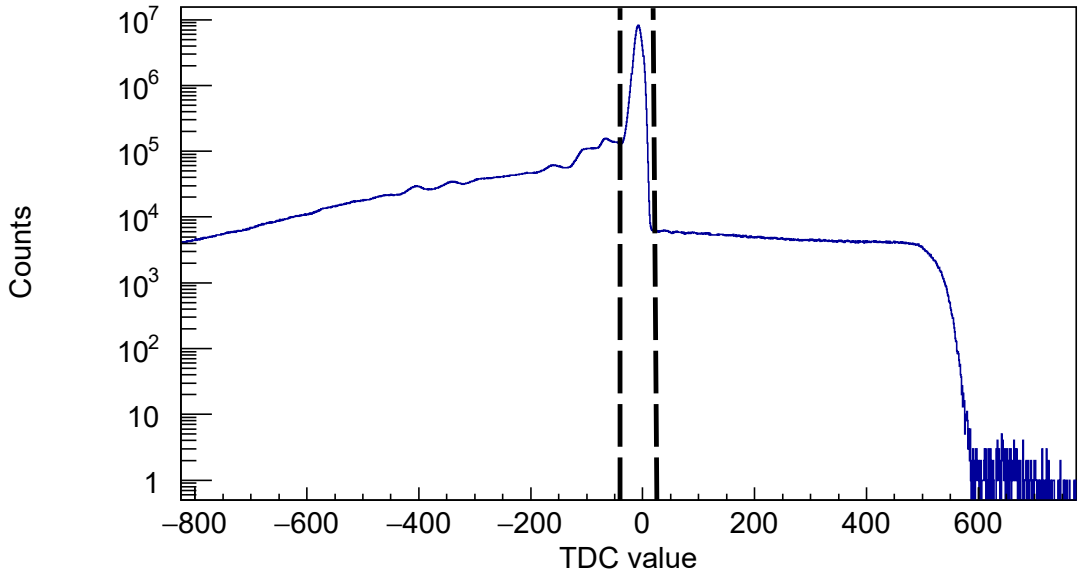

Figure 4.12: Summed TDC spectrum of the DSSSD sectors. Selected events are enclosed by the black, dashed lines.

4.4 Add-back on DSSSD energies

The inter-ring area of the DSSSD that isolates adjacent rings represents an 11% of its active area. Hence, there exists a relevant probability for a particle to impinge on the inter-strip region. Even a highly energetic α particle will be able to traverse more than one ring given the angular coverage of the detector, and in these cases the charge carriers released by the particle along its track will be collected in consecutive segments. As a consequence, the efficiency for full energy detection in a single segment is reduced and a diagonal correlation between the energy measured in adjacent segments is present. Therefore, neither the real particle multiplicity nor its energy can be derived in a straightforward manner from segment multiplicities and the individual energies in the DSSSD segments, but rather it is inferred from a combination of both. An

add-back algorithm was conveniently applied to the rings and sectors of the DSSSD for this purpose. The energy measured in consecutive DSSSD segments was considered to be produced by the same particle and added up by the algorithm. Besides the particle energy, an average entrance position in the DSSSD was also extracted with the purpose of carrying out the kinematical reconstruction of the alpha transfer reaction using the segmentation of the detector as explained in section 4.6. Figures 4.13(a) and 4.13(a) illustrate the above statements.

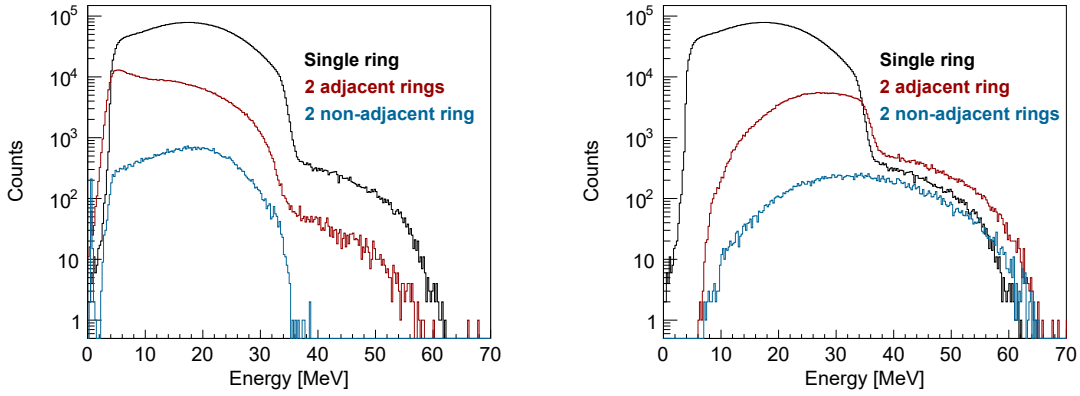

(a) Individual energies. **(b)** Total energy.

Figure 4.13: Comparison between individual and total ring energies measured in rings 5, 6 and 7 under different conditions on the fired rings.

A comparison of the energy spectrum measured in rings 5 to 7 under different selections on the fired rings is shown in figure 4.13(a). The individual energy depositions in those events simultaneously firing rings 5 and 7 only, shown in blue, are comprised between 10 MeV and 30 MeV. Events with energy deposition in a single ring are depicted in black and the energy spectrum shows an almost identical shape between 10 MeV and 30 MeV. It is thus concluded that ring multiplicity and particle multiplicity are virtually equivalent in this energy range. α particles with energies larger than $\sim$35 MeV are not stopped in the detector and deposit only a fraction of their energy in the active volume, which causes the pronounced decrease in the number of counts at this energy. Events with ring multiplicity equal to 1 show additional strength for energies above 36 MeV up to 60 MeV, which corresponds to the detection of two α particles in the same ring as evidenced from the comparison with the calorimetric energy spectrum of events firing rings 5 and 7, represented in figure 4.13(b). On the other hand, the energy spectrum of the events firing adjacent rings, either 5-6 or 6-7, shows a different shape with an accumulation of counts at lower energy. The latter is caused by the detection of a single particle which is able to traverse two rings. The corresponding calorimetric energy spectrum is shown in figure 4.13(b) and reveals

the two different energy regimes observed in the ring multiplicity 1 spectrum, one dominating below 35 MeV corresponding to the detection of a single α particle and the other one above 35 MeV caused by the detection of two α particles.

4.5 Geometrical correspondences

Knowing the pixel where the individual α particles impinged on the DSSSD is required for performing the Doppler correction and selecting the reaction channel using the energies. Nevertheless there is an ambiguity in the positions when two coincident particles are detected in two different sectors, S_1 and S_2, and two different rings R_1 and R_2, since two possible combinations of ring and sector can be constructed for each particle. This ambiguity was solved by invoking the consistency between the energies measured in both the n and p sides of detector. The process is illustrated in the matrices of figures 4.14(a) and 4.14(b) that show the correlation between ring and sector energies for events with energy signals in two different sectors and two non-consecutive rings. After imposing such consistency condition between the energies, the expected diagonal correlation between the energies in either sides is recovered as represented in figure 4.14(b). A selection of valid events with correlated energies on both sides of the detector was then performed for all events in the data regardless of the multiplicity. The selection is enclosed by the black cut in the panels of figure 4.14.

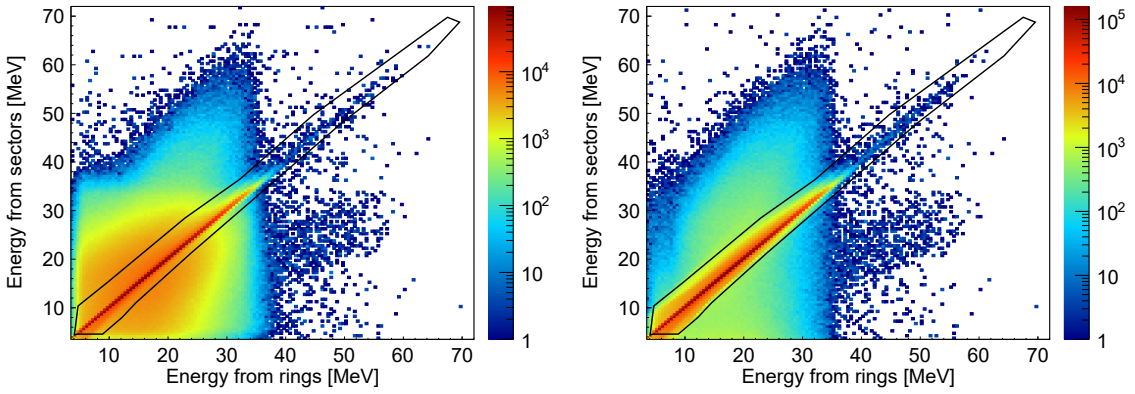

(a) Before matching the energies

(b) After matching the energies.

Figure 4.14: Illustration of the correct pixel assignment using the correlation between the energies measured on both sides of the detector for events firing two non-coincident rings and two different sectors. Events considered as valid are enclosed by the black cut.

4.6 Doppler correction

The gamma rays measured in AGATA are emitted in flight at $\beta = 0.1$, and the measured γ-ray energy for a particular transition depends on the β of the emitting nucleus and the angle between the γ ray and the nucleus in the laboratory (cf. eq. (1.47)). A Doppler correction based on the reaction kinematics and a proper characterization of the relative distances between the detectors is necessary for transfer reactions in order to profit from the exceptional position resolution of AGATA. This involves an event-by-event determination of β and θ_L using the coordinate system depicted in figure 4.15.

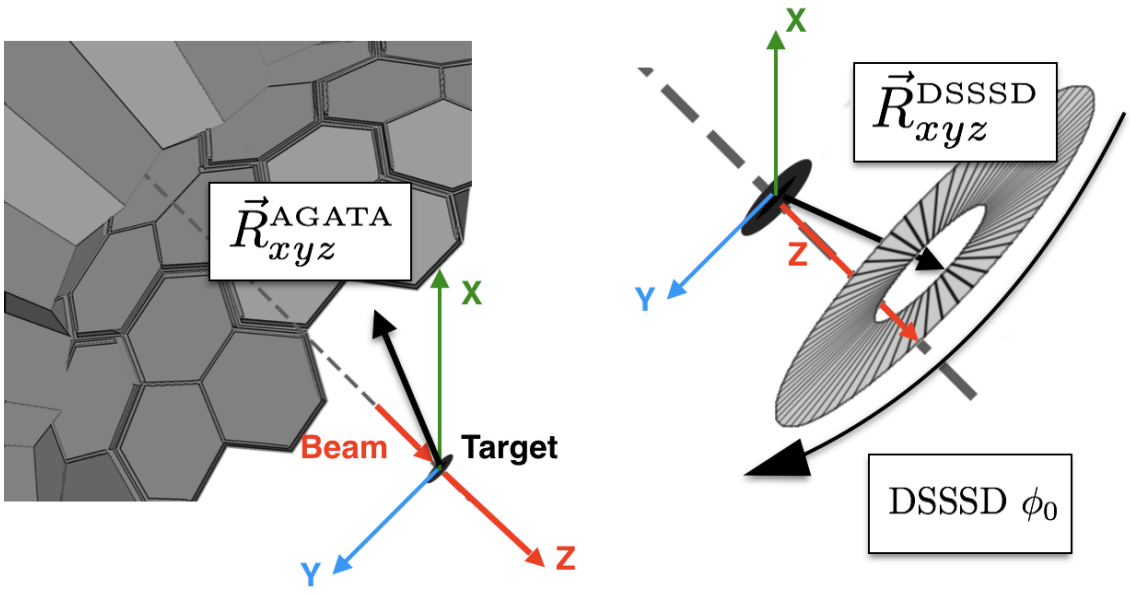

Figure 4.15: Sketch of the reference frame and detector positioning used for correcting the Doppler shifts. The absorber before the DSSSD is not shown for the sake of clarity.

The X and Y axis are parallel to the ones in the AGATA global frame, defined by the rotations and translations applied to the position of the crystal segments that correspond to the actual relative distances between crystals. The positioning has been provided by the AGATA collaboration and enables to perform tracking and add-back algorithms on the data. The Z axis is chosen parallel to the beam direction and the origin of the coordinate system is set at the beam spot on the target. The parameters defining the geometry of the setup were simplified to the position of AGATA, the position of the DSSSD centre and the physical orientation of the sectors, which is given by a rotation parameter ϕ_0.

Once these parameters are fixed, the starting point for the calculation of β and θ_L is the reconstruction of the direction of motion of the original ^{8}Be nucleus from the impact positions of the α particles on the DSSSD pixels. In the laboratory frame, the momentum $\vec{p}(^8\text{Be})$ is written in terms of the momenta $\vec{p}(\alpha_{1,2})$ of the outgoing α particles as

$$\vec{p}(^8\text{Be}) = \vec{p}(\alpha_1) + \vec{p}(\alpha_2) \tag{4.3}$$

A maximum asymmetry of 6%-7% between the momenta of the α particles is present in the laboratory frame for ^{8}Be breakups after a transfer reaction occurring at a beam energy of 1160 MeV under identical partition of the available kinetic energy in the CM frame. This maximum asymmetry happens when the emission of the α particles takes place along the direction of the moving ^{8}Be, but it is easily inferred that the individual $p(\alpha_{1,2})$ are not needed for calculating the ^{8}Be direction in this case, which is simply given by the direction of the α particles. Moreover, the straggling in the α particle energies traversing the absorber in front of the DSSSD prevents any reliable determination of $p(\alpha_{1,2})$ after the reaction. Instead, the approximation $p(\alpha_1) = p(\alpha_2)$ was made which results in the following equations:

$$\sin\phi_{^8\text{Be}} = \frac{\sin\phi_1\cos\theta_1 + \sin\phi_2\cos\theta_2}{\cos\theta_1 + \cos\theta_2} \tag{4.4}$$

$$\cos\theta_{^8\text{Be}} = \frac{\cos\theta_1 + \cos\theta_2}{2\,\cos\frac{\theta_{12}}{2}} \tag{4.5}$$

where ϕ is an angle in the XY plane, θ represents a polar angle, the subscripts 1 and 2 refer to the individual α particles and θ_{12} is the opening angle between them. In regard to the above approximation, it should be noticed that even knowing the exact values of $p(\alpha_{1,2})$ there would be little improvement over the calculated ^{8}Be direction of motion, whose uncertainty is dominated by the segmentation of the DSSSD because of the small opening angle between the α particles. A Monte Carlo simulation of the kinematics of the transfer reaction and the slowing down of the ions in the target was performed with StopSim[60] and two dimensional matrices correlating the $\beta(^{212}\text{Po})$ and $\theta(^{212}\text{Po})$ with $\theta(^8\text{Be})$ were generated. The maxima of $\beta(^{212}\text{Po})$ and $\theta(^{212}\text{Po})$ for several $\theta(^8\text{Be})$ slices were determined and fitted to smooth polynomial functions. The very same approach was followed to extract the parametrization of $\beta(^{212}\text{Po})$ and $\theta(^{212}\text{Po})$ behind the target for the DSAM data sets.

A first-order determination of the parameters defining relative distances between the detectors and the DSSSD orientation was performed from Doppler-corrected spectra as described below. Energy resolutions of 3.8 keV and 6.6 keV were attained, respectively, at 433 keV keV and 1680 keV after the optimization. These values are similar to those

observed in other experiments with AGATA after full reconstruction of the reaction kinematics[162].

DSSSD orientation

The orientation of the DSSSD was fixed to the value that optimizes the energy resolution of all peaks. A rotation parameter ϕ_0 of 95° was extracted upon inspection of the γ ray spectrum sorted in terms of ϕ_0 and represented in the two-dimensional matrix of figure 4.16.

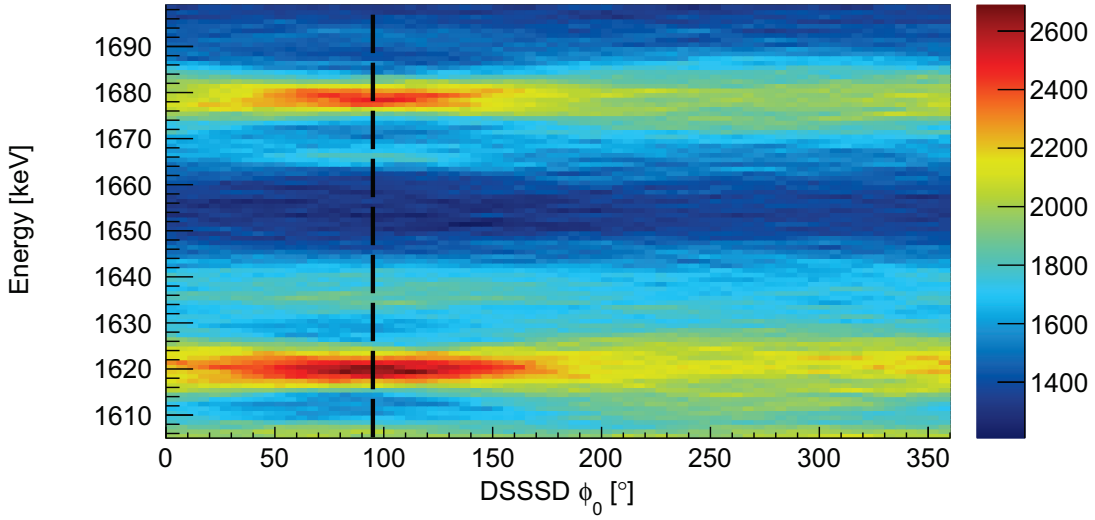

Figure 4.16: Illustration of the effect of the DSSSD orientation in the γ ray spectrum. The dashed line marks the ϕ_0 yielding the best resolution

DSSSD position in the XY plane

A small, oscillating dependence of the γ ray energies on $\phi_{^8\mathrm{Be}}$ was found, pointing out to a small misplacement of the DSSSD in the XY plane. The true XY position of the DSSSD was determined by requiring complete alignment of all lines regardless of the DSSSD portion in the XY plane triggering the event. The centroids of the ^{212}Po γ ray depopulating the 2_3^+ state towards the ground state, with an energy of 1680 keV, were sorted in terms of $\phi_{^8\mathrm{Be}}$ for this purpose. The χ^2 from fitting the dependence of E_γ on $\phi_{^8\mathrm{Be}}$ to a constant was calculated and minimized in terms of the applied offset. The calculated χ^2 matrix is shown in figure 4.17, from which the positioning of the DSSSD was fixed at $X = 1$ mm, $Y = 3$ mm.

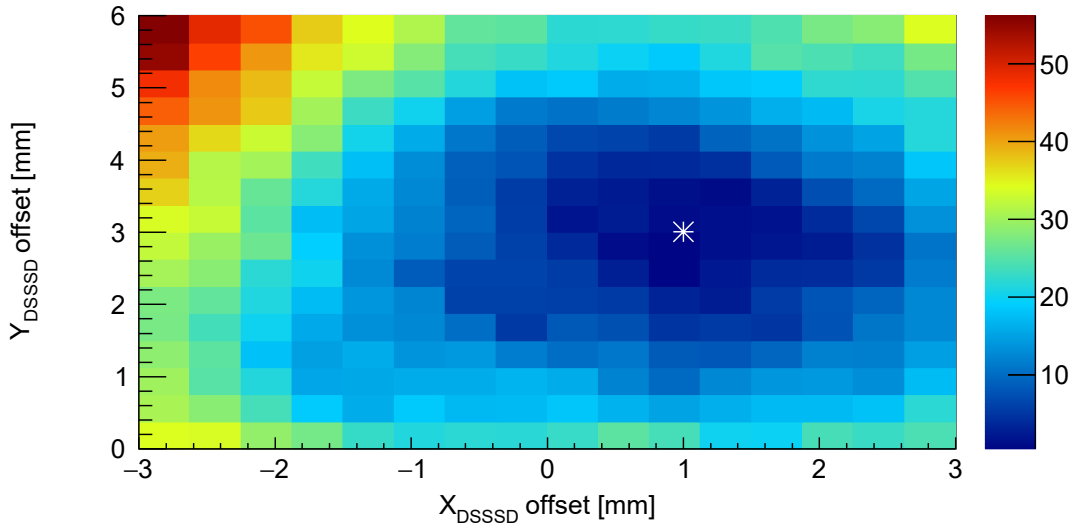

Figure 4.17: Calculated χ^2 values from fitting to a straight line the dependence of E_γ on $\phi_{^8\mathrm{Be}}$ for different DSSSD positions. The plot was constructed using the 1680-keV transition in ^{212}Po.

AGATA position in the XY plane

Offsets in the AGATA XY position were investigated by sorting the Doppler corrected energy of the γ ray in terms of its angle of detection ϕ. The Doppler-corrected energies showed low sensitivity to the XY position of AGATA, which was fixed to $X = 0$ mm and $Y = 0$ mm.

AGATA and DSSSD positions along Z

The positions of AGATA and the DSSSD along the beam direction correlate, hence they were determined simultaneously. The ^{212}Po nuclei have a maximum scattering angle of 2° (see figure 3.3(a)), so that the polar angle of the emitted radiation is very close to θ_L. Therefore, different AGATA crystals are more or less sensitive to the position of AGATA along the beam axis depending on their polar angle. If a wrong assumption is made regarding the separation between the array and the target, different γ-ray energies will be measured at different polar angles after correcting the Doppler shifts according to the nominal distances. However, a mismatch of the γ-ray energies at different polar angles may result not only from a wrong assumption on the position of the spectrometer, but also from an uncertainty in the position of the DSSSD. For instance, a DSSSD placed closer to the target results in a lower average β for the same event, meaning that a systematically higher $\beta(^{212}\mathrm{Po})$ is being used for correcting the Doppler shifts which in turn results in a systematic shift towards larger γ-ray energies given the position of AGATA at backward polar angles. Using the real

positions of AGATA and the DSSSD, the Doppler-corrected energy is not dependent on θ_γ and at the same time γ-ray energies should agree with the values in the literature. Therefore, two quantities were sampled in terms of Z_{AGATA} and Z_{DSSSD} for the joint determination of the two positions. The first one is the squared difference between the γ-ray energies for two groups of detectors, one covering polar angles smaller than 135° and the other one composed by the most backward crystal positions from 150° up to 170°. The other inspected quantity is the squared deviation of the Doppler-corrected γ-ray energy with respect to the literature value. These quantities were calculated for the short-lived, 1679.7-keV transition. Pronounced minima were found in terms of Z_{AGATA} and Z_{DSSSD} as illustrated in figures 4.18(a) and 4.18(b). The positions of these minima were extracted, and the correlation between Z_{AGATA} and Z_{DSSSD} from the position of the minima was fitted to a second order polynomial in both cases. From the intersection of the two curves values of $Z_{AGATA} = 1.5\,\text{mm}$ and $Z_{DSSSD} = 0\,\text{mm}$ were determined. This procedure was validated against systematic errors from the energy calibration of AGATA by inspecting two additional lines, the short-lived 433-keV γ ray and the 727-keV one. In the former, the residual θ_γ dependence of the γ ray energy can only be cured by fixing $Z_{AGATA} = 1.5\,\text{mm}$ if $Z_{DSSSD} = 0\,\text{mm}$, whereas a γ-ray energy of 727.1(1) keV was obtained for the latter using the extracted parameters, a value in good agreement with the previous results of Astier[109] in which the 727 keV γ was emitted at rest.

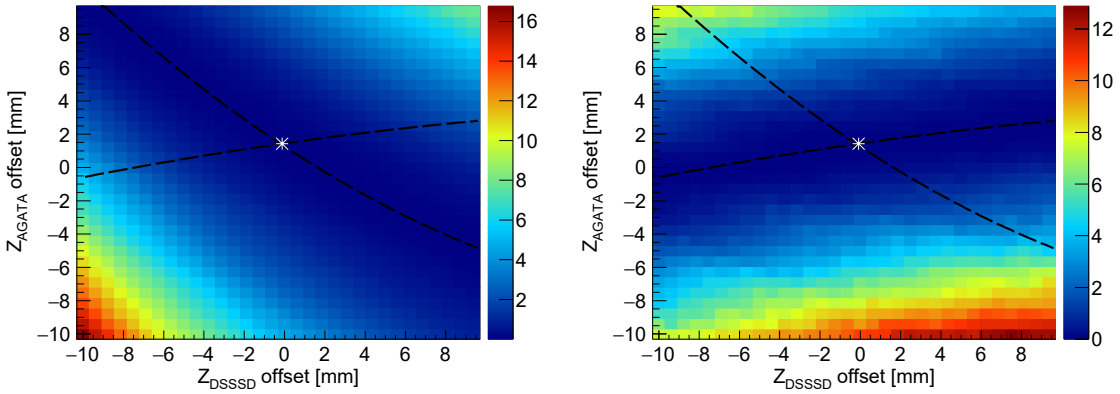

(a) $[E_\gamma(\theta_{\text{crys}} > 150) - E_\gamma(\theta_{\text{crys}} < 135)]^2$ **(b)** $(E_{\gamma,\text{measured}} - E_{\gamma,\text{literature}})^2$

Figure 4.18: Ilustration of the joint determination of Z_{AGATA} and Z_{DSSSD} from the difference of the centroid positions between the most forward and most backward rings of AGATA, as well as the difference between literature and measured E_γ. The position of the minima in both distributions are marked by the dashed, black lines.

Detector	ΔX [mm]	ΔY [mm]	ΔZ [mm]	ϕ_0 [°]
AGATA	0	0	1	-
DSSSD	1	3	0	95

Table 4.3: Summary of the extracted parameters defining the geometry of experiment E693 relative to the nominal positions $X = 0\,\text{mm}$, $Y = 0\,\text{mm}$ for AGATA and the DSSSD, $Z = 34\,\text{mm}$ for the DSSSD and $Z = -235\,\text{mm}$ for AGATA. The rotation parameter ϕ_0 specifies the orientation of the sector with ID "0" in the mapping between the electronics and the physical DSSSD sectors.

4.7 Selection of the reaction channels

Residual nuclei after reactions in the target were identified according to the γ ray spectra in coincidence with the charged particles in the DSSSD. γ-γ coincidence spectra, a comparison between DSSSD segment multiplicities and energies gated on prompt γ rays and the corresponding unrestricted distributions confirmed the presence of only α particles and protons in prompt coincidence with the γ rays. They are originating from the following reaction mechanisms:

- Fusion evaporation producing ^{214}Rn, with an α particle and two neutrons in the exit channel: ^{12}C(^{208}Pb,^{214}Rn)α2n. This deexcitation path of the compound nucleus is the second one with the largest intensity according to PACE4 and is open as a result of the range of beam energies within the target that covers values 5%-10% above the barrier.

- Fusion evaporation producing ^{217}Fr, with a proton and two neutrons in the exit channel: ^{12}C(^{208}Pb,^{217}Fr)p2n. Protons emitted between 25°and 52°as a result of this reaction have energies between 12 MeV and 23 MeV in the laboratory frame so that they are not stopped in the DSSSD when they impinge on the lower half of the detector. Consequently, a good separation from the other channels, based on DSSSD energies and the unphysical time delay explained in section 4.3, is possible when sorting the γ-ray spectrum of this channel.

- α-transfer reaction with ^{212}Po in the exit channel: ^{12}C(^{208}Pb,^{212}Po)^{8}Be

- Incomplete-fusion reaction[163] producing ^{211}Po: ^{12}C(^{208}Pb,^{211}Po)^{8}Be+n. In the breakup-fusion model[164], the ^{12}C nucleus breaks up into an ^{8}Be plus an α particle in the field of the projectile; the residual α particle fuses with the projectile resulting in an ^{212}Po nucleus excited above the neutron separation energy at 6 MeV [126]. The presence of this reaction channel is essentially

supported by the significantly lower α-particle energies as a result of the larger reaction Q-value as well as the detection of the two spatially correlated α particles from the ^{8}Be breakup. The other incomplete-fusion channel observed with ^{12}C targets[163], in which the ^{8}Be (instead of the α) fuses with the projectile, will end in almost 97% of the cases with a ^{214}Rn in the exit channel following the evaporation of two neutrons from ^{216}Rn according to PACE4 estimates. Hence, this latter channel would be indistinguishable from the α2n fusion-evaporation one (see below energy-based channel selection).

Figure 4.19 shows the prompt γ-ray spectra in coincidence with various DSSSD ring multiplicities and energies. γ-ray emissions far beyond the target, corresponding to transitions within the yrast band that have lifetimes in the range of nanoseconds, are responsible for the slight asymmetry observed in the full-energy peaks of the ^{214}Rn spectrum. The selective effect of the DSSSD segmentation is evident when selecting events firing two nonconsecutive rings. Reactions with a residual ^{8}Be in the exit channel are proposed as the only origin of those events since only spatially correlated DSSSD segments on both p and n sides compatible with the range of opening angles and α-particle energies expected from the kinematics showed coincident signals. Therefore, this selection is equivalent to a direct selection of α-transfer and incomplete fusion events totally free from contamination by the fusion-evaporation channels. However, it is clear from the spectra shown in figure 4.19 that a large number of ^{212}Po events resulted in a single detected α particle. Their origin is clarified in the next section.

Although the ^{212}Po singles spectrum of figure 4.19 contains only minor ^{211}Po contamination, it is not optimum in the sense that it does not contain all the ^{212}Po events that can be isolated using the information of the detected particles. For instance, those events in which the α particles hit either a single or adjacent rings are not included in the spectrum. They were recovered with an additional event-by-event selection using the energy after the add-back on DSSSD ring energies. As long as the DSSSD is centered with respect to the beam spot, any dependence of the measured energy on the reconstructed $\varphi(^{8}\text{Be})$ is prevented by the cylindrical symmetry of the detector, but the magnitude of the misalignment between the DSSSD and the beam spot extracted in section 4.6 breaks that symmetry and introduces an additional dependence of the energy pattern on $\varphi(^{8}\text{Be})$. Figure 4.20 illustrates this asymmetry in one of the central rings. This effect was compensated by extracting three different sets of cuts on the total energy as a function of $\theta(^{8}\text{Be})$ that are optimized for three different regions in the azimuthal plane. This was done for achieving the best separation with

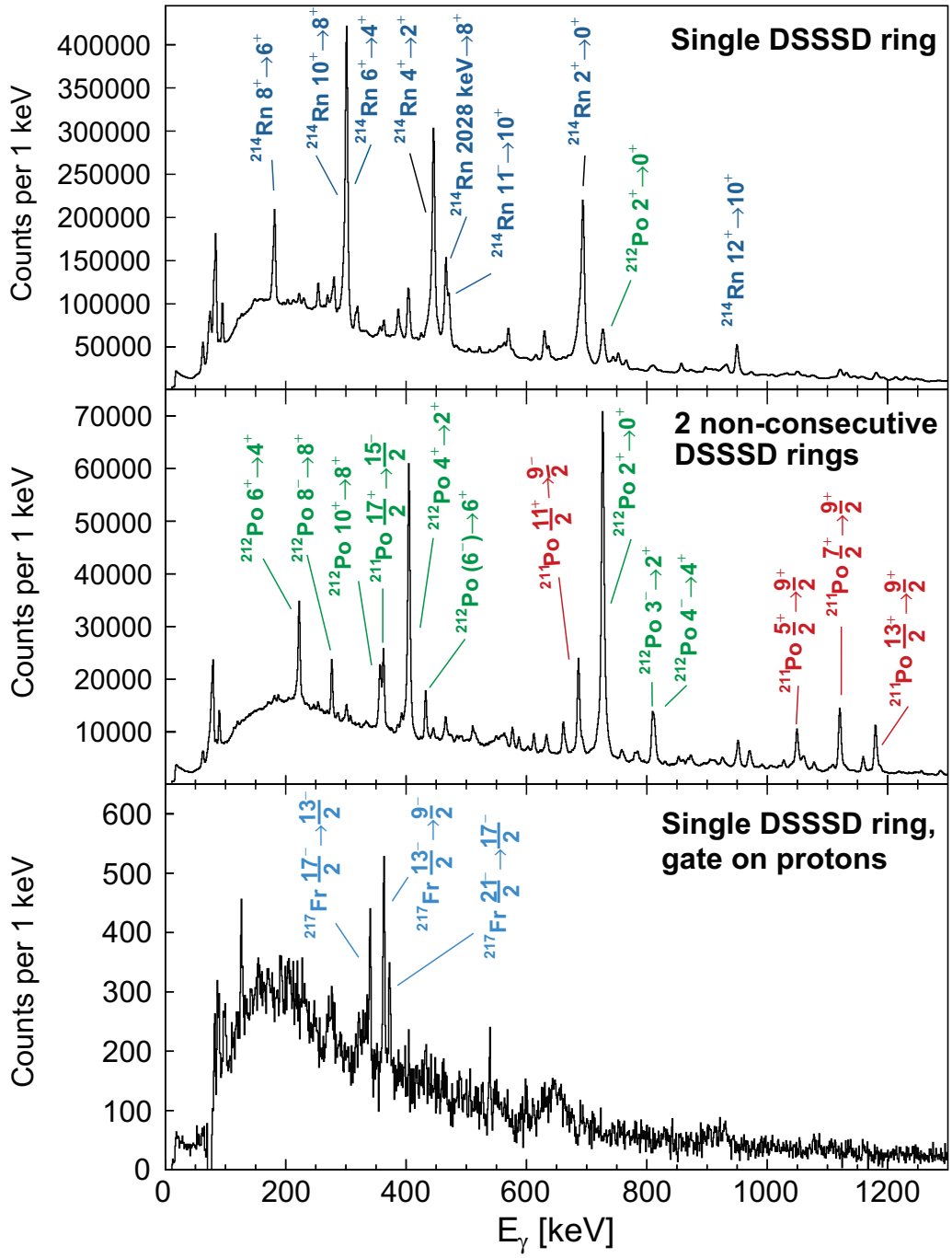

Figure 4.19: Singles γ-ray spectra taken with the unbacked target. The panels show spectra obtained after applying different multiplicity conditions on the number of fired DSSSD rings. The most intense transitions for each reaction channel are labelled in the figures.

respect to the α particles from the fusion-evaporation reactions. The regions comprise azimuthal angles between 0° and 100° for the first region, from 100° up to 150° as well as from 300° to 360° for the second region and angles ranging from 150° to 300° in the

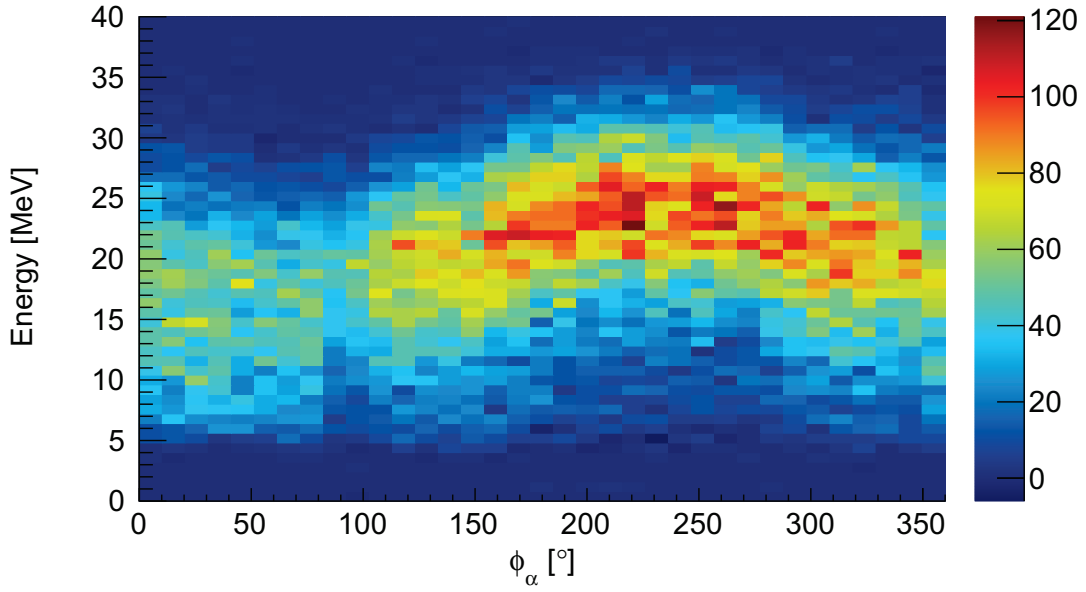

Figure 4.20: Energy depositions in ring 15 sorted in terms of ϕ_α. A selection on the most intense γ rays of ^{212}Po was performed to generate the distribution. The dependence with $\varphi(^8\text{Be})$ results from the missalignment between the beam spot and the DSSSD. Data corresponds to the self-supporting target.

last region. Identical multiplicity conditions on the DSSSD rings as in figure 4.19 were used in combination with gates on the most prominent transitions of ^{214}Rn, ^{212}Po and ^{211}Po for comparing the corresponding total energy distributions in the DSSSD and establish the cuts. In order to suppress contributions from Compton events below the gating peaks, two regions on either side of each peak were selected and the coincident energy spectrum in the DSSSD was subtracted. The obtained energy distributions and the energy cuts for ^{212}Po in the last region are compared in terms of $\theta(^8\text{Be})$ in figure 4.21 for the unbacked target data. A different set of cuts was used for the DSAM data sets to account for the energy loss in the backing and the replacement of the outermost layer of the Ta stopper by a thinner one of 12 µm. The distributions for all regions in both backed and unbacked target data sets are shown in appendix B. An 82% of the ^{212}Po events with both α particles hitting the same or adjacent rings are recovered as a result of this procedure with minimum ^{214}Rn contamination. In this way, 30% more ^{212}Po statistics was added to the spectrum in the second row of figure 4.19 after recovering the events with both α particles detected in a single or two consecutive rings as well as those events firing two non-consecutive rings after the add-back. This demonstrates that the reaction-channel sensitivity of the setup is preserved even in the presence of the Tantalum stopper as long as all the particles in the exit channel are detected.

It is anticipated that some of the excited states in ^{212,211}Po populated in the

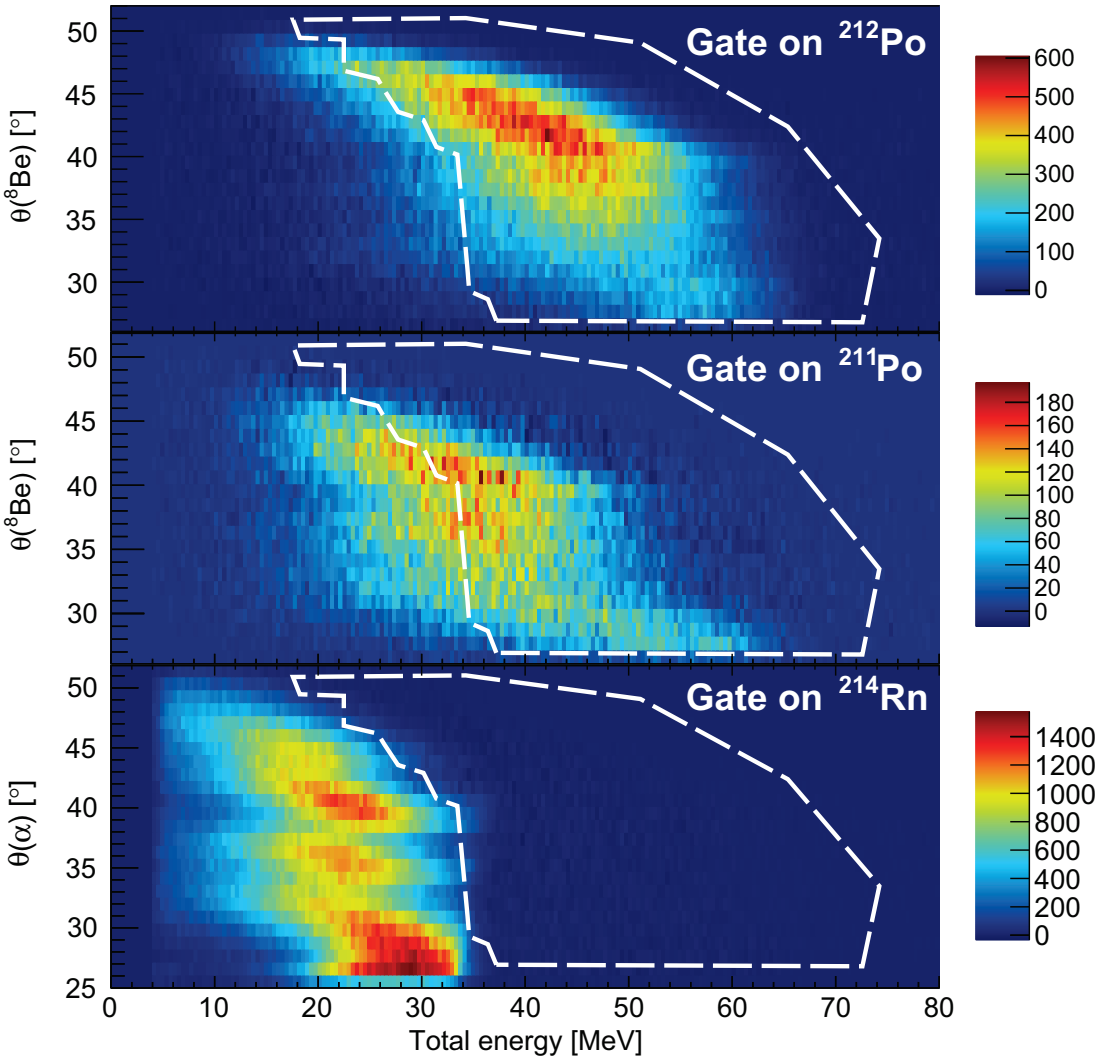

Figure 4.21: Distributions of total DSSSD energies observed in coincidence with ^{214}Rn, ^{211}Po and ^{212}Po γ rays. Only energy depositions in 2 non-coincident rings were considered to generate the ^{211}Po and ^{212}Po distributions. All the distributions are restricted to the region $150° < \varphi < 300°$. The region enclosed by the white, dashed line represents the selection used for recovering ^{212}Po events as described in the text. Data was taken with the self-supporting target.

experiment correspond to direct decays to the ground state without feeding. There are as well many previously unknown transitions with γ-ray energies larger than 1 MeV belonging to ^{212}Po and observed in cascades with low γ-ray multiplicity which are put in the ^{212}Po level scheme in section 5.1.3. Although it is not possible to achieve a complete separation between the α-transfer and the incomplete-fusion channels, it is useful to identify these transitions as belonging to either ^{211}Po or ^{212}Po in order to enable lifetime and intensity determination for these γ rays using singles spectra. Prompt γ ray spectra in coincidence with energy depositions in two non-consecutive

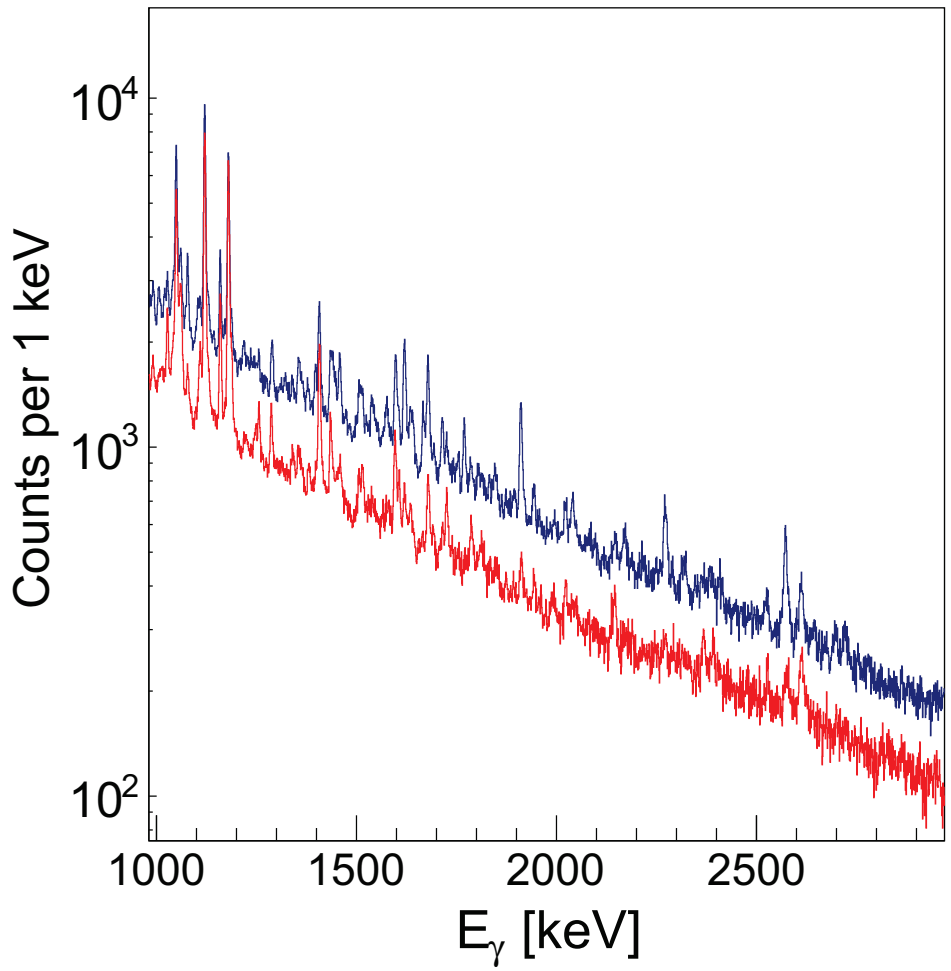

Figure 4.22: Comparison of γ-ray spectra after the selection on total energies (blue) and under inversion of that selection (red). Only events with energy deposition in 2 non-adjacent DSSSD rings were selected for generating the spectra. Data was taken with the self-supporting target.

DSSSD rings were compared after the selection on total energies and after inversion of that selection. This comparison, which is shown in figure 4.22 for γ-ray energies larger than 1 MeV, enabled a safe assignment of the transitions to either ^{211}Po or ^{212}Po.

Singles ^{212}Po γ-ray spectra generated for the 0.56 $^{mg}/_{cm^2}$ diamond target data comprising the majority of the data taking is compared in figure 4.23 with the equivalent spectrum observed during the short measurement around the barrier with a 1.05 $^{mg}/_{cm^2}$ Au degrader in front of a 0.51 $^{mg}/_{cm^2}$ thick diamond target. Besides the large suppression of the ^{211}Po incomplete fusion channel, no noticeable difference is spotted in the intensity pattern between the two measurements beyond statistical fluctuations, a result that is in line with comparisons of the excitation pattern at different energies near the Coulomb barrier made for other α-transfer reactions[165].

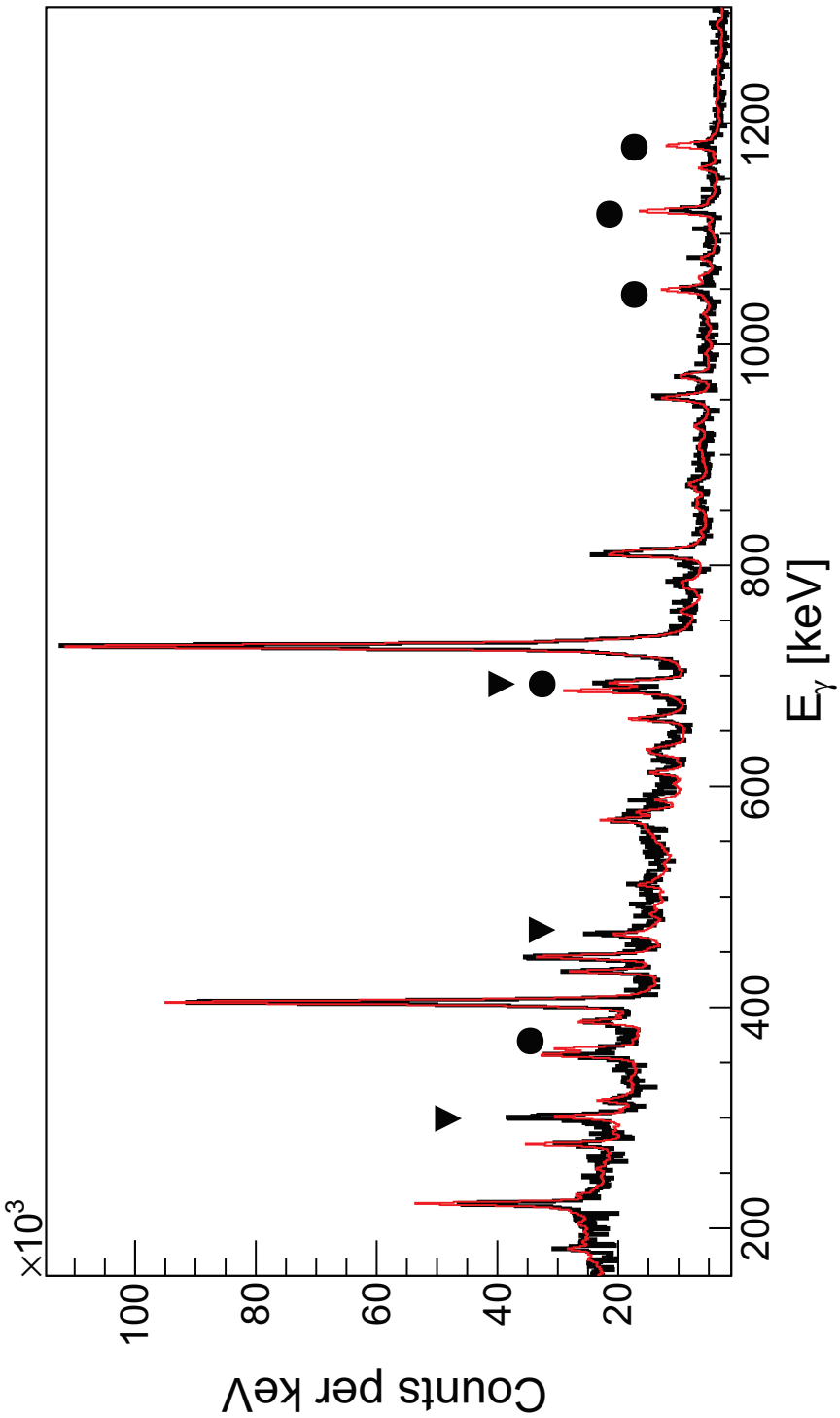

Figure 4.23: Comparison of ^{212}Po singles γ-ray spectra obtained with the 0.56 $^{mg}/_{cm^2}$ diamond target (in red) and the 0.51 $^{mg}/_{cm^2}$ diamond target with a 1.05 $^{mg}/_{cm^2}$ degrader mounted in front of it (in black). The latter spectrum has been scaled in order to overlay both spectra. Contaminant peaks from ^{214}Rn and ^{211}Po are indicated by the black triangles and squares, respectively.

4.8 Excitation of the target-like transfer partner

The excitation of the ^{8}Be nuclei produced in the α-transfer reaction was investigated in the data. The energy resolution of the present setup, however, is not sufficient to spot differences of a few MeV in the excitation energy spectrum according to the measured α-particle energies. Instead, the correlation between the energies on both DSSSD sides was explored as shown in the panels of figure 4.24. The add-back algorithm presented in section 4.4 was applied to both rings and sectors for generating the distributions shown in the figure. They were also restricted to coincidences with the most intense ^{212}Po γ rays. α particles detected in consecutive rings and sectors give rise to the diagonal elements of the matrix at $E_{\text{rings}} = E_{\text{sectors}}$. Detection of both α particles in either a single or consecutive sectors and non-consecutive rings are responsible for the events concentrating around $E_{\text{rings}} = 0.5\,E_{\text{sectors}}$. Additionally, $E_{\text{rings}} = 2\,E_{\text{sectors}}$ for a number of events, which points out to coincident detections in single or consecutive rings and non-consecutive sectors. The latter is certainly forbidden for breakups from the ^{8}Be ground state, resulting in a spatial separation between the particles which is covered by two consecutive DSSSD sectors at most (given the detector-to-target distance). On further investigation, an event-by-event calculation of the opening angle between the two α particles was performed using the positions of the segments. The calculated values were sorted in terms of the reconstructed $\theta(^{8}\text{Be})$ and the obtained distribution is represented in figure 4.25(b). Besides the expected maximum peaking near 4°, an additional, broader branch with a maximum near 20° is observed which moves toward larger values as $\theta(^{8}\text{Be})$ increases. According to eq. (3.1), the two α particles are less focused in the laboratory frame when they are emitted from an excited state instead of

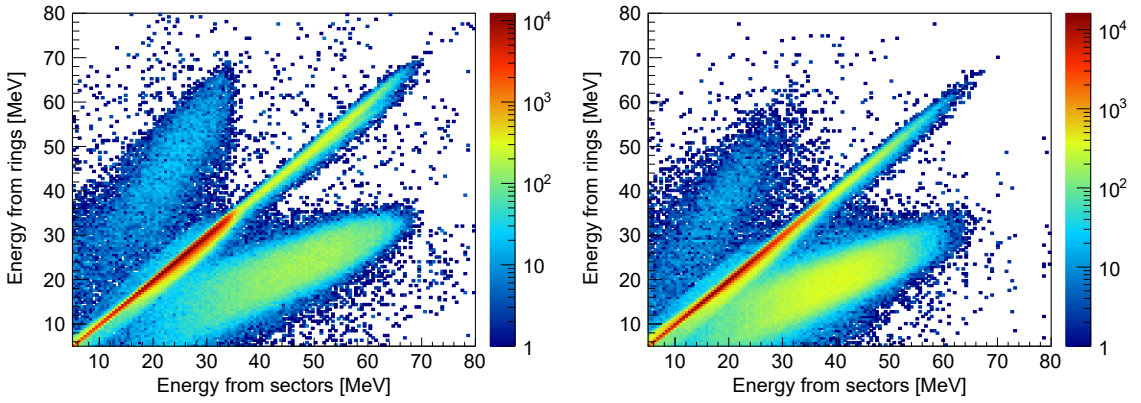

(a) $28° < \theta(^{8}\text{Be}) < 31°$ **(b)** $40° < \theta(^{8}\text{Be}) < 43°$

Figure 4.24: Correlation between ring and sector energies after add-back. A selection on azimuthal angles between 150° and 300° has been applied.

the ground state. Indeed, the expected opening angles for ^{8}Be deexcitations from its 2^+ state, shown in figure 4.25(a), are compatible with the experimental ones peaking around 20°. It is also worth stressing that the 2^+ and 4^+ states in ^{8}Be are resonances whose widths are 1.5 MeV and $\sim$3.5 MeV. These widths give rise to flatter opening angle distributions reaching slightly larger values than those shown in figure 4.25(a). Therefore, it was concluded that the concentration of events at opening angles near 20° results from ^{8}Be(2^+) decays.

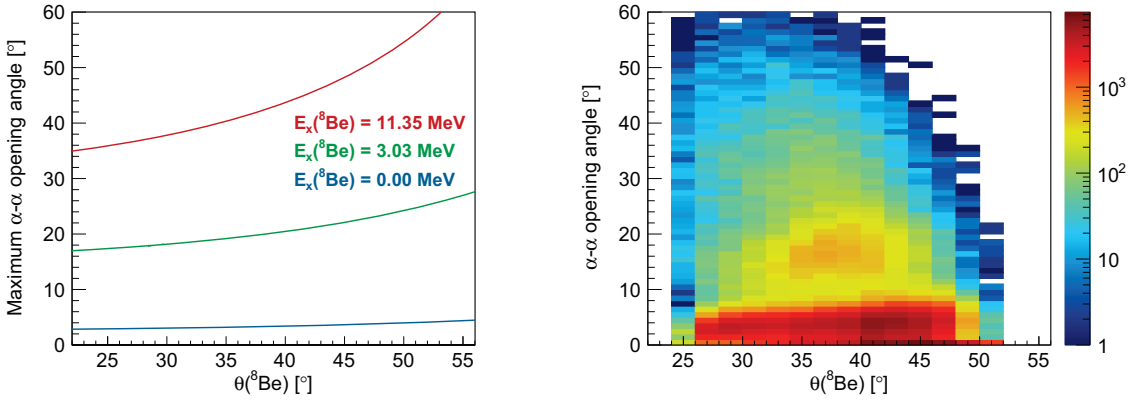

(a) Calculated **(b)** Experimental

Figure 4.25: Comparison between the experimental distribution of opening angles and the expected maximum opening angles. These were calculated for ^{8}Be decays proceeding from its ground state (blue), its 2^+ state (green) and its 4^+ state (red) after a transfer reaction occurring at the middle of target. The experimental distribution of opening angles was obtained with a γ gate on ^{212}Po. The impact position of the α particles was randomized within the corresponding DSSSD pixel for better visualization.

α-transfer events from ^{8}Be(G.S.) and ^{8}Be(2^+) were selected with gates on opening angles below 7° and between 10° and 22°. The coincident ^{212}Po singles γ ray spectra were sorted and are compared in figure 4.26, which demonstrates that the ^{212}Po population pattern does not significantly interfere with the excitation of the transfer partner. Hence, both ^{8}Be(G.S.) and ^{8}Be(2^+) events were equally included in this work when dealing with exclusive cross sections and γ-ray intensities.

A lower limit for the probability of exciting the ^{8}Be to its 2^+ state was estimated using a GEANT4 Monte Carlo simulation of the reaction kinematics and the ^{8}Be decay, with a detailed description of the geometry including the multilayered Ta stopper. Decays from the 2^+ were simulated by parametrizing the ^{8}Be excitation energy using a Breit-Wigner distribution with $\Gamma = 1.5$ MeV. Fitting the experimental opening-angle distributions to simulated ones for several $\theta(^{8}\text{Be})$ slices provided a lower limit of 20% for the excitation probability. The number of events with a missing α particle reaches

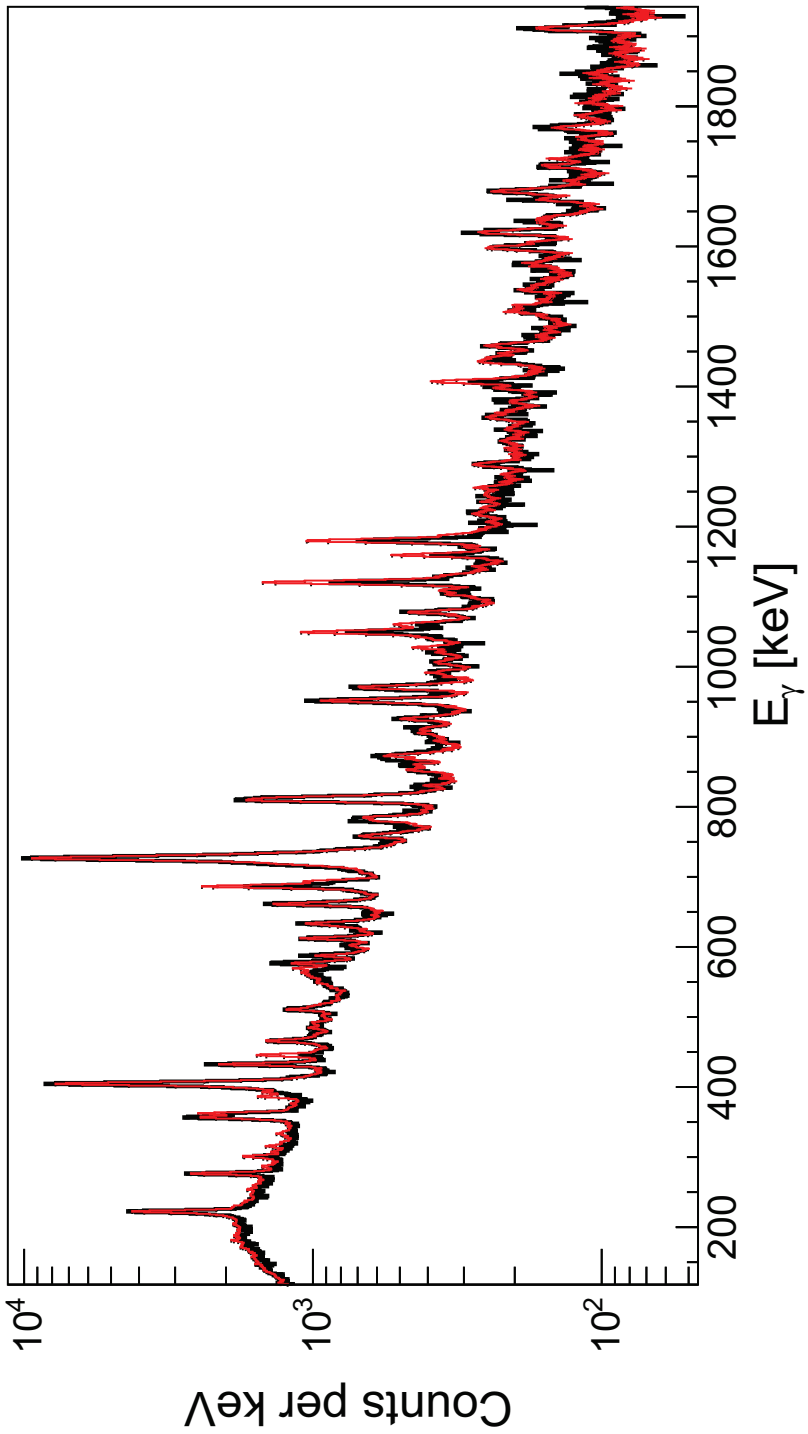

Figure 4.26: Comparison of ^{212}Po singles γ-ray spectra with a selection on ^{8}Be(G.S.) events (in red) and ^{8}Be(2^+) events (in black). The former has been scaled for the sake of an easier comparison.

30% in the central region of the DSSSD as quantified in section 4.9.2, which suggests that the actual excitation probability is close to 50%. This result is in contrast to

the partition of excitation energy in highly asymmetric transfers, typically governed by the direction of the nucleon flow, and indicates the strong contribution of nuclear structure effects in the reaction mechanism.

4.9 Performance of the experiment

It was demonstrated in section 4.7 that a good channel separation, based on measured total energy depositions in combination with the information provided by the DSSSD segmentation, is still preserved in the presence of the multilayered Tantalum stopper as long as all the α particles emitted after the reaction are detected. The limitations that influenced such detection efficiency in experiment E693 are discussed in sections 4.9.1, 4.9.2 and 4.9.3. Finally, section 4.9.4 is devoted to discussing the condition of the DSAM target throughout the experiment, which severely affected its performance for lifetime measurements. The purpose of these sections is to provide useful information for experiments aiming at DSAM lifetime measurements around the doubly-magic nucleus ^{208}Pb.

4.9.1 Channel selectivity and DSSSD positioning

It was shown in figure 4.20 that the measured particle energies are strongly lowered in the DSSSD portion that is further away from the beam spot. The α particles impinging on this region correspond to ^{8}Be decays at lower kinetic energy than in the opposite side of the DSSSD and, moreover, they have to traverse larger distances in the stopper.

Among the ^{8}Be(G.S.) decays, it is estimated that in 26% of the events either a single or no α particle reaches the DSSSD as a consequence of the misalignment. Unfortunately, the kinetic energy of the α particles emitted in fusion-evaporation reactions presents a narrow distribution peaked around 14-17 MeV in the CM frame, which prevents separating the alpha particles of the α2n channel from those of the transfer reaction on the basis of their measured individual energies only.

4.9.2 Channel selectivity and ^{8}Be(2^{+}) decays

30%-35% events in coincidence with a ^{212}Po γ ray are observed with a single detected α in the central polar angles of the detector, even in the DSSSD region that is closer to the beam spot where no α particle is expected to be stopped in the degrader and their individual energies are well above the 4 MeV hardware threshold. This is one of the fingerprints of ^{8}Be(2^{+}) decays as discussed in a previous section. The larger opening

angles may, however, result in one of the particles escaping through the central hole or being stopped in the absorber. This situation is exemplified in figure 4.27, which shows the maximum spatial separation between the particles as they impinge on the absorber surface. For a certain ^{8}Be nucleus emitted at a polar angle $\theta(^{8}\text{Be})$, one of the outgoing α particles may hit the absorber at a polar angle much lower than the original $\theta(^{8}\text{Be})$ and therefore its kinetic energy is not high enough to traverse all the layers. The other particle will, on the contrary, leave the stopper with a larger kinetic energy than the α particles from the ^{8}Be(G.S.) decays that are detected at the same polar angle. These single α particle events clearly result in an incorrect kinematical reconstruction with a bias towards larger γ-ray energies after Doppler correction.

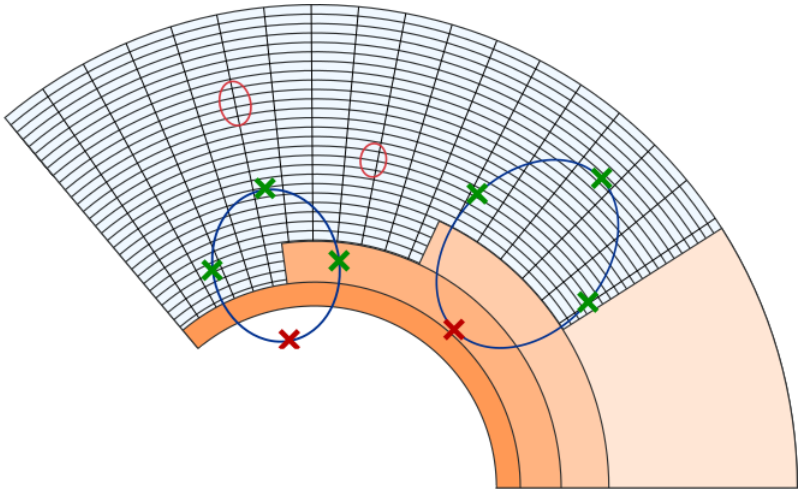

Figure 4.27: Illustration of the maximum spatial separation between the two α particles as they hit the absorber surface, delimited by the red ellipses for ^{8}Be decays from the ground state and by the blue ellipses for decays at an ^{8}Be excitation energy of 3.03 MeV. α particles impinging on the positions marked by the green crosses are able to traverse the absorber in the latter case. Red crosses indicate possible trajectories of undetected α particles.

This effect is illustrated in figures 4.28(a) and 4.28(b) showing DSSSD energy spectra observed in different groups of rings for ^{214}Rn and ^{212}Po γ-gated events, with single and 2α events sorted separately for the latter. Single α-particle detections in coincidence with ^{212}Po impinging on the first $\sim$ 19 rings display energy distributions skewed to lower energies, indicating that they are not stopped in the absorber. Those impinging in the outermost rings, on the other hand, deposit their full energy in the active volume and a number of them verify the cuts on total energies described in section 4.7. Totally removing those events can only be accomplished if the cuts on total energies are not used in the upper half of the detector. It was estimated that a single ring and a single sector would be fired in $\sim$ 90% of these events, so that they were

removed from the selection to a large extent by performing an event-by-event check on the ring and sector multiplicities. Notice that no apparent change of the peak positions was observed by excluding as well events firing two consecutive rings. A 46% of events with both particles detected in a single segment were rejected, dwindling by 5% the recoverable ^{212}Po statistics.

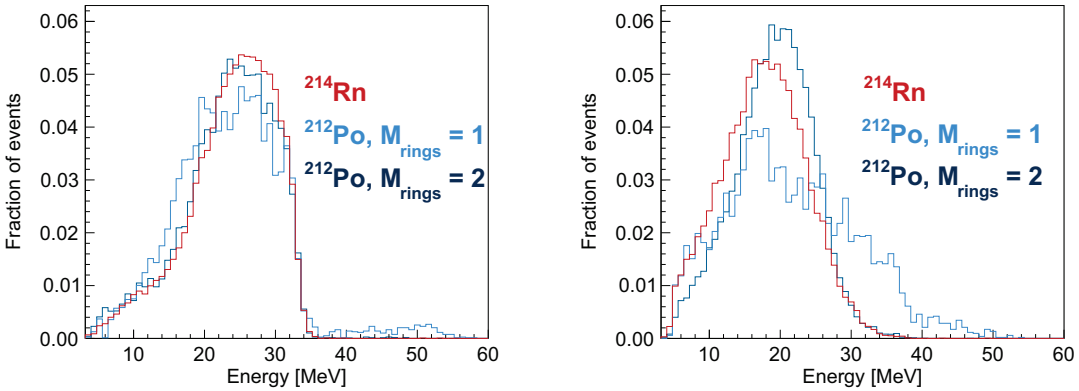

(a) Sum of rings 2-6 **(b)** Sum of rings 19-23

Figure 4.28: Comparison of the ring energy distributions gated on ^{212}Po (in blue) and ^{214}Rn (red). ^{212}Po events firing a single ring and two non-consecutive rings are represented separately. The distributions were gated on $150° < \varphi < 300°$.

A 20% smaller yield of single ^{4}He events coincident with ^{212}Po γ rays was observed during the short measurement at energies up to 5% above the barrier using the Au degrader mounted before the target. The latter was accompanied by a similar decrease of ^{8}Be decays with opening angles above 10° so that the ^{8}Be excitation probability is smaller for reactions at lower CM energy, an effect which is interpreted as a decrease of the available excitation energy compensated by the light transfer partner. Indeed, this is in agreement with the qualitative behavior of the excitation energy partition observed in these type of direct reactions: as explained in section 3.2.2, the excitation energy is proportional to the center of mass kinetic energy K_{CM} according to the semiclassical formula for the reaction Q-value (eq. (1.15)).

4.9.3 Particle rates and dead time in the DSAM data sets

Diamond targets and graphite targets, including the backed ones, were provided by two different manufacturers, respectively. Only a short, 90 minutes long data set was acquired with a backed diamond target, which was then changed to the main DSAM target of the experiment (see table 3.2). Particle rates larger by a factor 2 were observed during the latter measurement in spite that the density-equivalent thickness of the reaction layer was the same for all targets. The latter was traced

back to a much larger yield of protons based on the comparison of DSSSD energy distributions. The origin of those additional protons is not completely clear, although the presence of plastic traces in the target is a plausible explanation. They have no relevance when generating ^{212}Po γ ray spectra indeed, since their contribution in terms of random coincidences between protons and Au γ rays is removed by selecting prompt coincidences between the particles and the γ rays as explained in section 4.3. Their intensity, however, introduces a limit on the maximum beam intensity that keeps dead time losses below reasonable values, as described below.

The DAQ worked with a common dead time system in experiment E693. Every time an event was sent to the PSA farm and subsequently written to disk, the system underwent a 120 µs block, corresponding to the dead time of the VAMOS branch of the DAQ which was responsible for handling the information from the ancillary detector (DSSSD). Every other event, which otherwise would have been accepted, was automatically rejected within those 120 µs. Although the beam is spilled every 120 ns, the frequency of the beam bunches (MHz) is much higher than the measured particle rate (kHz) and Poisson statistics for describing rate fluctuations still holds to a good approximation. Therefore, the rate m written to disk relates to the true rate n and the dead time τ as[137]

$$n = \frac{m}{1 - m\tau} \tag{4.6}$$

Table 4.4 gives the average rate written to disk as extracted from the timestamped data itself under different beam intensities and trigger conditions, together with the calculated fraction of rejected events estimated as $m\tau$ from eq. (4.6). The similar rate of recorded events between the measurement with the pγ trigger at 30 enA and a p$\gamma\gamma$ trigger at 60 enA for the same target stems solely from the rejection of single γ rays with full energy deposition in a single AGATA crystal. Suppression of the fusion evaporation channels results in the much lower rates when using the diamond target with the Au degrader placed in front of it. It is to note that the original aim

Target Nr.	Beam intensity [enA]	Trigger	Recorded rate [kHz]	% lost
1	30	pγ	0.8	10
1	60	p$\gamma\gamma$	0.9	11
2	30	pγ	0.5	6
3	30	p$\gamma\gamma$	1.4	17

Table 4.4: Average rate of recorded events under different measurement conditions. Targets 1 and 2 correspond to the unbacked diamond without and with a thin Au degrader in front of it, respectively, whereas target 3 refers to the graphite target with an Au backing. See table 3.2 for the complete reference of the used targets.

of the DSAM measurements, based on the spectroscopic information available in the literature, was to accumulate as much statistics as possible in $\gamma\gamma$ coincidence spectra for DSAM measurements at $E_\gamma < 1\,\mathrm{MeV}$, a region with a high density of lines in singles γ-ray spectra, and at the same time to avoid reaching dead time losses close to 33% at 30 enA.

4.9.4 DSAM target condition throughout the data taking

The stability of composite targets is of paramount importance for DSAM lifetime measurements. Adherence of the reaction layer to the backing is sensitive to the temperature, and undesirable effects such as void formation in both the interface and the metallic backing, blistering and sputtering may occur depending on the temperature, fluence, crystal structure and composition. The response of the composite target was examined in the offline analysis as a function of time as represented in figure 4.29(a). Unfortunately, it was not noticed during the online monitoring of the data that every increase of the beam intensity, marked by the dashed lines in the figure, was followed by a sudden degradation of the energy resolution caused by blister formation and/or heat-related deformation in the backing that widens the ^{212}Po velocity distribution behind the target. A comparison of the same spectrum projected at different moments also shows the development of a crack, revealed by the different "backgrounds" of spectra in figure 4.29(b). This is most likely following the separation of the reaction layer and the backing at the beam spot. Occurrence of sputtering could not be neither confirmed nor ruled out given the uncertainty stemming from the slight oscillations in the beam intensity and the asymmetry of the Doppler-corrected peaks. Hence, lifetime values extracted by fitting to simulated lineshapes are not reliable. Two approaches were followed in order to extract relevant information from the DSAM data sets:

- A reduced DSAM data set spanning the first 4 hours of data taking was inspected and compared with the unbacked target data in order to search for short-lived transitions with a balanced probability of γ ray emission both in and off the target, namely $\tau \sim 0.3$ ps. Beyond the first 4 h the shifted and unshifted[2] components of the lineshape are strongly overlapping as a consequence of the deterioration of the target.

[2]The terms *shifted* and *unshifted* are referred in this work to γ-ray emissions within and behind the target, respectively, in analogy with the terminology employed in traditional thick target DSAM experiments in which the lineshape consists in a Doppler-broadened part from emissions at varying velocity (shifted part) and a stopped peak from deexcitations at rest (unshifted part).

- For shorter-lived states ($\tau < 0.2$ ps), deexcitation occurs always within the target and close to the reaction layer. It is thus helpful for identifying low intensity transitions to correct the Doppler shift as if γ-ray emissions always happen in the interface, that is, using calculated velocities of the outgoing ^{212}Po ions as they enter the backing. Since the angular and energy straggling is still small within the first few µm of Au, making use of the precise kinematical reconstruction enlarges the sensitivity to the lifetime. An upper limit of the lifetime can be set

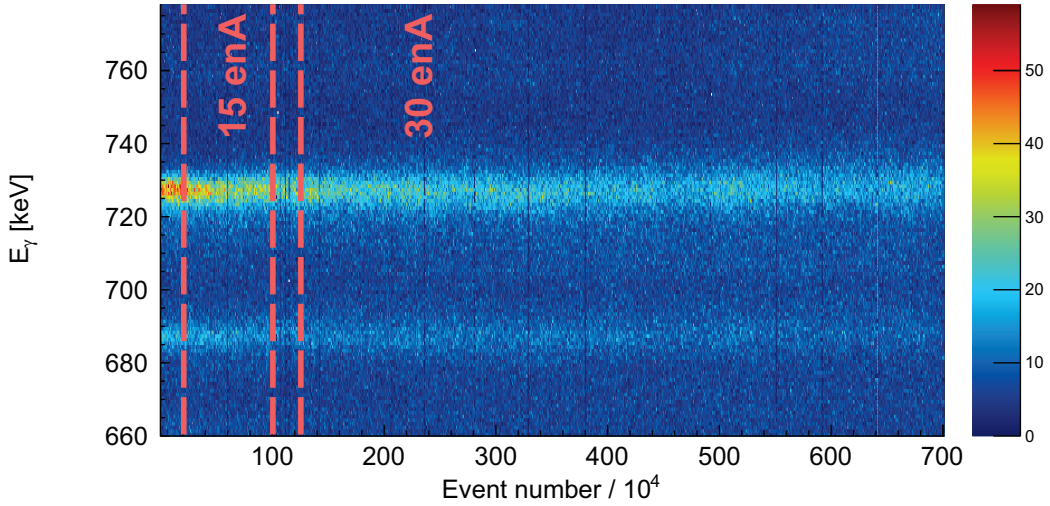

(a) γ-ray spectrum with a selection on ^{212}Po as a function of event number. Intervals corresponding to the sequential measurements at beam intensities of 10, 15, 20 and 30 enA are enclosed by the dashed lines.

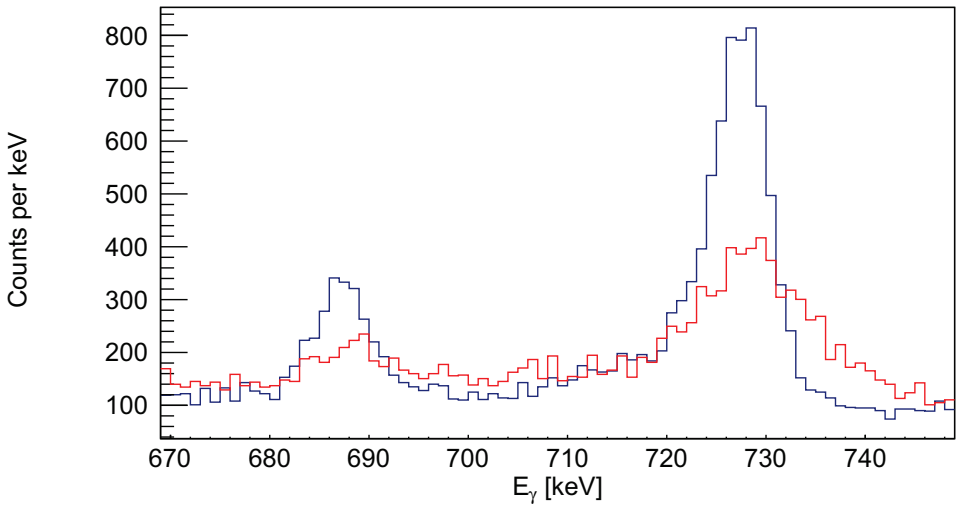

(b) Comparison of γ-ray spectra projected on the first 2×10^5 events (in blue) and the last 2×10^5 events (in red).

Figure 4.29: Illustration of the deterioration of the DSAM target in the course of experiment E693. Doppler correction has been applied assuming deexcitations just behind the composite target in all cases.

using the full collected statistics.

The outcome of both approaches is discussed in section 5.2.

Chapter 5

Results

5.1 Results from thin target data

5.1.1 $\gamma\gamma$ coincidence relationships

$\gamma\gamma$-coincidence matrices were constructed for the construction of the level scheme. Since only a single α particle was detected for a large fraction of ^{212}Po events, a choice between statistics and cleanliness has to be made when sorting coincidence spectra. Including as much statistics as possible in ^{212}Po coincidence spectra implies sorting coincidences using raw γ-ray spectra, that is, without conditions that remove the fusion-evaporation channels. This requires larger background subtractions correcting the coincidences with the Compton background from ^{214}Rn γ rays below the ^{212}Po peaks as well as including events with an incorrect kinematical reconstruction that worsens the energy resolution and introduces small systematic errors in the energies. On the other hand, purging the coincidence data by using the selectivity of the setup to the α-transfer reaction minimizes the background subtractions and optimizes the quality of the Doppler correction. The latter option was finally chosen since it was found to be more satisfactory for the identification of weak lines. Only those transitions whose intensities have statistical significances above 2σ were placed in a cascade.

First information on ^{212}Po excited states dates back to ^{212}Bi β-decay studies which established the first four 2^+ states at 727 keV, 1513 keV, 1680 keV, 1805 keV as well as the 1^+ state at 1621 keV [166–169]. The spin and parity assignments of these states were established on the basis of conversion-electron spectroscopy and $\gamma\gamma$ angular correlations[170, 169] with agreeing results from different works. The yrast band up to the 14^+ state was established in the late 80's by means of fusion-evaporation reactions[171, 108]. A significant extension of the level scheme including many more off-yrast states than observed by Poletti[108] and the interpretation of most of them as collective ones, was performed by Astier and collaborators[109].

Figure 5.1 shows the coincident γ rays with the $2_1^+ \longrightarrow 0^+$ (727 keV), $4_1^+ \longrightarrow 2_1^+$ (405 keV), $6_1^+ \longrightarrow 4_1^+$ (223 keV) transitions and with the 811/814 keV doublet.

The strongest feeder of the 2_1^+ is the 810 keV transition from the well established excited state at 1537 keV. This state was previously assigned spin and parity 3^- and was interpreted as a coupling of the seniority-excited neutron pair to an excited ^{208}Pb core in its 3^- octupole state, in analogy with the situation in the ^{148}Gd nucleus. Its deexciting transitions are coincident with three gamma rays with energies of 1104 keV, 1716 keV and 1440 keV. A new excited state at 2977 keV is proposed from the latter, although its interpretation as a branching from the state at 2976 keV identified by Astier is also possible within the statistical uncertainty in the γ-ray energy. The other two lines correspond to deexcitations from two new excited states at 2641 keV and 3253 keV.

Prominent transitions with energies of 785 keV, 952 keV and 1078 keV deexcite the well known $2_{2,3,4}^+$ states towards the 2_1^+. γ rays with energies of 1621 keV and 1680 keV are present in singles spectra with large intensities and without noticeable ^{211}Po contamination, being only a weak 1621 keV γ ray in coincidence with the 223 keV transition. The latter is identified as the one depopulating the 2976 keV state proposed in [109], thus we confirm the direct feeding of this transition, as well as the 1669-keV one, to the 6^+ instead of the 8_1^+ isomer whose deexciting gamma ray is emitted far off the target and can not be detected. Hence, the 1621-keV γ ray forms a doublet in singles spectra with the ground-state decay of the 1_1^+, whereas the strength at 1680 keV links the 2_3^+ to the ground state. The resulting branching ratio between the two transitions deexciting the 2_3^+ is 0.32(6), in agreement with the one adopted in the literature[90]. Transitions linking the second and fourth 2^+ states with the ground state could not be observed in this work, most likely because of their low intensity and the presence of strong ^{211}Po contamination in the case of the 2_2^+ state. Six new excited states are proposed at excitation energies of 1898 keV, 2175 keV, 2303 keV, 2327 keV, 2497 keV and 3000 keV from the observation of γ rays with energies of 1171 keV, 1448 keV, 1576 keV, 1600 keV, 1770 keV and 2273 keV which are exclusively coincident with the 727 keV transition. An additional 1357 keV γ ray has been identified as a decay path towards the 2_1^+ from the previously known excited state at 2085 keV whose main decay branch feeds the 4_1^+. The rather low density of states below 2.3 MeV having intense deexciting transitions towards the 2_1^+ and the large number of them that have already been experimentally fixed, supports this assignment instead of the presence of two nearly degenerate excited states (more on this in section 6.2 of the next chapter).

Three new excited states are placed at 2422 keV, 2592 keV and 3044 keV with deexciting gamma rays towards the 4_1^+ only. A 1398 keV γ ray is coincident with

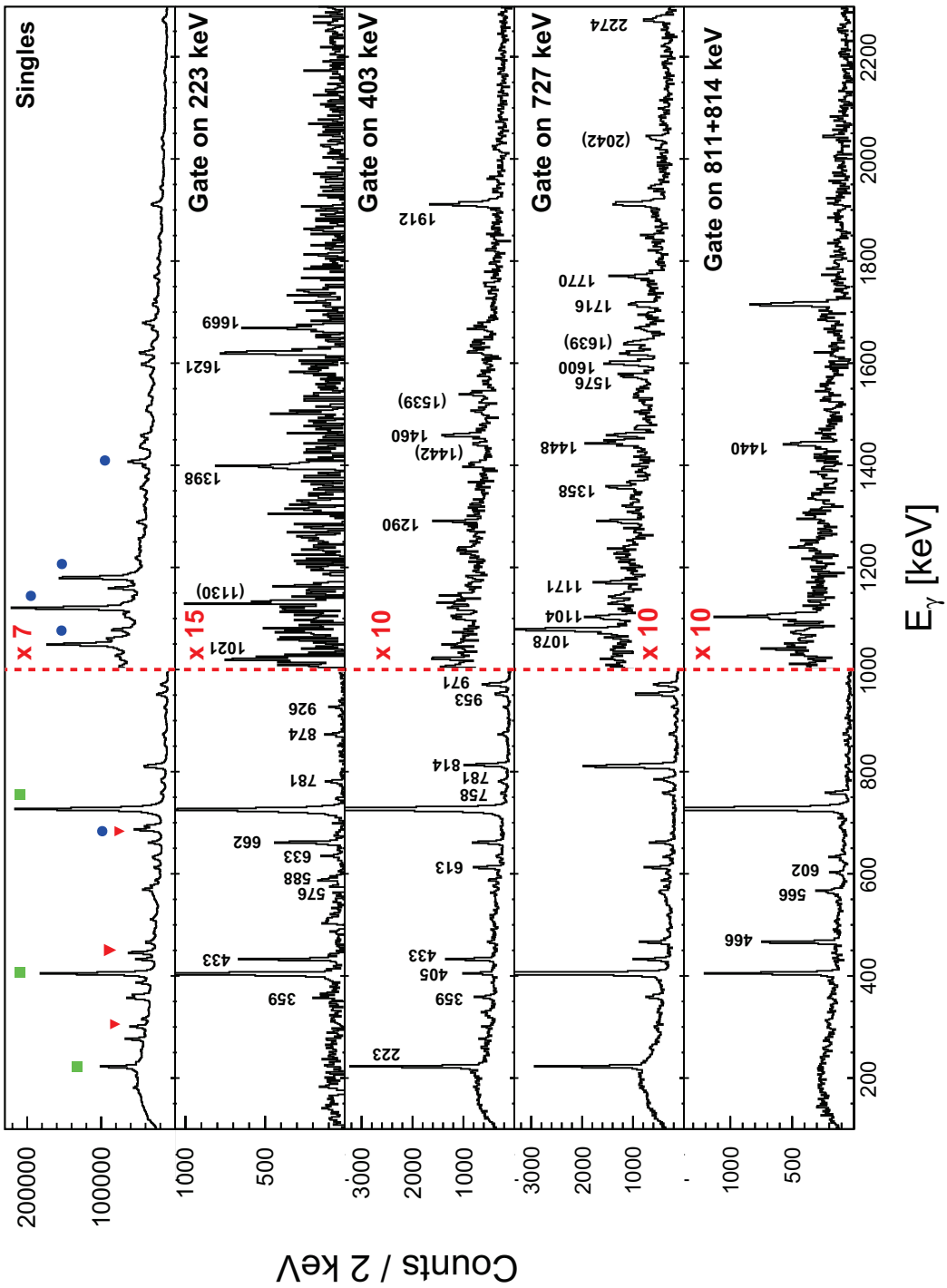

Figure 5.1: $\gamma\gamma$-coincidence spectra gated on the most prominent ^{212}Po transitions. The singles spectrum used for identifying ground-state decays and transitions feeding the isomer is represented in the uppermost panel, where the most intense transitions of ^{212}Po are indicated by green squares. Similarly, the most intense contaminant lines belonging to ^{211}Po are tagged by blue circles, whereas red triangles are referring to those of ^{214}Rn.

the 223-keV transition hence defining a new excited state at 2753 keV.

An intense 2574-keV line of ^{212}Po is only present in singles spectra, thus a new excited state is proposed at this energy. This assignment is supported by an almost identical number of counts in the 2273-keV γ ray and in the 2573-keV one. Whilst the former is detected in coincidence with the 727-keV transition, the latter is not coincident with any other line. An alternative placement, namely feeding of this line to the 8_1^+ isomer, seems unlikely given the relatively large intensity of the γ ray and the lack of observed excited states above 3.2 MeV.

The placement of the remaining transitions in the level scheme agrees with the previously published results. A discrepancy beyond error bars is present, however, in the branching fractions of the γ rays depopulating the 5^- state at 2103 keV. This mismatch most likely results from the presence of the 969-keV contaminant line reported in the previous thick target experiment[109]. The energy resolution of the present experiment does not allow for their separation so that, given the apparent similarity between the two level schemes, the intensity of the 971 keV transition should be regarded as an upper limit in this work.

5.1.2 Lines feeding the 8^+ isomer

Transitions feeding directly the $\tau = 14$ ns, 8_1^+ isomer[90] were identified with the help of feeding cascades from above as well as their intensities in singles spectra. These are the 511 keV, 277 keV and 357 keV transitions. No other transition corresponding to a direct decay to the 8_1^+ and having an intensity consistent with the adopted significance criterion has been observed.

Regarding the 358-keV γ-ray, the weak decay branches of the 2103-keV and 2376-keV excited states do not account for the full intensity of this peak in singles. Lines with energies of 868 keV, 577 keV, 633 keV, 1006 keV and 1049 keV were also found in coincidence with this peak, thus one of the strongest components of the line comes from the deexcitation of the 10^+ state towards the isomer. Inspection of singles spectra shows as well three remaining lines with energies of 277 keV and 511 keV which are not in coincidence with any other transition. These were identified as the decays from the 8^- states at 1752 keV and 1986 keV reported previously. The latter is fed by two transitions with energies of 719 keV and 853 keV, whereas no discrete feeding is observed in the former.

Intensities of transitions feeding the isomer were determined from singles spectra gated on ^{212}Po, from which contaminant peaks belonging to ^{211}Po are difficult to disentangle because of the isomeric character of some of its low-lying excited states.

There are multiple ^{211}Po lines with energies close to 511 keV, 277 keV and 357 keV feeding ^{211}Po isomers[172]. In order to take into account all possible contaminant peaks singles spectra were inspected for events with ring multiplicity equal to two under application of the cuts on total energy described in section 4.7 and under an inversion of such cuts. The amount of ^{211}Po can be estimated from a balance of peak areas between the two spectra. Let us suppose that the peak area of a certain contamined line is A_1 when a cut on total energies is applied, whereas an area A_2 is obtained when a different cut is applied. Then, under the assumption that all lines belonging to either nucleus have the same angular dependence with the polar angle of the residual nucleus in the laboratory frame, the fraction F of ^{211}Po strength in the peak relative to that of ^{212}Po in the spectrum with the first cut on particle energies is

$$F = \frac{R(^{211}\mathrm{Po})}{R(^{212}\mathrm{Po})} \times \frac{R(^{212}\mathrm{Po}) - \frac{A_1}{A_2}}{\frac{A_1}{A_2} - R(^{211}\mathrm{Po})} \tag{5.1}$$

where $R(^{211,212}\mathrm{Po})$ represents the ratio A_1/A_2 of peak areas for uncontaminated ^{211,212}Po transitions in the spectrum. The quantity $R(^{211}\mathrm{Po}) = 0.94(2)$ was obtained from the 1160 keV, 1121 keV and 694 keV lines, whereas $R(^{212}\mathrm{Po}) = 0.27(3)$ was deduced using the 811/814 keV doublet and the 433 keV, 612 keV lines. $F = 0.4(3), 0.9(5), 2.4(8)$ were deduced for the 511 keV, 277 keV and 357 keV γ rays, respectively, and the intensities of the $8^-_{1,2} \longrightarrow 8^+$ and $10^+ \longrightarrow 8^+$ transitions were corrected accordingly.

5.1.3 ^{212}Po level scheme

Figures 5.2 and 5.3 show the ^{212}Po level scheme determined in this work. The intensities of the observed transitions are given in table 5.1. The energies of the $8^-_{1,2} \longrightarrow 8^+_1$ and $10^+_1 \longrightarrow 8^+_1$ transitions were taken from [109]. The intensities given in table 5.1 are the same regardless of the presence of an excited ^{8}Be in the exit channel as explained in section 4.8. They are identical within statistical uncertainties for the short measurement around the barrier and well above the barrier (see section 4.7). The intensities and their uncertainties were determined as described in section 4.1.8.

E_i [keV]	E_f [keV]	E_γ [KeV]	I_γ	J^π_i	J^π_f
1355	1132	222.7(1)	15.3(7)	6^+	4^+
1751	1475	276.1*	6(2)	8^-	8^+
1832	1475	357.1*	7(3)	10^+	8^+
2103	1745	358.8(5)	0.4(2)	$5^{(-)}$	4^-
2376	2017	359.2(4)	0.5(2)	$7^{(-)}$	6^-
2781	2410	371.0(3)	0.7(3)	10	11^-

Continued on next page

Continued from previous page

E_i [keV]	E_f [keV]	E_γ [KeV]	I_γ	J_i^π	J_f^π
1132	727	405.0(1)	60(3)	4^+	2^+
1537	1132	405.1(2)	1.2(4)	$3^{(-)}$	4^+
1788	1355	432.7(1)	4.2(4)	6^-	6^+
2003	1537	466.3(1)	2.7(3)	$4^{(-)}$	3^-
1986	1475	510.9*	1.4(4)	8^-	8^+
2667	2103	564.2(5)	0.4(2)	$5^{(+)}$	5^-
2103	1537	565.7(4)	0.8(4)	$5^{(-)}$	3^-
2364	1788	575.5(2)	0.9(2)	6	6^-
2410	1832	577.5(2)	2.0(2)	11^-	10^+
2376	1788	588.2(2)	1.8(3)	$7^{(-)}$	6^-
2605	2003	601.6(4)	0.6(2)	5	$4^{(-)}$
1745	1132	612.7(2)	2.3(2)	4^-	4^+
2170	1537	632.5(6)	0.4(2)		3^-
2466	1832	633.4(3)	1.2(2)	10^-	10^+
2422	1788	634.4(4)	0.6(2)		6^-
2017	1355	661.8(2)	2.9(2)	6^-	6^+
2471	1751	719.2(4)	1.9(3)	$9^{(-)}$	8^-
727	0	727.2(1)	100(4)	2^+	0^+
2860	2103	756.9(4)	0.5(2)	$5^{(+)}$	5^-
2295	1537	758.4(4)	0.5(3)		3^-
3158	2376	780.9(2)	1.0(1)	$7^{(+)}$	7^-
1513	727	785.7(3)	2.2(3)	2^+	2^+
1537	727	809.6(1)	10.5(7)	$3^{(-)}$	2^+
1946	1132	813.7(1)	4.5(2)	4^-	4^+
2605	1751	853.2(2)	0.4(1)	8	8^-
2701	1832	868.4(4)	0.7(2)	12^+	10^+
2229	1355	873.5(3)	1.1(2)		6^+
2281	1355	926.0(2)	0.6(3)		6^+
1680	727	952.3(3)	3.8(3)	2^+	2^+
2085	1132	952.7(2)	1.8(2)	$(4^+)(\dagger)$	4^+
2103	1132	971.4(3)	4.2(3)	$5^{(-)}$	4^+
2838	1832	1005.8(4)	0.4(2)		10^+
2376	1355	1021.2(4)	0.3(1)	$7^{(-)}$	6^+
2882	1832	1049.4(4)	0.3(1)		10^+
1805	727	1078.4(2)	1.6(2)	2^+	2^+
2641	1537	1104.1(4)	0.4(2)		$3^{(-)}$
1898	727	1171.2(6)	0.6(3)	$(3^+)(\dagger)$	2^+
2422	1132	1290.1(4)	0.7(2)		4^+
2085	727	1357.6(5)	0.4(2)	$(4^+)(\dagger)$	2^+
2753	1355	1398.1(6)	0.9(4)		6^+
2977	1537	1440.3(5)	0.3(1)		$3^{(-)}$

Continued on next page

Continued from previous page					
E_i [keV]	E_f [keV]	E_γ [KeV]	I_γ	J_i^π	J_f^π
2175	727	1448.2(7)	1.1(4)		2^+
2592	1132	1459.5(5)	0.6(2)		4^+
2303	727	1575.7(7)	0.7(3)		2^+
2328	727	1600.3(4)	1.2(3)		2^+
1621	0	1620.6(2)	1.6(3)	1^+	0^+
2976	1355	1621.0(7)	0.6(3)		6^+
3024	1355	1669.2(8)	0.4(2)		6^+
1680	0	1679.7(1)	1.2(2)	2^+	0^+
3253	1537	1715.8(5)	0.5(1)		$3^{(-)}$
2498	727	1770.3(4)	1.0(2)		2^+
3045	1132	1912.3(4)	1.6(2)		4^+
3000	727	2272.6(7)	0.9(2)		2^+
2574	0	2574.0(2)	1.0(2)	$(2^+)(\dagger)$	0^+

Table 5.1: List of ^{212}Po γ-ray energies (E_γ) and their intensities (I_γ) as observed in this experiment. Tentative spin and parity assignments performed in this work are indicated by a (†) symbol and justified in chapter 6. The remaining spin and parity values have been adopted from [109]. Transition energies marked with an asterisk were taken from [109].

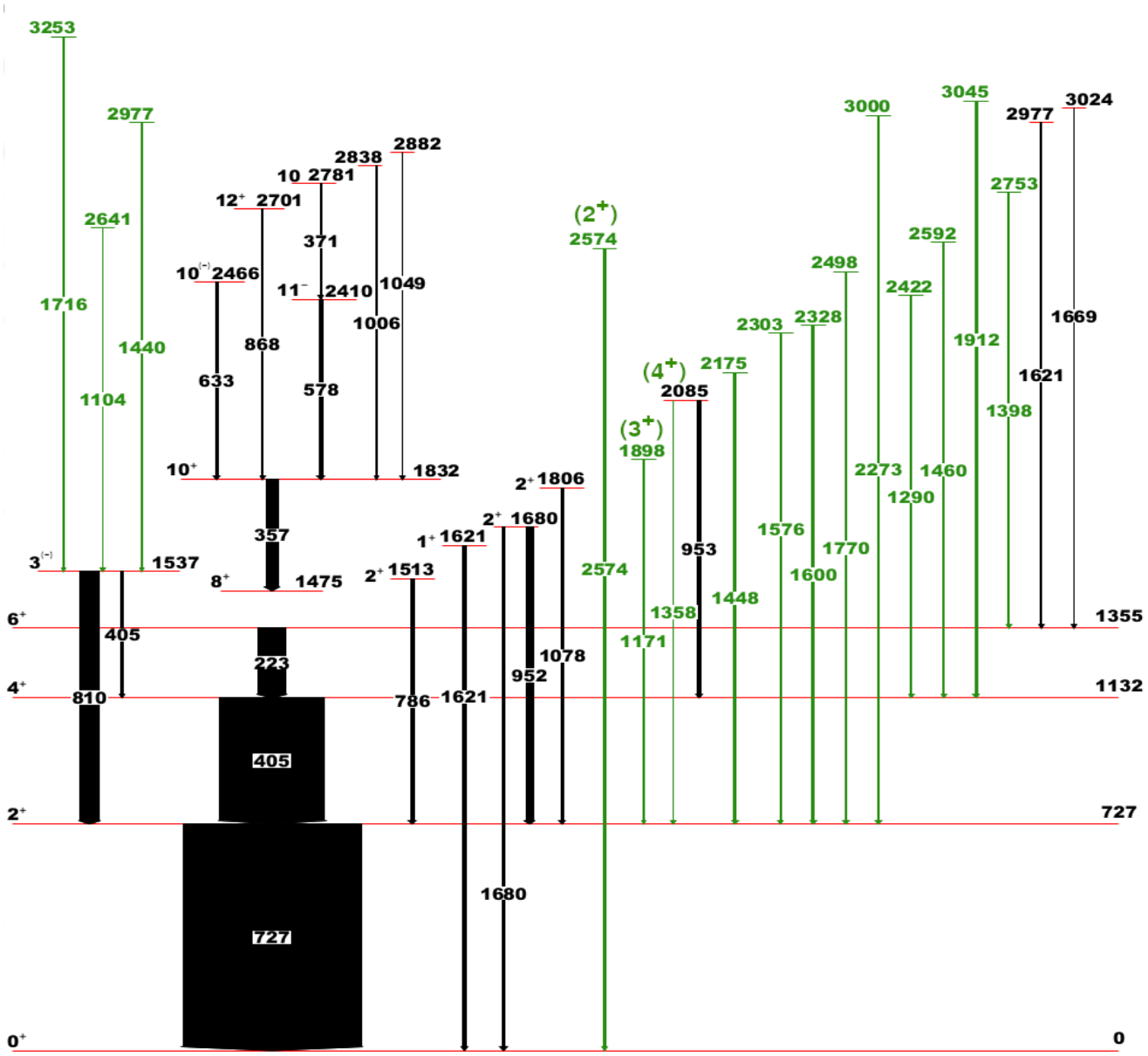

Figure 5.2: First part of the ^{212}Po level scheme determined in this work. The width of the arrows indicating the deexciting transitions is proportional to their intensity. New transitions and excited states are represented in green.

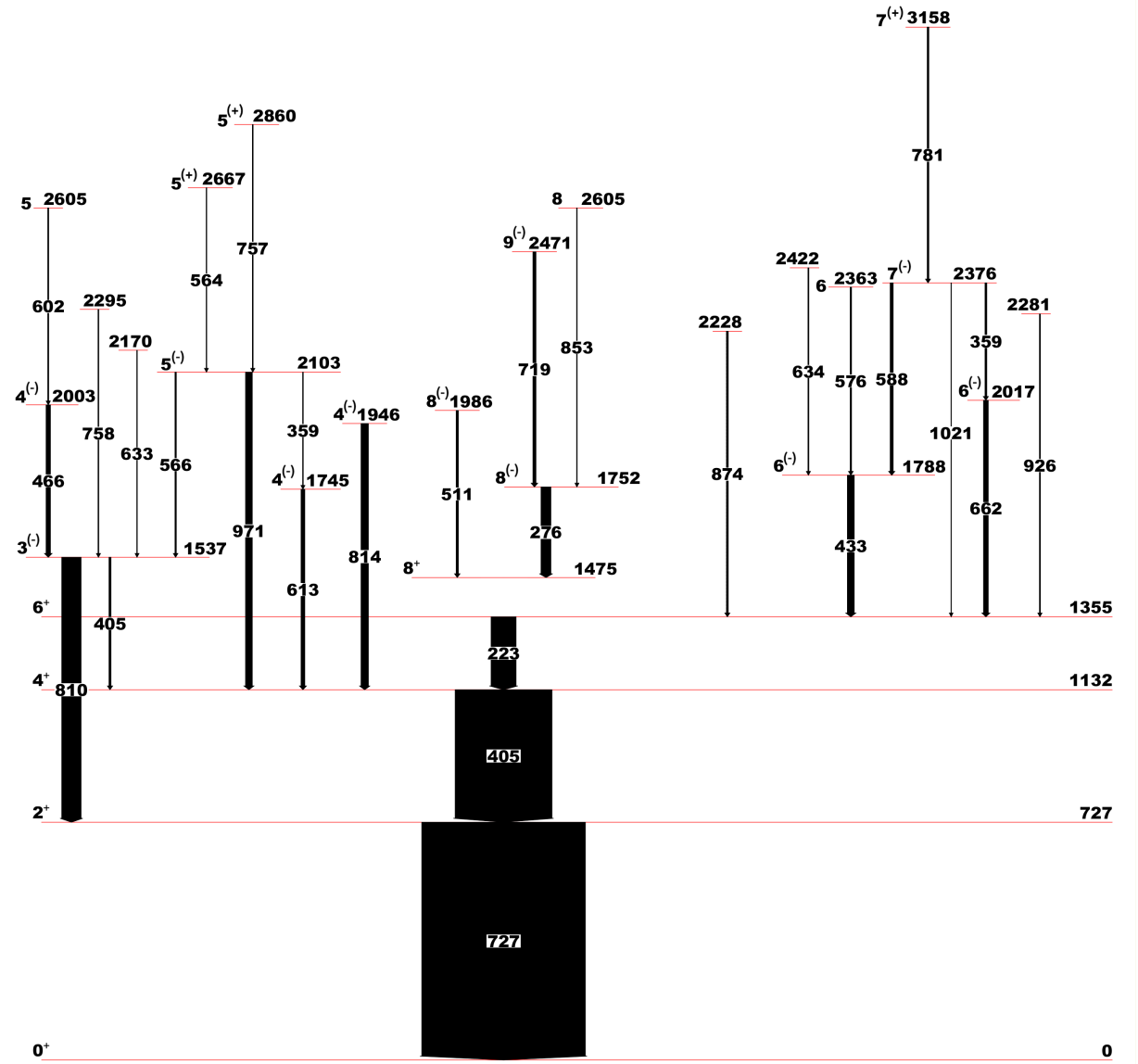

Figure 5.3: Second part of the ^{212}Po level scheme determined in this work. The width of the arrows is proportional to the intensity of the transition. All excited states and transitions represented in the figure have already been established in previous experiments.

5.1.4 Compton polarimetry analysis

A large degree of oblate alignment reaching 70% was reported in the previous work of Astier using a similar α-transfer reaction[109]. The limited solid angle coverage of AGATA combined with the systematic uncertainties in the efficiency hinders a meaningful analysis of the angular distributions in the present experiment. Nonetheless, the sensitivity of the experimental setup for Compton polarimetry studies is large in

general as shown in figure 5.4, where calculated γ-ray intensities are represented as a function of the Compton scattering angle ϕ with respect to the polarization plane (see section 1.3 for definitions and details on the technique). The values given in the figure were obtained by integration in the solid angle subtended by $\theta_\gamma = 120°$ and $\theta_\gamma = 140°$, and Compton scattering angles θ_c between 50° and 130°. The polar angles are chosen as close as possible to 90° in order to maximize the anisotropies for the transitions of interest and integrating in the solid angle window allows to accumulate a reasonable level of statistics in the experimental spectra. These calculated values are close to the expectation for transitions actually present in the data so that we shall use them for interpreting the experimental results. For instance, the 1051-keV, 1122-keV and 1181-keV γ rays in ^{211}Po correspond to the transitions $\frac{5}{2}^+ \rightarrow \frac{9}{2}^+$ (E2), $\frac{7}{2}^+ \rightarrow \frac{9}{2}^+$ (M1+E2, $\delta = +0.15(5)$) and $\frac{13}{2}^+ \rightarrow \frac{9}{2}^+$ (E2) with different degrees of anisotropy and a distinctive preference for Compton scattering around $\phi = 0°, 180°$ in the case of the 1122-keV γ-ray.

The M1 character of the 1621-keV transition in ^{212}Po depopulating the 1_1^+ state would be reflected in a much larger intensity around $\phi = 90°$ as well, in contrast with the case of the transitions between the first low-lying yrast states in ^{212}Po for which an a_2 coefficient of $\approx +0.2$ was reported. Beyond the precise value of the asymmetry when comparing spectra at different angles ϕ (which eventually depends on the feeding dimming the a_2 coefficient), it is possible to deduce the parity of the radiation, i.e. the phase $(\pm)_{L=2}$ in eq. (1.40), from a comparison with other known transitions and independently of the attenuation, namely taking into account the known sign of the a_2 coefficient only.

The second interaction point of the γ ray was reconstructed using the tracking algorithm in order to calculate the Compton scattering angle θ_c and the angle ϕ. Singles γ-ray spectra were then sorted for this study with the following selections:

- Polar angle of the γ-ray between 120° and 140°, polar angle θ_c ranging from 50° to 130°. These conditions were already used for generating the plots of figure 5.4 in the ideal case of a detector with infinite position resolution. The spectra corresponding to two intervals of ±20° centered around $\phi_c = 0°, 180°$ and $\phi = 90°, 270°$ were compared for extracting the phase $(\pm)_{L=2}$ and corrected for the instrumental asymmetry observed with the ^{152}Eu source. As a check, the same spectra centered around $\phi = 45°, 225°$ and $\phi = 135°, 315°$ were compared since in this case no anisotropy should be observed.

- Polar angle θ_c ranging from 50° to 130° without any restriction on the the polar angle of the γ-ray and in the same intervals in ϕ. The γ-ray spectra for different

intervals of ϕ were overlaid by means of an arbitrary scaling factor. Therefore, these spectra can not be used for a quantitative analysis and here they are shown on a twofold purpose: to show that the anisotropies persist in the same direction by comparing the relative intensities of the transitions using a case with more statistics and that, as expected, the magnitude of such anisotropies is reduced when the range of polar angles is opened.

The contrasting behavior of the anisotropies for the 1680-keV and 1621-keV γ rays is visible in the experimental spectra shown in figure 5.5. For the 1680-keV γ ray, the yield is larger for Compton scattering perpendicular to the polarization plane, whereas the opposite behavior is observed indeed for the M1, 1621-keV γ ray from the 1_1^+ to the ground state.

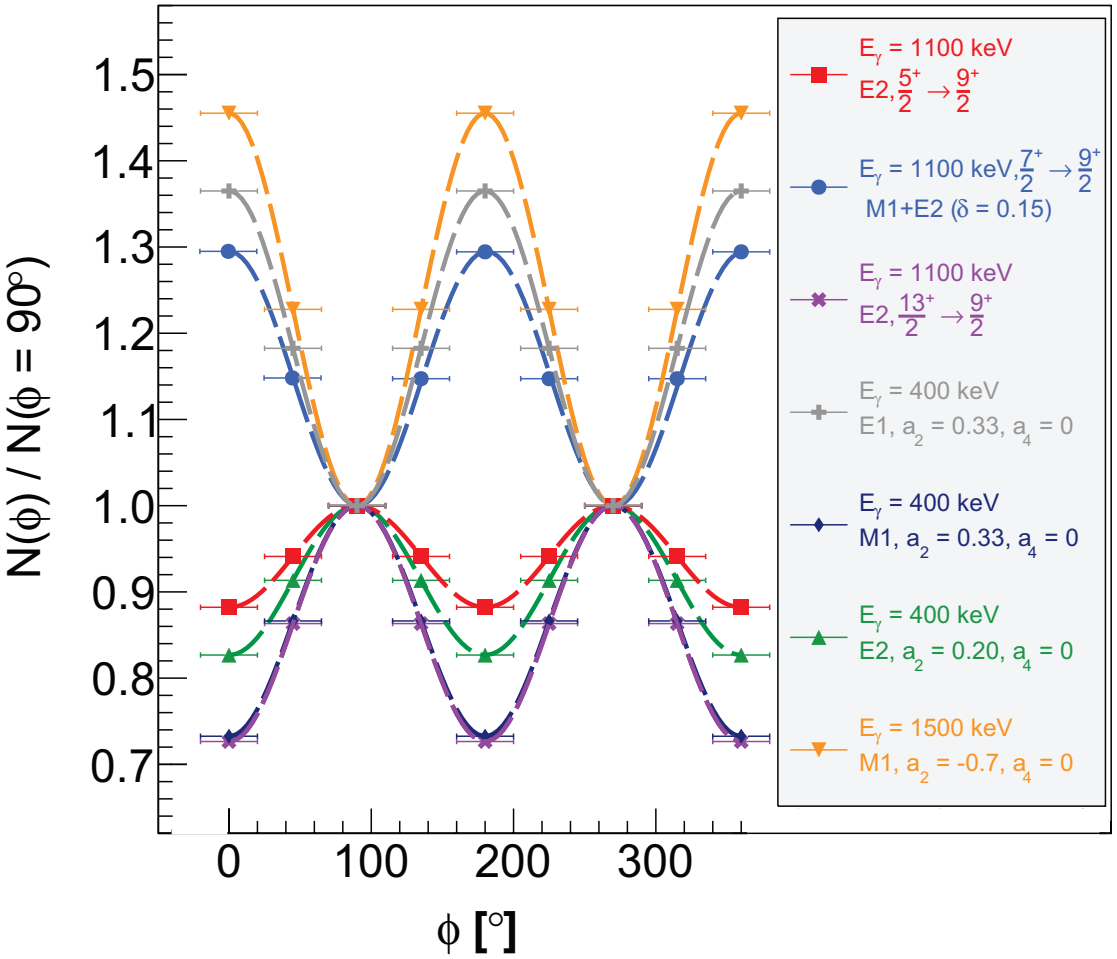

Figure 5.4: Calculated intensities as a function of the angle ϕ. The horizontal bars represent the integration window in ϕ and the dashed lines are depicted for easier visualization. Full alignment is assumed unless the a_2 coefficient is explicitly given in the legend. More details in the text.

The results for the ^{211}Po transitions are shown in figure 5.6. Since they have more statistics, the anisotropies are much more clearly evidenced beyond statistical uncertainties. A 10(3)% higher yield is obtained for $\phi \approx 0°$ than for $\phi \approx 90°$ for the 1122-keV γ ray. On the other hand, no clear anisotropy is present for the 1051-keV γ ray, in agreement with its E2 character linking the $\frac{5}{2}^+$ and $\frac{9}{2}^+$ levels.

Finally, figure 5.7 shows the same spectra in the energy range between 330 keV and 490 keV. The rather slight anisotropy in the 405 keV transition is attributed to the attenuation of the alignment. It can be nevertheless concluded that the phase is positive, in agreement with its E2 character. The 433-keV transition is the most interesting case since it shows the opposite behavior than expected for an unstretched E1 transition: the obtained anisotropy with the same selections of figure 5.4 is $N(\phi = 0°)/N(\phi = 90°) = 0.8(2)$ and indicates the predominance of Compton scattering perpendicular to the polarization plane, thus assuming the possitive a_2 coefficient reported in [109] this is an M1 γ ray. This conclusion contradicts the interpretation of this transition as an E1 proposed in refs. [113, 109]. The significance of this result, which implies a $J^\pi = 6^+$ assignment to the 1788-keV state, is discussed in the next chapter.

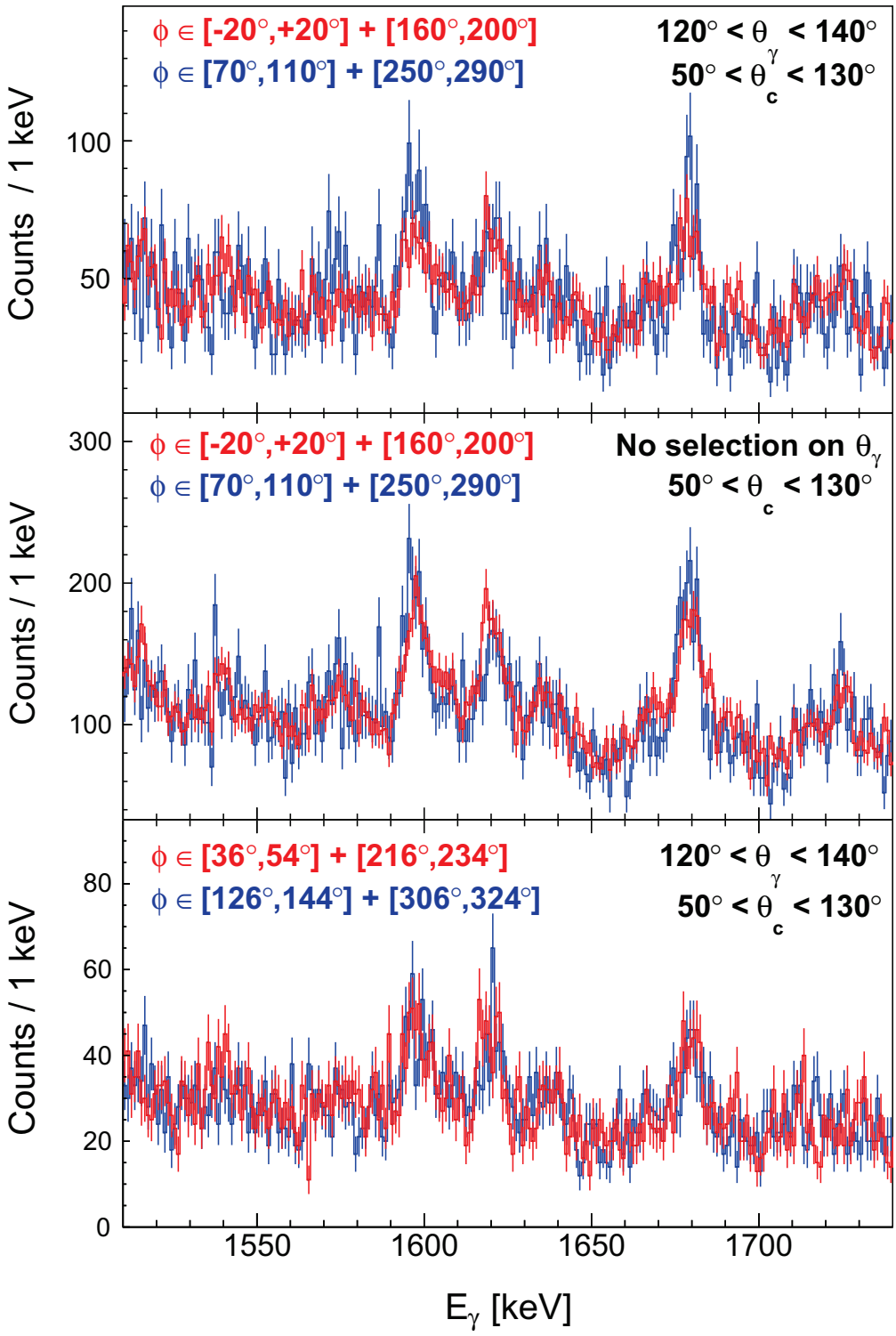

Figure 5.5: Comparison of γ-ray spectra between 1510 keV and 1740 keV obtained under different selections on the polar angle of the γ-ray, θ_γ, and the azimuthal angle ϕ of the Compton-scattered γ ray.

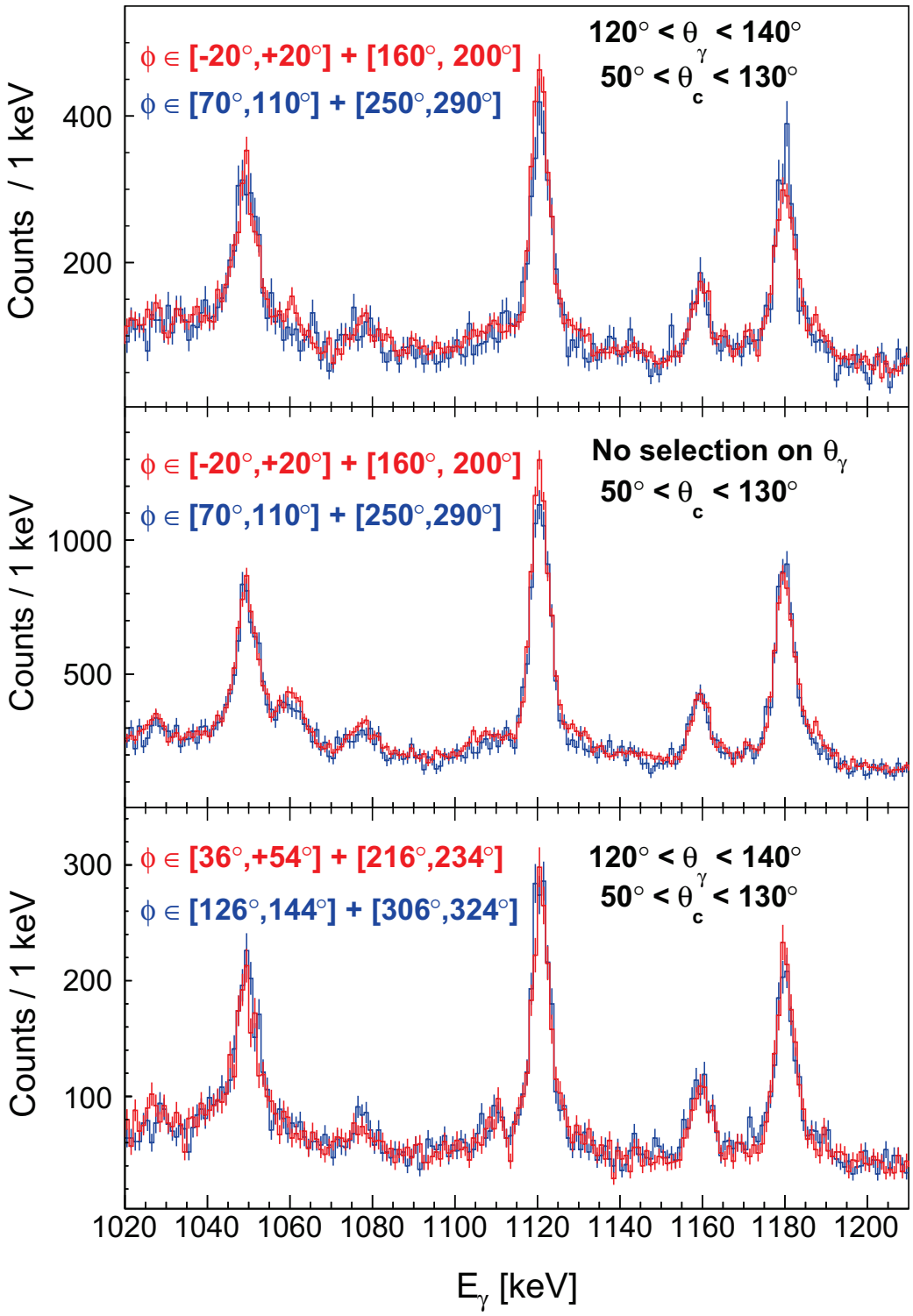

Figure 5.6: Comparison of γ-ray spectra between 1020 keV and 1210 keV obtained under different selections on the polar angle of the γ-ray, θ_γ, and the azimuthal angle ϕ of the Compton-scattered γ ray.

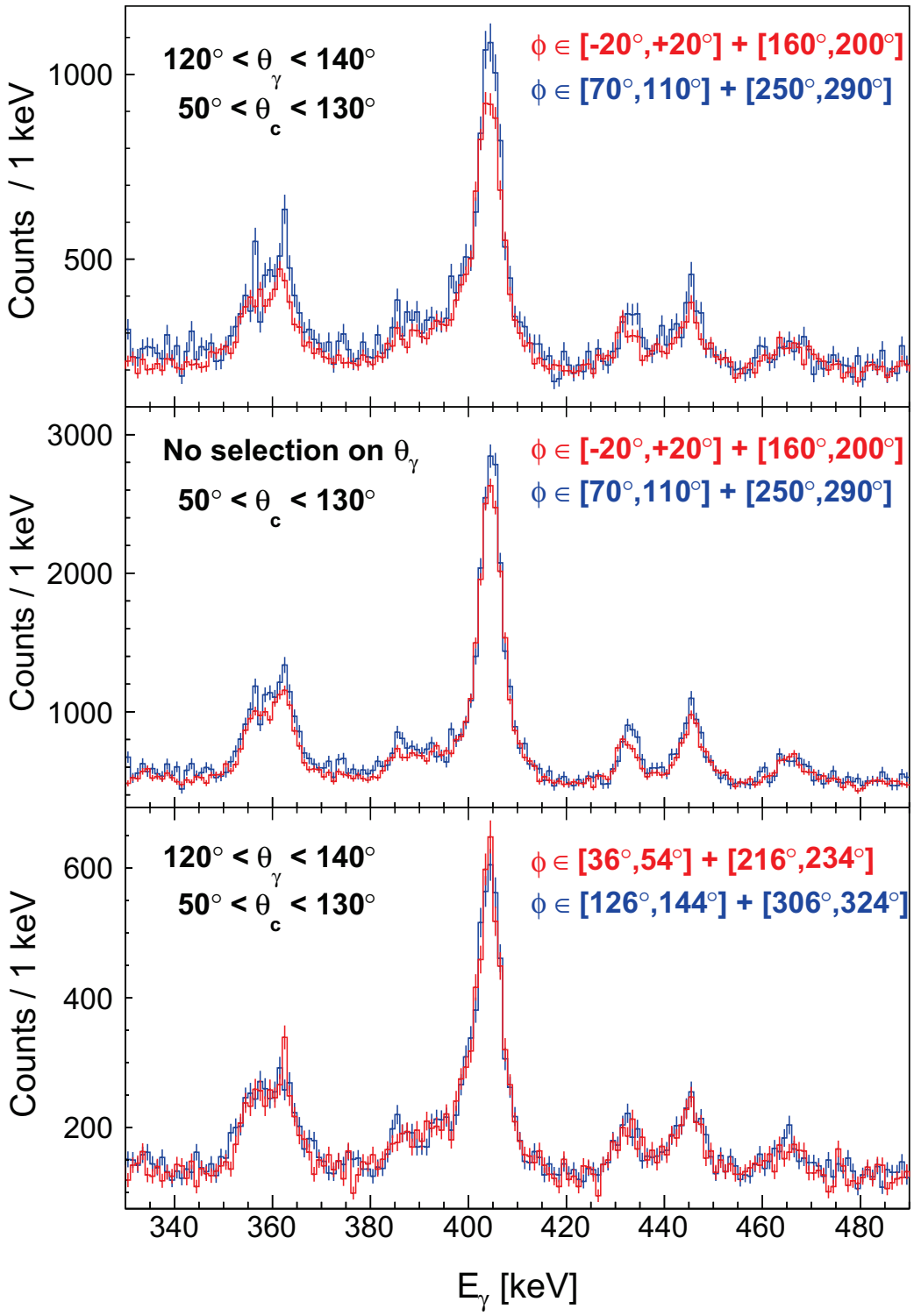

Figure 5.7: Comparison of γ-ray spectra between 330 keV and 490 keV obtained under different selections on the polar angle of the γ-ray, θ_γ, and the azimuthal angle ϕ of the Compton-scattered γ ray.

5.2 Results from DSAM target data

The accumulated statistics in the DSAM data sets is not sufficient to use the cleaner $\gamma\gamma$ coincidence spectra for DSAM analysis. Therefore, the present discussion is restricted to singles γ-ray spectra. The upper limits reported in this section were extracted by means of simulations using the code APCAD[60]. A realistic parametrization of the intrinsic resolution of the array as a function of the energy was used in the simulations. It was obtained from the calibration data taken with the ^{152}Eu source. The broadening of the peaks at the different angular slices that stems from the energy resolution of the beam and the position resolution in the first interaction point was taken into account by smearing both the energy of the incoming ^{208}Pb beam in the simulation and the position used for Doppler-correcting the simulated lineshape. Both variables were assumed to be normally distributed and choosing 6 mm (FWHM) for the uncertainty in the cartesian coordinates of the first interaction point and $\sigma = 3.5\%$ for the beam energy distribution, the FWHM of the Doppler-corrected peaks in the self-supporting diamond target data was well reproduced in the energy range of interest and in the entire angular range covered by AGATA. The effect of the DSSSD finite position resolution was taken into account as well yielding an uncertainty of 0.25% in the reconstructed β, which does not substantially contribute to enlarging the widths of the Doppler-corrected peaks. Pre-calculated stopping power tables from SRIM[66] were used in the simulations.

Two approaches were used to search for short-lived excited states. In the first one, only the first 4 hours of data taking are considered in order to minimize the impact of the target issues explained in section 4.9.4. Short-lived states were identified in this case by comparison with singles γ-ray spectra taken with the self-supporting target. Figure 5.8 shows this comparison in the energy range between 1200 keV and 2100 keV. Doppler correction in the DSAM data has been applied assuming deexcitations behind the backing. The ^{212}Po γ ray with an energy of 1290 keV, the ^{211}Po 1408-keV one and the γ-ray strength at 1430 keV are visible with similar relative intensities as in the unbacked target. On the other hand, the intensity of the ^{212}Po 1460 keV and 1621 keV γ rays dwindles with this Doppler correction even though their peak areas must be larger than the areas of neighboring peaks. An upper limit of 0.7 ps was established for the lifetime of the latter state on the basis that for a 0.7 ps transition, the height of the Doppler-corrected peak from γ ray emissions behind the target is dwindled only by 25% in comparison with the peaks from much longer-lived states with lifetimes in the range of tens of picoseconds. Since the γ strength at 1621-keV comes from two transitions, the one depopulating the 1_1^+ state towards the ground state and the γ ray

depopulating the level at 3024 keV for which an upper limit of 1.4 ps was proposed in [109], no upper limit is proposed for the corresponding lifetimes.

From this reduced data set, systematic uncertainties in the absolute scaling of the electronic stopping power and target thickness were explored. The centroid of the 727 keV line was found to be 726.8(2) keV, a value that is slightly beyond the reported interval from the unbacked target data sets. The mismatch could be originated by a wrong assumption of the target thickness, wrong scaling factors for the stopping powers or a combination of both. Scaling the electronic stopping power by $+5\%(-5\%)$ places the centroid of the Doppler-corrected peak at 725.6(2) keV (727.9(2) keV). Identical values for the position of the centroid are obtained by assuming a 5% thicker/thinner Au backing, that is, the maxima of the $\beta(^{212}\mathrm{Po}) - \theta(^{8}\mathrm{Be})$ distributions are virtually identical in the range of polar angles covered by the DSSSD if one considers the nominal thickness of the Au backing and a stopping power 5% lower or a 5% thicker Au backing and the unscaled stopping power. In any case, for a 0.7 ps transition around 1500 keV, the amplitude of the unshifted part is the same under such scalings and only the centroid position is shifted, hence it does not influence the proposed upper limit for the lifetime of the excited state at 2592 keV which is depopulated by the 1460-keV transition to the 6_1^+.

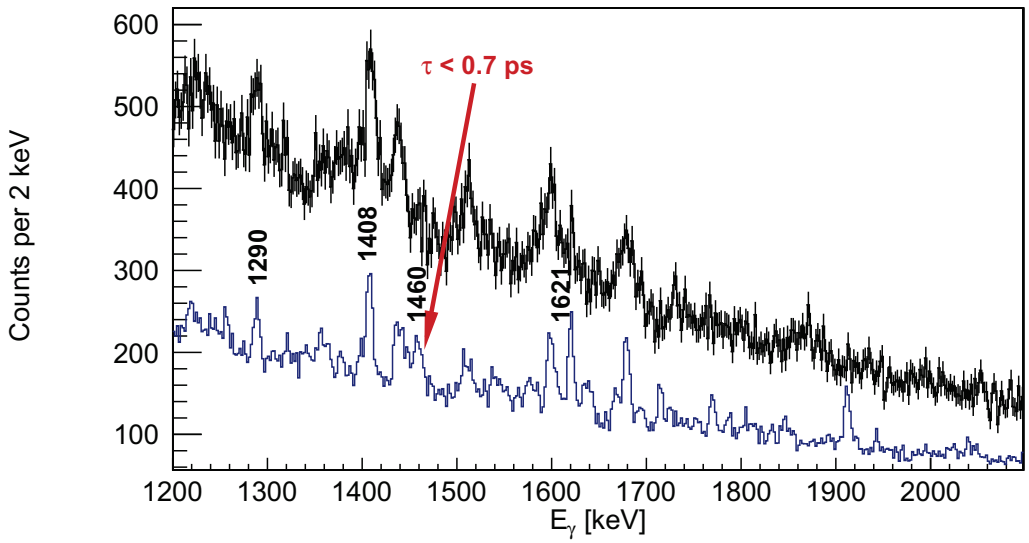

Figure 5.8: Comparison between singles γ ray spectra from the data taken with the composite target (in black) and the self-supporting diamond target (in blue). The latter has been arbitrarily scaled for the sake of comparison. An upper limit of 0.7 ps is established for the lifetime of the 1460 keV and the 1621 keV transitions based on this comparison. Details in the text.

In the second approach used for identifying short lived states, the full collected statistics with the DSAM target was used and Doppler correction was applied as

if the γ rays were emitted just behind the reaction layer, which eases the analysis of those transitions from short-lived states that have small intensities. Figure 5.9 demonstrates that the lifetimes of the 1912, 2273 and the 2574 keV transitions are accessible by DSAM. Upper limits of 0.3 ps, 0.3 ps and 0.4 ps for the lifetime of the states at 3045, 3000 and 2574 keV were established by comparison of summed singles spectra corresponding to a range of γ-ray polar angles between 130° and 160°.

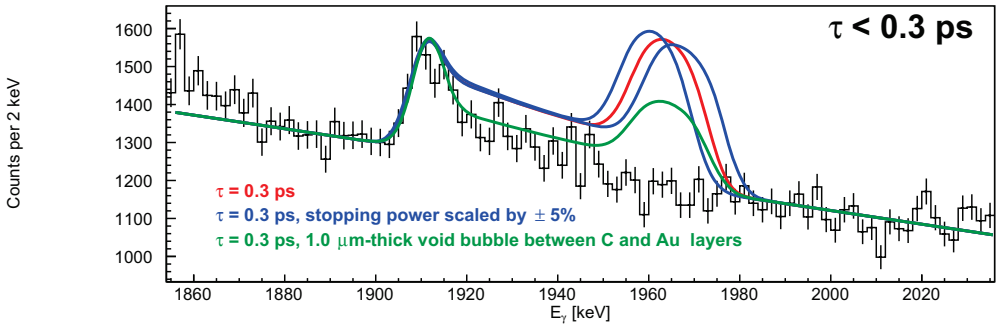

(a) 1912 keV transition towards the 4_1^+.

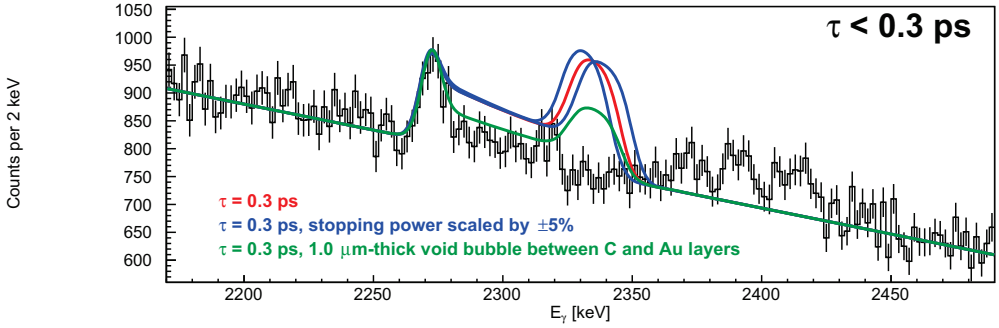

(b) 2273 keV transition towards the 2_1^+.

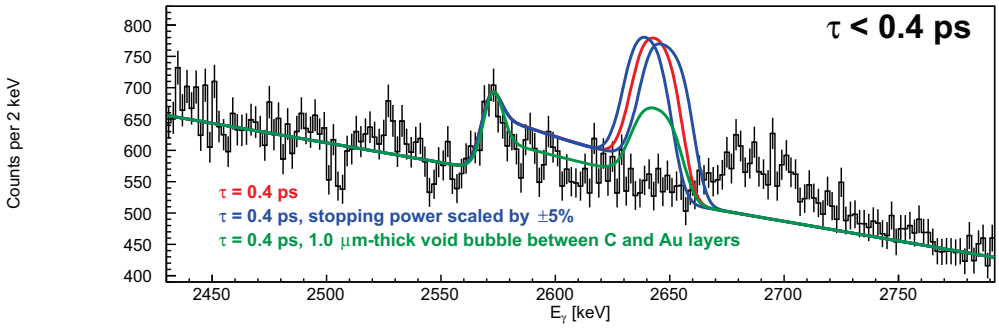

(c) 2574 keV transition towards the ground state.

Figure 5.9: Summed singles γ-ray spectra with γ-ray polar angles between 130° and 160° from the data taken with composite target. Doppler correction has been performed assuming deexcitations just behind the reaction layer. The upper limit of the transition lifetime was extracted by comparison with APCAD simulations, represented by the solid lines. Details in the text.

Formation of a gap between the reaction layer and the stopping layer was reported in a previous DSAM measurement in inverse kinematics [125], whose extension reached 50% of the thickness of the graphite foil. The lineshape of the $(7^+) \longrightarrow 7^-$ (781 keV) transition, whose lifetime τ is 0.12(6) ps[109], was inspected in singles spectra and the uncontamined fraction of its lineshape was found to be best described using $\tau = 0.06$ ps.

A 1-µm gap between the reaction layer and the stopper would result in a value close to 0.2 ps for the lifetime, a value which is beyond the interval reported in [109] for the lifetime of this transition. The presence of such a gap would be a strong systematic uncertainty and has been considered when extracting the upper limits as illustrated in figure 5.9.

The extracted upper limits for the lifetimes are summarized in table 5.2.

E_x [keV]	2592	3045	3000	2574
E_γ [keV]	1462	1912	2273	2574
τ^γ_{max} [ps]	0.7	0.3	0.3	0.4

Table 5.2: Upper limits for transition lifetimes extracted from the DSAM data sets.

Chapter 6

Discussion of the results

This last chapter focuses on the interpretation of the reported results. The predictions of the most recent models proposed for describing the so-called α-cluster doublets are examined in section 6.1 in the light of the obtained level scheme. We shall ignore in this first section the $J^\pi = 6^+$ assignment to one of those states on the basis of the Compton polarimetry study reported in section 5.1.4 as these models are supposed to describe octupole collectivity in ^{212}Po in general. Then, the tentative spin and parity assignments proposed for three of the excited states observed in this work are justified in section 6.2. Finally, the α-cluster nature of the even spin doublets is questioned in section 6.3 on the basis of the $J^\pi = 6^+$ assignment to the state at 1788 keV. An alternative interpretation of the doublets is also given in that section.

The shell model calculations presented in this chapter were performed using the Kuo-Herling interaction as modified by Warburton and Brown[22, 24], with the same scaling factors for the core polarization term of the proton-proton, neutron-neutron and proton-neutron interactions. The hamiltonian was diagonalized in a valence space composed of the $0h_{9/2}$, $1f_{7/2}$, $0i_{13/2}$, $1f_{5/2}$, $2p_{3/2}$, $2p_{1/2}$ proton shells and the $1g_{9/2}$, $0i_{11/2}$, $0j_{15/2}$, $2d_{5/2}$, $3s_{1/2}$, $1g_{7/2}$, $2d_{3/2}$ neutron shells. Effective charges of $e_\pi = 1.5e$, $e_\nu = 0.5e$ and bare g factors for neutrons and protons were systematically used in all the reported calculations.

6.1 Search for collective $(1,2)^-$ states

The unnatural parity doublets were interpreted in [109, 113] et al. as a unique fingerprint of α-^{208}Pb vibrational states on the basis of their reported lifetimes. Only two theoretical models trying to explain the structure and the supposedly enhanced collectivity of the states (based on their proposed negative parity) are published, and in both of them the simple picture of an α particle moving around an inert ^{208}Pb

core, initially proposed by Astier[109], was disregarded since only natural-parity states would emerge from such a model. Collective states with negative parity emerge in both cases by the couplings of valence particles or clusters to an excited ^{208}Pb core in its 3^- state, the well-known octupole phonon state. The models aimed at a simultaneous description of both the natural and unnatural negative-parity states by such couplings.

The collective states were described by Suzukiand Ohkubo[114] considering the coupling of a pure α cluster to the excited core. The hamiltonian contains a kinetic-energy term from the relative motion of the α around the core, the intrinsic hamiltonian of the excited core and an interaction potential expanded up to $\lambda = 3$ octupole terms. The $\alpha+$ ^{208}Pb(3^-) states are obtained by a coupled-channels calculation. The calculation is able to reproduce the almost degenerate energies of the unnatural-parity band, and many new states are predicted. In particular, one of the key experimental fingerprints of the model is the existence of an additional doublet of 2^- states at a similar excitation energy than the other negative-parity doublets with even spin, decaying by E1 transitions to the 2^+_1 state. Moreover, two 1^- states are predicted to lie near the excitation energy of the doublets which would not have been observed yet.

On the other hand, Delion et al.[115] suggested that seniority-excited neutron pairs coupled to total angular momentum I^- to the excited core can generate odd-spin doublets at the same excitation energy than observed in the experiment. Additionally, the saturation of the excitation energy at higher spins is fairly well reproduced for the natural-parity states. The model wave functions used in the calculations are quoted below for more clarity,

$$|^{212}\mathrm{Po}(J^+)\rangle = |^{210}\mathrm{Pb}(J^+)\rangle \; |^{210}\mathrm{Po}(\mathrm{G.S})\rangle \tag{6.1}$$

$$|^{212}\mathrm{Po}(I^-)\rangle = \left\{|^{210}\mathrm{Pb}(J^+)\rangle \; |^{208}\mathrm{Pb}(3^-)\rangle\right\}_{I^-} \; |^{210}\mathrm{Po}(\mathrm{G.S})\rangle \tag{6.2}$$

where ^{210}Pb(J^+) represents the states belonging to the ^{210}Pb ground state band up to $J^\pi = 8^+$. The right order of magnitude in the calculated E1 transition probabilities was achieved by adding a cluster component to the shell-model wave function, as it was done in the past for the calculation of the α-decay width from the ^{212}Po ground state. Likewise, a 2^- doublet is predicted whose members would lie around 1.2 MeV and 1.9 MeV, with a clear positioning at lower energies than the other calculated multiplets with even spin and negative parity. A 1^- level is also predicted near 2 MeV. The excited states calculated in refs. [114] and [115] are shown in figure 6.1.

Two new excited states feeding the 2^+_1 have been observed in this experiment at a similar excitation energy than the even-spin doublets with negative parity. They are the 1898-keV and the 2175-keV states. There are other excited states at higher excitation energy feeding the 2^+_1 observed for the first time in this experiment, such as

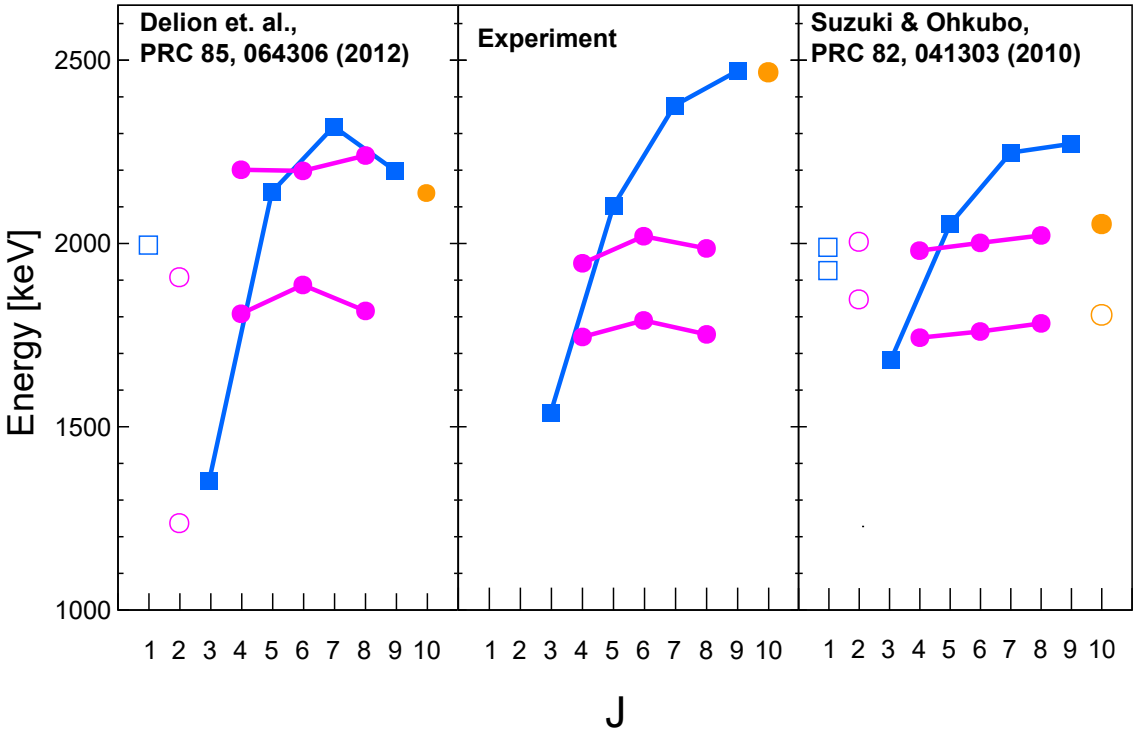

Figure 6.1: Comparison with experiment of the predicted negative-parity states arising from couplings with the octupole vibration in ^{208}Pb, according to refs. [115, 114]. Filled symbols refer to states identified in the experiment. Empty symbols represent predicted states that have not been observed in the experiment. Only a limited number of states among those calculated in [114] are shown in the plot.

the 2303-keV one. Nevertheless, their importance in the present discussion is limited since they are closer in energy to the (10^-) state at 2465 keV, whose position at higher energy than the other negative parity states is suggested by the dominance of the configuration $\nu g_{9/2} i_{11/2}$ in the $J^\pi = 10^+$ yrast state according to the description of ref. [115]. All the other negative-parity, low-spin states would arise from the $(\nu g_{9/2})^2$ excitations that are responsible for the ground-state band in ^{212}Po up to $J^\pi = 8^+$ state so that they lie at a similar excitation energy. Indeed, the attempts to describe a 10^- doublet with the same structure as the other doublets seemingly results in a significant underestimation of its excitation energy. The $(1,2)^-$ states would simply emerge, according to [114] and [115], from the same couplings that generate the $3^- - 8^-$ states. Therefore, fragmentation of the 2^- states can be ruled out according to these models since only two 2^- are expected to stem from the $^{208}\mathrm{Pb}(3^-) \otimes {}^{212}\mathrm{Po}(2^+)$ and $^{208}\mathrm{Pb}(3^-) \otimes {}^{212}\mathrm{Po}(4^+)$ configurations where, according to the choice of [115], the $^{208}\mathrm{Pb}(3^-) \otimes {}^{212}\mathrm{Po}(2^+)$ is the one giving rise to the 3^- and $^{208}\mathrm{Pb}(3^-) \otimes {}^{212}\mathrm{Po}(4^+)$ gives rise to one of the 4^-. Moreover, all the three possible 4^- states arising from such

couplings have been populated in the experiment, the third one being the 2003-keV state.

The following conclusions can be drawn from the comparison of the experimental results with both calculations:

1. There is *at most* a single 2^- state observed in the experiment. Only the 1898-keV level is a feasible candidate according to the models. The 2175-keV state is disqualified as a feasible candidate because of its placement at higher excitation energies than the other doublets, a shift which is not predicted in any of the calculations. Quite the contrary, a shift towards smaller energies is expected, if any[115].

2. It is possible that the 1898-keV and 2175-keV states are 1^- states. Moreover, three other 3^- states resulting from the remaining couplings $(3^- \otimes 0^+)_{3^-}$, $(3^- \otimes 4^+)_{3^-}$ and $(3^- \otimes 6^+)_{3^-}$ could be as well candidates for the 1898-keV and the 2175-keV states. Unfortunately, their energies are not given in [115].

3. Therefore, there are large diferences in the population pattern between the available two candidates and the other states comprising identical collective excitations involving the 3^- and low ($J \leqslant 4$) angular momentum which were strongly and directly populated. Indeed, there are more predicted states at low spin than observed candidates.

To understand the above puzzle it is profitable to look first at both the kinematical and spectroscopical selectivity of the transfer reaction in populating the states in both "bands", namely the odd-spin band and the even-spin doublets with negative parity according to refs. [109, 113]. Figure 6.2 shows the exclusive cross sections for the direct population of the natural and unnatural-parity states. They have been calculated by subtracting the feeding from higher-lying states and adding the intensities from the observed decay paths. The uncertainties were quadratically propagated as

$$\delta I = \sqrt{\sum_n (\delta I_{\text{feeder n}})^2 + \sum_m (\delta I_{\text{decay path m}})^2} \tag{6.3}$$

All the above allows a comparison of the direct population of the different states, which is shown in figure 6.2(a) for the ^{12}C(^{208}Pb, ^{212}Po)^{8}Be reaction used in this work and for the reaction ^{208}Pb(^{18}O, ^{14}C)^{212}Po of refs. [113, 109] in figure 6.2(b). Whereas there is no evident pattern in the exclusive cross sections sorted according to the energy of the state, the population of low-spin states is favored with a rather smooth decrease of the cross sections for increasing values of J. All the low-lying states in ^{212}Po previously

identified as "collective" are among the strongest ones populated by the α-transfer reaction as suggested from their similar structure if one follows the published theories. This results in the observation of all their strongest depopulating transitions regardless of the feeding in the corresponding excited states.

Since there are no substantial changes in the population of these excited states at different energies slightly above the barrier and no dependence on the structure of the light transfer product is suggested from the presented analysis (see figures 4.26 and 4.23), the trend to populate more strongly the collective states with the lowest spins observed in both α-transfer reactions is most likely the sole effect of the kinematical selectivity of the reaction. Its effect can be qualitatively understood from simple estimates of $\Delta\ell$ using eq. (1.19). The velocity v can be estimated as $\sqrt{\frac{2(E_{\mathrm{lab}}-V_B)}{m(^{12}\mathrm{C})}}$ in the ^{208}Pb rest frame, with $V_B = 58.85\,\mathrm{MeV}$ according to the Bass formula[119]. R is taken as the grazing distance, estimated as the half-density radius $1.27(A_1^{1/3} + A_2^{1/3})$[4, 173] plus 2.1 fm, a mismatch between such grazing distance and the actual distance that maximizes the transfer probability as reported by Hasan[174] for the ^{208}Pb(^{16}O,^{12}C)^{212}Po and ^{40}Ca(^{12}C,^{8}Be)^{44}Ti reactions and attributed to the size of the α particle. From the above set of parameters and estimating $R_{1,2}$ as $\sim 1.2A_{1,2}^{1/3}$,

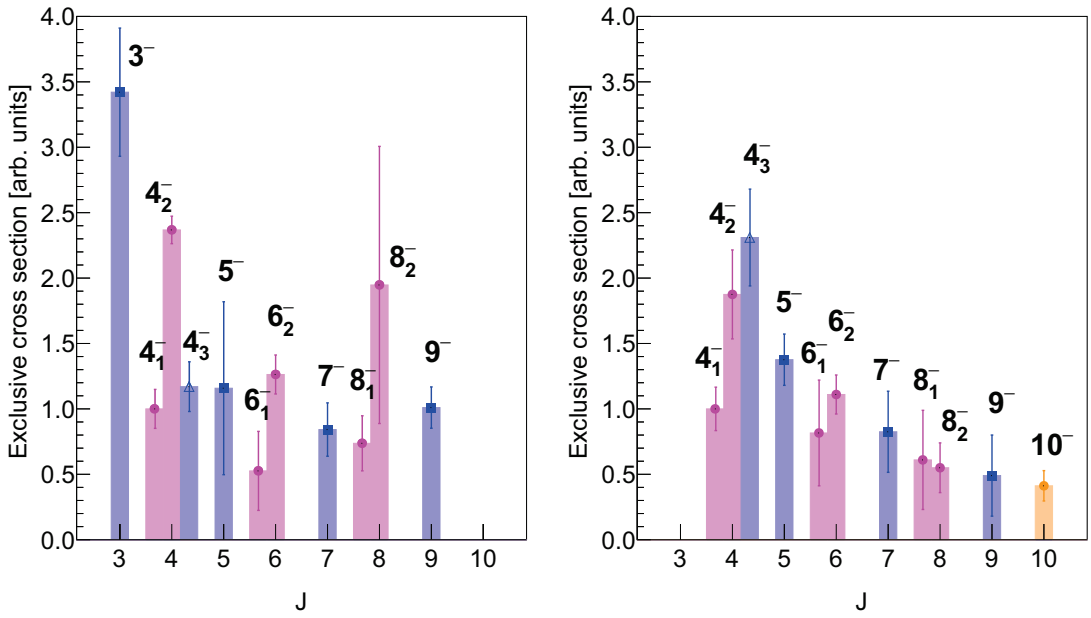

(a) ^{12}C(^{208}Pb, ^{212}Po)^{8}Be **(b)** ^{208}Pb(^{18}O, ^{14}C)^{212}Po

Figure 6.2: Comparison of exclusive cross sections for the population of the lowest-lying negative-parity states, according to refs. [109, 113], observed with the reactions ^{12}C(^{208}Pb, ^{212}Po)^{8}Be (this work) and ^{208}Pb(^{18}O, ^{14}C)^{212}Po (from [109]). They have been normalized to the exclusive cross section of the 4_1^- state at 1745 keV.

optimum $\Delta\ell$ values around $2\hbar$ are calculated for the α-transfer reactions shown in figure 6.2.

The very weak population of the 1898-keV state having a decay branch towards the 2_1^+ with I=0.6(3) indicates a different microscopic structure than the other unnatural-parity doublets. From the aforementioned arguments, the deexciting transitions from all the 1^-, 2^- and 3^- states would have been clearly observed[1], hence their existence is questioned. There is no apparent way of reconciling this conclusion with the calculation performed by Suzuki and Ohkubo[114], that is, with models comprising relative motion of an α particle around the ^{208}Pb core. It is possible, on the other hand, to gain more insight from these results by examination of the hypothesis underlying the calculation performed in ref. [115]. This hypothesis is that the interaction of the $|^{210}\mathrm{Pb}(J^+)\rangle\,|^{208}\mathrm{Pb}(3^-)\rangle$ states with two protons in a ^{210}Po(G.S.) configuration lowers the energy of the collective states well below 2.6 MeV.

6.1.1 Octupole vibrations near ^{208}Pb

It has been observed since the late 60's that the octupole vibration 3^- in ^{208}Pb is a source of fragmentation of single-particle/hole strength in nuclei around ^{208}Pb. As an example, the collective E3 strength in ^{209}Bi is splitted among a septuplet of states concentrated around 2.6 MeV, the energy of $^{208}\mathrm{Pb}(3^-)$. The energy splitting among the states in the multiplet is the result of admixtures with single-particle states. The unperturbed configuration $\pi(h_{9/2})\otimes 3^-$, formed by the odd proton in the ^{209}Bi ground state and an excited core $^{208}\mathrm{Pb}(3^-)$, is slightly mixed with the $\pi(i_{13/2})$ single particle state giving rise to the whole $J^\pi = \left\{\frac{3}{2}^+,\ldots,\frac{15}{2}^+\right\}$ septuplet, with an additional correction for the $\frac{3}{2}^+$ member stemming from the coupling to $^{210}\mathrm{Po}(0^+ d_{3/2}^{-1})$. The experimental excitation energies and B(E3) values in ^{207}Tl and ^{207}Pb reveal as well large admixtures involving the $h_{11/2}^{-1}$, $d_{5/2}^{-1}$ proton holes in the former and $i_{13/2}^{-1}$, $f_{7/2}^{-1}$ neutron holes in the latter[176].

These couplings for few-particle/hole nuclei around the doubly-magic ^{208}Pb were described in the past by the particle-vibration coupling calculations of Hamamoto[177, 178], which later were succesfully used to describe E3-decaying high-spin isomers found well beyond ^{208}Pb (see for instance [179]). The salient features observed in experiment are reproduced in a perturbative calculation. In particular, is observed a preference for admixtures involving single-particle states with opposite parity is observed, whereas couplings to single-particle configurations involving spin-flipped states are hindered.

[1] It is interesting to note that negative parity 1^- and 2^- states belonging to $\alpha + {}^{16}$O rotational bands in ^{20}Ne were populated in the past using the α transfer reaction (^{12}C, ^{8}Be)[175].

Moreover, the couplings are stronger when the single-particle configurations are close in energy to the unperturbed configuration and they satisfy the rule $\Delta j = \Delta \ell = 3$. The weak coupling found in ^{209}Bi was attributed to the spin flip between the involved states.

A similar situation is found in ^{210}Po. The collective E3 strength in this nucleus was probed by Ellegaard et al.[180] using inelastic scattering of deuterons, protons and tritons and only one 3^- state at 2.39 MeV, exhausting $\sim 90\%$ of the E3 strength, was found. The slight lowering in energy with respect to the unperturbed $\pi(h^2_{9/2}) \otimes 3^-$ configuration which should lie at 2.6 MeV was explained by a slight admixture with the $\pi(h_{9/2}i_{13/2})_{3^-}$ two-proton state expected close in energy, although the coupling is hindered by the flipped spin between the two proton states as in ^{209}Bi. A candidate for the other missing 3^-, expected at higher energy, was reported by Mann[181] et al. at 2846 keV as a member of the $\pi(h_{9/2}i_{13/2})$ multiplet with an M1 deexciting transition to the 2386-keV state observed by Ellegaard et al.

A different situation is observed, on the other hand, in ^{209,210}Pb. The only negative-parity state available for the valence neutron in ^{209}Pb is the $\nu(j_{15/2})$, which mixes with the $\nu(g_{9/2}) \otimes 3^-$ configuration giving rise to the $\frac{15}{2}^-$ state at 1423 keV [176]. The strong octupole character of this state is evidenced by its B(E3) of 16 W.u. to the $\frac{9}{2}^+$ ground state, being the large admixture with the $\nu(j_{15/2})$ configuration, exhausting 23% of the $\nu(j_{15/2})$ single-particle strength [176, 178], responsible for the fragmentation of the collective E3 strength. Inelastic excitation by deuterons and tritons[182] confirmed the persistence of strong couplings involving the $\nu(j_{15/2})$ orbital to the $\nu(g_{9/2})^2 \otimes 3^-$ configuration in ^{210}Pb by the splitting of virtually all the collective E3 strength between two 3^- states at 1.87 MeV and 2.83 MeV. The apparent difference between ^{209}Pb and ^{210}Pb in the energy of the collective E3-decaying states points to a significant difference in their wave functions. For ^{210}Pb, the coupling proceeds via the 3^- member of the $\nu(g_{9/2}j_{15/2})$ multiplet, calculated close to 2.6 MeV. 13 additional configurations resulting in much higher excitation energies and lower amplitudes are included in a realistic calculation of the excitation energies of the two 3^- states performed by Hamamoto for ^{210}Pb[177]. The wave functions have the form

$$|3^-_{1,2}\rangle = a_{1,2}\,|^{208}\mathrm{Pb}(3^-) \otimes \nu(g_{9/2})^2_{J=0,2,4,6}\rangle_3 + b_{1,2}\,|^{208}\mathrm{Pb}(0^+) \otimes \nu(g_{9/2}j_{15/2})_3\rangle + \ldots \quad (6.4)$$

where the amplitudes $a, b, \ldots$ are determined by diagonalization of the hamiltonian since perturbation theory was not applicable in practice, given the large couplings.

A strong, neutron-driven fragmentation of the B(E3) seemingly persists when adding protons to Pb. For instance, the lifetimes of the isomeric states at 1064 keV and

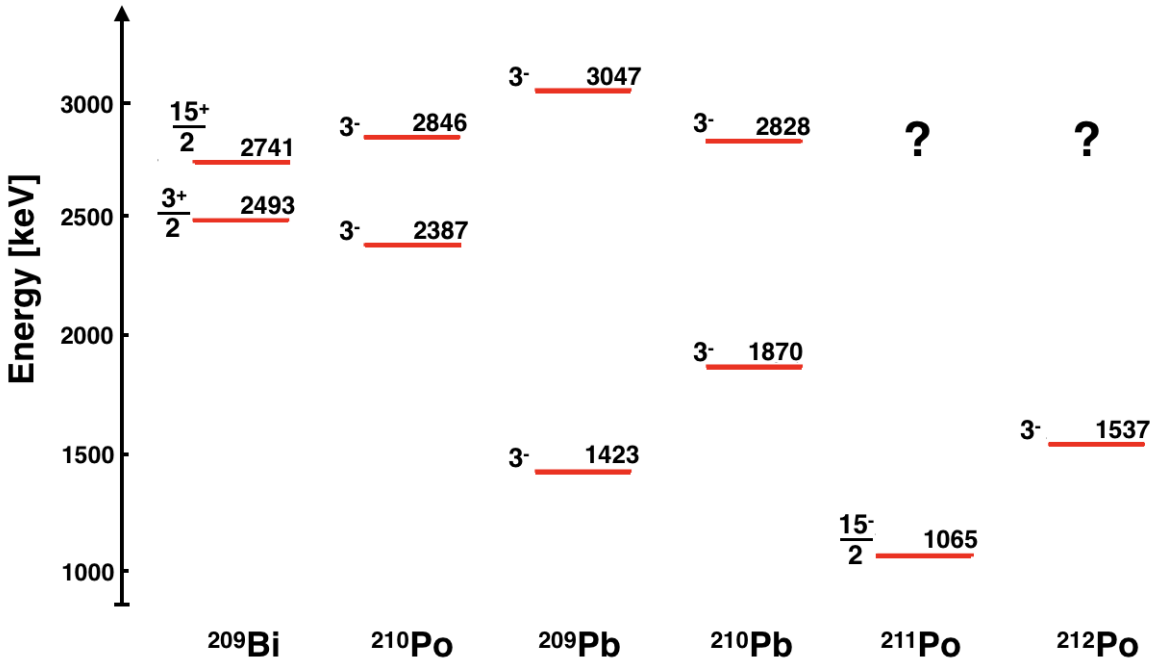

Figure 6.3: Illustrates the splitting of the lowest-lying collective states resulting from couplings of the octupole vibration in ^{208}Pb with single- and multi-particle states. The $\frac{3}{2}^+$ and $\frac{15}{2}^+$ are the states at lowest and highest energy within the $\nu g_{9/2} \otimes {}^{208}\mathrm{Pb}(3^-)$ septuplet in ^{209}Bi.

2135 keV in ^{211}Po are known to be 14.0(2) ns and 243(21) ns[90] resulting in collective E3 transitions of 19.2(9) W.u. and 22.5(23) W.u., respectively.

The discussion of the previous paragrapahs is summarized in figure 6.3, which shows a comparison of the 3^- energy in ^{212}Po with the energy of the collective 3^- states in ^{210}Po, ^{210}Pb and the low-lying $\frac{15}{2}^-$ states in ^{209}Pb and ^{211}Po. The lack of candidates for collective $(1,2)^-$ states and the remaining 3^- states around 2 MeV given the selectivity of the reaction as well as the rather low excitation energy of the remaining octupole states as in $^{209}\mathrm{Pb}(\frac{15}{2}^-)$, $^{210}\mathrm{Pb}(3^-)$ and $^{211}\mathrm{Po}(\frac{15}{2}^-)$ suggests that both the natural- and unnatural-parity states with $J^\pi = I^-$ take strength from pure shell model configurations as in neighboring isotopes. In particular, an admixture of the unperturbed configurations $^{208}\mathrm{Pb}(3^-) \otimes \nu(g_{9/2})^2_{J=0,2,4,6} \otimes {}^{210}\mathrm{Po}(\mathrm{G.S.})$ with the $^{208}\mathrm{Pb}(0^+) \otimes \nu(g_{9/2}j_{15/2})_{I^-} \otimes {}^{210}\mathrm{Po}(\mathrm{G.S.})$ may be introduced in their description.

Since the unperturbed configurations $^{212}\mathrm{Po}(2^+_1, 4^+_1, 6^+_1, 8^+_1) \otimes {}^{208}\mathrm{Pb}(3^-)$ are expected above 3 MeV in energy, shell model calculations have been performed to locate the position of the $\nu g_{9/2}j_{15/2}$ multiplet in ^{212}Po and to verify that the excitation energy of its members enables an admixture with such unperturbed configurations as in the case of ^{209,210}Pb, hence resulting in a small shift of the entire multiplet towards lower energies. The latter is confirmed from the comparison of the energies that is shown in

figure 6.4. Moreover, the trend of increasing excitation energy with increasing angular momentum is seemingly dominated by the position of the members belonging to the multiplet. This feature questions the comparison made in [109] in which the octupole nature of these states was established by an analogy with ^{148}Gd, since the situation in ^{148}Gd is "inverted" with respect to ^{212}Po: in ^{148}Gd the $\nu f_{7/2} i_{13/2}$ multiplet, the only one with $\Delta j = \Delta \ell = 3$, is calculated above 3.5 MeV in energy whereas the unperturbed configurations $(\nu f^2_{7/2} \otimes 3^-)_{I^-}$ are located below the $\nu f_{7/2} i_{13/2}$ multiplet[183], thus the low-lying octupole vibrations in this nucleus are dominated by the $\nu f^2_{7/2} \otimes 3^-$ configuration.

Within the proposed picture, breaking the ground state proton pair would be required to form 2^- states by a coupling to the $\nu g_{9/2} j_{15/2}$ configuration. Neglecting residual interactions, these states are expected above 3 MeV and, indeed, the first of them is predicted at 3308 keV in the calculation.

The presented results thus provide some evidence for the description of the low-lying octupole states in ^{212}Po as admixtures involving the $\nu(g_{9/2})^2_J \pi(h_{9/2})^2_0 \otimes {}^{208}\mathrm{Pb}(3^-)$ states and the lowest-lying $\nu g_{9/2} j_{15/2}$ multiplet, which is a different model than those proposed in [115] and [114].

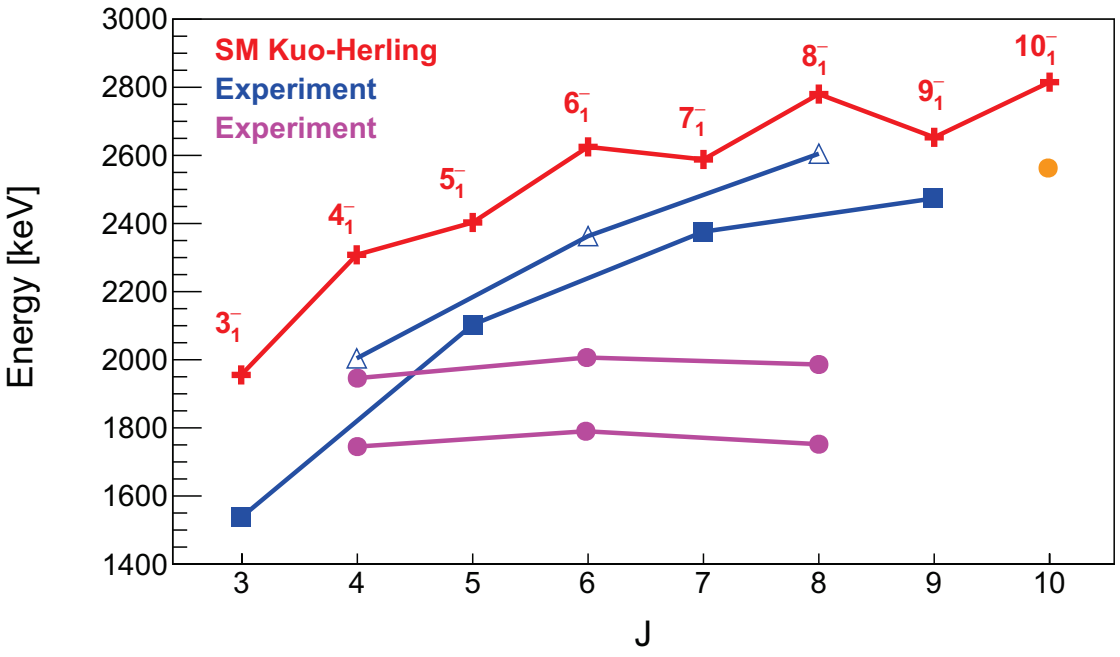

Figure 6.4: Comparison between experimental negative-parity states according to ref. [109] and the calculated energies of the multiplet $\pi(h^2_{11/2})_{0^+}\nu(g_{9/2}j_{15/2})_{I^-}$ (in red). Filled symbols represent states decaying by E1 transitions to the yrast band.

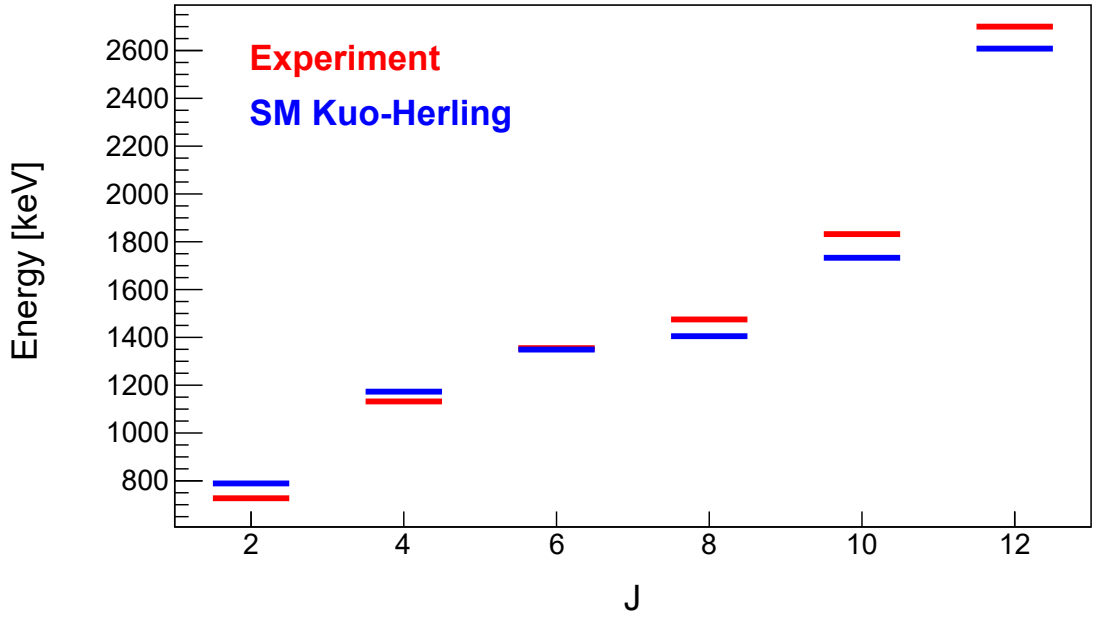

Figure 6.5: Comparison between experimental and calculated excitation energies of the states belonging to the ^{212}Po ground-state band up to the 12^+ state.

6.2 Spin and parity assignments

Tentative spin and parity assignments have been made for the 1898 keV, 2085 keV and 2574 keV states on the basis of a comparison of their energies and decay paths with the energies and decay paths predicted by the shell-model calculation. The calculation reproduces within 100 keV the position of the yrast band and the known $1^+, 2^+_{2,3,4}$ states. The branching fractions of the 2^+ states are in good agreement with the experimental results[2]. These preparatory comparisons, which are summarized in figures 6.5 and 6.6, are intended to elucidate the accuracy of the calculation.

Figure 6.7 shows a calculated level scheme up to 2300 keV composed of the states with angular momentum smaller than 5 and positive parity. Among the negative-parity states, only the 3^- member of the $\nu g_{9/2} j_{15/2}$ multiplet and a 2^- at 2288 keV lie below 3 MeV. No experimental candidates have been proposed for any of the non-yrast 4^+ states. Among them, the 4^+_2 at 1670 keV is predicted to deexcite towards the 4^+_1 with a probability of 96%. The 2^+_5 state is calculated at 2197 keV with a branching fraction of 84% to the 2^+_1. The 1^+_2 state would present more fragmented deexcitation paths, in particular to the 2^+_1 (40%), the 1^+_1 (37%) and the 2^+_3 (17%) states. The most intense deexcitation path of the 3^+_1 state calculated at 1858 keV would be to the 2^+_1 with a

[2]The calculation fails to reproduce the strong ground-state decay of the 1^+_1. However, the calculated transition probabilities for all decay branches of this level are very small:
$B(M1; 1^+_1 \longrightarrow 0^+_1) = 1.1\times10^{-4}\mu_N^2$, $B(M1; 1^+_1 \longrightarrow 0^+_1) = 3.5\times10^{-3}\mu_N^2$, $B(E2; 1^+_1 \longrightarrow 0^+_1) = 0.7 e^2\mathrm{fm}^4$
so that the decay pattern is very difficult to predict.

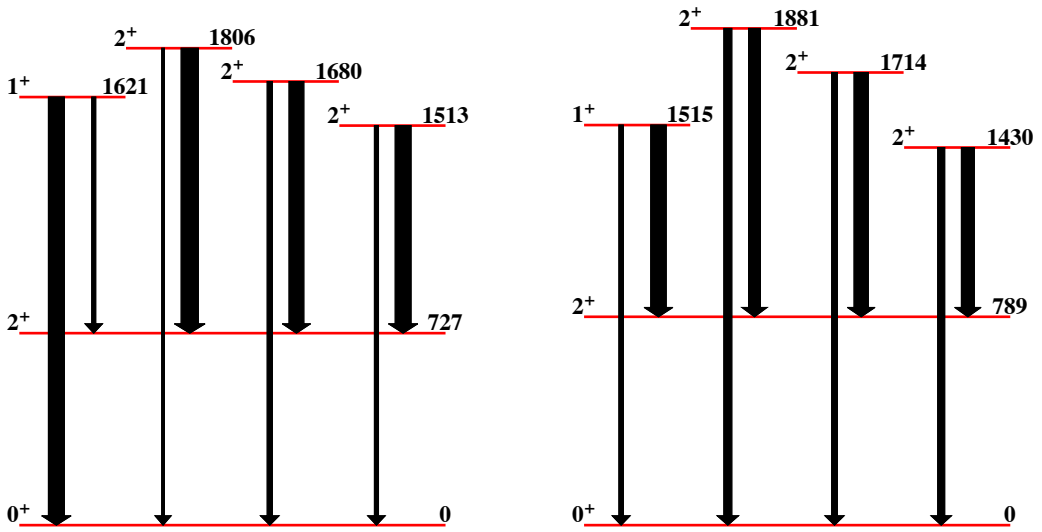

(a) Experiment. **(b)** Calculated.

Figure 6.6: Comparison of calculated and experimental energies and branching fractions of the 1^+ and $2^+_{2,3,4}$ states in ^{212}Po. The widths of the arrows are proportional to the branching fractions.

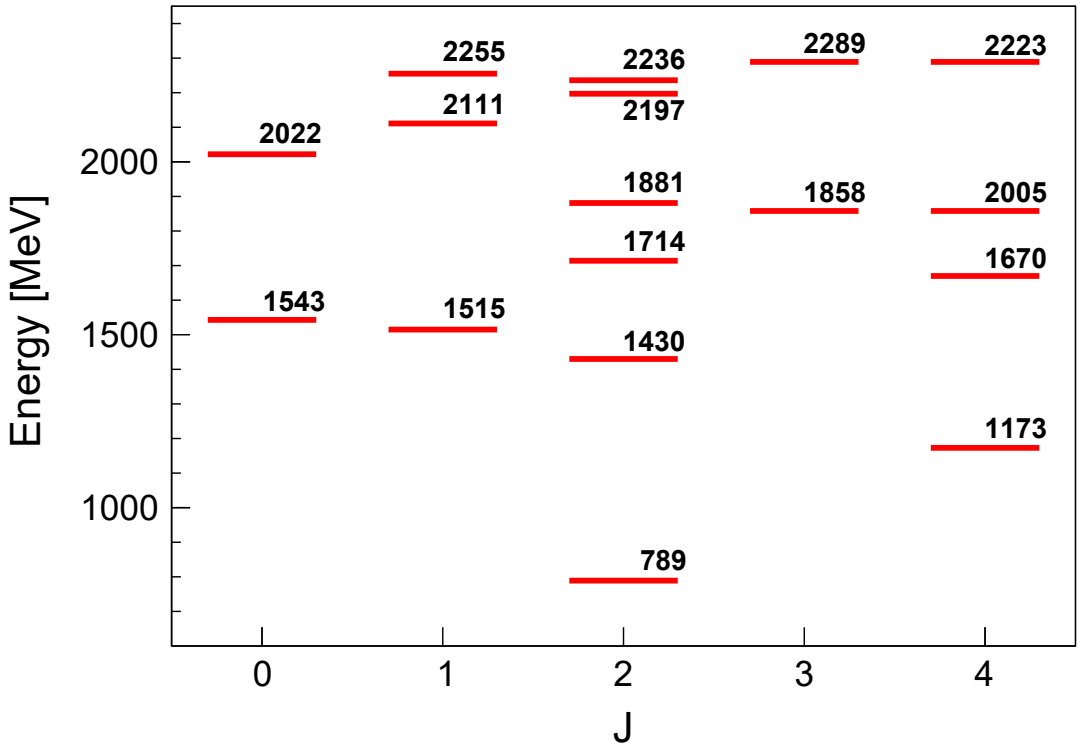

Figure 6.7: Calculated level scheme of ^{212}Po up to 2300 keV. Only positive-parity states with angular momentum below 5 are shown.

branching fraction of 61%. The experimental 0^+ state at 1801 keV [90] most likely corresponds to the 0^+_3 state, since the 0^+_2 is calculated at lower energy (1543 keV).

This latter assertion is also supported by the position of the known $0^+_{2,3}$ in ^{214}Po at 1415 keV and 1743 keV[90].

The 1898 keV is tentatively identified as a 3^+ state on the basis of these results, with a structure similar to the 10^+_1 state, namely $\pi h^2_{9/2}\nu g_{9/2}i_{11/2}$. Neither the calculated 2^+ states nor the 3^+ ones feed the 4^+_1, hence the 2085 keV state is assigned $J^\pi = 4^+$.

The 2574-keV state, for which an upper lifetime limit of 0.4 ps was established, most likely corresponds to the 2^+_9. A $J^\pi = 3^-$ assignment is not considered because of the large, non-physical B(E3) that would result. Among the calculated 2^+ states, all of them save the 2^+_9 at 2579 keV have very weak decay branches towards the ground state. Regarding the 1^+ states, a similar scenario is found and only the 1^+_5 at 2767 keV would be a feasible candidate, nevertheless the resulting energy difference disqualifies a $J^\pi = 1^+$ assignment to this state. Similarly, the first 1^- state occurs at 3057 keV in the calculation so that this assignment is not considered either. Table 6.1 gives the energies and decay paths of some of the calculated $1^+, 2^+$ states.

No tentative assignments are proposed for the remaining excited states, for which multiple candidates can be found among the calculated low-spin states. The spin and parity assignments performed in this work are summarized in figure 6.8.

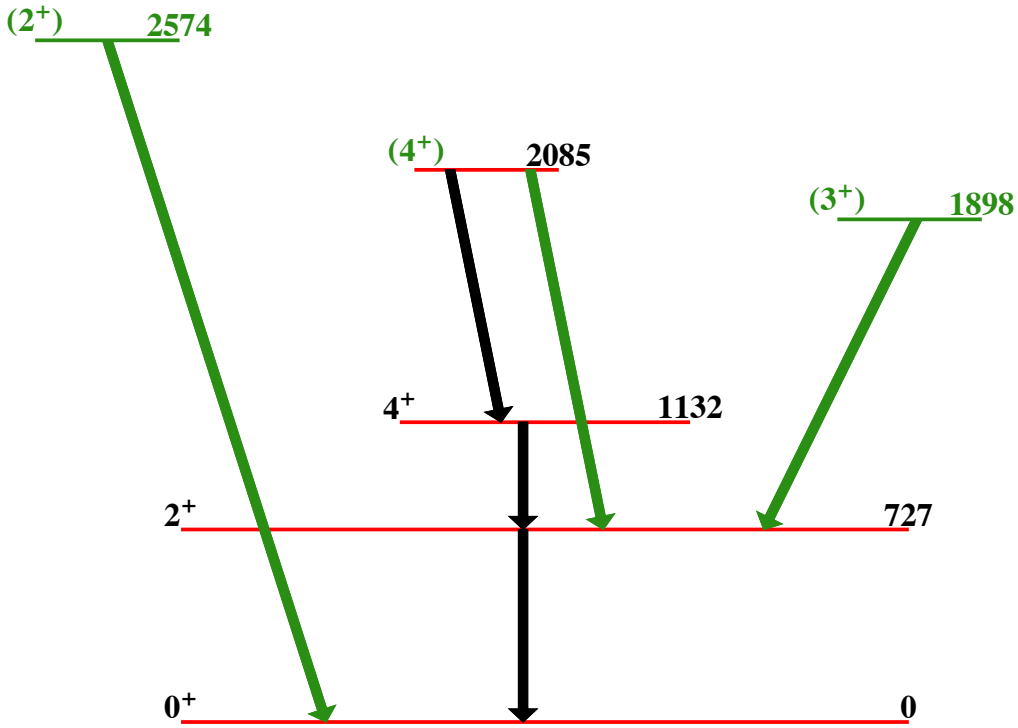

Figure 6.8: Summary of spin and parity assignments. Levels and transitions observed for the first time in this work are represented in green. Tentative spin and parity assignments are indicated in green.

J^π_{level}	E_{level} [keV]	$J^\pi_{\text{final level}}$	b_γ [%]
2^+_5	2197	2^+_1	84.25
2^+_6	2236	0^+_1	11.98
		2^+_1	40.70
		1^+_1	39.57
1^+_3	2255	0^+_1	81.69
		2^+_1	6.98
2^+_7	2436	2^+_1	97.19
2^+_8	2498	0^+_1	10.49
		2^+_2	83.77
2^+_9	2578	0^+_1	51.40
		2^+_2	35.56
1^+_4	2650	0^+_1	15.45
		2^+_2	30.24
		2^+_3	20.56
		2^+_4	11.76
		2^+_7	6.76
2^+_{10}	2660	0^+_1	8.76
		2^+_1	50.93
		2^+_2	22.65
1^+_5	2767	0^+_1	79.36
		0^+_2	6.54
		0^+_4	6.36

Table 6.1: Energies and branching ratios of calculated 1^+, 2^+ states. Only branching ratios larger than 5% are given. Deexcitation of the levels via γ-ray emission with 100% probability is assumed.

6.3 Reinterpretation of the dipole-decaying doublets

No direct measurement of the linear polarization was reported in [109, 113] so that a negative parity was assigned to the dipole-decaying doublets on the basis that an E2 component in the transition results in large levels of quadrupole collectivity, a feature that is not supported by the known B(E2) values of transitions within the ground-state band. Here we understand that, according to the authors of [109, 113], a pure M1 decay, that is, with virtually no E2 mixing, is not feasible and for that reason a positive-parity assignment to the doublets was not considered. We remark that the interpretation of these states as α-cluster states is based solely on their enhanced E1 decay.

The $J^\pi = 6^+$ state at 1788 keV would correspond, according to the calculations, to the 6_2^+ state which is essentially generated by the configuration $\pi h_{9/2}^2(\nu g_{9/2}^2)_{0^+}$. Although the accumulated statistics as well as the contamination from other ^{211,212}Po transitions does not allow to perform this study for the γ rays depopulating the remaining "α-cluster" states, by the same argument pushed forward in section 6.1 it is reasonable to identify the remaining doublets with the second and third positive-parity state of a certain even angular momentum since they are generated by the similar valence configuration and their relative population is of the same magnitude. Their calculated energies and decay properties compare favourably with the experimental ones as shown in table 6.2. It was noticed that, without exception, their main decay branch has more than 93% of probability and proceeds towards the yrast state with the same spin and parity by means of a sizeable and pure M1 transition.

J_n^+	E_x^{th} [keV]	E_x^{exp} [keV]	$B(M1; J_n^+ \to J_1^+)^{\text{th}}$ [μ_N^2]	$B(M1; J_n^+ \to J_1^+)^{\text{exp}}$ [μ_N^2]
2_2^+	1430	1513	0.293	0.126(16)
2_3^+	1714	1680	0.060	0.042(20)
4_2^+	1670	1745	0.564	0.52(16)
4_3^+	2005	1946	0.056	0.23(7)
6_2^+	1718	1788	0.723	1.56(12)
6_3^+	2081	2017	0.134	0.40(13)
8_2^+	1732	1752	0.933	5.6(2.3)
8_3^+	1908	1986	0.254	-

Table 6.2: Calculated and experimental energies and transition probabilities of the second and third excited state of even angular momentum $2 \leqslant J \leqslant 10$ and positive parity. Experimental $B(M1)$ were calculated from the lifetimes reported in [109] and [17].

The question of how such a large[3] B(M1) can arise with so little configuration mixing was recently addressed by Kocheva et al.[17] motivated by the B(M1) values of $0.126(16)\mu_N^2$ and $0.042(20)\mu_N^2$ that they measured for the $2_2^+ \to 2_1^+$, $2_3^+ \to 2_1^+$ transitions. These states are pointed as fragments of the one-phonon mixed symmetry state decaying to the fully symmetric state which is the 2_1^+. Indeed, according to their

[3]Note that M1 strengths in the order of $1\mu_N^2$ would be among the largest ones known all over the chart of nuclides.

calculation the wave functions of the $2^+_{1,2}$ states are of the form[17]

$$|2^+_1\rangle = 0.448\,|J_\nu = 0, J_\pi = 2, J = 2\rangle + 0.819\,|J_\nu = 2, J_\pi = 0, J = 2\rangle + \dots \quad (6.5)$$

$$|2^+_2\rangle = 0.813\,|J_\nu = 0, J_\pi = 2, J = 2\rangle - 0.517\,|J_\nu = 2, J_\pi = 0, J = 2\rangle + \dots \quad (6.6)$$

so that this antisymmetry against exchange of a proton and neutron boson would be responsible for their large B(M1). Given the rather low level of configuration mixing involved, the above picture is expected to hold also for the other doublets that we identify as states exhausting a significant fraction of the mixed-symmetry state (MSS) built on the grounds of $\pi h^2_{9/2}\nu g^2_{9/2}$ isovector excitations.

Chapter 7

Summary and conclusions

The ^{212}Po nucleus has been studied by means of the α-transfer reaction (^{12}C, ^{8}Be) in inverse kinematics. Its level scheme has been extended by including 14 new excited states and tentative spins and parities have been assigned to three of them with the assistance of energies and decay paths of excited states predicted by the shell model. Upper limits for the lifetime of five excited states have been extracted.

Having in mind the convenience of transfer reactions in inverse kinematics as a qualified tool for DSAM lifetime measurements, the experiment was originally proposed with the goal of performing a more accurate and direct lifetime measurement of the so-called "α-cluster" states. This is the first attempt to perform such a measurement in the region around ^{208}Pb using a high-intensity stable beam and a multilayered target with a dense stopping material such as Au. The faced target issues and the limitations of the experiment have been described in detail with the hope that the presented analysis will be of help in the preparation of future experiments exploiting this or a similar technique. The extracted lifetime limits demonstrate the usefulness and sensitivity of the technique in this particular case, enabling future γ-ray spectroscopic studies of ^{212}Po probing excited states decaying by high-energy transitions with $E_\gamma \gtrsim 2\,\mathrm{MeV}$.

Triggering the data acquisition on the detection of the residual α particles enabled us to combine an analysis based on singles and double-fold coincidence spectra without sacrificing detection efficiency for low-multiplicity cascades. Moreover, the reaction mechanism is a highly selective probe for all the states identified as collective in previous works: the low-lying negative parity states with odd spin and the so-called α-cluster doublets with even spin near 2 MeV have been strongly and directly populated. This feature has prompt us to examine our level scheme in the light of the proposed models for describing the octupole collectivity in ^{212}Po and the emergence of E1-decaying doublets with large α-cluster correlations. However, in spite of the selectivity of the

reaction mechanism and the experimental setup, no evidence has been found for the existence of any of the additional states predicted with spin equal to or smaller than 3. This observation has lead us to explore the possibility of describing the observed negative-parity states as admixtures involving the ^{212}Po$(0_1^+, 2_1^+, 4_1^+, 6_1^+, 8_1^+)\otimes^{208}Pb(3_1^-)$ configurations and the low-lying $\pi(h_{9/2}^2)_0\nu(g_{9/2}j_{15/2})_{I^-}$ multiplet in ^{212}Po. One finds that the experimental energies of the negative-parity states are only slightly but systematically overestimated with respect to the energies of single- and multi-particle states, in a similar fashion to ^{210}Pb and ^{211}Po. One finds as well that the saturation of the excitation energy with increasing spin, experimentally observed in the odd spin band, is seemingly mirrored in the odd-spin members of the multiplet.

Continuing with this study of collectivity in ^{212}Po, AGATA has been used as a Compton polarimeter in order to perform the fist direct determination of the parity of the dipole-decaying doublets with even spin. The accumulated statistics of singles γ rays allows this study for the 433 keV γ ray only, and it is found that this corresponds to an M1 transition. Nevertheless the selectivity of the reaction mechanism previously noted suggests that also the remaining doublets decay by M1 γ rays to the yrast states so that they have positive parity. From the performed shell model calculations we identify the doublets as the second and third positive-parity states of a certain even angular momentum. The excitation energies of the states, their only detected branching towards the first excited state with the same angular momentum as well as the large B(M1) in the deexciting transition are mirrored in the calculation, hence raising doubts with respect to their interpretation as pure α cluster states.

A dedicated experiment aimed at performing a direct measurement of the parity of the doublets is desirable in order to draw definitive conclusions regarding these states. Future experiments may as well be focused on extending the level scheme of ^{214}Rn and ^{214}Po nuclei, studied by fusion-evaporation reactions in the past. Radioactive ^{210}Pb and ^{210}Po targets have already been used[182, 180] and may be combined with a similar experimental setup as the one described in this thesis in order to populate ^{214}Rn and ^{214}Po by means of transfer reactions in normal kinematics.

Part II

First spectroscopy of excited states in the $T_z = -2$ nucleus ^{56}Zn: isospin symmetry towards the proton drip-line

Chapter 8

Introduction

8.1 Isospin symmetry breaking in nuclei

Almost identical nuclear structure properties are known in nuclei with interchanged numbers of protons and neutrons: this is the so-called mirror symmetry. At a more fundamental level, phase shifts observed in nucleon-nucleon scattering experiments suggest that the nucleon-nucleon interaction is of almost identical strength regardless of the nature of the interacting pair when the effects of the known electromagnetic interaction are subtracted. This symmetry is formally expressed by introducing a quantum number T, the total isospin of the nucleus, which is additive in the isospin of the individual nucleons. Along with its third component $T_z = \frac{N-Z}{2}$, this quantum number defines each nuclear state when combined with its angular momentum and parity: in the isospin formalism, the charge-independence property of the nuclear interaction means that the nuclear hamiltonian is invariant under any rotation in isospin space, hence commuting with both the T^2 and T_z operators.

Isospin, however, is only an approximate symmetry of the nuclear interaction which is not only broken by the Coulomb repulsion between protons but also by the bare short-range nuclear interaction, though to a much lesser extent. These two kinds of isospin non-conserving (INC) interactions of both electromagnetic and nuclear origin acting in the nuclear medium break the degeneracy between isospin multiplets introducing differences among excitation energies of isobaric analogue states (IAS), namely excited states of a given angular momentum, parity and isospin T within an isobaric chain. It is now well established that these differences can not be reproduced in calculations using effective interactions derived from realistic parametrizations of the free nucleon-nucleon potential[184, 185]: theoretical studies show that a significant and systematic deviation with respect to the experimental data is present regardless of the chosen nucleon-nucleon potential and that this deviation is model dependent,

as shown in figure 8.1. As discussed in ref. [185], this may point to significant INC contributions from three-body interactions, an amplification of the isospin-symmetry breaking (ISB) by the renormalization of the interaction or even deficiencies in our understanding of ISB in the nucleon-nucleon interaction.

The INC interaction represents only a slight perturbation to the solutions obtained from isospin-conserving shell model hamiltonians. The differences in excitation energies between analogue states can be measured relative to the ground state and probe the charge-independence and charge-symmetry aspects of the nuclear interaction, which are related respectively to Mirror Energy Differences (MED) and $T = 1$ Triplet Energy Differences (TED), two quantities defined as

$$\mathrm{MED}_J(T, T_z) = E_J(T, T_z = T) - E_J(T, T_z = -T) \tag{8.1}$$

$$\mathrm{TED}_J = E_J(T_z = 1) + E_J(T_z = -1) - 2E_J(T_z = 0) \tag{8.2}$$

Starting from the solutions of an isospin-conserving shell model hamiltonian in the valence space, MED and TED can be reproduced below tens of keV in first order perturbation theory by assuming the structure of the INC interaction as originally employed by Zuker in the $f_{7/2}$ shell[187], from the doubly magic ^{40}Ca up to ^{56}Ni. Within this approach, the contribution from the monopole part of the INC interaction cancels out in the TEDs, which are the sole result of the multipole terms. On the other hand, both monopole and multipole terms contribute to the MED. MED and TED are thus useful and complementary probes of the INC part of the nuclear interaction

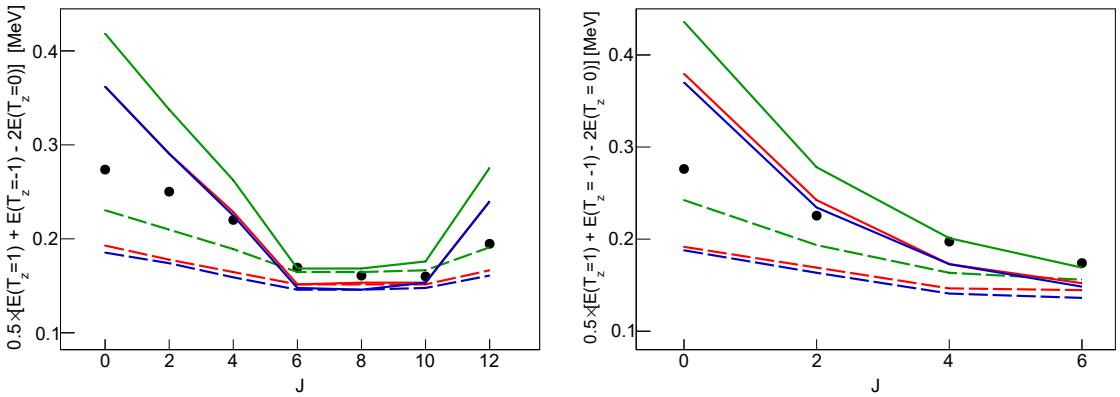

(a) $A = 46$ **(b)** $A = 54$

Figure 8.1: Triple-energy differences as a function of angular momentum for $T = 1$ states in $A = 46$ and $A = 54$ nuclei. Experimental data is represented by filled circles. Theoretical predictions of the CD-Bonn potential at first, second and third order are depicted in blue, red and green. The Coulomb and Coulomb plus nuclear contributions are represented by the dashed and solid lines, respectively. Data is from [185] and updated with the recent $J^\pi = 6^+$ data for ^{54}Co from [186].

that contain information of the isovector ($v^{(1)}$) and the isotensor ($v^{(2)}$) parts of the two-body interaction, respectively. They are defined in terms of the proton-proton, proton-neutron and neutron-neutron two-body interactions as

$$v^{(1)} = v_{pp} - v_{nn} \tag{8.3}$$

$$v^{(2)} = v_{pn} - \frac{1}{2}(v_{pp} + v_{nn}) \tag{8.4}$$

The monopole INC interaction.

According to the formalism employed by Zuker[187], the monopole part of the interaction is of Coulomb origin and in the middle of the $f_{7/2}$ shell mostly results from the contribution of a radial term. This term stems from differences in charge radii that arise either as a bulk effect in deformed nuclei or just by an increased occupancy of the $p_{3/2}$ orbital belonging to the pf shell[1]. This orbital has a much larger radius than the $f_{7/2}$, $f_{5/2}$ ones hence decreasing the static Coulomb energy. Since the occupancy of the $p_{1/2}$ orbital is usually negligible and the $p_{3/2}$ orbital has a key role in the emergence of collectivity in the lower fp shell, the radial term is taken proportional to the difference of average proton plus neutron $p_{3/2}$ occupancy between the ground state and the excited state[188],

$$V_{\mathrm{Cr}} = 2Ta_m \left(\frac{m_\pi(\mathrm{G.S.}) + m_\nu(\mathrm{G.S.})}{2} - \frac{m_\pi(J) + m_\nu(J)}{2} \right) \tag{8.5}$$

The value of the a_m factor is deduced empirically when the effect of the other two monopole interactions, an electromagnetic spin-orbit one and an $\ell\ell$ term accounting for shifts in single-particle orbitals induced by the Coulomb interaction with the core, is included. The former is the result of Larmor and Thomas precessions for a nucleon in a shell-model orbital,

$$V_{\mathrm{ls}} = \frac{(g_s - g_l)e}{2\, m_N^2 c^2} \left\langle \frac{1}{r} \frac{\mathrm{d}V_C(r)}{\mathrm{d}r} \right\rangle \langle \vec{l} \cdot \vec{s} \rangle \tag{8.6}$$

being g_s, g_l the gyromagnetic factors, m_N the nucleon mass and V_C the Coulomb potential generated by the core. The energy shift induced by the single-particle correction $V_{\ell\ell}$ for an orbit with principal quantum number N above the closed core with proton number Z_{cs} can be estimated as[189]

$$\varepsilon_{ll} = \frac{-4.5 Z_{\mathrm{cs}}^{13/12} [2\ell(\ell+1) - N(N+3)]}{A^{1/3}(N+3/2)} \text{ keV} \tag{8.7}$$

The importance of the radial term has been pointed out since the earliest studies of mirror energy differences in the middle of the $f_{7/2}$ shell. These nuclei were accesible

[1]Notice that ^{56}Ni is a rather soft SM core.

by fusion evaporation reactions and the MEDs were used to probe the underlying structures involved in high-spin phenomena such as backbending[190]. As an example, in ref. [191] the spectroscopy of the $A = 47$ pair ^{47}V-^{47}Cr shows how the transition from a deformed to a spherical shape towards the $\frac{31}{2}^-$ band-terminating state is reflected in a smooth rise of the MED even though a dwindling of the mutual repulsion between the valence particles is expected from the aligned angular momenta of the proton-neutron pairs involved in the formation of this state. However, it has been claimed that in the lower part of the upper pf shell the radial term as proposed in the middle of the $f_{7/2}$ shell is not important since it is purely a measure of the deformation[192]: the MEDs in this region would emerge as an interplay between the spin-orbit interaction and the Thomas-Ehrman shift in the monopole term, combined with the Coulomb multipole term. The Thomas-Ehrman shift was originally introduced to explain the large MED (-725 keV) of the $\frac{1}{2}^+$ state in the $A = 13$ mirror pair[193, 194]. It arises due to changes in the spatial spread of the proton wave function, for a given orbital, that change the Coulomb energy. This situation is e.g. realized in the case of the ^{41}Sc-^{41}Ca mirror pair, where the $p_{3/2}$ orbital is unbound in ^{41}Sc thus resulting in a larger radius responsible for the enhanced MED in the $\frac{3}{2}^-$ state.

Figure 8.2 shows that the large negative MEDs for $T = 1$ states in the ^{70}Br and ^{70}Se nuclei contrasts with the overall trend of MED above $A = 66$ and represents an illustrative example of the spin-orbit effect[195]. The low-lying states in these nuclei are formed by significant occupancies of the $g_{9/2}$ orbital that increase as a function of the angular momentum for the $J = 2^+, 4^+$ and 6^+ states. As the spin-orbit interaction shifts the energy of the $g_{9/2}$ and $f_{5/2}$ orbitals in opposite directions for protons and neutrons and also for $j = l - s$ and $j = l + s$ states, its increased occupancy costs more energy in ^{70}Se than in ^{70}Br. Configuration mixing, however, makes extreme cases like this one the exception rather than the rule.

The multipole INC interaction.

Regarding the multipole part of the interaction, it was noticed that a two-body Coulomb interaction alone acting between protons does not account for the magnitude of neither MED nor TED. Parallell to the study of Zuker[187], an anomalous behaviour of the two-body INC matrix elements having similar strength for $J = 2$ couplings than for $J = 0$ ones, was reported by Williams et al. from MED data in the whole $f_{7/2}$ shell[197]: the maximum contribution of a multipole term of Coulomb origin is expected for states with maximum overlap of the wave functions, a situation realized for a pair of protons in time reversed orbits and hence coupled to $J = 0$. Subsequent recouplings to $J = 2, 4, 6$ obtained by breaking the pair must decrease the Coulomb

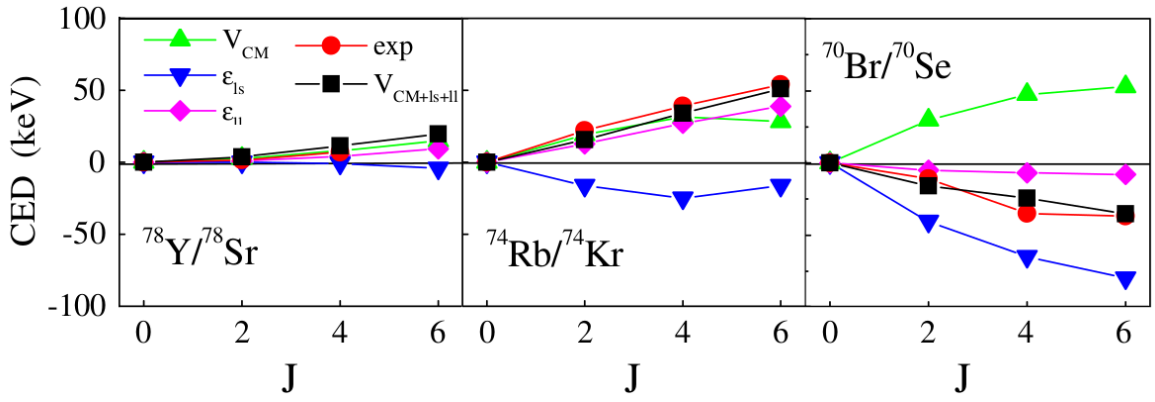

Figure 8.2: MED analysis in some $A = 78$, 74 and 70 nuclei. The similar MED pattern for the $A = 74$ and $A = 78$ pairs reflects how the generation of angular momentum weakens pairing correlations in these nuclei (see [196]): the larger number of proton pairs in the most neutron rich nucleus yields a larger decrease of Coulomb energy at increasing J. The inverted behaviour of the MED in the $A = 70$ nuclei is discussed in the text. Adapted from [195].

energy. Further MED analyses confirmed the necessity of the additional two-body non-Coulomb interaction V_B of unknown origin which is traced back to the $J = 2$ coupling in the isovector channel[198, 199] and to $J = 0$ in the isotensor one[200]. The J-dependence of the isovector V_B matrix elements was studied in ref. [201], where they were extracted from a fit to MED in the $A = 42-54$ region. It was demonstrated that both their strength and J-dependence is statistically significant and rather uniform

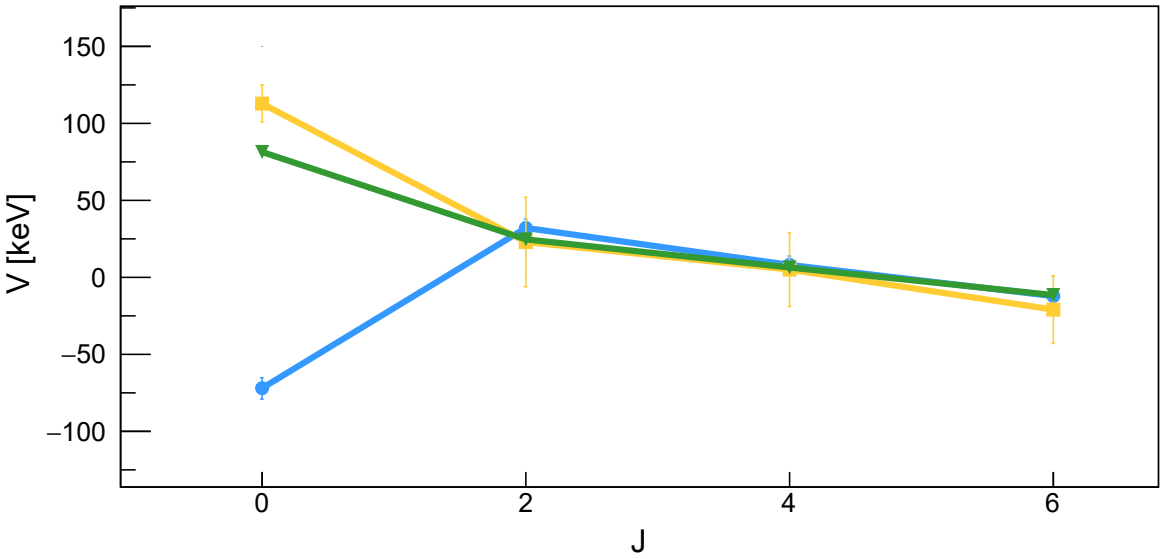

Figure 8.3: Matrix elements of the multipole part of the INC interaction in the fp shell. The Coulomb, V_B isovector and V_B isotensor matrix elements are represented in green, blue and orange, respectively and were taken from [187, 200, 201].

throughout this region. The matrix elements of the Coulomb and V_B multipole terms are represented as a function of J in figure 8.3. A similar study has been conducted in ref. [200] for the isotensor interaction V_B. This interaction has a single statistically significant non-zero matrix element for $J = 0$ couplings in $A = 42 - 54$ and its contribution for TED is as important as the Coulomb one. The data from the $A = 66$ triplet provides evidence for an isotensor interaction V_B of the same strength also in the upper fp shell[200]. MED calculations for pairs heavier than $A = 66$, however, show good agreement with the experimental data in both MED and TED without including the V_B term[202, 195, 203]. The V_B interaction is seemingly not uniform throughout the nuclear chart, a puzzle related to its origin.

8.2 Scope of this work

MEDs at large isospin magnify charge-symmetry breaking effects. They can only be studied near the $N = Z$ line where both members of the mirror pair are bound: the fp shell is the heaviest region allowing such studies at large isospin using radioactive beams. This work presents the first γ-ray spectroscopy of the $T_z = -2$ nucleus ^{56}Zn: with two neutron holes in the $f_{7/2}$ shell and two protons in the upper fp shell, this nucleus constitutes a good probe for elucidating the actual nature of the radial effects and at the same time for addressing the question of the persistence of the isovector V_B interaction into heavier mass regions in a sensitive way through the interplay between both.

Chapter 9

Experimental setup

The in-flight separation technique[204] was pioneered in the 80's for the production and identification of radioactive ion beams (RIB) and has significantly enlarged the spectrum of experimentally accessible nuclei far away from the valley of stability. The starting point for the production of exotic nuclei is a primary beam of a stable species accelerated to kinetic energies above 100 $^{\mathrm{MeV}}/_{\mathrm{u}}$ that impinges on a lighter target. At these relativistic energies, fragmentation reactions occur: the reacting nuclei break into smaller pieces that retain most of the velocity of the original projectile. It has been experimentally observed that the salient features of this reaction mechanism remain essentially constant from 10-50 $^{\mathrm{MeV}}/_{\mathrm{u}}$, where other reactions such as nucleon transfer are able to compete, up to 2 $^{\mathrm{GeV}}/_{\mathrm{u}}$.

The reaction is a peripheral one described as a two-stage process according the abrasion-ablation model[205, 206]. Only the nucleons within the overlap region between the target and the projectile, depending on the impact parameter, participate in the first stage, whereas the remaining nucleons are considered as spectators in this fast (direct) "abrasion" step. The overlap region is ripped off from the projectile and the residues continue to move along the projectile direction with almost the same relative velocity. A statistical deexcitation process occurs during the second stage, in which the residues may undergo fission, eventually thermalizing by emission of light particles and γ rays. The whole process is sketched in figure 9.1.

Yields of residual nuclei after projectile fragmentation depend exponentially on the mass number[207]. Parametrizations of the cross sections, such as the EPAX ones[208], are used when preparing RIB experiments. As a general feature, more neutron-rich projectiles, such as ^{238}U, tend to populate neutron-rich nuclei, whereas neutron-deficient projectiles are employed to access $N \approx Z$ neutron-deficient nuclei.

Inverse kinematics is customarily used at RIB facilities in order to profit from a larger kinematical focusing of the reaction products that improves the detection

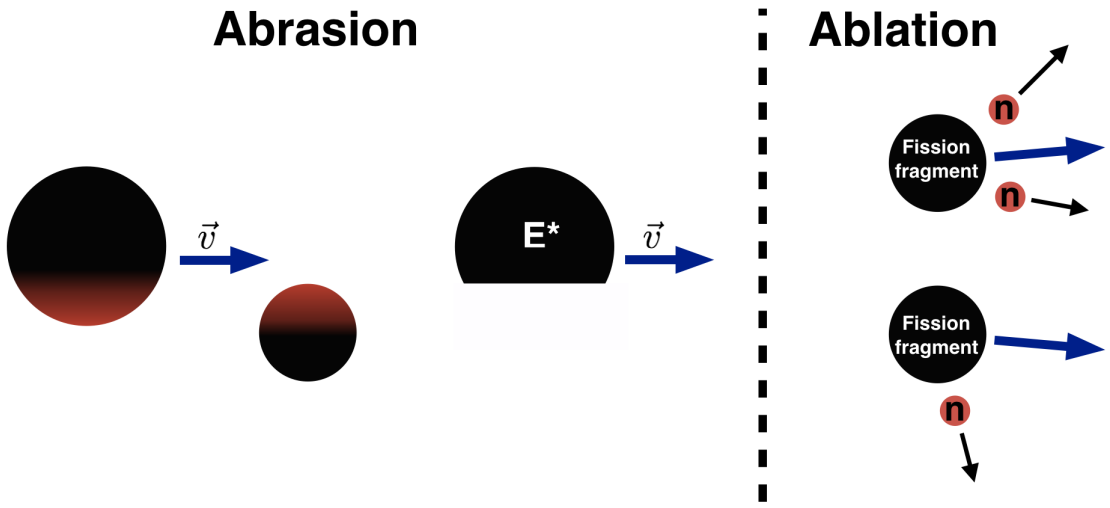

Figure 9.1: Illustration of a projectile fragmentation reaction in the laboratory frame according to the abrasion-ablation model.

efficiency of the fragments and avoids the need of reaccelerating them. The fragments are headed into an in-flight separator, which is a magnetic spectrometer that allows the individual identification of the isotopes composing the cocktail beam. The working principle of these devices is based on the bending of the ion trajectory as it traverses the magnets. The "resistance" to the bending is quantified in terms of the product of the magnetic field and the radius of the trajectory, the so-called magnetic rigidity:

$$B\rho = \frac{p}{Q} = \frac{\gamma m v}{Q} \tag{9.1}$$

It is possible to determine the experimental $B\rho$ and, since the fragments composing the cocktail beam share virtually the same initial velocity, it already provides a crude A/Q separation. This quantity, however, does not uniquely identify a species so that additional beam line detectors are used to resolve the ambiguity by measuring e.g. the total kinetic energy. It is then common to deliver the tagged RIB to a secondary target and use a selective reaction mechanism such as nucleon removal to conduct the spectroscopy of the nuclei of interest.

In this experiment, fragmentation was induced on a primary ^{78}Kr beam impinging on a natural Be target and the cocktail beam was directed onto a 6-mm thick secondary Be target. The experiment was conducted at the Radioactive Isotope Beam Factory (RIBF) in the laboratory of RIKEN[209, 210] (Tokyo, Japan). The production of the secondary beam is introduced in section 9.1. The detectors for beam tagging and the identification of the knockout products are described in section 9.2. These products are correlated with the γ rays measured in DALI2+, a scintillator array described in section 9.3.

9.1 Beam production at the RIBF

The ^{78}Kr primary beam is produced in the 28-GHz superconducting ECR source and then accelerated in the RILAC2 (RIKEN heavy-ion Linear Accelerator) injector. The acceleration mode used in the experiment involves a chain of 4 cyclotrons and 2 charge strippers[211]. The first three cyclotrons compensate energy losses in the strippers before injection of fully stripped ions in the last cyclotron, a K 2600-MeV superconducting ring cyclotron which is well known for its large bending power: it receives ions with energies up to 127 $^{\mathrm{MeV}}/_{\mathrm{u}}$ and delivers the primary beam with an energy of 345 $^{\mathrm{MeV}}/_{\mathrm{u}}$. The ions are then directed to the production target at the entrance of the BigRIPS separator at a beam intensity of 300 pnA. Figure 9.2 shows a scheme of the primary beam production.

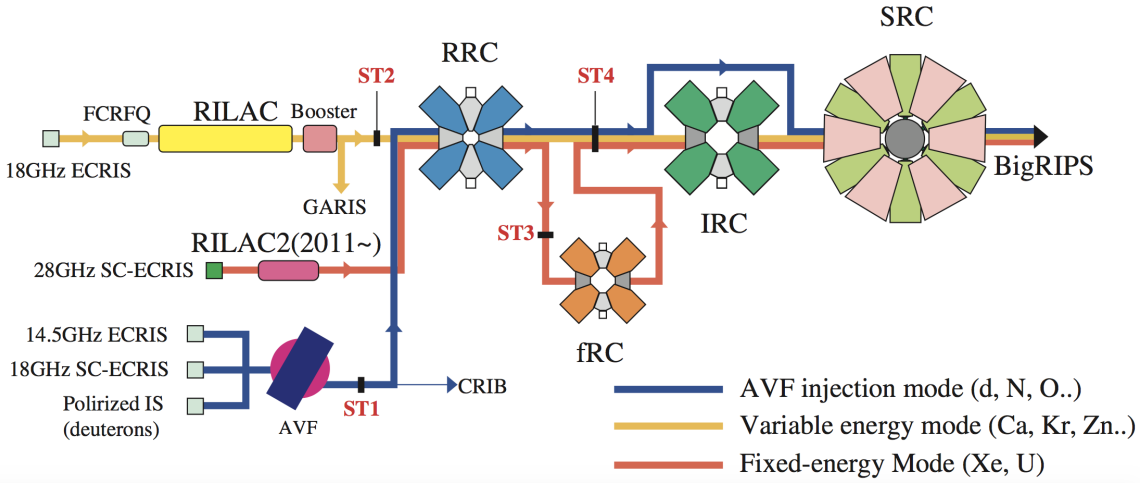

Figure 9.2: Scheme of the three modes used for primary beam production at the RIBF. The fixed energy mode was used in the experiment to produce a ^{78}Kr primary beam. Image taken from [211].

9.2 Beam tagging at the RIBF

9.2.1 BigRIPS spectrometer

BigRIPS[210, 212] is a 78.2-m, two-stage separator with a large acceptance that achieves a collection efficiency superior to 50% for the secondary beam ions, including those emerging from fission that have larger angular and momentum spreads. Its horizontal and vertical angular acceptances are ±40 mrad and ±50 mrad, respectively, and its momentum acceptance is ±3%. This six-bend separator is composed of 14 large-aperture superconducting triplet quadrupoles (STQ) that are responsible for its

large acceptance as well as six dipoles operated at room temperature and located in-between the 7 foci denoted as F1-F7. Among them, F1, F4, F5 and F6 are momentum dispersive whereas F2, F3 are achromatic and F7 is doubly achromatic.

The first stage of the spectrometer is devoted to the purification of the beam and comprises the first 6 STQs and the first 2 dipoles. A beam dump in the first dipole stops the unreacted beam, and an Al achromatic degrader at F1, combined with a system of slits at each focus, serves to purify the beam before its injection into the second stage of the separator, where the complete isotope separation is achieved by the combined analysis of magnetic rigidity and energy loss using the so-called momentum-loss achromat technique through a simultaneous $B\rho$-ΔE-TOF measurement. The beam tracking, timing and energy-loss detectors used for this purpose are described in section 9.2.3. They include two plastic scintillators at F3 and F7, two double PPACS at F3, F5 and F7 and a tilted electrode gas ionization chamber (TEGIC) at F7. The achromatic Al energy degrader at F5 serves to further purify the beam.

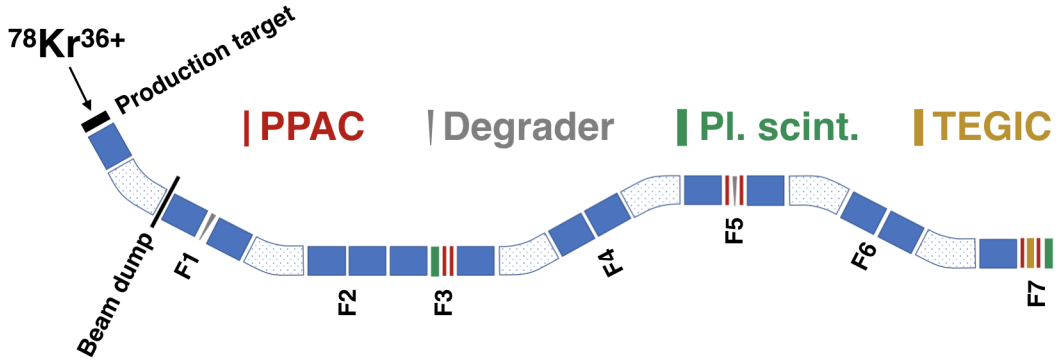

Figure 9.3: Sketch of the BigRIPS separator. STQs and dipoles are represented by the blue and dot-filled magnets. Detectors used for particle identification are indicated in the figure.

9.2.2 ZeroDegree spectrometer

ZeroDegree[210, 212] is a two-bend separator used in combination with BigRIPS to identify the outgoing reaction products behind the secondary target. It has a length of 36.5 m and and is composed of 2 dipoles and 6 STQ with its 4 foci labelled as F8-F11. The magnets composing the spectrometer are designed similarly to those of BigRIPS and the separator also follows the same principle for the isotope separation, namely the $B\rho$-ΔE-TOF method. The entrance of the separator is connected with F7 in BigRIPS through a telescopic section and two STQs. It is at the end of this section where the secondary target was placed surrounded by the DALI2+ array.

The spectrometer is able to work in three different modes with varying degrees of angular acceptances. The large acceptance achromatic mode is the standard mode and was used in this work. It maximizes the angular acceptances hence minimizing the momentum dispersion. In this mode, the angular acceptances are ±45 mrad and ±30 mrad in the horizontal and vertical directions, respectively. The momentum acceptance is ±3%. The intermediate foci F9 and F10 are momentum dispersive whereas F11 is fully achromatic. A couple of plastic scintillators at F8 and F11, three sets of double PPACS at F8, F9 and F11 and a TEGIC placed at F11 are the beam line detectors used for the particle identification in the spectrometer.

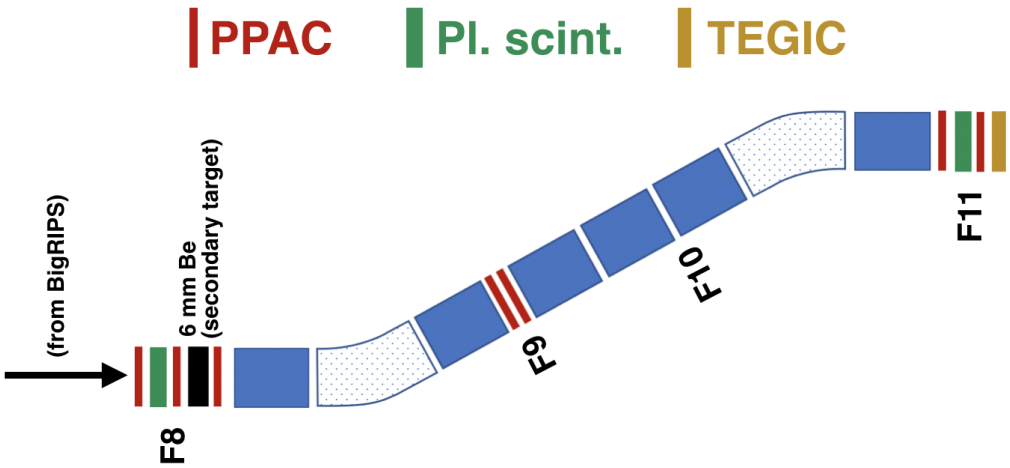

Figure 9.4: Sketch of the ZeroDegree separator. STQs and dipoles are represented by the blue and dot-filled magnets. Detectors for particle identification are indicated in the figure.

9.2.3 Beam line detectors

Plastic scintillators

The time of flight of every beam ion is measured as the difference between the start and stop signals of the two scintillators in the separator. The ion velocity needed for a refined A/Q and Z determination is deduced using the known path length between the two detectors and taking into account the energy loss in the F5 degrader when performing the particle identification in BigRIPS.

Each scintillator has two photomultiplier tubes (PMT) attached to its horizontal edges. A twofold information is extracted from each PMT: the collected charge, provided by a charge-to-digital converter (QDC), and the timing of the particle deduced by a multi-hit TDC (mh-TDC) using a leading-edge algorithm on the PMT signal. The mh-TDC module stores the TDC values within a certain time window so that the

efficiency of the identification is enhanced in those situations dealing with higher rates downstream the separator as long as all the timing signals along the spectrometer are properly correlated (more on this in the next chapter).

The twofold signals are used to improve the timing and charge resolution by deducing position-independent values. The charge collected in either PMT relates to the horizontal position via[213]

$$Q_L(x) = Q_{\text{tot}} \exp\left(-\frac{L/2 + x}{\lambda}\right) \tag{9.2}$$

$$Q_R(x) = Q_{\text{tot}} \exp\left(-\frac{L/2 - x}{\lambda}\right) \tag{9.3}$$

In the above formulae L is the horizontal distance between the two PMTs and λ is the attenuation length of light in the detector. Hence, the product $Q_L Q_R$ is proportional to the charge released in the plastic regardless of the incoming species. Similarly, the difference between left and right TDC values is proportional to x,

$$x = -\frac{V}{2}(t_R - t_L) \tag{9.4}$$

where $V/2$ is the propagation speed of light in the scintillator material. The average of left and right signals provides the position-independent timing of the particle,

$$T_{\text{start/stop}} = \frac{t_L(x) + t_R(x)}{2} \tag{9.5}$$

Selection criteria are often established based on the above correlations in order to reject spurious events and perform a cleaner particle selection[213].

Parallel Plate Avalanche Counters (PPACs)

A measurement of the ion position at each focus enables a precise $B\rho$ determination by reconstructing the ion path through the spectrometer. This is accomplished using Parallel Plate Avalanche Counters (PPACs)[214, 215], a proportional counter able to provide the (X, Y) coordinates of the entry point in the detector using the timing properties of the charge collection process.

As shown in figure 9.5 the detector is composed of an anode inserted between two cathode plates and separated 4.3 mm from them. They are applied a bias voltage of around 700 V and collect the electrons and positive charges generated by the ion along its track. Electrode strips are deposited in the first and second cathode parallel to the X and Y directions, respectively, and preserving an inter-strip spacing of 0.15 mm. Each of these strips is a 300-Å thick, 2.4-mm wide aluminum film deposited onto a

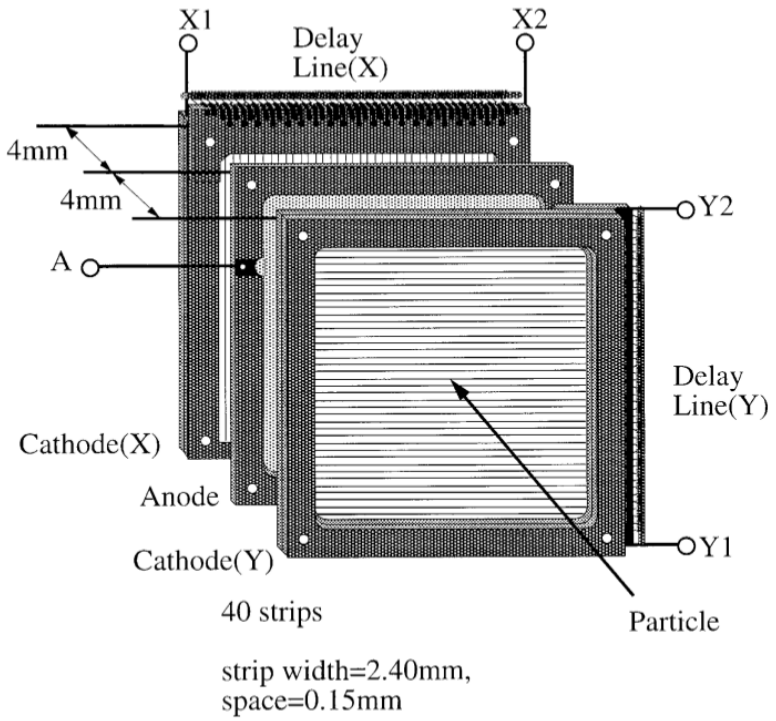

Figure 9.5: Illustration of the delay-line PPAC detector showing the electrode setup. Picture taken from [214].

thin polyester layer that is pasted onto a frame board. The total active area of the used PPACs is 240x150 mm.

The operation of the PPACs used in the RIBF follows the delay-line readout method, in which the position is determined from the time difference between the signals on the cathode ends measured by a TDC,

$$x = k_x(T_{x1} - T_{x2}) + x_{\text{offs}} \tag{9.6}$$

$$y = k_y(T_{y1} - T_{y2}) + y_{\text{offs}} \tag{9.7}$$

Furthermore, the sum of delay times is a constant value regardless of the incident position,

$$T_{\text{sum},X(Y)} = T_{X(Y)1} + T_{X(Y)2} \equiv \text{constant} \tag{9.8}$$

and this feature is often used to remove spurious events ascribed to pile up or δ-ray generation.

At the RIBF, two delay-line PPACs are sealed within a single container filled with a C_3F_8 gas. This double PPAC system is specially designed to enhance the efficiency and deal with higher beam rates, since it is possible to determine the position using a single PPAC in case of a faulty event in one of them.

Tilted electrode gas ionization chamber (TEGIC)

The atomic number of the beam ions is deduced from its partial energy loss in the TEGIC[216] according to the Bethe formula,

$$\frac{\mathrm{d}E}{\mathrm{d}x} = \frac{4\pi e^4 Z_p^2}{m_e v^2} N_t Z_t \left[\ln\left(\frac{2m_e v^2}{I}\right) - \ln\left(1-\beta^2\right) - \beta^2 \right] \tag{9.9}$$

which is used for deducing the atomic number of the projetcile, Z_p, from its measured velocity.

The ΔE detectors used at the RIBF are specially designed to bear high counting rates. The TEGIC overcomes some of the common limitations of gridded MUSICs[217] by using a grid-less design that suppresses position-dependent delay times in the anode pulses. The entry windows of the Al housing are made of 50- µm thick Kapton foils and the detector is composed of an alternating structure of 12 anodes and 13 cathodes separated by 20 mm and made of 4- µm thick mylar on each side, composing a system of virtually 6 ionization chambers filled with Ar-CF_4 gas which is represented in figure 9.6. The electrodes are tilted 30° and this arrangement results in a more efficient charge collection with little chance of charge recombination during the drift of the charge carriers. Pairs of consecutive anodes are electrically connected together and their signals are summed, whereas all the cathodes are grounded together.

The drop in the electrostatic potential of the anodes induced by the charge carriers as they drift is what provides the information on ΔE. The anode pulses are amplified

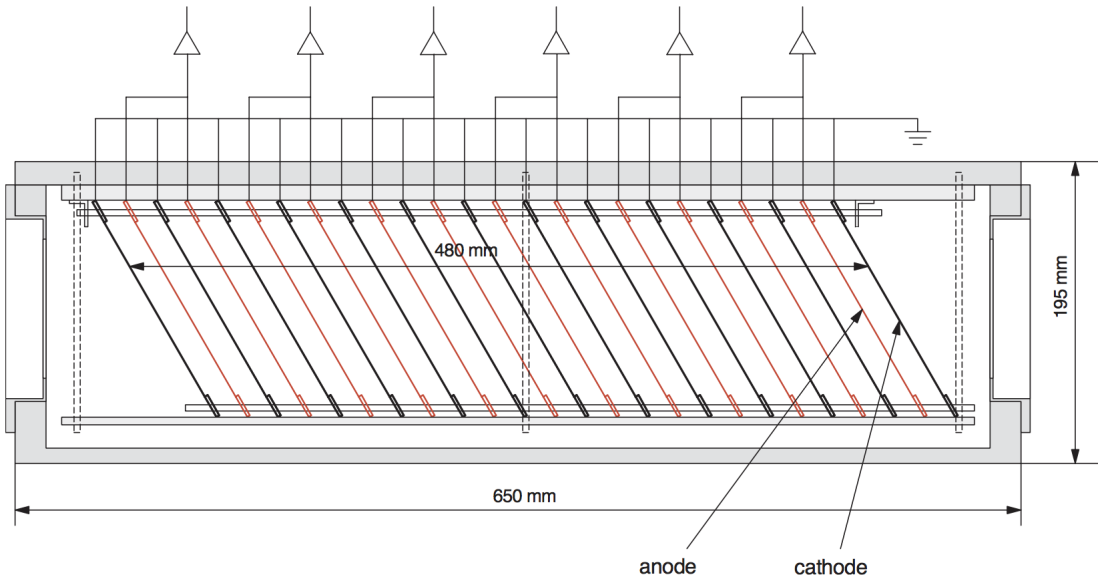

Figure 9.6: Schematic view of the tilted electrode gas ionization chamber. Image taken from [216].

by charge-sensitive preamplifiers and digitized by a QDC that provides a quantity proportional to the energy loss.

The ΔE value of the ion is calculated as the geometric average of the six signals of the anodes,

$$\Delta E = \sqrt[6]{\prod_{i=1}^{6} \Delta E_{\text{anode i}}} \tag{9.10}$$

where the above average provides a better ΔE resolution than the arithmetic one.

9.3 DALI2+

The detector array for low-intensity γ-rays [218, 219], DALI2+, is a γ-ray spectrometer used for detecting the deexciting radiation from the reaction products produced in the secondary target. At the time of the experiment, the array accommodated 226 NaI(Tl) scintillator crystals arranged in 10 layers perpendicular to the beam direction and encapsulated in a 1-mm thick aluminum housing. The first nine layers are composed of 10-17 crystals whereas the most forward layer contains 64 detectors. The crystals of each layer are attached onto aluminum plates allowing the adjustment of the geometry to the experimental purposes. The spectrometer is characterized by its high efficiency as well as its high granularity. The former is a prerequisite in low-intensity RIB experiments whereas the latter aims at minimizing the uncertainty in the γ-ray emission direction which is required for correcting the Doppler shift in the γ-ray energy. The array is composed of three types of crystals provided by three different manufacturers: $80 \times 45 \times 160\,\text{mm}^3$ (88 crystals provided by Saint-Gobain), $80 \times 40 \times 160\,\text{mm}^3$ (50 crystals provided by Scionix) and $61 \times 61 \times 122\,\text{mm}^3$ (88 crystals provided by Bicron).

The detectors composing the first 9 layers are arranged with their widest side facing the beam direction. The layout of the forward wall is intended to provide a larger solid-angle coverage compensating the focusing of the γ-ray emission probability towards forward angles as well as an enhanced efficiency for the add-back, the procedure of adding the energy depositions among neighboring crystals of a single Compton-scattered γ ray in order to recover its full energy, where the latter is more important at the highest Doppler-shifted energies.

The energy resolution after Doppler correction is the result of three contributions: the angular aperture of the crystals, the spread in the beam velocity behind the target and the intrinsic energy resolution. These contributions depend on the polar angle of the γ ray emitted in flight and the beam velocity, where each individual contribution to the energy resolution is represented in figure 9.8 for 1.0 MeV γ-rays.

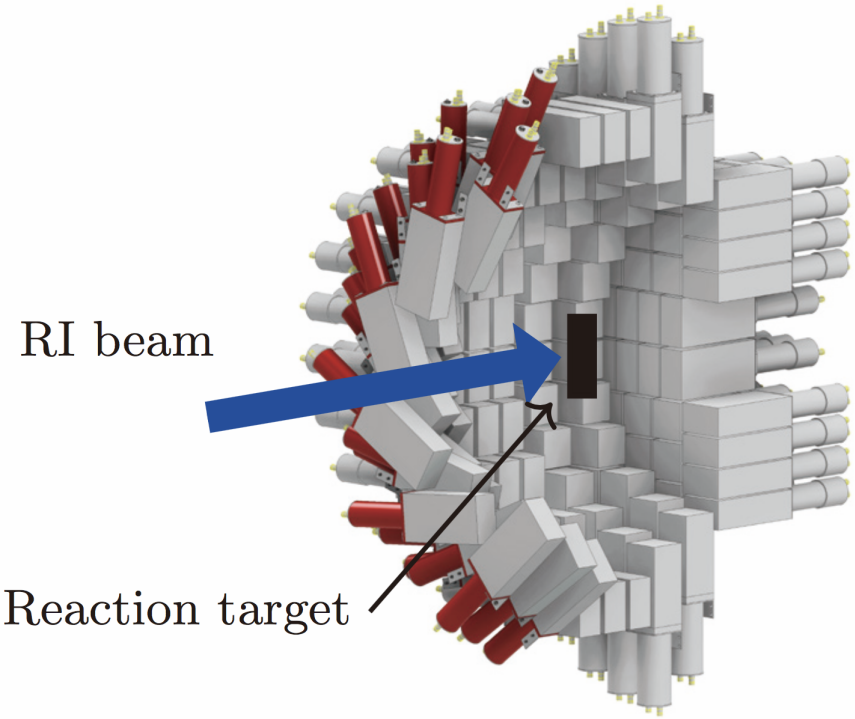

Figure 9.7: Side view of the DALI2+ array. Only a portion of the total number of crystals on each layer is shown. Source: [219].

The secondary target was placed in the plane of the fifth layer. The range of polar angles covered by the array was from 20° to 140° for γ rays emitted within the target. The target frame was located inside the 5-mm thick beam pipe with an inner radius of 70 mm. The beam pipe was enclosed by two shields made of Pb and Sn of 1 mm each. They were included in order to remove the rates of X-rays originating from by atomic processes such as electron capture and the stopping of highly-energetic secondary electrons either within the target or in the surrounding passive elements.

A time and energy value is extracted from the shaped PMT signals using a CAEN V785 ADC and a CAEN V1190A TDC with the CFD timing of the shaped signal as input. In order to construct the DALI2+ trigger, a logic OR signal of all the CFD outputs is made.

The photopeak efficiency of the array in the present experiment was 20(1)% at 662 keV (10.3(5)% at 1836 keV) for γ rays emitted at rest, and an energy resolution of 10% was attained at 662 keV (6% at 1836 keV). Intensity measurements of γ rays emitted in flight must take into account all the geometrical effects and the Lorentz boost by means of a Monte Carlo simulation as detailed in section 10.3. The agreement between simulated and experimental efficiencies deduced from the calibration sources is within 5%.

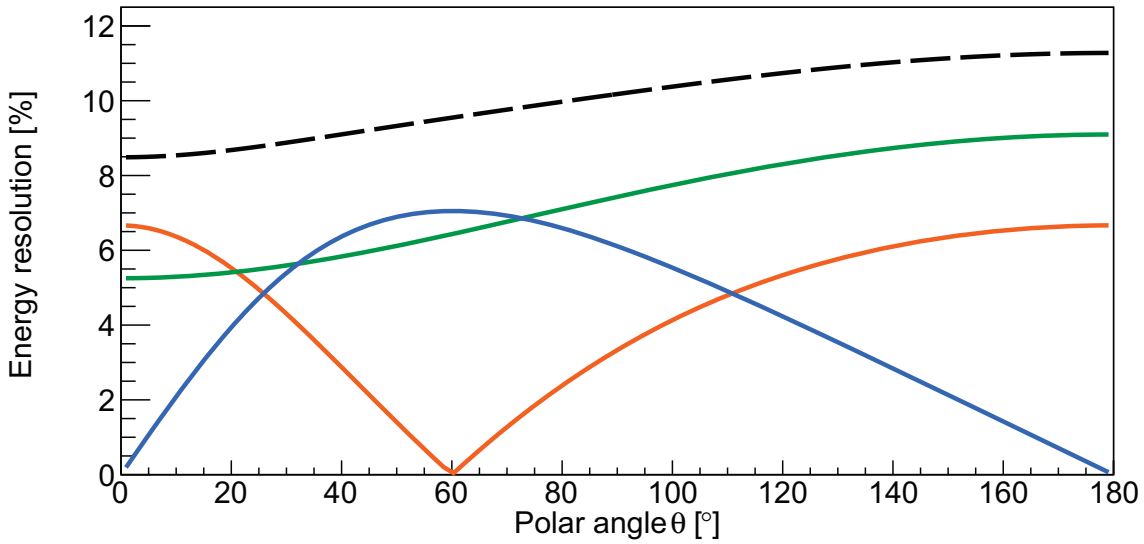

Figure 9.8: Illustration of the energy resolution after Doppler correction for 1 MeV γ rays in DALI2+, as a function of their polar angle. The position resolution of the crystals, the spread of the beam velocity and the intrinsic energy resolution yield Doppler broadenings represented by the blue, orange and green curves. Their joint effect is given by the black dashed line. An angular resolution of 6°, a spread of 10% in the velocity and a dependence of the intrinsic energy resolution given by $2.3\sqrt{E_\gamma(\mathrm{keV})}\,\mathrm{keV}$ is assumed.

9.4 Data acquisition and measurement conditions

The RIBF operates a data acquisition system[220] which is characterized by its versatility and its capacity to process high data throughputs reaching values as large as 40 $^{\mathrm{MB}}/_{\mathrm{s}}$. It handles the parallel processing of the data from all the front-end computers (FECs) reading the VME and CAMAC modules. Data from the different FECs are combined using a hierarchical event-building system online where each FEC works as a "sub-DAQ", acting as a slave event builder whose data is eventually merged with the other DAQ branches by a master event builder. All computers share the same data storage system located on a storage area network.

The DAQ works using a common trigger logic handled by a general trigger operator module. Data acquisition is blocked until all the end-of-busy signals have been received by the GTO, hence the FEC with the longest dead time determines the dead time of the entire system. The dead time of the beam line detectors is longer than that of DALI2+ and they determine the dead time of the DAQ (around 200 µs).

The DAQ load is alleviated by virtue of writing to disk only those events that can be used either for γ-ray spectroscopy or the determination of inclusive cross sections. The complete separation of the incoming beam in BigRIPS and the outgoing reaction products in ZeroDegree is required in the former purpose, thus useful events include

signals in the F7 and F11 plastics. Beam events without a coincident γ ray in DALI2+ are only used for cross section determination, and reasonable levels of dead time are attained in those cases by sending the F7 signal to a rate divider. A downscale factor establishing the proportion of used F7 events is set in this module. This provides the downscaled F7 trigger -F7(DS)-, that used a downscale factor of 15 in this work. The trigger condition giving rise to every event is recorded in the data using a binary flag called *fbit*.

The common triggers used in the data analysis are listed below:

- F7(DS): fbit equals 1.
- F7(DS) and F11: fbit equals 3.
- F7 and F11 and DALI2+: fbit equals 6.
- F7(DS) and F11 and DALI2+: fbit equals 7.

Chapter 10

Data analysis

In the preceding chapter, the details of the in-flight separation technique used for particle separation and identification combined with γ-ray detection using the DALI2+ array were introduced. This chapter is focused on the optimization of the particle identification and the determination of transition energies. The corrections and background reduction conditions imposed in the particle identification are presented in section 10.1. The presorting of DALI2+ data is the subject of section 10.2. The correction of the Doppler shift and the fitting technique used for extracting information from the experimental γ-ray spectrum are presented in sections 10.3, 10.4, 10.5 and 10.6. The inclusive cross section for neutron removal from ^{57}Zn is extracted in section 10.7.

10.1 Particle identification

The particle identification in BigRIPS by means of the $B\rho$-ΔE-TOF method takes into account the presence of the degrader at F5 which introduces a significant change in the β. The $B\rho$ is calculated separately before and after the Al wedge,

$$\left(\frac{A}{Q}\right)_{3-5} = \frac{c}{m_u}\frac{B\rho_{3-5}}{\gamma_{3-5}\beta_{3-5}} \tag{10.1}$$

$$\left(\frac{A}{Q}\right)_{5-7} = \frac{c}{m_u}\frac{B\rho_{5-7}}{\gamma_{5-7}\beta_{5-7}} \tag{10.2}$$

In the above equations the subscripts 35 and 57 refer to the quantities between the F3-F5 and F5-F7 focal planes. The corresponding $B\rho$ values at every stage are deduced from the position measured by the PPACs. The time of flight between the plastics at F3 and F7 links the ion velocities in the two stages of the separator,

$$\mathrm{TOF}_{37} = \frac{L_{3-5}}{\beta_{3-5}c} + \frac{L_{5-7}}{\beta_{5-7}c} \tag{10.3}$$

All the above equations can be solved for β_{3-5}, β_{5-7} and $\frac{A}{Q}$ on an event-by-event basis provided that the charge state of the ion remains unchanged after the degrader. This condition yields the additional equation

$$\frac{\gamma_{3-5}\beta_{3-5}}{\gamma_{5-7}\beta_{5-7}} = \frac{B\rho_{3-5}}{B\rho_{5-7}} \tag{10.4}$$

Once β_{5-7} has been obtained, its value is used to deduce the atomic number from the energy deposition in the TEGIC at F7 according to the Bethe formula -eq. (9.9)- which is solved for Z:

$$Z = C_1\beta_{5-7}\sqrt{\frac{\Delta E}{\ln\frac{2m_ec^2\beta_{5-7}^2}{I} - \ln\left(1-\beta_{5-7}^2\right) - \beta_{5-7}^2}} + C_2 \tag{10.5}$$

where C_1 and C_2 depend on the density of the gas, the thickness of the ionization chamber as well as the atomic number and the mass number of the counter gas. In the practice both coefficients are determined by calibration using known species in order to obtain absolute Z values.

10.1.1 A/Q reconstruction

Timing of the beam

The timing of the ion in the plastic scintillators was calculated by averaging the time signals from the right and left photomultipliers (cf. section 9.2.3). Then the physical time of flight was obtained after adding an offset to the time difference between the two plastics in order to compensate for the delays induced by the electronics:

$$\mathrm{TOF}_{3-7} = \mathrm{T}_7 - \mathrm{T}_3 + \mathrm{T}_{\mathrm{offs},3-7} \tag{10.6}$$

$$\mathrm{TOF}_{8-11} = \mathrm{T}_{11} - \mathrm{T}_8 + \mathrm{T}_{\mathrm{offs},8-11} \tag{10.7}$$

$\mathrm{T}_{\mathrm{offs},3-7}$ was adjusted according to the identification performed by the BigRIPS staff using the isomer tagging method[221] and $\mathrm{T}_{\mathrm{offs},8-11}$ is determined by selecting the same isotope in ZeroDegree and BigRIPS once the identification in the latter has been performed. The obtained offsets are $\mathrm{T}_{\mathrm{offs},3-7} = 295.7$ ns and $\mathrm{T}_{\mathrm{offs},8-11} = -134.5$ ns.

Since the rates at F3 are high, the Multihit TDC yields multiplicities larger than one in many cases. In order to calculate the proper start time for the TOF the diagonal cuts shown in red in figures 10.1(a) and 10.1(b) for the F3 and F7 plastics were used to select the left and right time signals of the same particle and remove unwanted background from the identification plots. An event is not included in the analysis should more than one left or right timing value satisfy the above cuts, since the ambiguity in the velocity can not be resolved. Moreover, only events displaying TDC

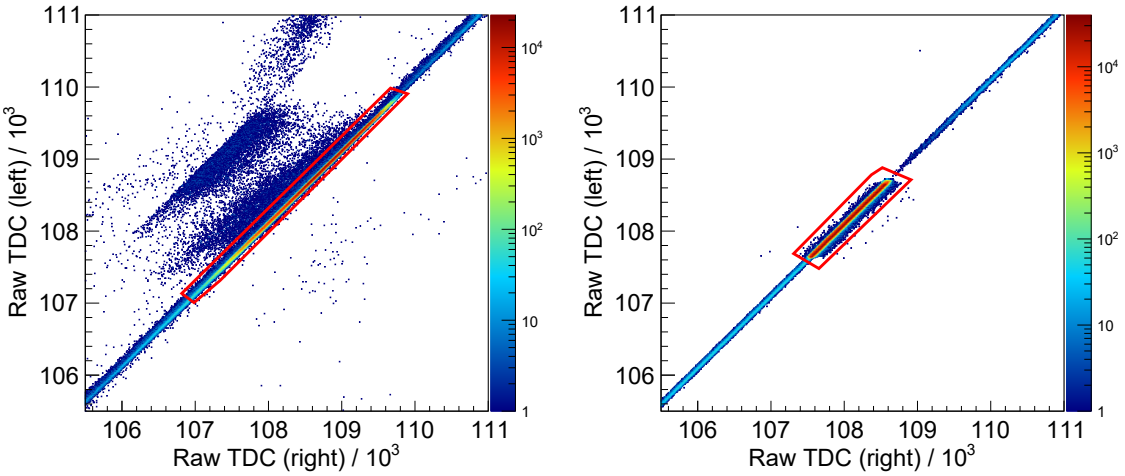

(a) $t_L - t_R$ matrix for F3 plastic

(b) $t_L - t_R$ matrix for F7 plastic

Figure 10.1: Correlation plots used for selecting events with consistent timing in BigRIPS. The selected events are marked in red.

multiplicities smaller than 4 were accepted in the analysis for a cleaner identification. Figure 10.2 illustrates the reduction of the background in the A/Q spectrum from events with more than one hit in the F3 plastic after applying all the above selections.

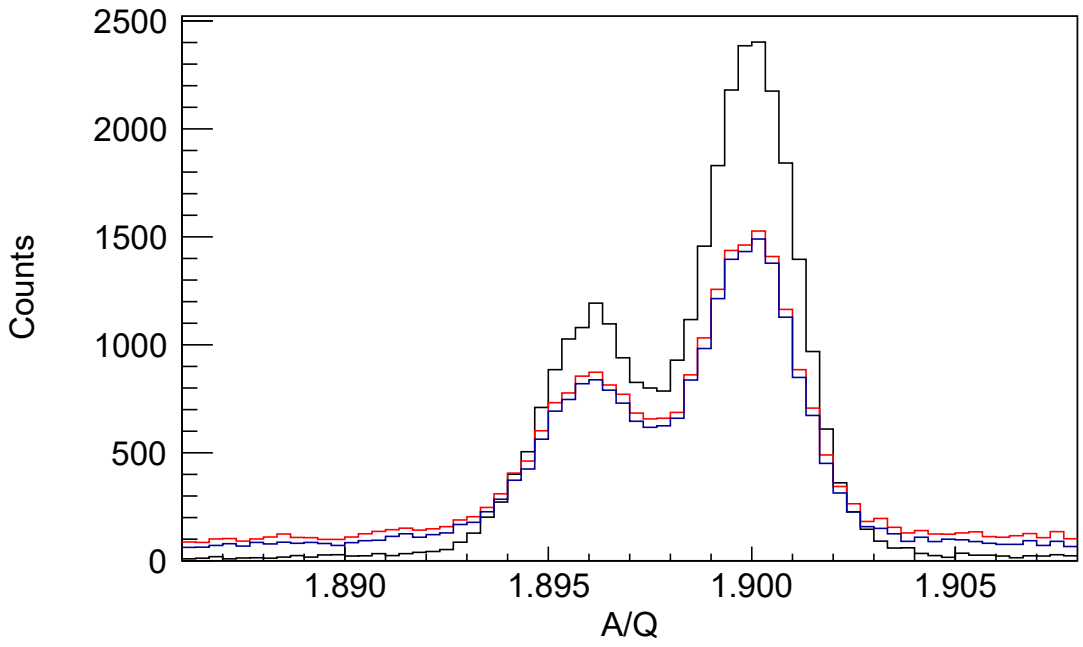

Figure 10.2: A/Q distributions for multi-hit TDC multiplicity equal to 1 -in black- and for multiplicities larger than 1 before (red) and after (blue) applying the background-reducing conditions discussed in the text.

$B\rho$ determination

The relation between the horizontal positions and the relative deviation δ from the central $B\rho$ value, $\delta = (B\rho - B\rho_0)/B\rho_0$, is given in the simplest case by an optical transformation linking the position x_d in the momentum dispersive focus with the position x_a in the achromatic one and δ,

$$x_d = M\, x_a + D\, \delta \tag{10.8}$$

where M and D are the magnification and the momentum dispersion, respectively. This equation is solved for the δ in BigRIPS between the F3-F5 stage and the F5-F7 stage thus allowing an independent determination of the two $B\rho$ values. The small energy loss in the F9 PPACs yields virtually identical $B\rho$ values before and after F9 in ZeroDegree so that it is possible to perform the identification using only the position information of either F8-F9 or F9-F11. For the identification in BigRIPS, however, the beam has to be tracked through the whole separator.

PPAC events having less than two cathodes with a valid signal can not be used for the determination of the $B\rho$ since knowledge of the angle is required to extrapolate the position of the isotope at the focus. 6% of the events have PPAC multiplicity less than 2 in F3, whereas for the F5 and F7 PPACS these events amount to 5% and 0.8% of the total events. This drop in PPAC efficiency in the first stages of the separator is caused by the higher beam rates before the additional momentum selection in the upstream dipoles. It is the main limiting factor for the efficiency of the particle identification in BigRIPS. Although using the position information between the 5-7 and 7-8 stages as well as the TOF_{7-8} it is certainly possible to perform the tracking of the beam before the secondary target, this approach demands substantial changes in the software processing the raw data written by the DAQ which are beyond the scope of this work. Hence a simpler approach was followed instead based on the proportionality between the position of the ion impinging on the plastic and the timing of photomultipliers -cf. eq. (9.4)-. The correlation between the positions in the F3 focus and the right-left time differences in the plastic is shown in figure 10.3(a) where the observed offset in the distribution stems from the shift of the plastic scintillator with respect to the position of the F3 focus. Those events outside the red region were considered as background and were rejected. Events in which less than 2 PPACs yielded position information in F3 were assigned a position using the slope and offset according to the dashed line shown in the figure. The obtained A/Q distributions are represented in figure 10.3(b) and 6% more statistics was recovered in the region of interest. The A/Q resolution for these events is $\sim$15% worse than for those events with a position deduced from the PPACs but does not significantly impact the overall resolution. It is also evident from

the plot in figure 10.3(b) that higher background levels are introduced when events with low PPAC multiplicity are used. Therefore, additional conditions for cleansing the identification spectra were introduced as described hereafter.

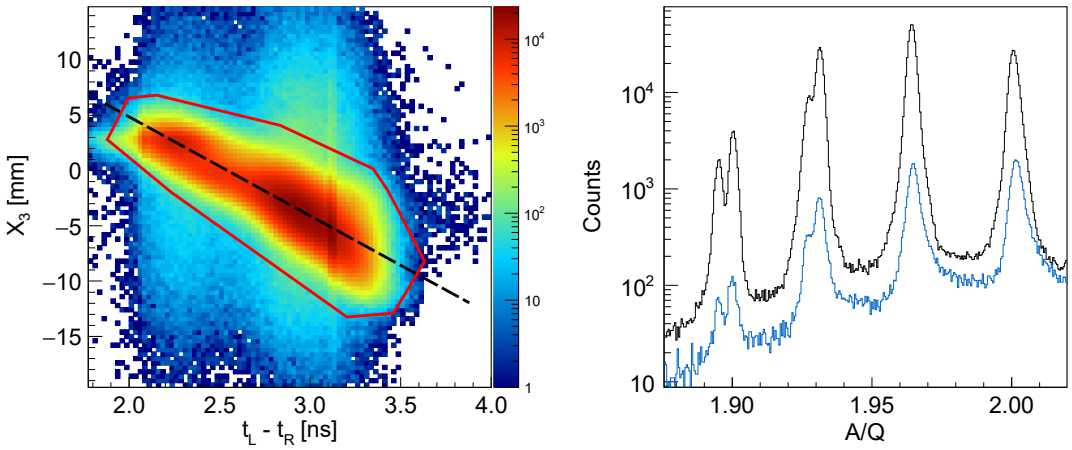

(a) X_3 correlation with $t_L - t_R$ in F3 plastic **(b)** A/Q spectrum (BigRIPS)

Figure 10.3: Illustration of the A/Q reconstruction using the timing difference in the plastic. The figure on the right shows in black the A/Q spectrum obtained using the position information from the PPACs in black. The spectrum in blue corresponds to events with PPAC multiplicities smaller than 2 with the position reconstructed using the timing information in the plastic. The plots do not contain all the collected statistics.

As an example, events with consistent beam trajectories along the separator were selected at this point by imposing the cuts displayed in figure 10.4 in the correlation

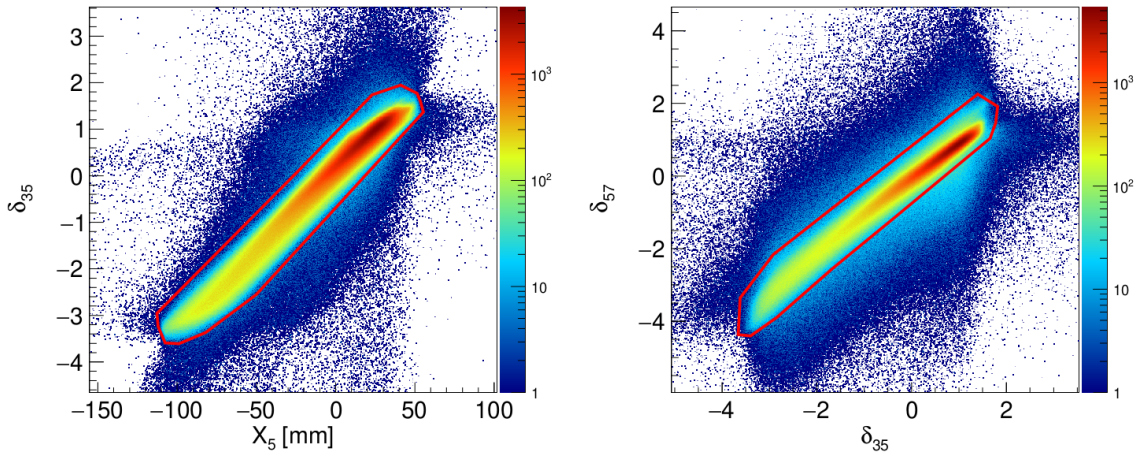

(a) δ_{35} versus horizontal position on F5 **(b)** δ before and after the degrader in F5

Figure 10.4: Correlation plots used for selecting events with consistent trajectories in BigRIPS. The selection is enclosed by the red polygon.

between the position at F5, δ_{35} and δ_{57}.

The reconstructed magnetic rigidity should be independent of the measured positions and angles in the horizontal plane of the foci, otherwise higher order terms can be added to eq. (10.8) in order to compensate for the optical aberrations until a satisfactory resolution in δ is achieved. Although a good separation of the different isotopes was already possible without the need of introducing further terms into eq. (10.8), attaining the optimum resolution in the particle identification helps to identify more clearly the most exotic nuclei that are produced at very low rates as well as to confirm the integrity of the data and the correct performance of the detectors. With this in mind, higher order elements for the optical transformation were extracted following the empirical method proposed in ref. [213]. A dependence of the A/Q on the horizontal position in

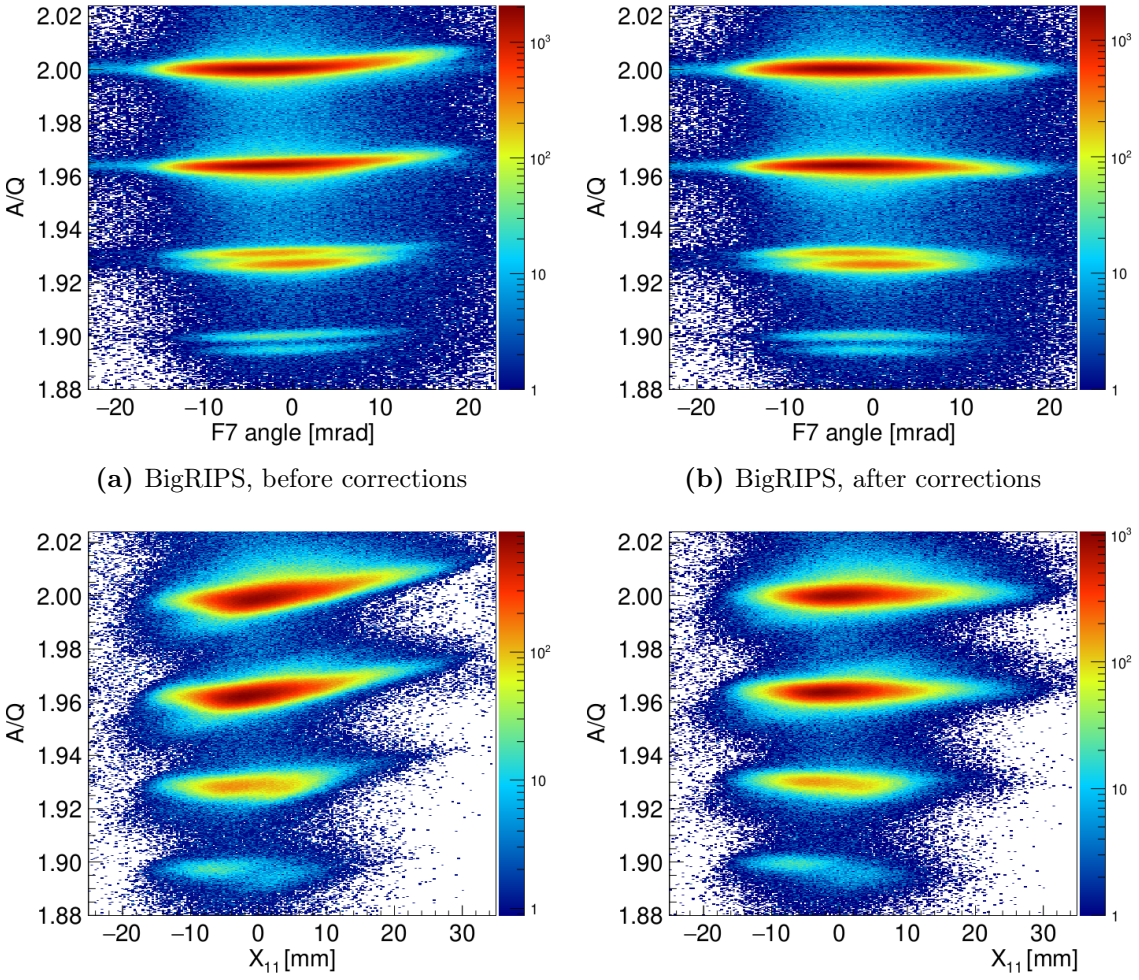

(a) BigRIPS, before corrections

(b) BigRIPS, after corrections

(c) ZeroDegree, before corrections

(d) ZeroDegree after corrections

Figure 10.5: Example of the removal of A/Q dependencies with respect to the horizontal angles and positions in BigRIPS and ZeroDegree introducing higher-order transfer elements.

the F11 focus of ZeroDegree is visible in the plot shown in figure 10.5(c). Therefore, this matrix was projected onto several slices of X_{11} and a second order polynomial was calculated from the maxima of the distributions and substracted in order to remove this artifact. This process is repeated for the other angles and positions, adding the corresponding terms to the polynomial until all the aberrations have been removed. The matrix after the correction is shown in figure 10.5(d). A similar procedure was followed for the calculated A/Q in BigRIPS, where the residual dependency of the A/Q on the F7 horizontal angle is represented in figure 10.5(a) and the matrix of figure 10.5(b) results from removing all the spurious correlations.

The impact of these corrections was stronger in ZeroDegree where a 35% better resolution was achieved. For BigRIPS the improvement was marginal and the resolution was increased by 10% only. The final A/Q resolutions in BigRIPS and ZeroDegree are given at the end of this chapter in table 10.1.

10.1.2 Determination of the atomic number

A calibration of the F7 and F11 TEGICs that provides absolute Z values was performed before the experiment and it was not modified in the course of the analysis. Nevertheless two issues regarding the assignment of the atomic number in ZeroDegree needed to be addressed.

The first one is related to the observed drift of the calibrated energy deposition in the F11 TEGIC when comparing the data taken at different times as it is shown in figure 10.6(a). Such a drift is not observed in the velocity between the F9 and F11 stages so that it was ascribed to a change in the gain that was compensated in the individual data sets of figure 10.6(a). The result of this correction is shown in panel 10.6(b).

Lastly, a residual dependence of Z on the velocity of the incident ion was observed in ZeroDegree. This correlation was removed following the prescription proposed in [222] that consists on first applying a rotation in the $Z-\beta$ space around a specific velocity value, which is denoted as β_{avg}, followed by a recalibration with a slope and offset. The complete correction consists of 4 parameters a, b, c and β_{avg} and is written as:

$$Z_{\text{corrected}} = a(Z_{\text{uncorrected}} + b(\beta - \beta_{\text{avg}})) + c \tag{10.9}$$

The uncorrected Z spectrum is shown in figure 10.6(c) and the removal of the Z-β correlation after applying the above correction is illustrated in figure 10.6(d).

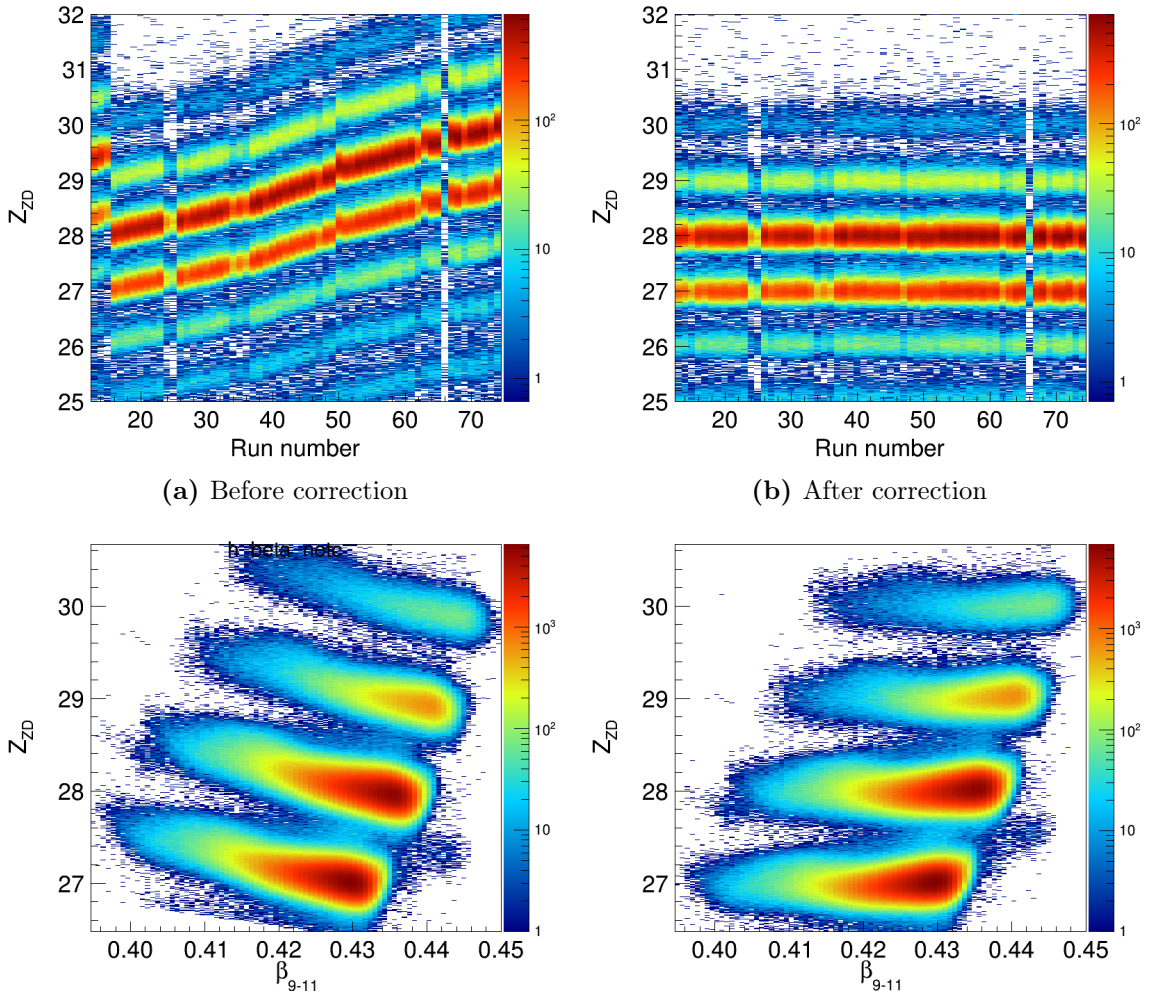

(a) Before correction

(b) After correction

(c) Before correction

(d) After correction

Figure 10.6: The upper row illustrates the cancellation of the gain drift in the F11 MUSIC. Correction of the residual β dependence in the MUSIC is shown in the bottom. The plots were obtained using a gate on the $N = 26$ isotones in ZeroDegree.

10.1.3 Additional cuts for background removal

The cuts for selecting events with consistent information between the time of flight and the tracking of the beam were already introduced in section 10.1.1 on occasion of the special treatment of the multi-hit TDC multiplicities and the PPACs at F3. This section focuses on additional selections constraining the valid signals in the PPACs and in the plastics. In the former, the sum of delay times ocurring on both electrodes of each cathode plate should be independent of the position of the incident ion (cf. sec. 9.2.3). A smaller total delay time occurs should δ-ray generation or multiple ion hits take place, invalidating the calculation of the position and resulting in additional background. Gates were set on the $T_{\mathrm{sum},X(Y)}$ distributions of all the beam line PPAC

cathodes for removing these events. The $T_{\mathrm{sum},X}$ distributions of the 1A and 2A cathodes of the F3 double PPAC system are exemplarily shown in figures 10.7(a) and 10.7(b).

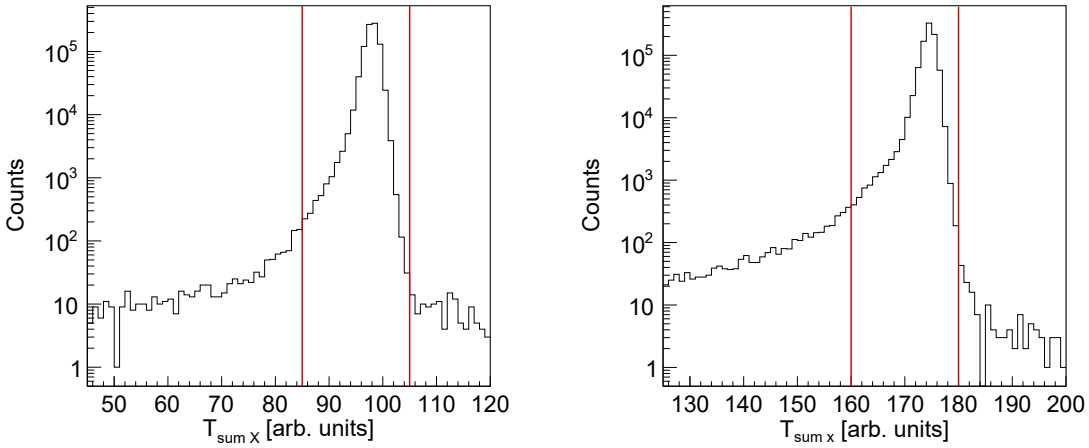

(a) F3PPAC 1A **(b)** F3PPAC 2A

Figure 10.7: $T_{\mathrm{sum},X}$ distributions observed in the first and third cathodes of the F3 PPACS.

An additional selection was applied based on the relation between the position of the incident ion, its timing and the charge-integrated signals obtained from the PMTs. Such a relation is linear between the position and the time difference as given by eq. (9.4) and confirmed in figure 10.3(a). Additionally, the relation between the position of the incident ion and the charge signals on the left and on the right, denoted by Q_L and Q_R, respectively, is written as:

$$x = -\frac{\lambda}{2} \ln\left(\frac{Q_L}{Q_R}\right) \tag{10.10}$$

where λ is the attenuation length of light in the detector. Hence consistent events must display a linear correlation between the timing difference and $\ln \frac{Q_L}{Q_R}$. The corresponding two-dimensional matrices are shown in figures 10.8(a) and 10.8(b) for the plastics in BigRIPS and figures 10.8(c) and 10.8(d) for the plastics in ZeroDegree, confirming the presence of such a correlation in the data. The cuts used for selecting proper events in the plastics are enclosed by the red polygons in the figure.

A binary flag was used for tagging every event in such a way that the cuts used for cleansing the PID in ZeroDegree could be lifted when calculating inclusive cross sections as described in section 10.7. These cuts were, on the other hand, applied when sorting γ-ray spectra.

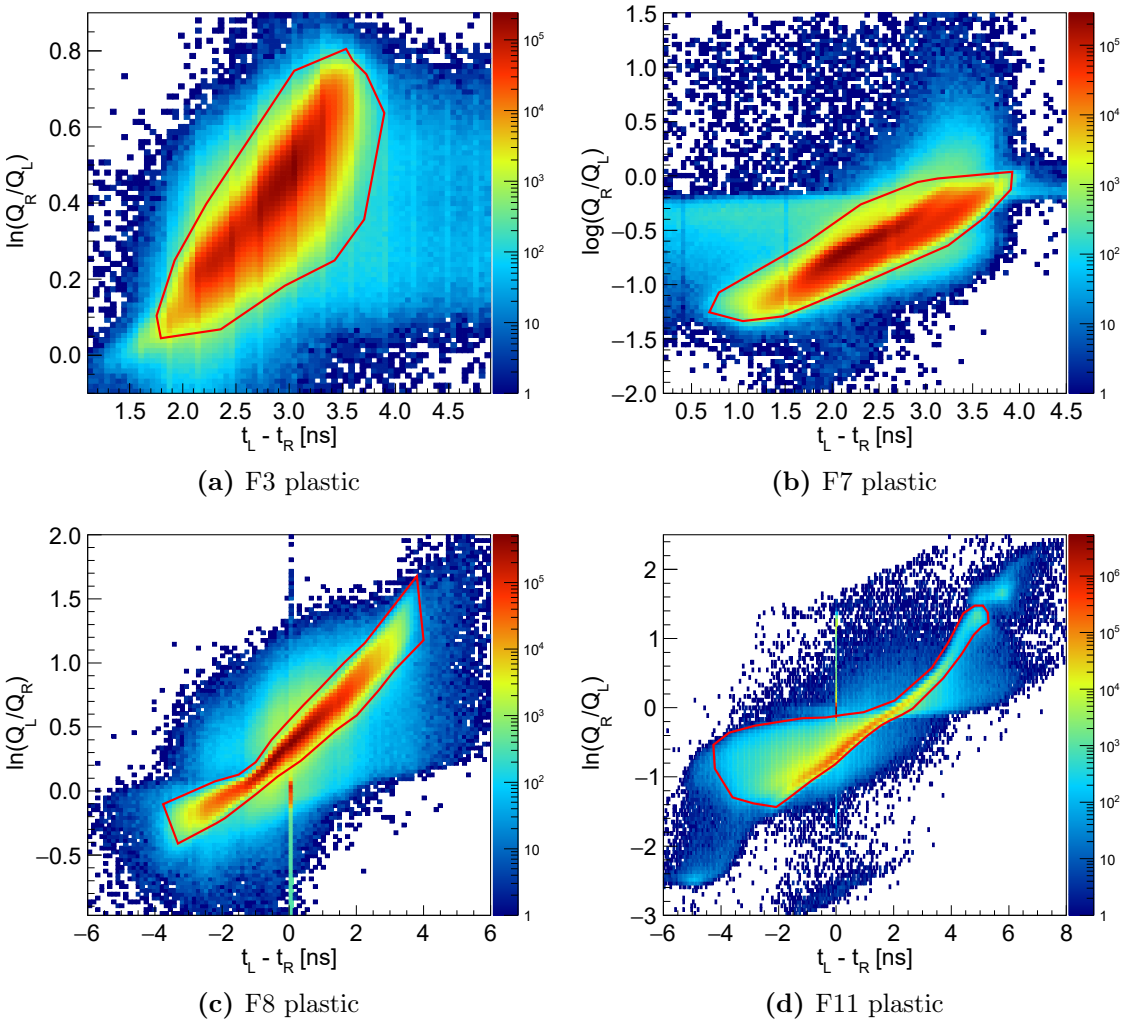

(a) F3 plastic **(b)** F7 plastic

(c) F8 plastic **(d)** F11 plastic

Figure 10.8: Correspondence between the charge and the timing signals at both ends of the plastic detectors. The selections applied in the analysis are marked in red.

10.1.4 Final particle identification plots

A comparison of the PID plots before and after the data treatment described in this section is shown in figures 10.9(a) and 10.9(b) for BigRIPS and figures 10.9(c) and 10.9(d) for the identification in ZeroDegree. The final resolutions are quoted in table 10.1.

	BigRIPS	ZeroDegree
$\sigma(A/Q)$ [%]	0.06	0.09
$\sigma(Z)$ [%]	0.56	0.42

Table 10.1: A/Q and Z resolutions for ^{57}Zn in BigRIPS and ZeroDegree after the corrections described in the text.

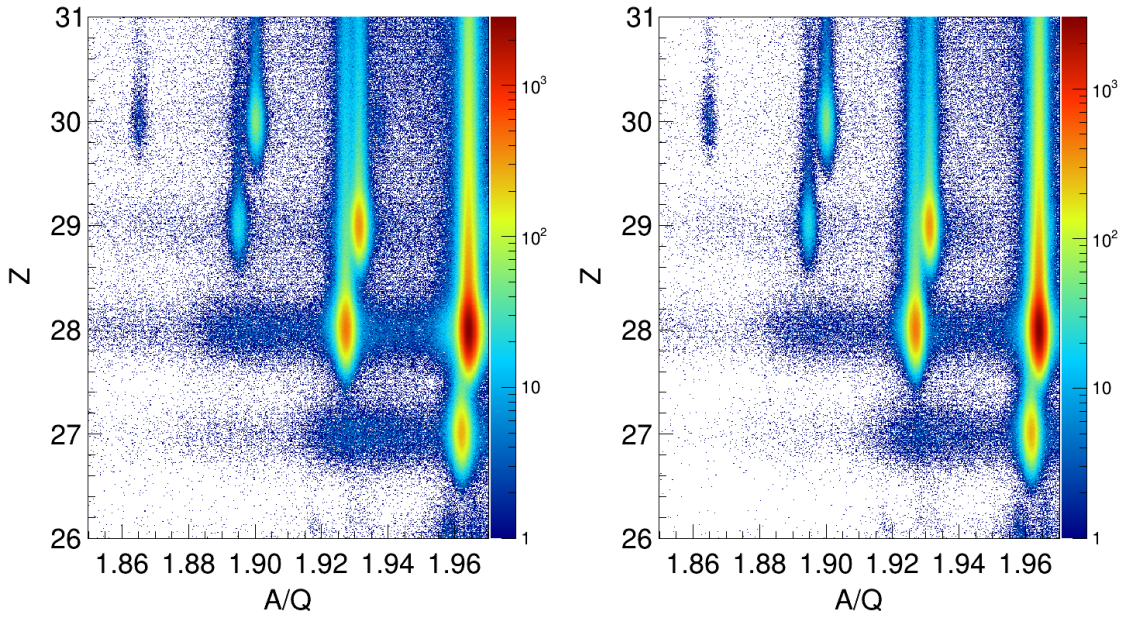

(a) BigRIPS, before corrections

(b) BigRIPS, after corrections

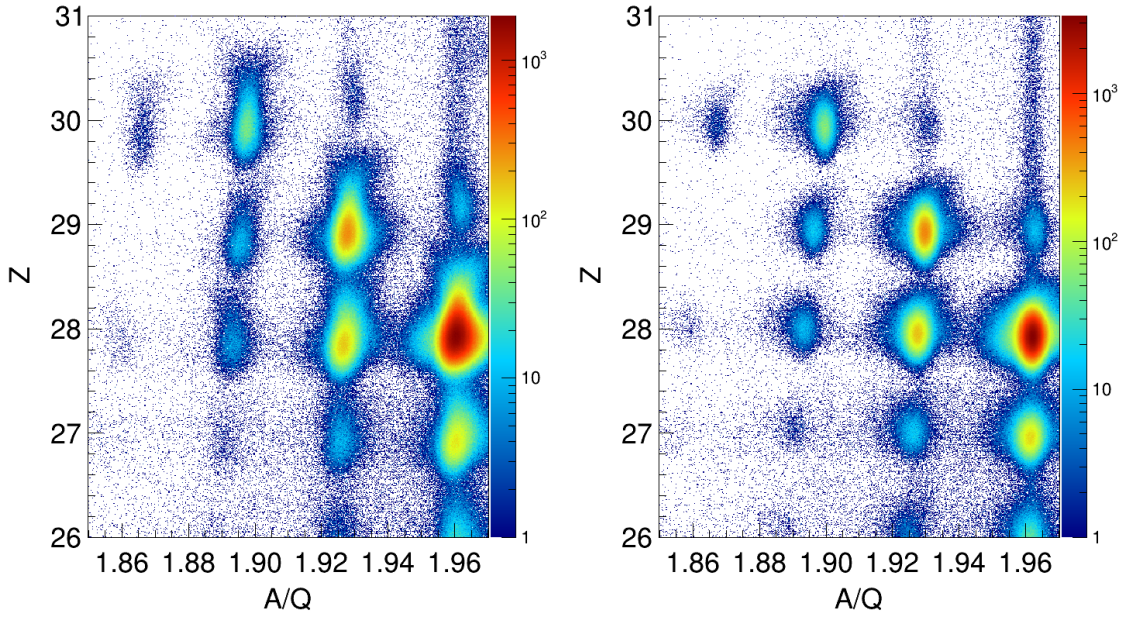

(c) ZeroDegree, before corrections

(d) ZeroDegree, after corrections

Figure 10.9: Comparison of particle identification plots in BigRIPS and ZeroDegree. A partial number of events was used to generate the plots.

10.2 DALI2+ spectrometer

10.2.1 Energy calibration

The crystals composing the DALI2+ array were individually calibrated using ^{88}Y, ^{60}Co and ^{137}Cs sources. The 661.7 keV gamma ray from the ^{137}Cs source, the two coincident gamma rays with energies of 898.0 keV and 1836.1 keV in the gamma-ray spectrum of the ^{88}Y source as well as the 1173.2 keV and 1332.5 keV lines from the ^{60}Co data were used for calibrating the crystals. The position of the photopeaks in the ADC spectrum was obtained from a fit to a model consisting of a gaussian response plus a smooth background below the peak represented by a second order polynomial. The 1373.2 keV and 1332.5 keV photopeaks were simultaneously fitted with the same polynomial background below the doublet. The adequacy of this model was verified using realistic simulations of the γ-ray detection (introduced later on in section 10.3) and adding the experimental spectrum taken without γ source[1] in such a way that the experimental spectrum is well reproduced. Only DALI2+ events firing a single crystal were considered for determining the photopeak positions in order to reduce the intensity of the Compton edge and the Compton background below the peaks.

A first order polynomial reproduced the relation between the peak position in the ADC spectrum and the nominal energy of the transition down to the 661.66 keV γ rays from the ^{137}Cs data without any noticeable deviation ascribed to the well known non-linear energy response of the NaI detectors at low energies[137].

The calibration data for the ^{57}Zn setting was taken at the beginning and after the experiment with an additional measurement conducted through the physical runs and separated by 35 hours from them. The latter measurement was used for extracting the calibration parameters used in the offline analysis which were then applied to the other two source measurements in order to infer the additional systematic uncertainty in the energies and the deterioration of the energy resolution as a result of small changes in the calibration that occurred in the course of the in-beam measurements.

The summed ADC spectrum of the three sources for the midway calibration data is shown in figure 10.10(a) for all the crystals. The observed photopeaks are well aligned to their nominal values after the first order calibration whose result is represented in figure 10.10(b). Crystals at positions 0 and 1 were not operated in the experiment and detectors 112 and 207 were not used in the analysis since the ADC spectrum was compressed into a small number of channels thus requiring much larger gains and offsets for calibrating them.

[1] Stemming from the natural background.

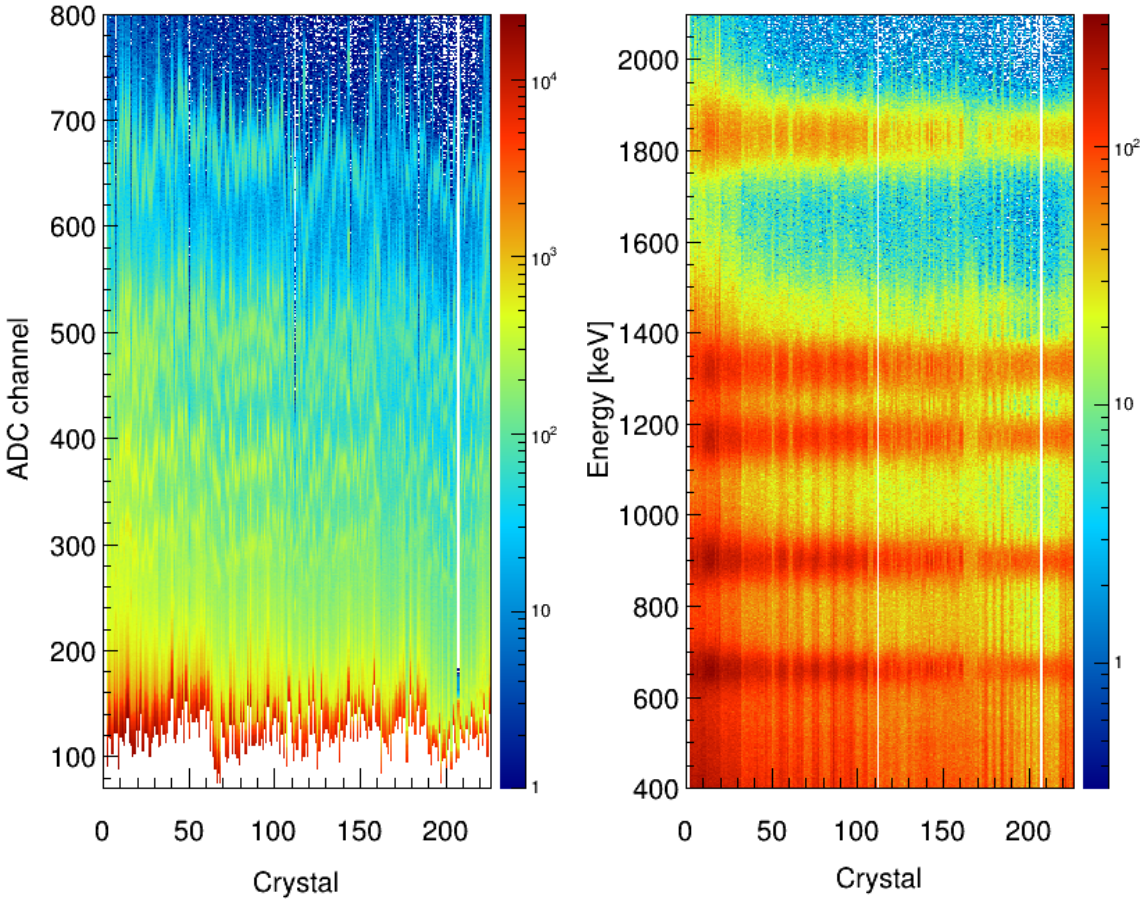

(a) Before calibration

(b) After calibration

Figure 10.10: Comparison between the summed spectrum of the three gamma sources before and after the calibration.

The shift in the 1836 keV photopeak between the calibration data taken at the middle and at the end of the experiment amounts to 0.02% in the summed spectrum of all crystals and to 0.01% only in the 4 most forward DALI2+ layers, whereas its FWHM was preserved to 50.4(1) keV and 46.5(1) keV, respectively. On the other hand, a much larger shift of 7 keV was present in the summed γ-ray spectrum of all DALI2+ layers in the initial calibration data. This drift is stronger in the most forward scintillators: it amounts to 11 keV in the summed spectrum of the 4 most forward layers. Therefore the departure from the original calibration parameters between both calibration data sets had to be corrected and was monitored using the position of the 511 keV annihilation peak. Selecting gamma rays with delays comprised between 10 and 190 ns was required to achieve a reasonable sensitivity in the determination of the photopeak position by reducing the low energy background in prompt coincidence with the isotopes arriving at F8. The physical runs were grouped into 5 sets that

covered data acquired during 6-7 hours of data taking. The summed γ-ray spectra in the group enabled to monitor shifts larger than $\sim 0.05\%$ between consecutive groups for the crystals in layers 7 to 10, which suffered the largest deviations. This precision is in the range of the systematic uncertainty introduced by the calibration itself in the spectra of the individual DALI2+ layers. As a general guideline, specific crystals were not corrected if the shifts between consecutive groups range within their statistical uncertainty, which was the case for all crystals at positions ranging from 0 to 85 since the lower intensity of the line and the worse resolution prevented an accurate extraction of the centroid energy. Moreover, 40% of the crystals in layers 7 to 10 were not corrected following this criterion. Nevertheless their deviations between consecutive calibration measurements were below $\sim$0.06%.

The photopeak position of the 511 keV γ ray was obtained from a fit to a gaussian response plus a polynomial background. A gain factor relative to the data set containing the last in-beam measurements was calculated from the extracted peak positions and was applied for realigning the energies to their unshifted values,

$$E^{\text{group i}}_{\text{corrected}} = E^{\text{group i}}_{\text{uncorrected}} \frac{E^{\text{group 5}}_{511\text{ keV}}}{E^{\text{group i}}_{511\text{ keV}}} \tag{10.11}$$

The determination of the correction is illustrated in figure 10.11 for crystal 199, which suffered the largest shift. The drift of the 511-keV peak position between the first and last group is evident in figure 10.11(a) and the correction coefficients are represented in figure 10.11(b).

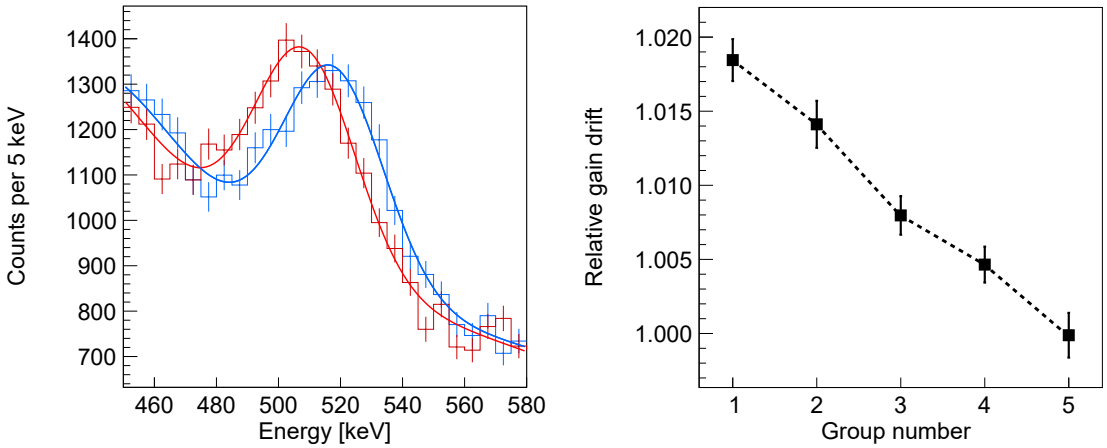

(a) Fits of spectra from group 1 (red) and 5 (blue)

(b) Extracted gain factors for the 5 groups

Figure 10.11: Determination of the gain correction used to compensate for the energy shifts in crystal 199.

Validating the assumptions underlying the correction and its overall quality was possible by applying the correction coefficients of the first group to the initial calibration data, demonstrating the linearity of the energy shifts and supporting the extrapolation to the entire energy range covered by the γ-ray sources. Figure 10.12 shows the effect of such correction in the initial γ source measurement, where a better alignment of the photopeaks in different crystals and a net reduction of all the photopeak energies towards their nominal values is achieved. A deviation towards larger values is still observed in figure 10.12(b) after correcting the energies which is most likely caused by a drift in the calibration that happened during the lapse of 7 hours between the beginning of the first group and the source measurement.

A comparison of systematic uncertainties before and after the gain correction is represented in figure 10.13 and compared with the uncertainties that remain after

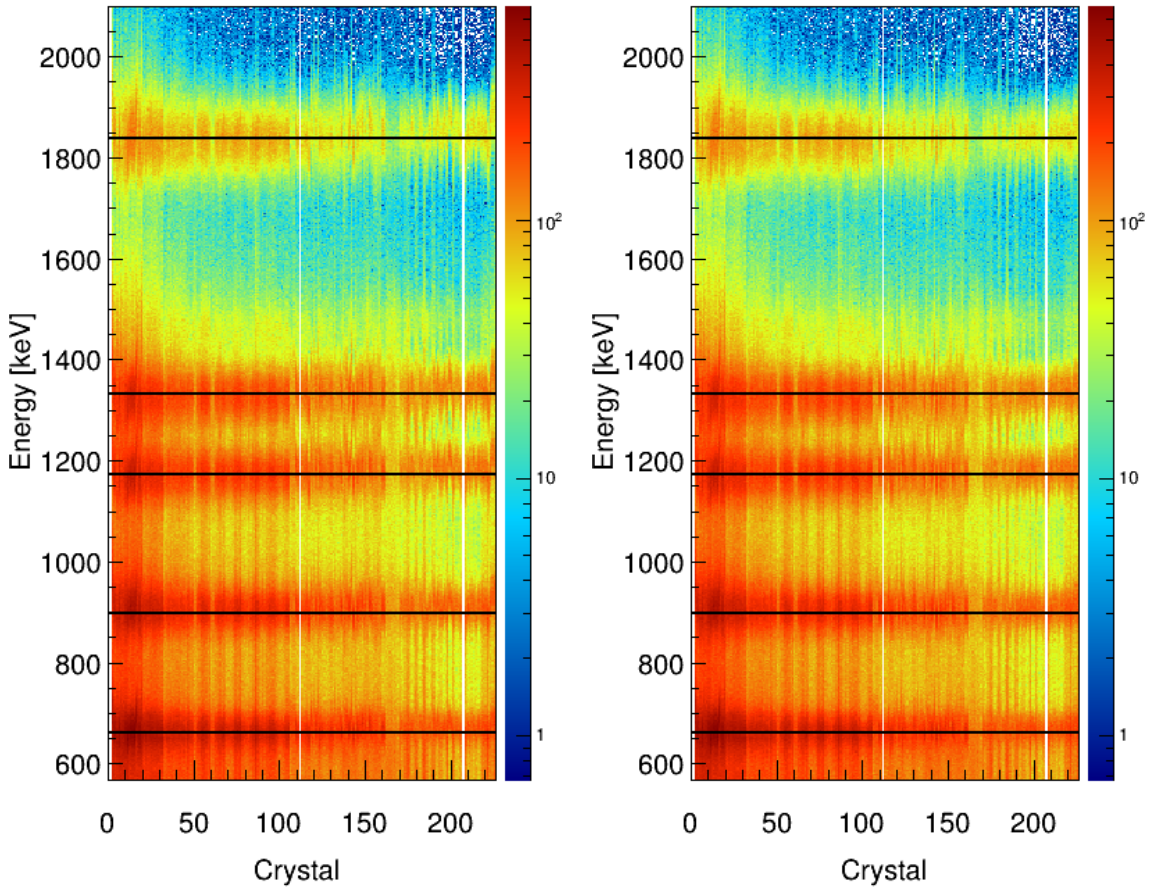

(a) Uncorrected **(b)** Corrected

Figure 10.12: Illustrates the correction of the energy shifts in the initial calibration data using the gain factors from the first group of runs. The expected energies are marked by the black lines.

proper recalibration. The systematic deviation is reduced to a half in the two most forward layers that hold 40% of the DALI2+ crystals and where statistics is enhanced in the in-beam measurements as a consequence of the Lorentz boost. The effect of this residual uncertainty in Doppler-corrected spectra is determined in section 10.6 together with other additional systematic uncertainties introduced after correcting the Doppler shifts.

The dependence of the energy resolution on the γ-ray energy was extracted from

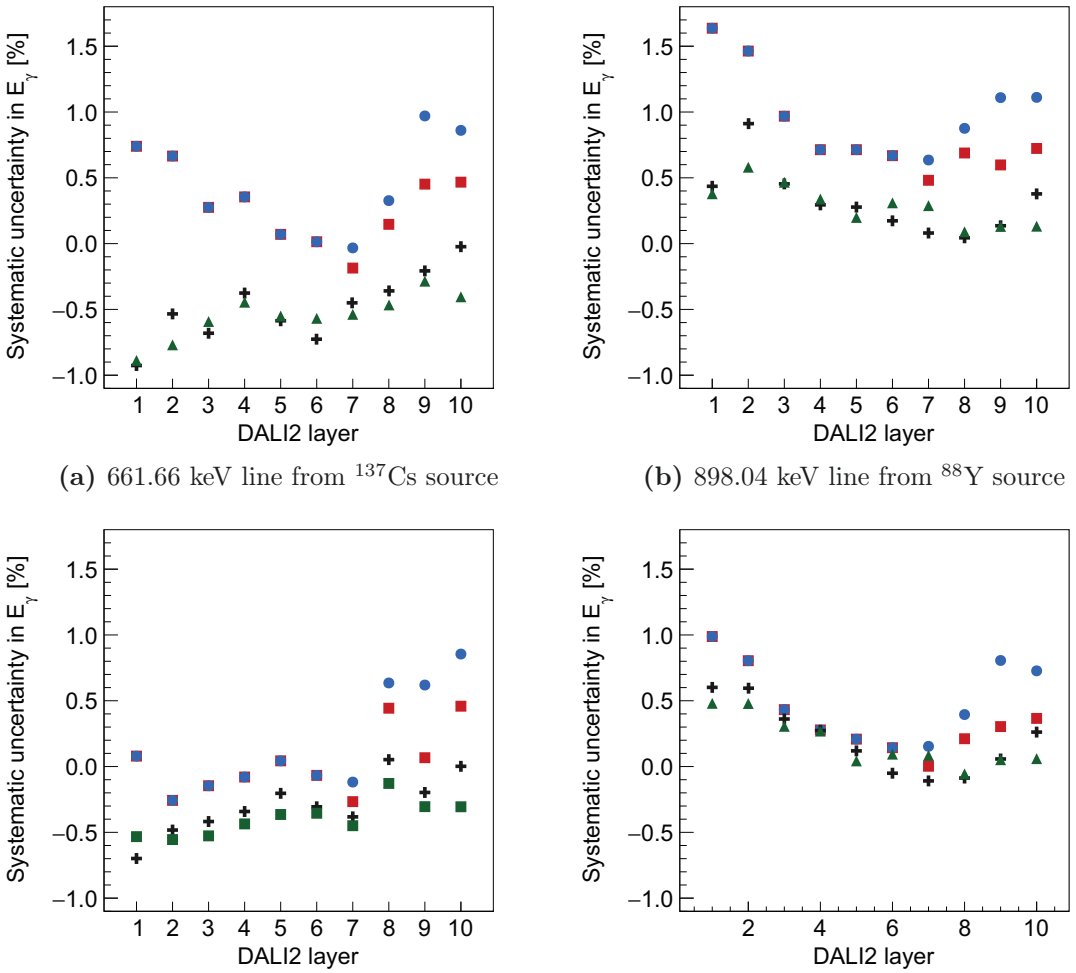

(a) 661.66 keV line from ^{137}Cs source

(b) 898.04 keV line from ^{88}Y source

(c) 1173.24 keV line from ^{60}Co source

(d) 1836.04 keV line from ^{88}Y source

Figure 10.13: Systematic errors in the γ-ray spectrum of the DALI2+ layers. The lowest deviations are attained after recalibration whose impact in the calibration data taken before the ^{57}Zn runs is represented by the green squares. Systematic deviations in the uncorrected calibration from the source measurement halfway the ^{57}Zn runs is represented by grey crosses. The same comparison is made using the calibration coefficients of the analysis plus the gain drift correction (red squares) and without the drift correction (blue circles).

the source measurements and it is represented in figure 10.14. This figure reveals a general trend of a better intrinsic resolution towards more forward angles, which is a desirable feature given the angular dependence of the Doppler-shifted energies and the γ-ray angular distributions in the laboratory frame. Resolutions of crystals at positions 162 to 169, 179 to 181 and 184 to 185 are significantly worse than the other crystals, nevertheless they are placed in the outermost positions of the layer and they are shadowed by the innermost crystals: their contribution to the overall resolution is not important.

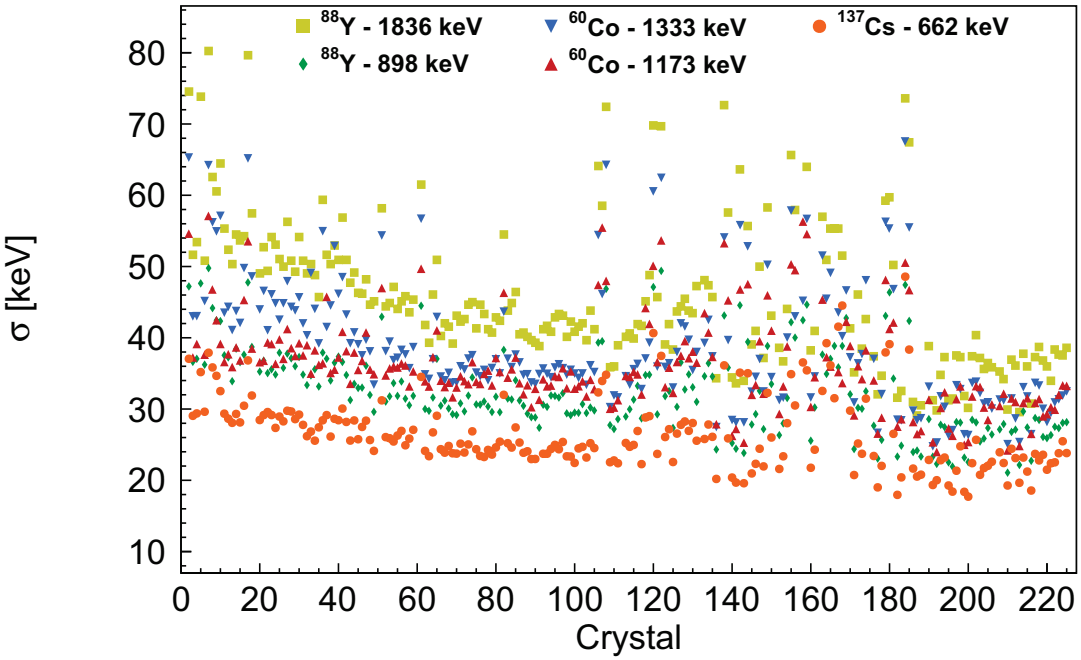

Figure 10.14: Energy resolution σ of the DALI2+ crystals measured with the calibration data.

The energy resolution of every crystal was parametrized in order to faithfully reproduce the energy response of the detectors when fitting simulated lineshapes to experimental spectra as described later on this chapter. The peak width is proportional to the square root of the energy deposition, $\sigma \propto \sqrt{E}$, provided that the relation between the energy deposition and the light yield is linear and Poisson statistics holds for describing the statistical fluctuations[137]. Other sources of loss in energy resolution were taken into account in this model by letting the exponent of the energy slightly vary around 1/2. Therefore the fit comprised two adjustable parameters a and b:

$$\sigma(E) = aE^b \tag{10.12}$$

The resultant parametrizations of σ are shown in figure 10.15(b) for all detectors and the details of the fit for crystal 195 are depicted in figure 10.15(a).

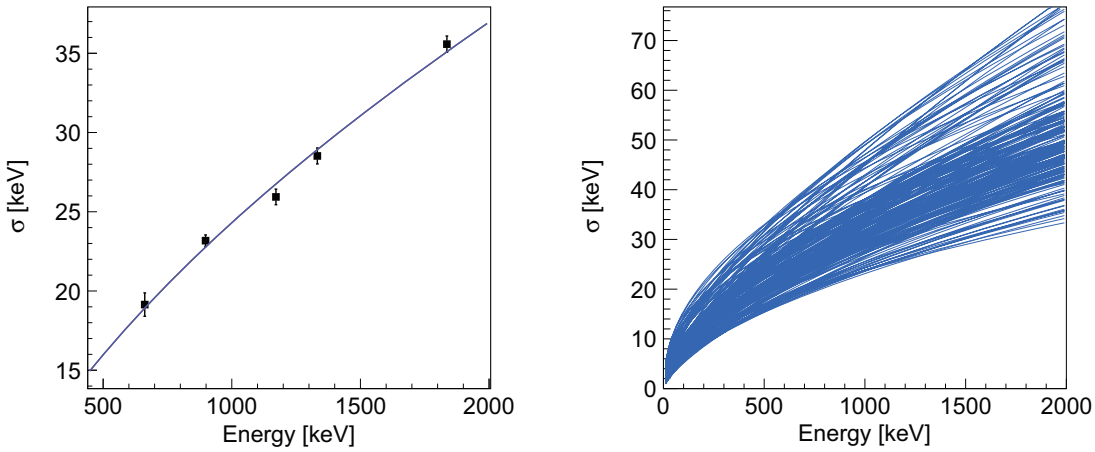

(a) Fit of crystal 195 ($a = 0.37$, $b = 0.60$) **(b)** σ vs E curves for all crystals

Figure 10.15: Parametrization of the energy resolution of the DALI2+ crystals.

10.2.2 Timing condition

The timing of the DALI2+ scintillators is used to construct the time difference between the ion reaching the F7 plastic and the gamma-ray detection. Therefore, uncorrelated radiation from the natural background and the activity of beam species implanted near the array can be largely removed by setting a gate around the prompt peak. The

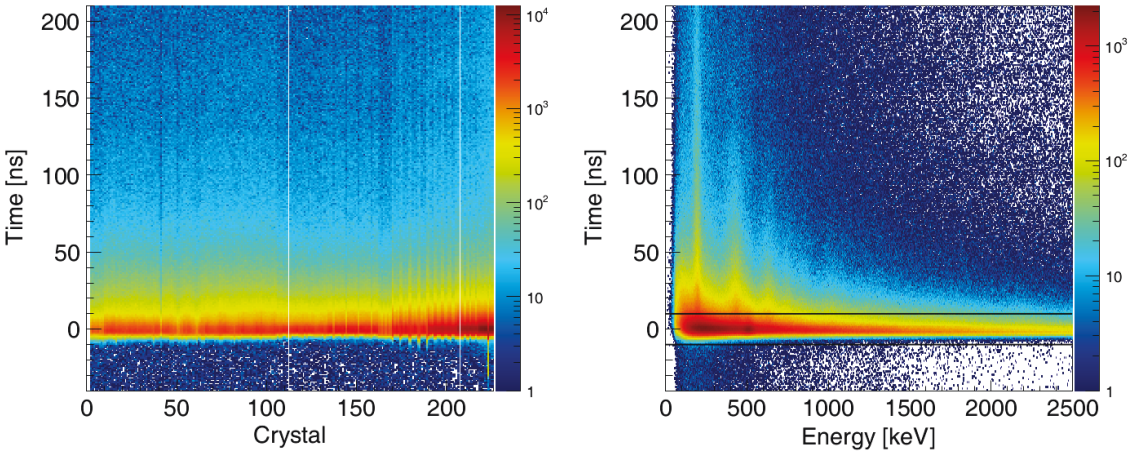

(a) Time spectrum vs DALI2+ crystal **(b)** Time spectrum vs energy

Figure 10.16: Shows the time difference between DALI2+ crystals and the beam in F7 after the time alignment. The selection of prompt coincidences is enclosed by the black lines on the right panel.

time distributions of the crystals were aligned to the same referece by adding an offset to the timing. This offset was extracted by selecting a specific isotope in BigRIPS and then determining the maxima of the time spectra. Furthermore, the dependence of the timing on the velocity of the incoming nucleus between the F7 plastic and the target was eliminated using the TOF between F7 and F8. Figure 10.16(a) shows the alignment of the DALI2+-F7 time differences for all crystals, and the selection of prompt gamma rays is enclosed by the black lines depicted in figure 10.16(b). The time resolution of the array was in the order of 1.7 ns for energies larger than 500 keV.

10.2.3 Add-back

Compton scattering is the dominant process in NaI for photons with energies between 300 keV up to 6000 keV. Since a gamma ray undergoing Compton scattering may have its energy scattered among multiple crystals, an addback routine can be conveniently applied to recover the full energy deposition. The sensitivity for determining energies and intensities of gamma rays by fitting Monte Carlo simulations to experimental spectra (see next section) is mostly dominated by the full energy peak (FEP). Hence removing the Compton background that overlaps less intense transitions at lower energies helps in reducing the larger uncertainties inherent to low P/T ratios.

The add-back algorithm decides which energy depositions belong to the same incident gamma ray according to the relative distance between crystals. A cutoff distance is specified when constructing a table of adjacent detectors in which energy depositions are added up to the γ-ray energy. The crystal with the largest energy deposition is always taken to be the one in which the first Compton interaction took place. The cutoff distance for constructing the add-back table was set to 15 cm on the basis of the saturation of the FEP efficiency curves as a function of this distance. A shift of the FEP towards smaller energies is visible in the spectrum of the ^{88}Y source after add-back which is shown in figure 10.17(a). According to the coincidence matrix represented in figure 10.17(b), most Compton events firing two adjacent crystals yield an energy deposition of 400 keV in one of them and there is a shift of 0.08% towards lower energies in the FEP of the 1836 keV line in these events. The deviation is partially explained by the well-known non-linear response of the crystal at low energies[137] that introduces a bias towards lower energies when the linear calibration is extrapolated. Calibrating with a second order polynomial did not significantly improve the situation, since a systematic deviation of 0.05% towards smaller energies still persists even when the energy depositions in the crystals are all above 700 keV. A dependence on the depth of the interaction point within the detector is invoked as an explanation of

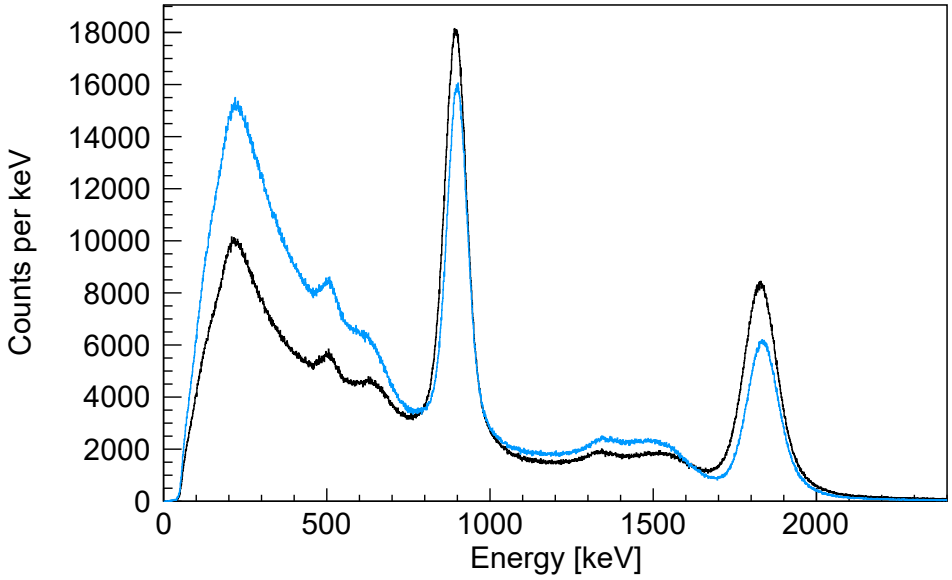

(a) Singles spectrum before and after addback depicted in blue and black, respectively.

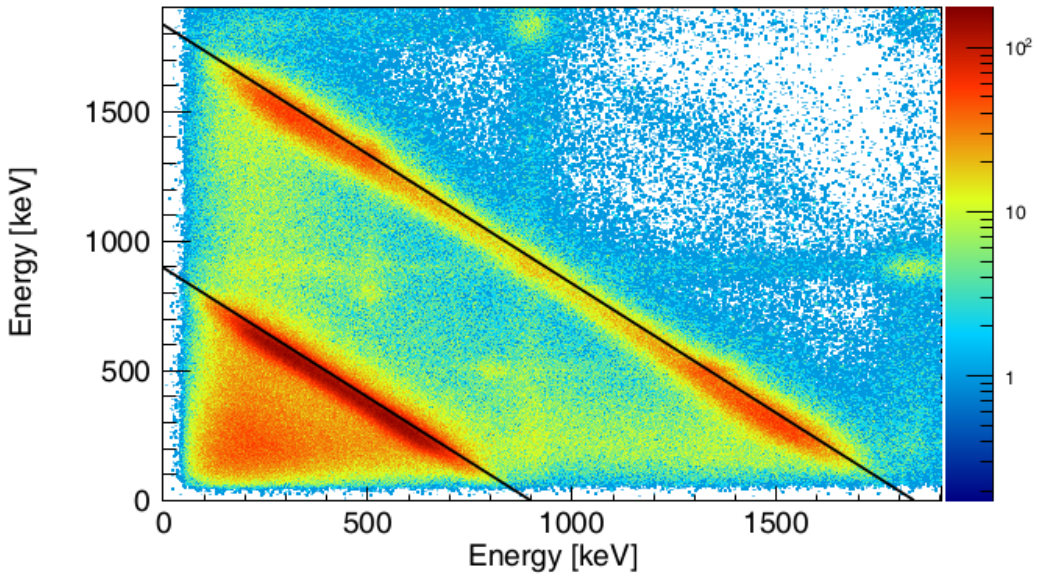

(b) Coincidence matrix restricted to events with γ-ray multiplicity of 1 after addback.

Figure 10.17: Illustration of the addback on the γ-ray spectrum taken with the ^{88}Y source. The expected correlation between the energies measured in adjacent crystals is marked by the black lines in the $\gamma\gamma$ matrix represented in the lower panel.

this effect[223], an assertion that is supported by the 8 keV deviation found in the photopeak of the well known 1461 keV γ-ray originated in the surroundings.

Given all the above, add-back was not employed for deducing transition energies in this work since, as demonstrated in next sections, the systematic uncertainty introduced in the energies is in general not negligible in comparison with the statistical one.

Nevertheless, the algorithm was useful for validating the consistency between model fits and statistical uncertainties in model parameters for γ-ray spectra sorted under different conditions. It was also used when sorting $\gamma\gamma$ coincidences because of their much lower statistics.

10.3 GEANT4 simulations of gamma-ray detection

The detection of γ decays in DALI2+ was simulated using a package developed by P. Doornenbal[224] that is based on the GEANT4 toolkit. These simulations mimic the actual geometry of the experiment and use accurate cross sections for the physics of gamma ray emission and detection. Their output can be analyzed in the same way as the experimental data and enables the extraction of physical quantities of interest after a proper characterization of the response of the array to gamma rays subject to strong relativistic effects in the laboratory, non-zero lifetimes and non-isotropical γ-ray emission in the rest frame.

The geometry of the experiment was specified by means of the target thickness, its placement relative to the crystals composing the array and the accurate placement of the detectors. The latter is read from a table publicly available to all the experimentalists. The production of gamma rays at different velocities in the target was modelled by specifying the atomic number and mass of the beam, its velocity profile before the target as well as the density and elementary composition of the target itself. The slowing down of the ions in the target was modelled using pre-calculated stopping power tables from ATIMA[225]. The parametrization of the energy resolutions of the DALI2+ crystals discussed in the previous section was used in the simulation when comparing simulated data sets with experimental data. The simulated responses of the array at different energies were validated at this point against the calibration data by adding a properly scaled sample of natural background. Figure 10.18 shows the comparison between simulations of the calibration sources and experimental spectra. They support the adequate modelling of the detector response in the whole energy range covered by the sources. Additionally, the detection efficiency for the crystals of different layers was also well reproduced.

10.4 Doppler correction

At the typical beam velocities of $\beta = 0.5 - 0.6$, γ rays following the deexcitation of the reaction products will have their measured energies Doppler-shifted over a large range of values. The velocity β at the moment of emission and the angle θ_L in the

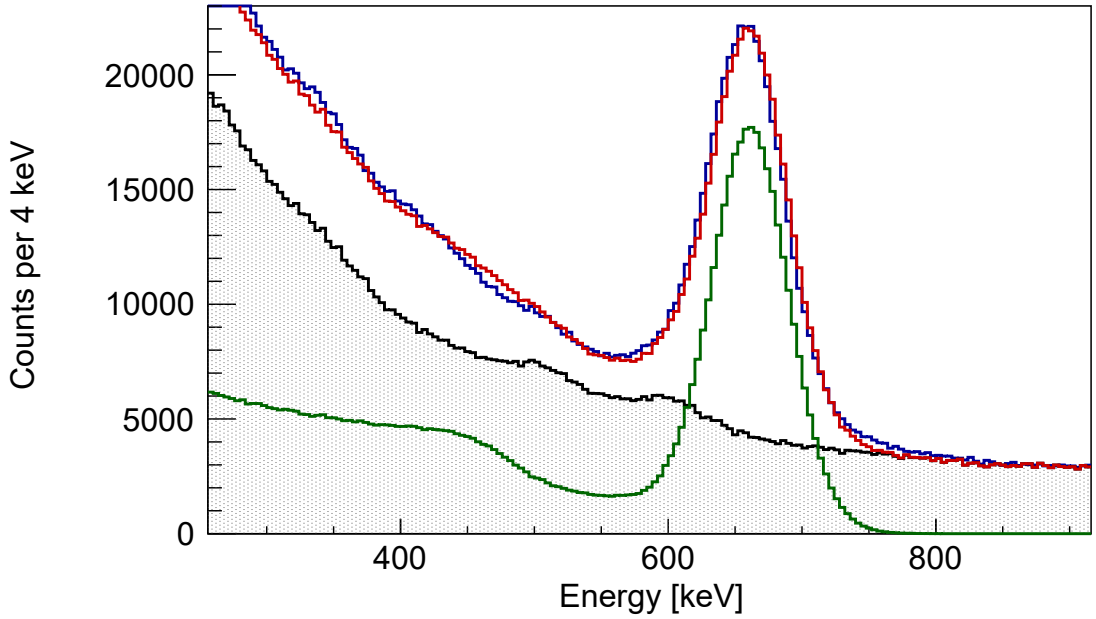

(a) ^{137}Cs source, sum of crystals 3-86.

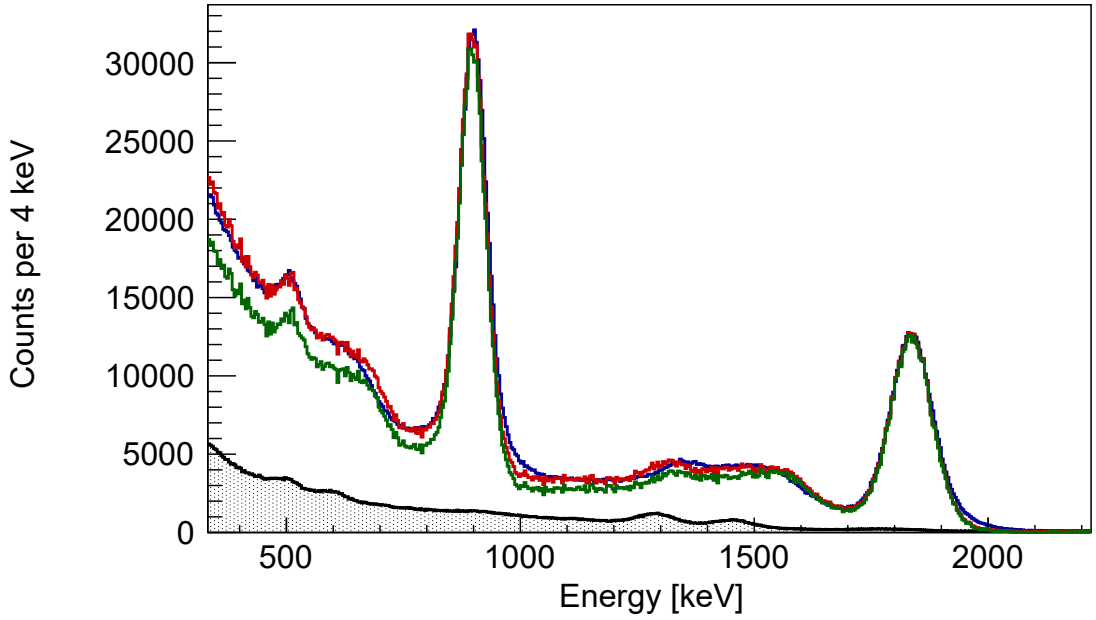

(b) ^{88}Y source, sum of crystals 87-226.

Figure 10.18: Comparison between simulated (red) and experimental (blue) spectra of the calibration sources. The simulated responses are shown in green and the filled histogram is a sample of background from the measurement closest in time which was added to the simulated histograms.

laboratory frame between the gamma ray and the deexciting product determines the relation between the unshifted energy in the rest frame of the nucleus, $E_{\gamma 0}$, and the

energy in the laboratory, E_γ, according to:

$$\frac{E_{\gamma 0}}{E_\gamma} = \frac{1 - \beta \cos\theta_L}{\sqrt{1-\beta^2}} \tag{10.13}$$

Neither the velocity nor the angle at the deexcitation point are directly measured, and they are conditioned by the combined effect of the probabilistic nature of the deexcitation process, the large beam velocities and the thick secondary target of 6 mm. A pre-calculated beam velocity and a table of average interaction coordinates for every DALI2+ crystal, which differs in general from its geometrical center, is used for correcting the Doppler shift.

Based on known lifetimes in this region of the nuclear chart and a comparison with mirror partners when no experimental information was available, the vast majority of lifetimes were estimated to fall below ∼10 ps for the most exotic species considered in this work: deexcitations within the target will occur in most cases. Hence, a precalculated mid-target velocity for the particular reaction under study and a table of average interaction points obtained under the assumption of instantaneous deexcitation were used in the analysis.

It is worth pointing out here that the shape of the DALI2+ responses was actually insensitive to lifetimes of a few picoseconds. This follows from the small widening of the photopeak, as a consequence of wrong assumptions regarding the emission point and the β, in comparison with other sources of peak broadening after Doppler correction such as the finite position resolution and the energy straggling in the target. Therefore, lifetimes were not treated as a degree of freedom in the analysis. Instead, systematic uncertainties in the fitted energies were studied in a reasonable range of lifetimes and they are reported in this work when relevant. They imply two apparent effects, one of them is the difference in the angle of observation for a certain crystal when the emission occurs at different positions and the other effect is the tendency towards emission at lower β for longer lifetimes.

The velocity of the ion traveling along the stage 5-7 of BigRIPS was calculated from the measured TOF as explained in section 10.1. Before reaching the target, a small fraction of the energy is lost as the ion traverses multiple beam line detectors placed downstream the F7 PPAC before the F7 plastic. In particular, the energy loss in the two plastics at F7 and F8 are the most important ones. Starting from the average β for an incoming species in BigRIPS, the velocity at the mid-target position was calculated by applying an offset to the average β for the isotope. This offset was obtained from a LISE++ calculation using the list of materials and thicknesses given in appendix D. Since a specific daughter nucleus is selected in ZeroDegree when sorting the γ-ray

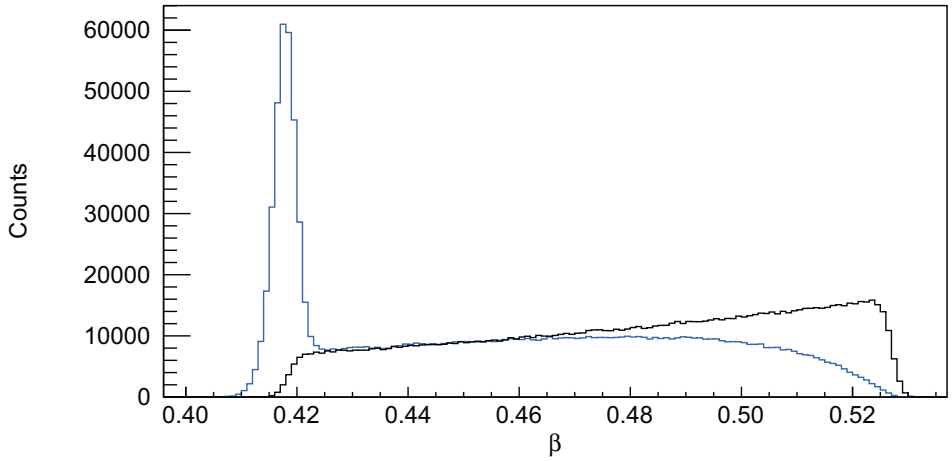

Figure 10.19: Simulated distributions of velocities at the γ ray emission point for transitions with half lifes of 0.3 ps (black) and 7.8 ps (blue).

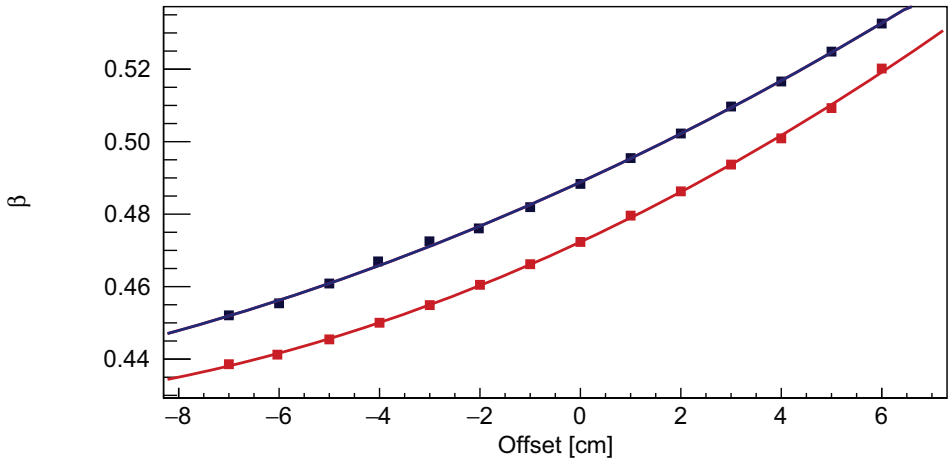

Figure 10.20: β values giving the smallest difference between backward and forward angles in the Doppler-corrected spectrum, as a function of the offset in the target z position. The calculation has been made for the 849.5 keV (red) and 1535.3 keV (blue) γ rays assuming the lifetimes from the literature.

spectrum, also the average of the β_{5-7} distribution resulting from such selection was used as input in the calculation.

Consistency in the entire energy range between the calculated β and the description of the geometry in the simulation was verified using ^{52}Fe, produced via knockout of a neutron from ^{53}Fe, as a test case. γ-ray spectra were sorted and Doppler-corrected using a number of values of the offset in the target position and the β. Differences in photopeak positions among detectors at different angles were extracted for each combination of β and offset. The procedure was performed for the most intense lines which are the 849.5-keV ($2_1^+ \longrightarrow 0^+$) and the 1535.3-keV ($4_1^+ \longrightarrow 2_1^+$) ones depopulating excited states with respective half-lifes of 7.8 ps and 0.3 ps [226]. As

illustrated in figure 10.19, the very short lifetime of the latter results in deexcitation when the nucleus is still in the target and the calculated mid-target β of 0.481 is nearly identical to the average β at which emission occurs. On the contrary, a longer half-life of 7.8 ps results in deexcitation behind the target in many cases so that the average β will be smaller than at mid-target.

Figure 10.20 shows the correlation between mid-target velocity and offset that yields the smallest energy difference between photopeaks in the summed spectrum of crystals at positions from 20 to 60 and from 180 to 220, for the 1535 keV γ-ray. A calculated mid-target β of 0.481 results in a target positioned -1.5 cm upstream. This analysis was also performed for the 849.5 keV line using the lifetime of the 2_1^+ state for calculating the table of average interaction points. In the latter case an offset of -2 cm results in an optimum β of 0.460, which matches the average β deduced from the simulation. The mismatch between both stems from the systematic uncertainty in the energy calibration whose overall contribution is determined in section 10.6.

Indeed, the position of the target relative to the DALI2+ array was adjusted before the experiment and was fixed to yield a difference of -2 cm along the beam axis between the target center and the DALI2+ crystals of the fifth layer so that this value was used during the analysis. It is explicitly shown in figure 10.21(b) that the Doppler-corrected energy of the 1535 keV line is well aligned to the same value regardless of the crystal position where the photon was detected.

10.5 Fitting technique and interval construction

The standard maximum likelihood method for Poisson distributed histograms [227] was used for fitting a combination of simulated lineshapes on top of a smooth background[2], described by a double exponential function[229], to the experimental spectrum.

Correlations between the parameters were accounted for by simultaneously minimizing the Poisson-likelihood χ^2_{P}[230],

$$\chi^2_{\mathrm{P}} = 2\sum_i n_i - \nu_i + \nu_i \ln\left(\frac{\nu_i}{n_i}\right) \tag{10.14}$$

as a function of all the model parameters. In the equation above ν_i and n_i are the number of counts in bin i predicted by the model and contained in the experimental histogram, respectively. This χ^2 was minimized using the MIGRAD minimizer provided by the MINUIT package[231]. Occurrence of a global minimum was verified by feeding

[2]The origin of the non-Compton background is manifold and has been discussed in detail in the literature (see for instance [228]).

different seeds to the minimizer. Two parameters, an energy shift and a scaling factor, were allowed to vary for each of the lineshapes included in the fit. The energy shift is applied to the Doppler-corrected energies returned by the simulation, after which a histogram with the same binning and scaled is constructed for computing

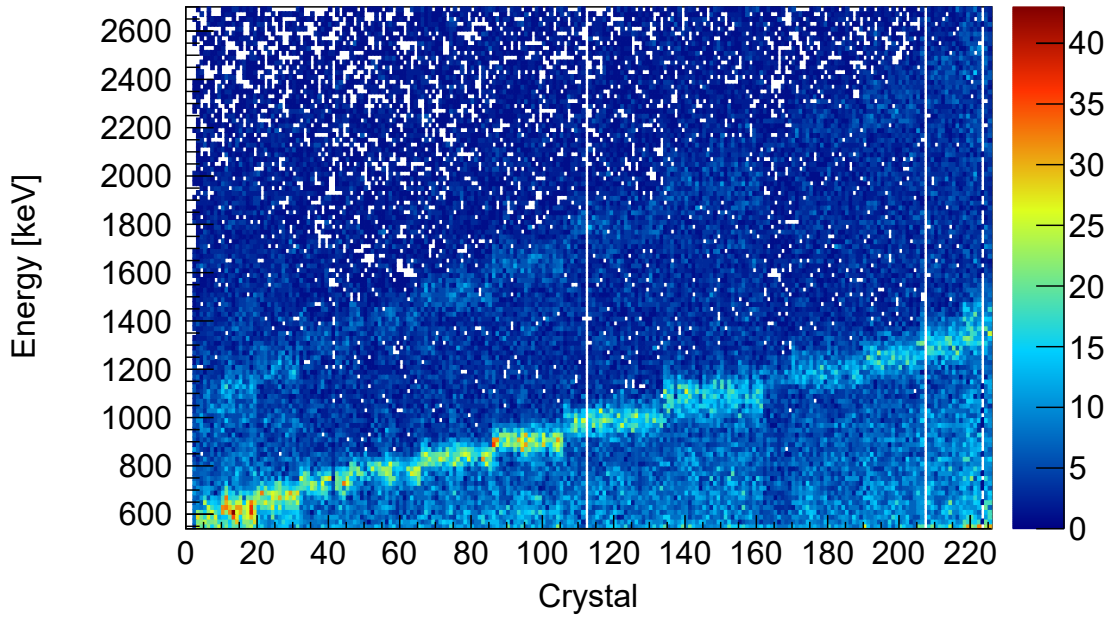

(a) Before Doppler correction.

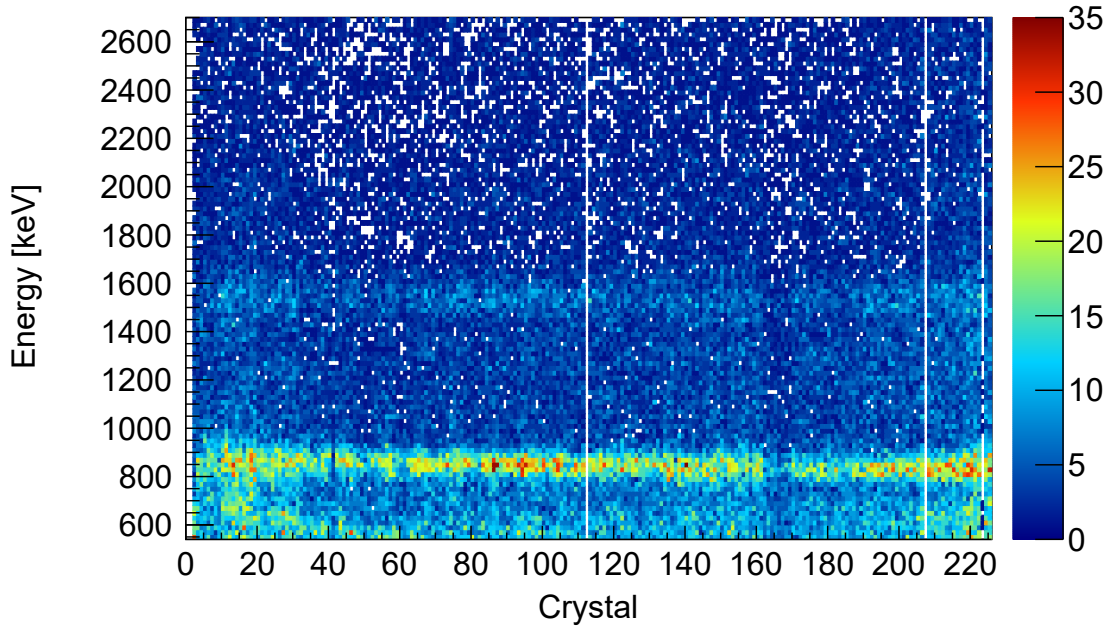

(b) After Doppler correction.

Figure 10.21: Illustration of the Doppler correction on the γ-ray spectrum of ^{52}Fe produced by neutron knockout from ^{53}Fe. Only crystal multiplicities smaller than 5 were included.

the χ^2_P. Shifting the simulated lineshapes is justified by the similarity between the two responses, namely the shifted response and the simulated response at the shifted energy, an assertion illustrated in figure 10.22. The figure shows the overlap between

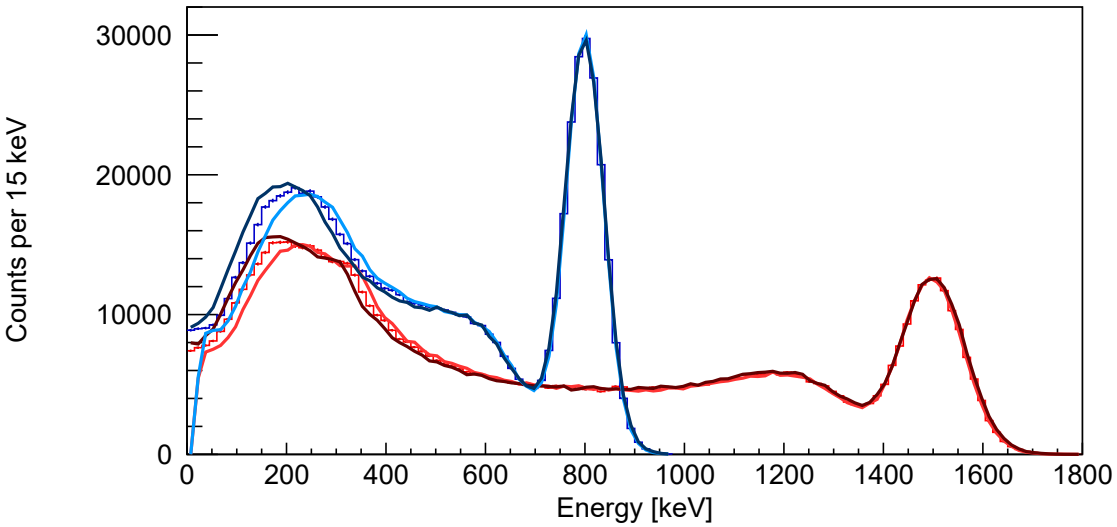

Figure 10.22: Doppler-corrected lineshapes simulated for 800 keV (blue histogram) and 1500 keV (red histogram) γ rays. The result of fitting those lineshapes by simulated responses shifted by $\pm$20 keV after Doppler correction is depicted by the solid lines.

three simulated responses, two of them simulated at energies of 1480(780) keV and 1520(820) keV in the rest frame and shifted by +20 keV and -20 keV, whereas the lineshape depicted as red(blue) histogram was simulated for a 1500(800) keV γ ray. The bias introduced in the deduced energy when fitting the 1500 keV lineshape in terms of the shift applied to the fitting response is smaller than 0.5 keV when considering only energies above 400 keV in the fit. This is the lowest energy used in this work for the analysis of experimental spectra and, moreover, all the shifts were kept well below 20 keV when fitting the spectra. The bias introduced by this fitting technique is included in the systematic uncertainties reported in this work, which originate from the energy calibration mainly (this systematic uncertainty is determined in section 10.6).

The statistical error in the estimators can be given in different ways[232]. The most common ones essentially refer to the shape of the χ^2 around the minimum, although Monte Carlo methods using resampled data sets are widely used as well[233]. Different error bars will be deduced in general depending on the method of choice, so that the construction and interpretation of the reported intervals in this work is clarified through the example discussed in the following subsection which is close to the situation found later on in the data.

10.5.1 Interval construction

Let us consider the case of two gaussian signals from which the spectrum shown in figure 10.23(a) was sampled. The gaussians have the same width and are not resolved, namely the separation between them is less than 1 FWHM. However, a model consisting of a single gaussian for describing this doublet results in a poor description of the spectrum, hence a second gaussian is added to the model. A strong correlation is present between the centroid energies and the heights of the two gaussians. Moreover, different χ^2 shapes as a function of the parameters will be obtained if the same spectrum is repeatedly measured over fixed periods of time while maintaining the same experimental conditions. Consequently, either larger or smaller, more or less asymmetric error bars can be deduced when fitting different spectra even if they are samples containing the same number of events. For this reason, estimating the statistical uncertainties from the covariance matrix may not be appropiate in this case: the extremes of the multi-parameter 1σ contour are given as statistical uncertainties instead. This is the way the MINOS minimizer gives the error in the parameters[234]. It has also been a usual way of reporting intervals in the matrix elements extracted from Coulomb excitation experiments[235]. However, due to the obvious difficulties in graphically determining the 1σ contour for dimensions larger than two, its extremes were obtained by generating χ^2 curves as a function of a single parameter, replacing the value of the remaining parameters by their correlated estimators at each point.

A number of Monte Carlo simulations of the aforementioned doublet were performed and the resulting spectra were fitted in order to verify that the χ^2 contours are sufficiently well behaved in such a way that their calculated extremes from the correlated χ^2 curve indeed provide the standard 70% confidence interval. This process is illustrated in figures 10.23(b) and 10.23(c) for the simulated spectrum shown in figure 10.23(a). Two χ^2 curves were extracted for each parameter: the first one is obtained by varying the χ^2 in terms of a single parameter while fixing the others to their values in the global minimum, whereas the other curve is calculated by correlating the parameters as described previously. A comparison between both χ^2 curves for the centroid energy of the gaussian at lower energy shows indeed that taking into account the correlations between the 4 parameters results in a much less pronounced χ^2 and much larger error bars. Additionally, the fully correlated χ^2 can be used to extract the extremes of the 1σ contour shown in figure 10.23(b).

Parameter inference, interval construction and significance criteria in this work are summarized as follows:

1. Fully correlated χ^2 curves were generated to verify the existence of a well defined global minimum.

2. The reported intervals correspond to the extremes of the multi-parameter 1σ contour obtained from the fully-correlated χ^2 curves. For each parameter, the center of the interval is used as estimator.

3. A peak is considered statistically significant if the intensity is larger than twice its uncertainty: the significance level in this work is 2σ. Otherwise the response is not included in the fit but possible systematic errors resulting from this are studied if necessary.

10.6 Validation of the model fits

The cuts and parameters used for correcting the Doppler shifts, the residual gain drift in the uncorrected crystals and deviations from the lineshapes used for fitting experimental spectra restricted to certain crystal multiplicities are some of the possible sources of systematic uncertainty in the parameters deduced from the fit.

The joint contribution of all these factors is difficult to asses in a simple manner for the individual reaction channels, hence an alternative approach was followed instead. A number of byproducts with well known transition energies and lifetimes is present in the data. Their γ-ray spectra were sorted and fitted using lineshapes that were constructed using the lifetimes found in the literature. The vast majority of the observed deviations in transition energies amount to less than 0.5% within statistical uncertainties in the 7 reaction channels analyzed comprising both inelastic excitation as well as single proton or neutron removal. No clear dependence of this deviation with the transition energy is observed, and the deviations result in both over- and underestimation of the deduced transition energies. Therefore an additional uncertainty of 0.4% was quadratically added to the statistical uncertainty in the energy in order to account for all these systematic deviations.

This procedure is illustrated in figures 10.24 and 10.25, which shows fits to ^{52}Fe γ-ray spectra after neutron knockout from ^{53}Fe. The spectra were generated with different cuts on the crystal multipicity per event, where stricter cutoffs on multiplicities trade statistics off for larger P/T. Three photopeaks are clearly visible regardless of the condition imposed on the data: these corresponds to the transitions depopulating the 6_1^+ (E_γ =1941.0 keV, τ = 0.2 ps), the 4_1^+ (E_γ =1535.3 keV, τ = 0.22 ps) and the 2_1^+ (E_γ =849.4 keV, τ = 7.8 ps) states. Events with an energy deposition in only one crystal enhance the intensity of the 2_1^+ relative to the $4_1^+ \longrightarrow 2_1^+$ and $6_1^+ \longrightarrow 4_1^+$

γ rays, indicating both a strong direct population of the 2_1^+ state as well as the coincidence between the three γ rays in the cascade. Unresolved gamma strength is present for energies between 2400 keV and 2800 keV as well as around 1325 keV. Their contributions to the Compton background at lower energies was taken into account in an "effective" way by including two lineshapes for reproducing the shape of the spectrum between 2400 keV and 2800 keV plus another lineshape at 1325 keV. It is worth remarking here that "fitting ^{52}Fe" is not the purpose of this section, but to

- show that the lineshapes used for fitting Doppler-corrected spectra are accurate enough under a proper description of the background below the peaks: a high statistics case such as the ^{52}Fe of this section is needed for this.
- estimate systematic uncertainties using experimental lineshapes with negligible statistical fluctuations.
- demonstrate that even selecting crystal multiplicities below 6 certainly results in slight deviations with respect to the adjusted model, as visible in the region between 500-700 keV in panel 10.24(a). However, the bias in the energies is still covered by the 0.4% systematic uncertainty.

The energies of the most intense gamma rays observed in the ^{52}Fe γ ray spectra are given in table 10.2. Only the statistical error in the γ-ray energies (without the additional 0.4% of uncertainty) is reported in the table.

	Without addback		With addback	
E_γ^{lit}	E_γ ($m_{\text{crys}} < 5$)	E_γ ($m_{\text{crys}} = 1$)	E_γ ($m_\gamma < 4$)	E_γ ($m_\gamma = 1$)
849.5	848.6(5)	851(1)	847.4(5)	848.2(8)
1535.3	1540(2)	1537(4)	1532(1)	1533(3)
1941.0	1953(7)	1960(41)	1945(5)	1944(11)

Table 10.2: Comparison between gamma-ray energies (in keV) from literature and the energies of the most intense transitions observed in ^{52}Fe produced after neutron knockout from ^{53}Fe. The comparison is made for spectra obtained with different multiplicity conditions, with and without addback. Only statistical errors are quoted.

10.7 Inclusive cross section

It is possible to deduce inclusive and exclusive cross sections using this experimental setup. Several corrections must be introduced and a number of checks were performed

to validate the results. This analysis, which is based on previous works[236], is briefly described below.

The inclusive cross section is defined as the number of daughter nuclei produced in the target per parent nuclei incident on the target and scattering center per unit area n,

$$\sigma_{\text{inc}} = \frac{N_{\text{daughter}}}{N_{\text{parent}} n} \tag{10.15}$$

where n is calculated using the formula

$$n = \rho L \frac{N_A}{M_H} \tag{10.16}$$

and $\rho = 1.848\,\text{g/cm}^2$ is the target density, $L = 0.6\,\text{cm}$ is the length of the target, $N_A = 6.022 \times 10^{23}\,\text{mol}^{-1}$ is the Avogadro constant and $M_H = 9.012\,\text{g/mol}$ is the molar mass of Be. Neither N_{daughter} nor N_{parent} in eq. (10.15) are directly accesible from the data and their values must be deduced from the amount of parent nuclei reaching the F7 plastic and the number of daughter nuclei succesfully identified in ZeroDegree per incident parent nucleus in BigRIPS. A selection on downscaled (DS) events was performed for a consistent determination of the cross section according to the trigger logic introduced in section 9.4.

Eq. 10.15 can be written in terms of the number of nuclei within the isotope selection cuts in BigRIPS ($N_{\text{parent, BR}}$) and ZeroDegree ($N_{\text{daughter, ZD}}$) as

$$\sigma_{\text{inc}} = \frac{N_{\text{daughter, ZD}}}{N_{\text{parent, BR}}\, n\, \varepsilon_{\text{det}}\, \varepsilon_{\text{loss}}\, T}\, R \tag{10.17}$$

where the additional factors ε_{det}, $\varepsilon_{\text{loss}}$, T and R entering the above equation are explained as follows. Firstly, a certain daughter nucleus produced in the target may undergo nucleon removal reactions in the beam line detectors of ZeroDegree. Likewise, the passive elements between the F7 plastic and the target reduce the actual number of parent nuclei impigning on the target. Even though the daughter nucleus reaches the ionization chamber at F11, its successful identification in the PID matrices is bound to the efficiency of the beam line detectors in ZeroDegree. These spurious contributions to the cross section were estimated using a measurement without target and selecting the same species in BigRIPS and ZeroDegree. Figure 10.26(a) shows the distributions in the horizontal position at F5 for ^{57}Zn, the nucleus centered in both separators, with and without the same selection in ZeroDegree. The difference between the two distributions is a scaling factor resulting from all the discussed contributions that are grouped into ε_{det} in this case. A value of $\varepsilon_{\text{det}} = 0.93(2)$ overlays both distributions. Since no dependence on the momentum in the ZeroDegree-gated distribution is observed, this nucleus is fully transmitted in the empty target runs (that is, $T = 1$ for this

nucleus). Repeating the same procedure for other nearby nuclei in the PID and focusing on the momentum range that is fully transmitted, similar values are obtained within statistical uncertainties. This means that ε_{det} is virtually indepedendent of the incoming nucleus in the PID region of interest as expected from their similar velocities, proton and neutron numbers.

The placement of the secondary target reduces the incoming flux as a consequence of reactions within it. The $\varepsilon_{\text{loss}}$ factor is used for compensating losses in the target and was derived in a similar way as ε_{det}. As shown in figure 10.26(b), selecting ^{57}Zn in both spectrometers results in lower statistics in the F5X histogram in comparison with a selection in BigRIPS only, as a consequence of such reactions. Now, a single scaling factor is not sufficient to overlay both histograms since the ^{57}Zn is less transmitted ($T < 1$) at low momentum. Nevertheless, a region of full momentum acceptance ($T = 1$) is still present between $F5X = -30$ and $F5X = 10$ and the product of the two correction factors, $\varepsilon_{\text{det}}\varepsilon_{\text{loss}} = 0.81(2)$, is readily obtained as the scaling factor that overlays both histograms between these two values of $F5X$. $\varepsilon_{\text{loss}} = 0.87(3)$ was calculated using the ε_{det} coefficient from the empty target and compares favourably with a 12% less of incoming flux according to LISE++.

The last factor in eq. (10.17) to be discussed is R, a correction stemming from the production of the selected knockout residue anywhere between the F7 plastic and the third F8 PPAC in ZeroDegree. Knockout reactions in the F9-F11 PPACS, the F11 MUSIC and the F11 plastic are not considered, since production in the F9 PPACs can be totally neglected and both proton and neutron removal in F11 result in an isotope identified as having same A/Q as the unreacted beam so that such events are fully removed after selecting the daughter nucleus in the ZeroDegree PID. For the knockout of a neutron from ^{57}Zn, the accumulated statistics in the empty target runs prohibited the experimental determination of this ^{56}Zn yield produced before the target. Instead, R was calculated using LISE++ according to the list of materials and thicknesses between the 1st PPAC at F7 and the third F8 PPAC in appendix D. It was approximated as the fraction of reactions occuring in the target relative to the total number of reactions in the list of materials including the target. The validity of this approximation was verified by examining the products of proton knockout reactions on the most intense beam species as observed in the empty target runs. Finally, $R = 0.83(5)$ was calculated for neutron knockout reactions. The uncertainty in R allows a safe margin that reproduces all the observed differences between experimental and calculated proton knockout yields observed in the empty target runs.

The inclusive cross section for ^{57}Zn(Be,X)^{56}Zn was extracted by selecting ^{56}Zn in ZeroDegree and ^{57}Zn in BigRIPS. The X distributions in F5 of the parent nucleus

are shown in figure 10.27 with and without a selection of the knockout residue ^{56}Zn in ZeroDegree. A scaling factor was extracted which overlays both histograms for X values comprised between -35 and 15, corresponding to full transmission ($T = 1$), and the cross section was obtained by multiplying such scaling factor by $\frac{R}{n\,\varepsilon_{\mathrm{det}}\,\varepsilon_{\mathrm{loss}}}$ according to eq. (10.17). The uncertainty in the cross section is the result of a statistical uncertainty, calculated by propagation of the independent uncertainties on $\varepsilon_{\mathrm{det}}\varepsilon_{\mathrm{loss}} = 0.81(2)$, $N_{\mathrm{daughter,\ ZD}}/N_{\mathrm{parent,\ BR}} = 7.5(5) \times 10^{-4}$ and R as

$$\delta\sigma = \sigma\sqrt{\left(\frac{\delta(N_{\mathrm{daughter,\ ZD}}/N_{\mathrm{parent,\ BR}})}{N_{\mathrm{daughter,\ ZD}}/N_{\mathrm{parent,\ BR}}}\right)^2 + \left(\frac{\delta(\varepsilon_{\mathrm{det}}\varepsilon_{\mathrm{loss}})}{\varepsilon_{\mathrm{det}}\varepsilon_{\mathrm{loss}}}\right)^2 + \left(\frac{\delta(R)}{R}\right)^2} \tag{10.18}$$

plus a systematic uncertainty which is reported separately and stems from the imposed cuts on the PID as well as background in BigRIPS. The latter was estimated by applying different cuts (in the identification and PID cleansing) and examining the corresponding change in the cross section. An upper limit of 10% was established for this particular channel based on this analysis. The obtained inclusive cross section is

$$\boxed{\sigma_{\mathrm{inc}} = 10(1)(1)\ \mathrm{mb}} \tag{10.19}$$

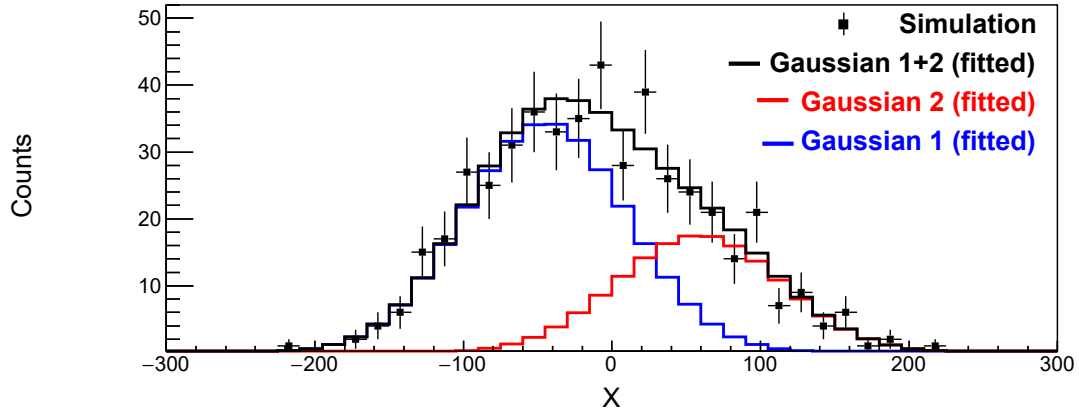

(a) Simulated spectrum of a gaussian doublet and its χ^2_P fit. The simulated distribution was sampled from 2 gaussians centered at $X = -50$ and $X = 50$.

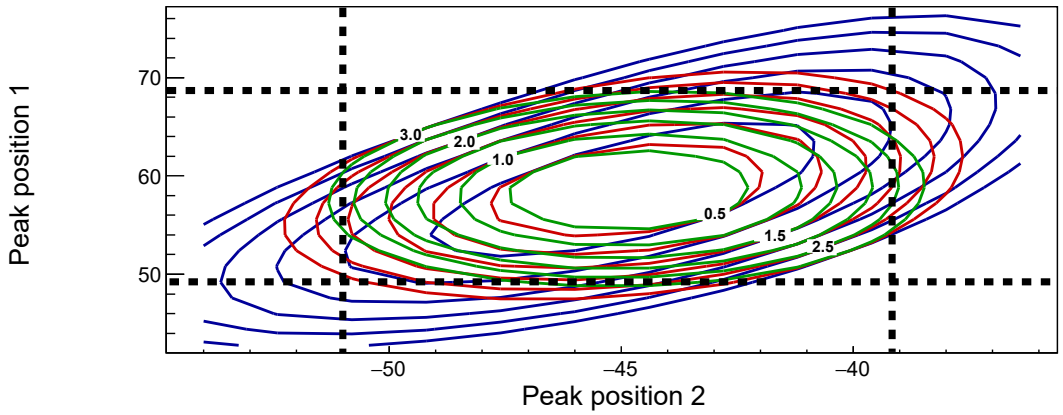

(b) χ^2_P contours for the peak positions, calculated by fixing the intensities at their global estimators (green), correlating the intensity of the gaussian at higher energy (red) and correlating both intensities (blue). The extremes of the 1σ contour are marked by the black dashed lines.

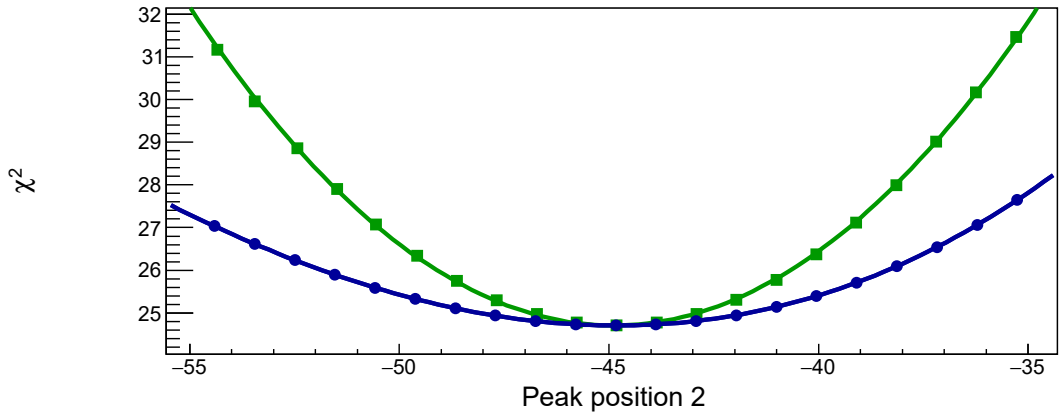

(c) Comparison between the uncorrelated (green) and the fully correlated (blue) χ^2_P curves.

Figure 10.23: Illustration of the technique for determining statistical uncertainties in this work when there is a strong correlation among the model parameters. The error analysis is made for the simulated doublet shown in the uppermost panel.

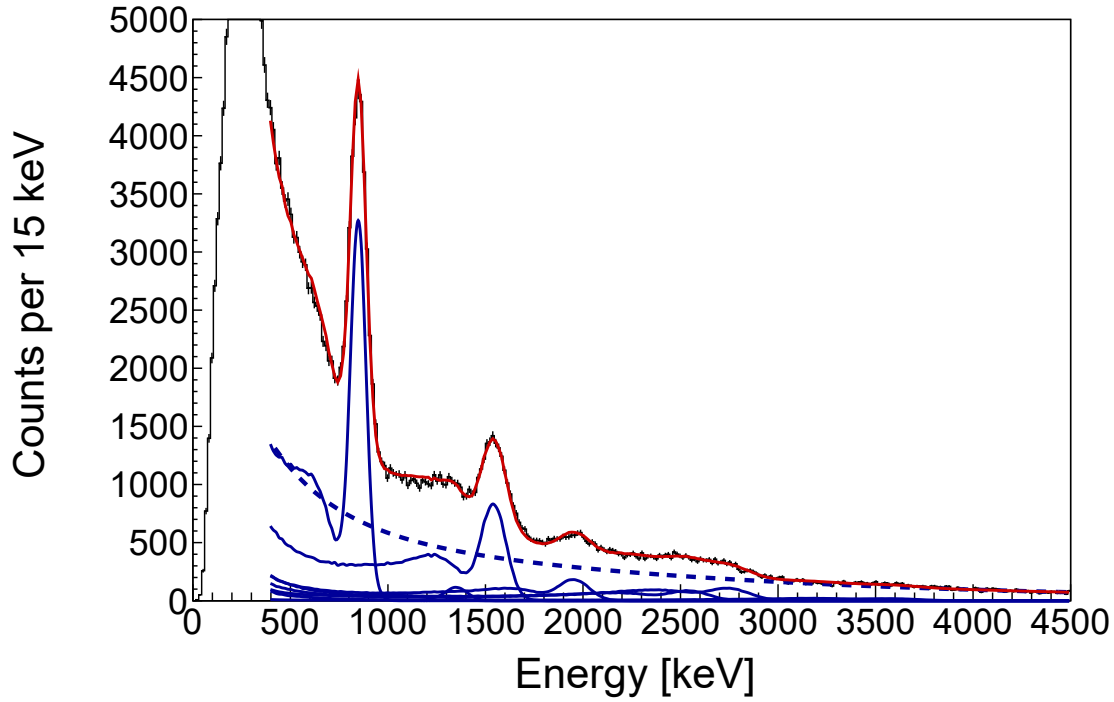

(a) Selection on events firing less than 5 DALI2+ crystals.

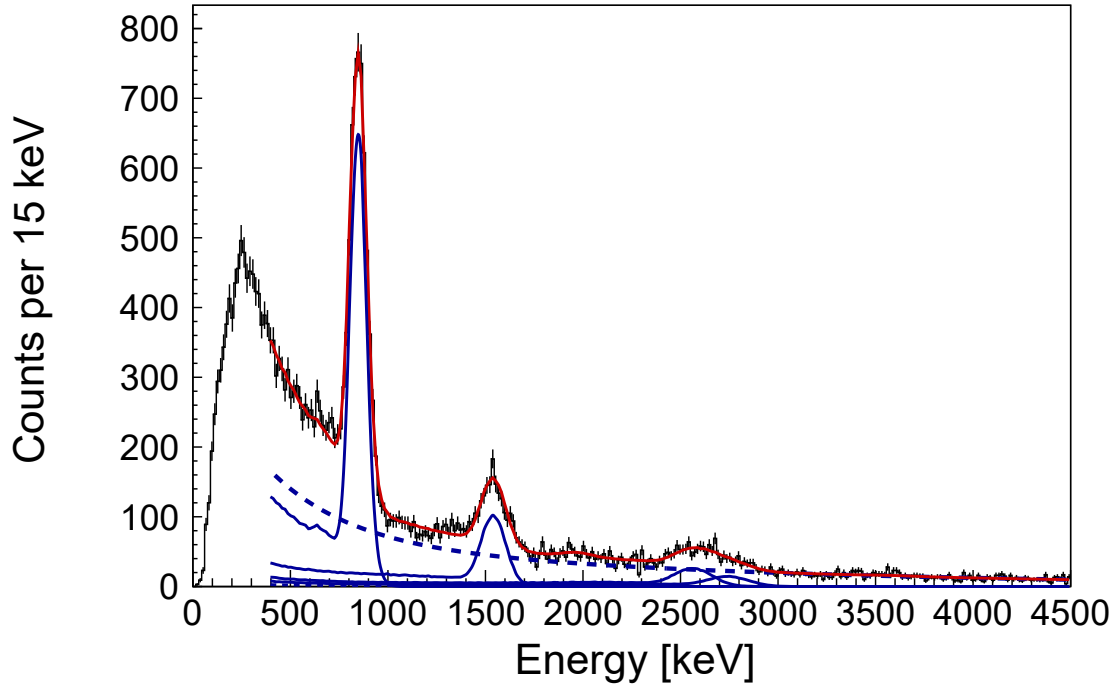

(b) Selection on events firing a single DALI2+ crystal.

Figure 10.24: ^{52}Fe γ-ray spectra without add-back, produced by neutron knockout from ^{53}Fe. The fits are shown in red and the individual lineshapes composing the fit are represented in blue. The dashed line represents the non-Compton background.

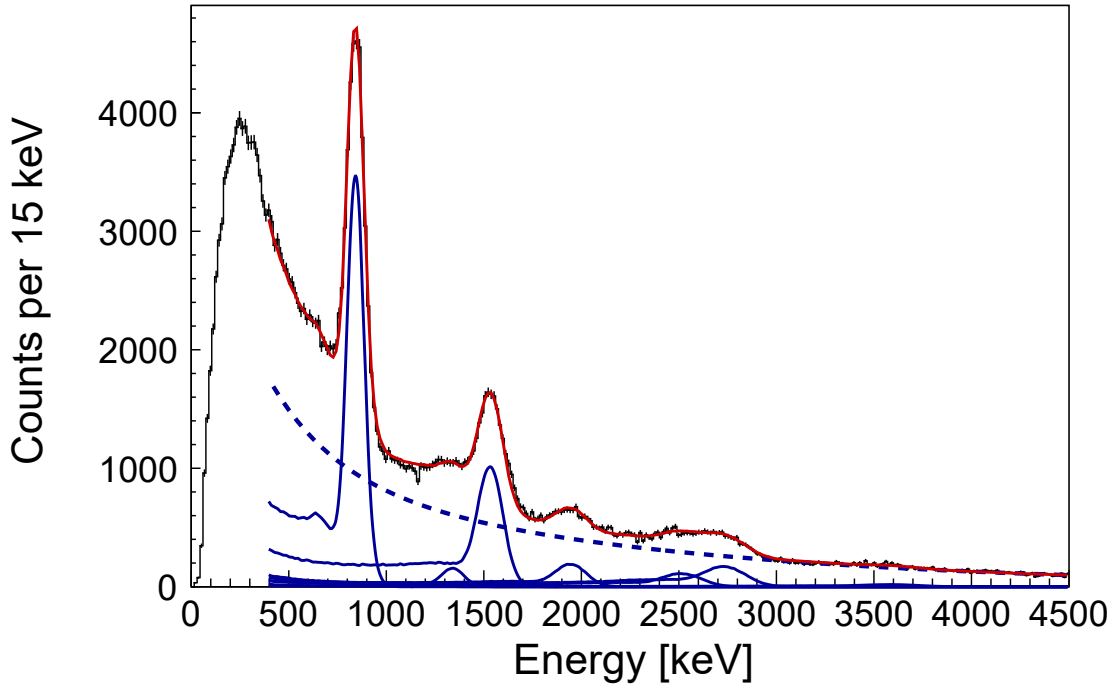

(a) Selection on γ-ray multiplicities below 4.

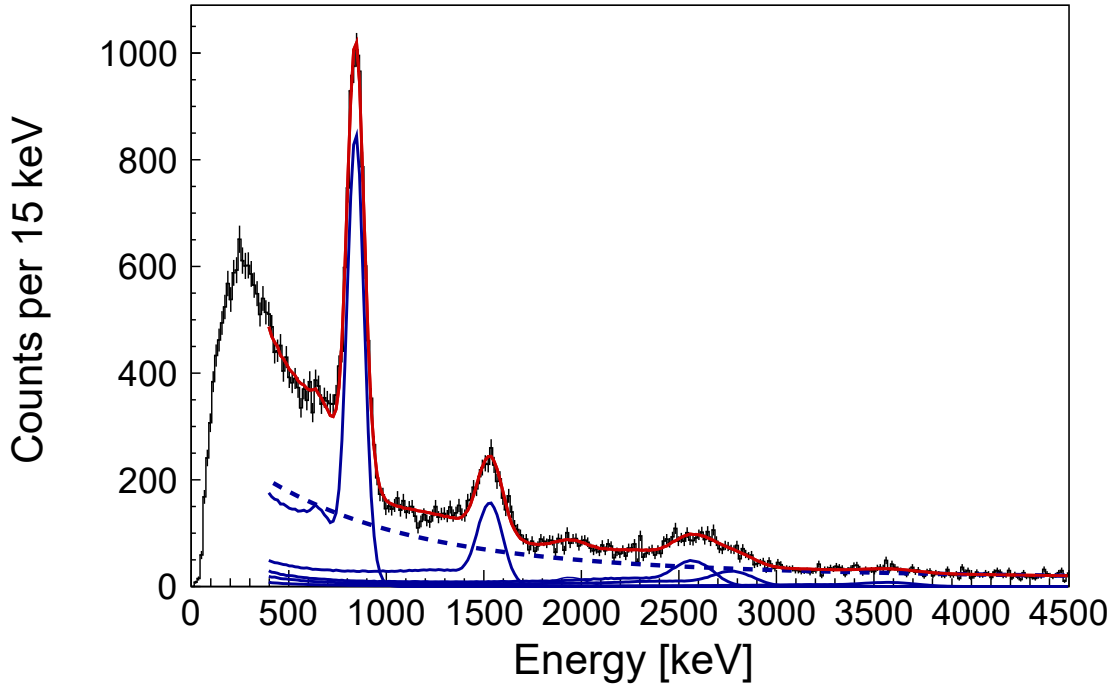

(b) Selection on events with a single detected γ ray.

Figure 10.25: ^{52}Fe γ-ray spectra after add-back, produced by neutron knockout from ^{53}Fe. The fits are shown in red and the individual lineshapes composing the fit are represented in blue. The dashed line represents the non-Compton background.

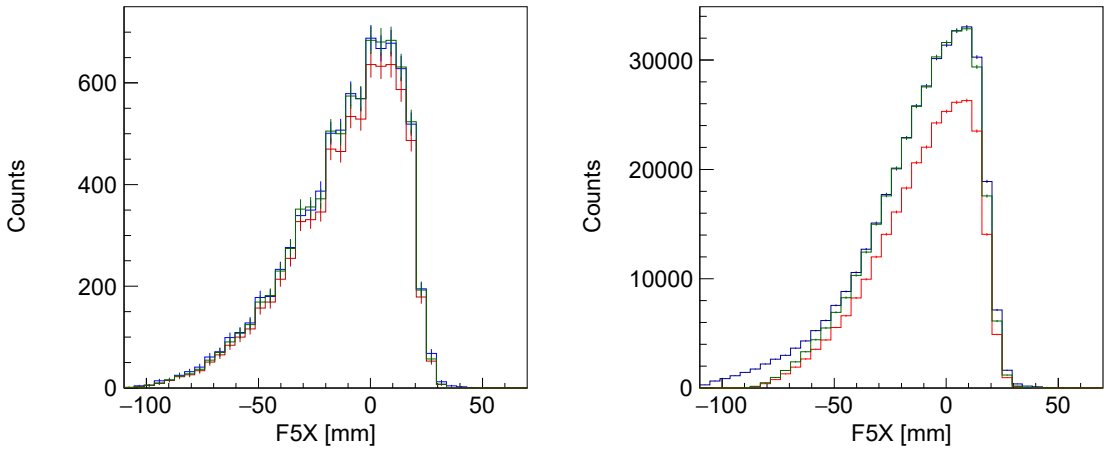

(a) Empty target **(b)** Physical runs

Figure 10.26: Determination of the beam-line efficiency ε_{det} and the product $\varepsilon_{\text{det}}\varepsilon_{\text{loss}}$ for ^{57}Zn. The X distribution for ^{57}Zn in BigRIPS is shown in blue. Selecting ^{57}Zn in BigRIPS and ZeroDegree results in the distributions depicted in red. Both histograms overlay in the region of full transmission after scaling the latter by $1/\varepsilon_{\text{det}} = 1.075$ (empty target) and by $1/\varepsilon_{\text{det}}\varepsilon_{\text{loss}} = 1.235$ (physical runs), which is shown by the green histograms.

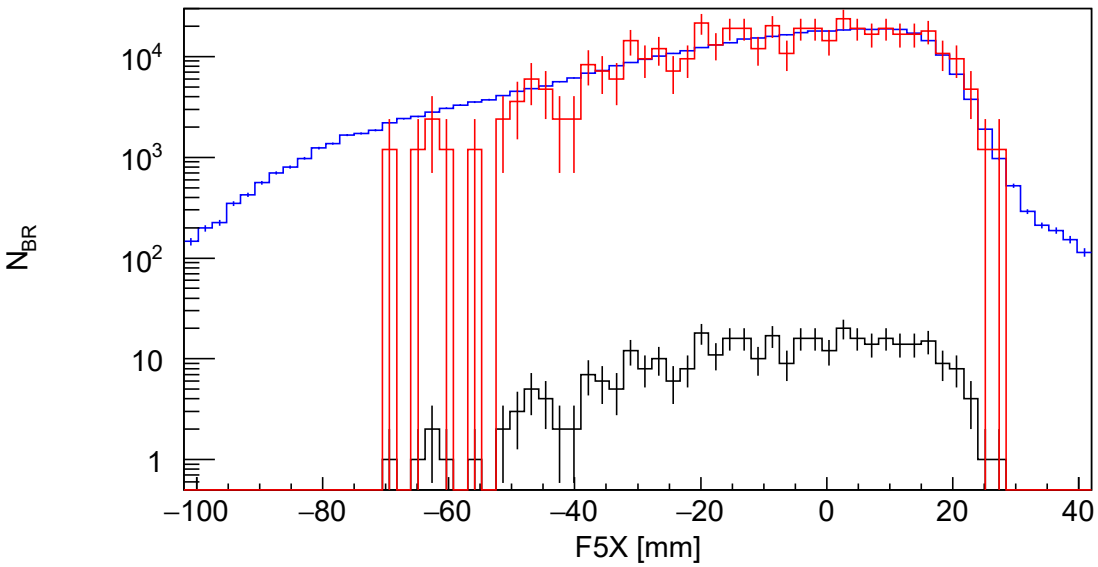

Figure 10.27: Illustration of the determination of the $N_{\text{daughter, ZD}}/N_{\text{parent, BR}}$ ratio needed for the ^{57}Zn(Be,X)^{56}Zn cross section calculation. The histogram represented in blue is the F5X distribution of the incoming ^{57}Zn nuclei. The black histogram was obtained after selecting ^{56}Zn in ZeroDegree. Both histograms overlay when the latter is scaled by $\left(N_{\text{parent, BR}}\,\varepsilon_{\text{det}}\,\varepsilon_{\text{loss}}\right)/N_{\text{daughter, ZD}}$ in the region of full transmission (red histogram).

Chapter 11

Results

This chapter presents the first γ-ray spectroscopy of ^{56}Zn following the data analysis presented in the preceeding sections. The number of identified transitions, their adopted energies, intensities and uncertainties as well as the placement of the corresponding excited states in the level scheme is discussed hereafter. The experimental results are discussed according to shell-model calculations performed by S. M. Lenzi.

11.1 γ-ray spectra.

According to the PID plot shown in figure 10.9(b), γ rays detected in DALI2+ in coincidence with ^{56}Zn nuclei stem from two possible mechanisms of excitation. On the one hand, incoming ^{56}Zn nuclei in BigRIPS may undergo inelastic excitation on the Be target and, on the other hand, ^{56}Zn may be produced by one-neutron knockout from ^{57}Zn. The corresponding γ-ray spectra without any constraint on crystal multiplicity are compared in figure 11.1, demonstrating that one-neutron knockout is the main source of ^{56}Zn excitations in this experiment. The much lower rate of incoming ^{56}Zn ions in BigRIPS also explains the much smaller number of counts in the γ-ray spectrum with a selection on ^{56}Zn in both spectrometers.

All the above suggests that it is possible to attempt the fit of the ^{56}Zn γ-ray spectrum by selecting ^{56}Zn in ZeroDegree only while still assuming a double exponential function for describing the background below the lineshapes[1]. By doing so it is possible to include a number of events in which the incoming ^{57}Zn was not successfully identified in BigRIPS due to the limited efficiency of the beam-line detectors and pileup events in the F7 TEGIC that give rise to the tails extending towards larger vlues of Z in the PID of figure 10.9(b). This spectrum trades cleanliness off for larger statistics and results in a larger γ-ray background since only the selection of prompt γ rays

[1]It is anticipated here that the correlation of the parameters describing the background with the fitted γ ray energies is weak.

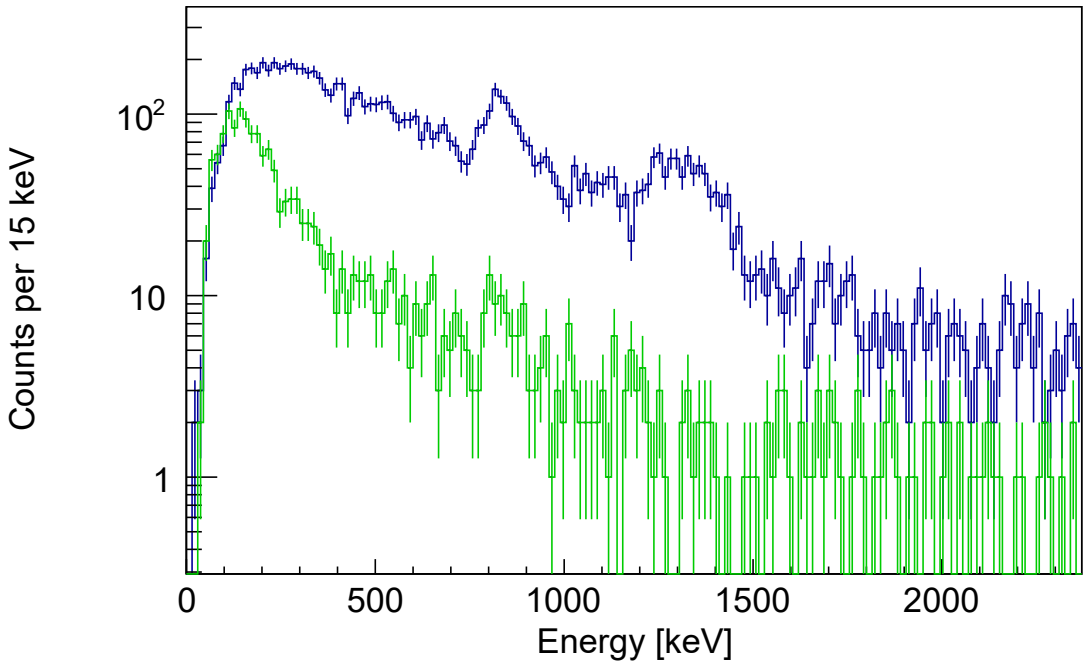

Figure 11.1: Comparison between γ-ray spectra with a selection of ^{56}Zn in BigRIPS and ZeroDegree (green) and a selection of ^{57}Zn in BigRIPS and ^{56}Zn in ZeroDegree (blue).

(besides the cut on the ZeroDegree identification plot) was imposed for generating the spectrum. The example of the $6_1^+ \longrightarrow 4_1^+$ γ ray in the ^{52}Fe test case discussed in the previous chapter also showed that imposing restrictive multiplicity conditions may hamper the identification of weaker lines in cascades with many γ rays in spite of the larger P/T. Hence this case was chosen in order to get a preliminary hint on the number of lineshapes that should be included when fitting cleaner spectra. Including a single lineshape was sufficient for reproducing the photopeak at 830 keV, whereas this was not possible for the strength between 1200 keV and 1500 keV which was modelled by two lineshapes in an unresolved doublet. The fit is compared with the experimental spectrum in figure 11.2.

Then, experimental spectra were generated under more restrictive conditions in order to enhance the P/T. They were fitted including the three transitions in all cases as shown in figures 11.2, 11.3, 11.4 and 11.5. All spectra were Doppler-corrected using a calculated mid-target β of 0.517 and a table of polar angles constructed assuming instantaneous γ-ray emission. Immediate deexcitation was assumed for simulating and Doppler-correcting the lineshapes used for fitting as well. The latter results in deviations below 1 keV for lifetimes up to 10 ps for the three transitions so that lifetime effects were not considered as an additional source of systematic uncertainty. The lifetime of the simulated γ decays included in the fit was varied in this study while

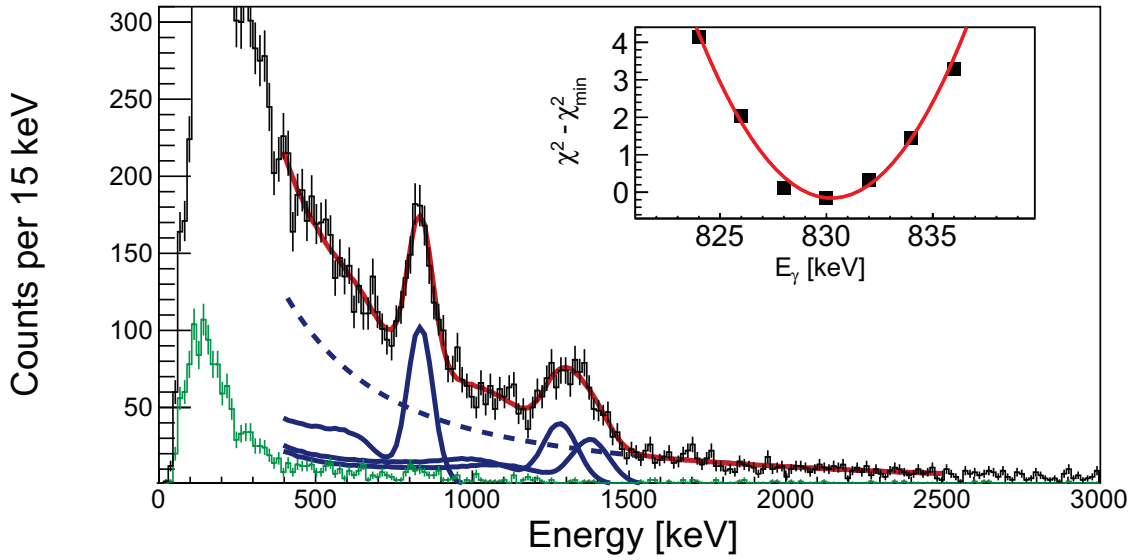

Figure 11.2: γ-ray spectrum without add-back, observed in coincidence with ^{56}Zn in ZeroDegree only. The spectrum shown in green is obtained by selecting ^{56}Zn in both separators. The fit was performed between 400 keV and 2500 keV.

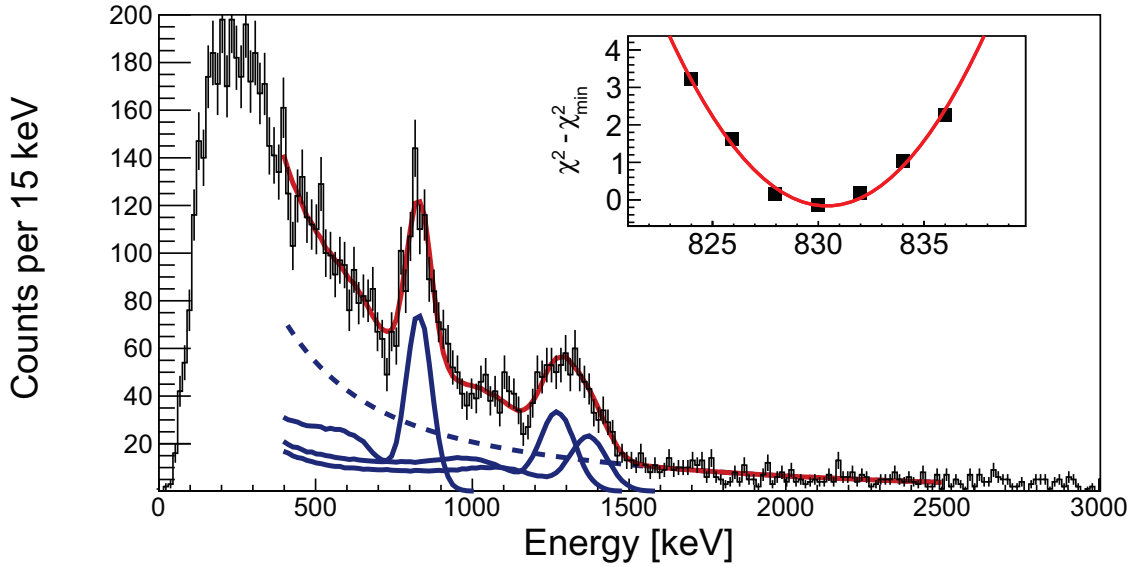

Figure 11.3: γ-ray spectrum without add-back, observed in coincidence with ^{56}Zn in ZeroDegree and ^{57}Zn in BigRIPS. The fit was performed between 400 keV and 2500 keV.

maintaining the same table of angles and using the mid-target β for correcting the Doppler shifts in the simulation.

The experimental spectrum that provides the lowest uncertaintities in the energies was chosen among those of figures 11.2, 11.3 and 11.4. Statistical uncertainties between 3-4 keV were obtained without applying the add-back procedure. They are reduced to 3 keV when using the add-back, nevertheless this spectrum was not used

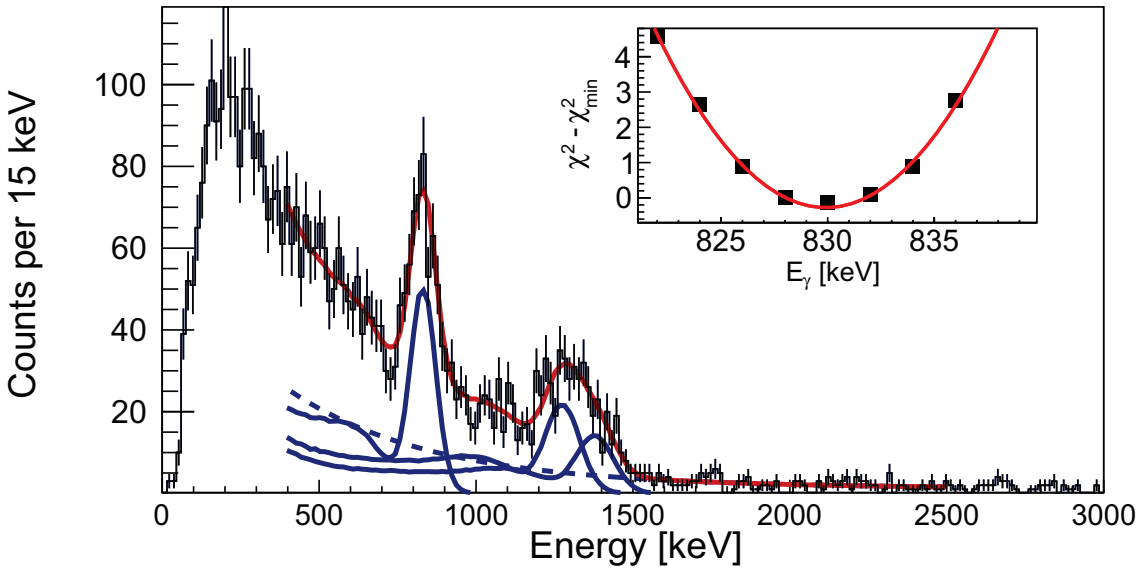

Figure 11.4: γ-ray spectrum without add-back, observed in coincidence with ^{56}Zn in ZeroDegree and ^{57}Zn in BigRIPS and restricted to events with crystal multiplicities below 5. The fit was performed between 400 keV and 2500 keV.

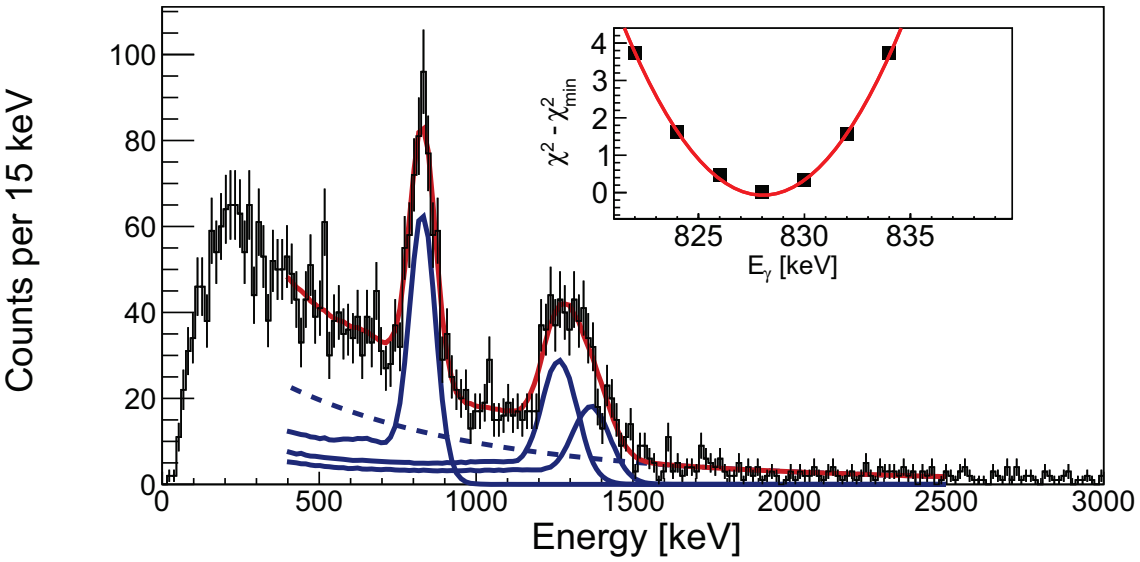

Figure 11.5: γ-ray spectrum with add-back, observed in coincidence with ^{56}Zn in ZeroDegree and ^{57}Zn in BigRIPS and restricted to events with γ-ray multiplicities below 4. The fit was performed between 400 keV and 2500 keV.

for choosing the adopted energies in this work because of the systematic shift towards lower energies illustrated in section 10.6 and explained in section 10.2.3. Calculated χ^2 curves for the γ rays forming the doublet are represented in figure 11.6, which demonstrates the existence of a well-defined global minimum regardless of the data set

under consideration. Slightly different error bars, however, were deduced depending on the data set and the transition. For the $\sim 1270\,\text{keV}$ γ-ray (which is the more intense in the doublet), statistical uncertainties dwindle when the P/T is enhanced and the spectrum gated on the knockout channel with a cutoff on DALI2+ multiplicities below 5 was the optimum one, among those without addback, for determining the energy of this γ ray. The uncertainty in the energy of the $\sim 1380\,\text{keV}$ γ ray is, on the other hand, unaffected by the data set. More restrictive cutoffs on crystal multiplicities yielded larger uncertainties and were not imposed.

Spectrum	$E_{\gamma 1}$	$I_{\gamma 1}$	$E_{\gamma 2}$	$I_{\gamma 2}$	$E_{\gamma 3}$	$I_{\gamma 3}$
Fig. 11.2	830(4)	100(5)	1278(13)	74(16)	1376(15)	58(11)
Fig. 11.3	830(4)	100(7)	1272(15)	87(16)	1380(16)	64(13)
Fig. 11.4	830(4)	100(5)	1272(12)	76(18)	1380(15)	58(13)
Fig. 11.5	828(3)	100(7)	1260(10)	79(17)	$1371(^{+21}_{-15})$	52(24)

Table 11.1: γ ray energies in keV and intensities obtained from the fits of ^{56}Zn γ ray spectra.

It can be noticed in the χ^2_P plots that different energies are deduced when using the spectrum without a selection on ^{57}Zn in BigRIPS. This is simply attributed to a change in the χ^2_P shape following the difference in statistics. The extracted energies and their uncertainties for the spectra represented in figures 11.2, 11.3, 11.4 and 11.5 gspec are given in table 11.1. The adopted intervals for the γ ray energies that are used for discussing the results are those of the spectrum with a selection on ^{57}Zn in BigRIPS and crystal multiplicities below 5, that is, 830(5) keV, 1272(13) keV and 1380(16) keV, in which the additional 0.4% of uncertainty discussed in section 10.6 was quadratically added to the statistical uncertainty given as a symmetric confidence interval. The inclusive cross sections for the population of the corresponding excited states are 8(1)(1) mb, 7(1)(1) mb and 5(1)(1) mb.

11.2 Level scheme

The level scheme of ^{56}Zn was constructed on the grounds of $\gamma\gamma$ coincidences, γ-ray intensities and a comparison with the mirror nucleus ^{56}Fe.

Figure 11.7(a) shows the $\gamma\gamma$ matrix constructed with a selection on the one-neutron knockout channel and using the γ-ray energies after add-back, without any constraint on the multiplicity of γ rays. The 830 keV line is coincident with the 1272 keV and 1380 keV transitions and projecting the matrix on the upper and the lower portions of the doublet, marked in red in figure 11.7(a), reveals the coincidence between these two γ rays. This is also evident in the background-substracted projections of the $\gamma\gamma$ matrix

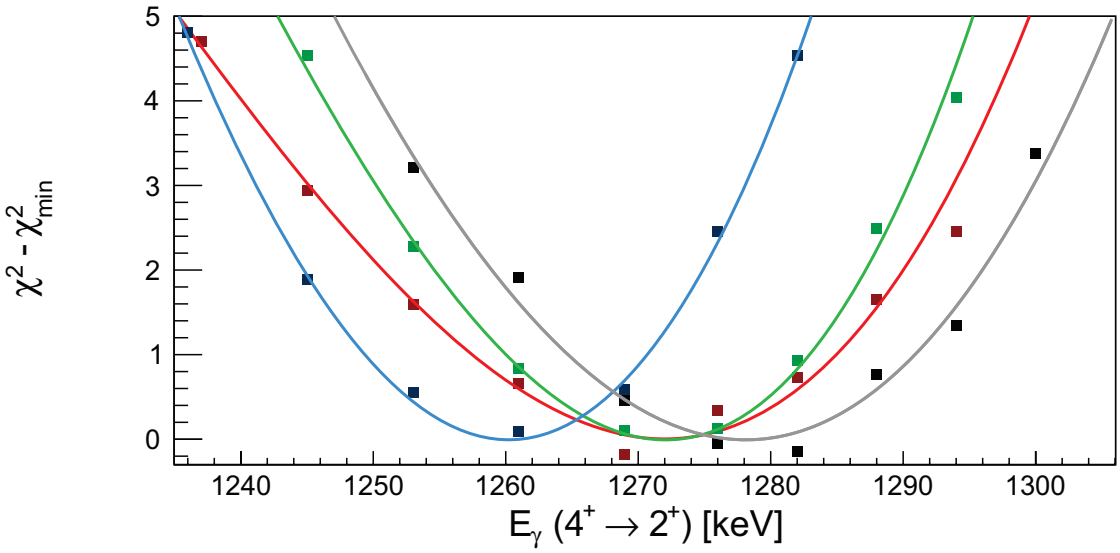

(a) $4_1^+ \longrightarrow 2_1^+$ transition.

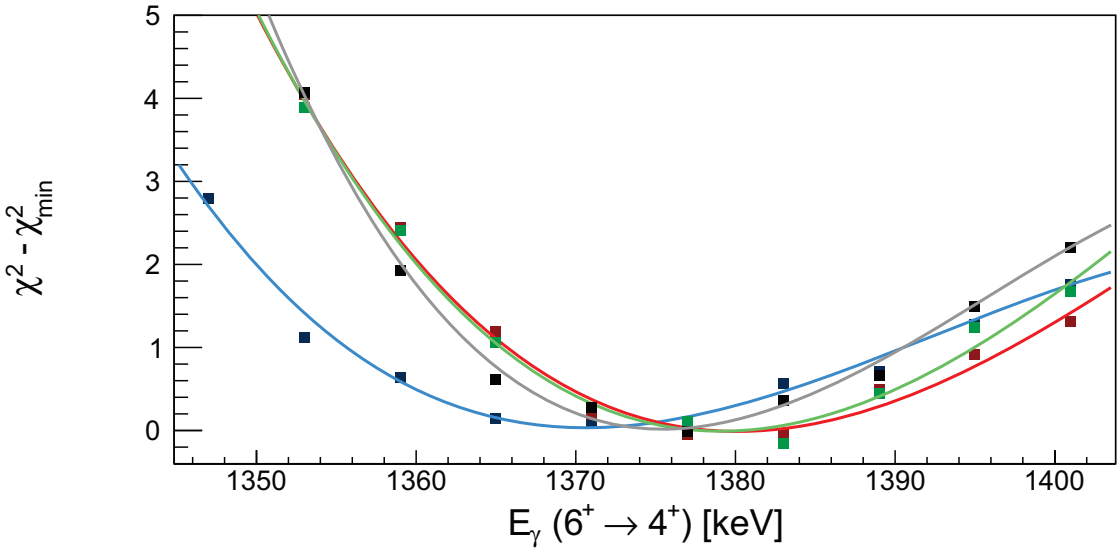

(b) $6_1^+ \longrightarrow 4_1^+$ transition.

Figure 11.6: χ^2 values for the energy of the anticipated $6_1^+ \longrightarrow 4_1^+$ and $4_1^+ \longrightarrow 2_1^+$ transitions in ^{56}Zn obtained from different selections on the data: selection of ^{56}Zn in ZeroDegree only w/o addback (black), ^{57}Zn in BigRIPS and ^{56}Zn in ZeroDegree w/o addback (red), ^{57}Zn in BigRIPS and ^{56}Zn in ZeroDegree w/o addback and cutoff on crystal multiplities below 5 (green), ^{57}Zn in BigRIPS and ^{56}Zn in ZeroDegree with addback and cutoff on γ multiplicities below 4 (blue). Calculated values were fitted by the third order polynomial functions represented by the solid lines.

represented in figure 11.7(b). The intensities are given in table 11.1 and suggest the ordering of the transitions in the cascade. Among the observed γ rays, the 830-keV one is the most intense whereas the 1380-keV γ ray is the least intense and starts the

cascade. The proposed level scheme is summarized in figure 11.8(b) and consists of three excited states with energies of 830(5) keV, 2102(14) keV and 3482(21) keV. The spin and parity assignments are based on a comparison with the level scheme of the $T_z = +2$ mirror partner ^{56}Fe[90] which is represented in figure 11.8(a). The latter shows all the known excited states in ^{56}Fe up to 3.8 MeV that give rise to 3-fold γ ray cascades.

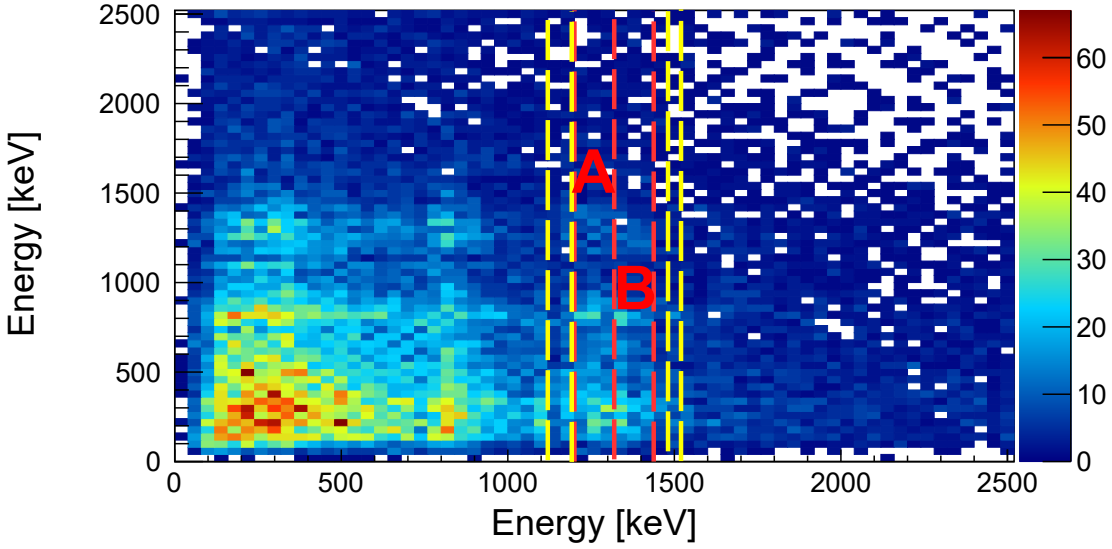

(a) $\gamma\gamma$ coincidence matrix.

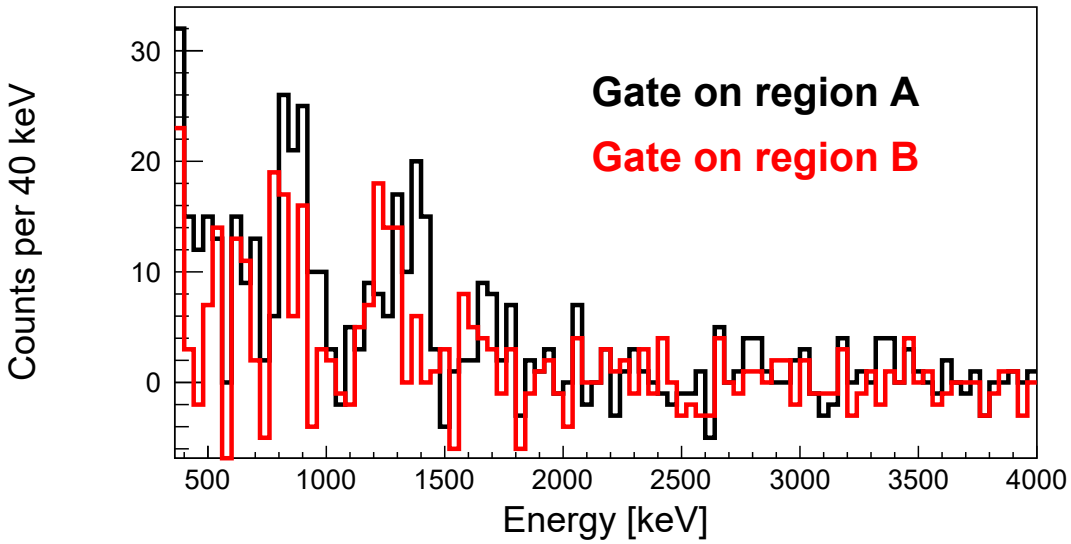

(b) Background-substracted coincidence spectra.

Figure 11.7: The lower panel shows coincidence spectra projected onto the energy ranges marked in red in the $\gamma\gamma$ matrix. Coincidence spectra gated on either side of the doublet are marked in yellow and were substracted from the projections in order to remove spurious coincidences. The add-back algorithm was applied to generate the spectra.

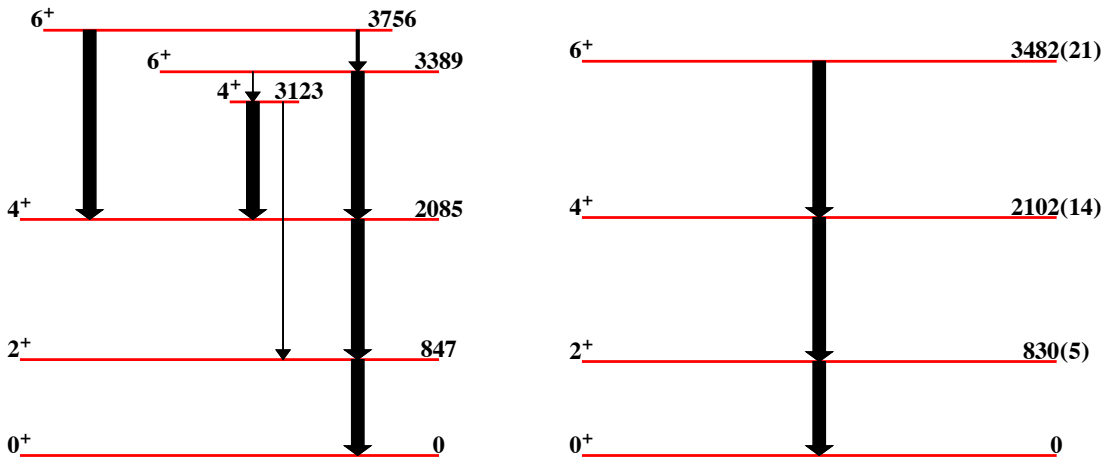

(a) ^{56}Fe (b) ^{56}Zn

Figure 11.8: Comparison between the level scheme of ^{56}Zn determined in this work and the $T_z = +2$ mirror partner ^{56}Fe[90]. Only excited states decaying by cascades with 3 γ rays are included in the level scheme of ^{56}Fe. The width of the arrows is representative of the branching fraction, if any. Spin assignments for the ^{56}Zn excited states are indicated in the level scheme and are based on this comparison.

11.3 Discussion

The available experimental information of MEDs and TEDs in the $f_{7/2}$ shell is abundant since proton-rich nuclei close to the $N = Z$ line were easily populated in the past using fusion-evaporation reactions and their γ-ray spectroscopy was customarily conducted with conventional HPGe arrays. The information regarding MEDs in the upper fp shell, that is, for those nuclei whose valence nucleons fill the $p_{3/2}$, $p_{1/2}$ and $f_{5/2}$ orbitals is, on the contrary, scarcer. According to the analysis performed by Ekman et al.[192], MEDs in this region arise as a result of the interplay between the Coulomb multipole term and the monopole term only where the latter would be given by the Thomas-Ehrman shift. In spite that its contribution was empirically deduced from the $A = 57$ mirror pair, a particularly good agreement with experimental data was found and in general it matched the accuracy of the MED studies in the $f_{7/2}$ shell.

More information has been published since then and specifically for nuclei above $A = 60$. Kaneko et al.[202] analyzed the MEDs in the ^{67}Se/^{67}As pair and found that a radial term proportional to the occupancy of the $p_{3/2}$ orbital with $a_m = 280\,\text{keV}$ reproduced the MED in the $\frac{25}{2}^+$ and the $\frac{29}{2}^+$ states, in which a sharp drop of the $p_{3/2}$ occupancy towards the $g_{9/2}$ orbital occurs. Although initial studies in this region

did not include the V_B multipole term, MED and TED analyses in $A = 66$[203, 237] showed that the Coulomb multipole term alone did not account for the experimental data. The apparent mismatch was compensated by introducing the V_B interaction acting systematically in all the shells with the same strength[203] and a comparison of the recently published spectroscopy of ^{70}Kr[238] with the calculations performed by Kaneko et al.[203] further corroborates this description and the persistence of V_B into the upper fp shell. The contributions stemming from the radial term have been neglected in these works so that the electromagnetic spin-orbit term and the Coulomb correction are the only monopole corrections that break isospin symmetry significantly.

For nuclei with a few valence nucleons outside a ^{56}Ni core, the occupancies of the p orbitals will be large so that a strong interplay between radial effects and the ISB multipole term is expected. It is the aim of this section to address this topic and gain insight into the actual role of the p orbitals in the MEDs of this region and thus to shed light on the interpretation of the monopole radial term at the same time.

Wave functions of excited states were computed with the shell model using the KB3G interaction. The MEDs are described following the approach presented in the introductory chapter: the ll and ls terms are well established ISB monopole interactions of electromagnetic origin and the Coulomb interaction between the valence particles is introduced in the multipole term which is calculated from theory. The first γ-ray spectroscopy of ^{58}Zn was recently published[239] and allows a simultaneous MED analysis of the $T_z = -2$, $A = 56$ and the $T_z = -1$, $A = 58$ pairs in order to validate the model. For the $A = 58$ pair, the $f_{7/2}$ shell remains fully filled and the number of pairs in each shell does not change significantly between the 2^+ and the 4^+ state: in such a situation the multipole term yields the same contribution to the MED in both states. There is, as shown in figure 11.9, a pronounced change in the MED of the 2^+ in comparison with that of the 4^+. As it is shown in figures 11.11(a) and 11.11(b), this pattern occurs in parallel with a higher occupancy of the p orbitals, and specially the $p_{3/2}$ one, by the valence neutrons in ^{58}Ni in the 4^+ state in comparison with the 2^+ state. Such change in the MED from the 2^+ to the 4^+ can be well reproduced in the same manner as in the $f_{7/2}$ shell, namely introducing two radial terms each one proportional to the corresponding occupancy of the p orbital and with the constant $a_m \approx 300$ keV -see definition in eq. (8.5)-. The MEDs calculated according to this model are underestimated by around 100 keV so that this prompts one to add the V_B multipole term acting in all the shells with the same strength as in the $f_{7/2}$ shell, $\sim$-75 keV [201], which finally yields good agreement between experimental and calculated MEDs. Since the $f_{7/2}$ contributions to the multipole term are negligible, the case of the $A = 58$, $T_z = -1$ pair gives strong evidence of V_B acting in all the

orbitals of the valence space regardless of the actual nature of the radial term, which is responsible for the change in the sign of the MED in the 4^+ state in comparison with the 2^+.

Bearing in mind this information, we now turn to the $A = 56$, $T_z = -2$ mirror pair in order to test the model employed for the radial term. The MED analysis for this pair is shown in figure 11.10. The small MED in the 2^+ state, as well as its microscopic configuration similar to the ground state results in a rather low sensitivity to the different ISB terms. On the contrary, the MED in the 4^+ state is a sensitive probe for the radial term: as shown in figure 11.11(d) (11.11(c)), the neutron (proton) occupancy of the $p_{3/2}$ is higher (smaller) in the 4^+ state of ^{56}Fe and, furthermore, the multipole term plus the ll and ls terms give an almost vanishing contribution to the MED. The analogue situation for the $p_{1/2}$ occurs in the 6^+ in which the $p_{3/2}$ occupancy is restored to the values of the ground state and the 2^+. The MEDs of the 4^+ and the 6^+ are thus sensitive to the $p_{3/2}$ and $p_{1/2}$ radial terms, respectively, and can be reproduced within 20 keV in exactly the same manner as in $A = 58$ and with identical a_m strengths of 300 keV for both orbitals. Notice that this accuracy is virtually the same than in previous studies of MEDs using the KB3G interaction[192].

The link of the employed prescription for the radial term with a huge radius of p orbits was already pointed out in a calculation performed by Ekman[192]. The presented data thus provides evidence that the monopole radial effects in the lower

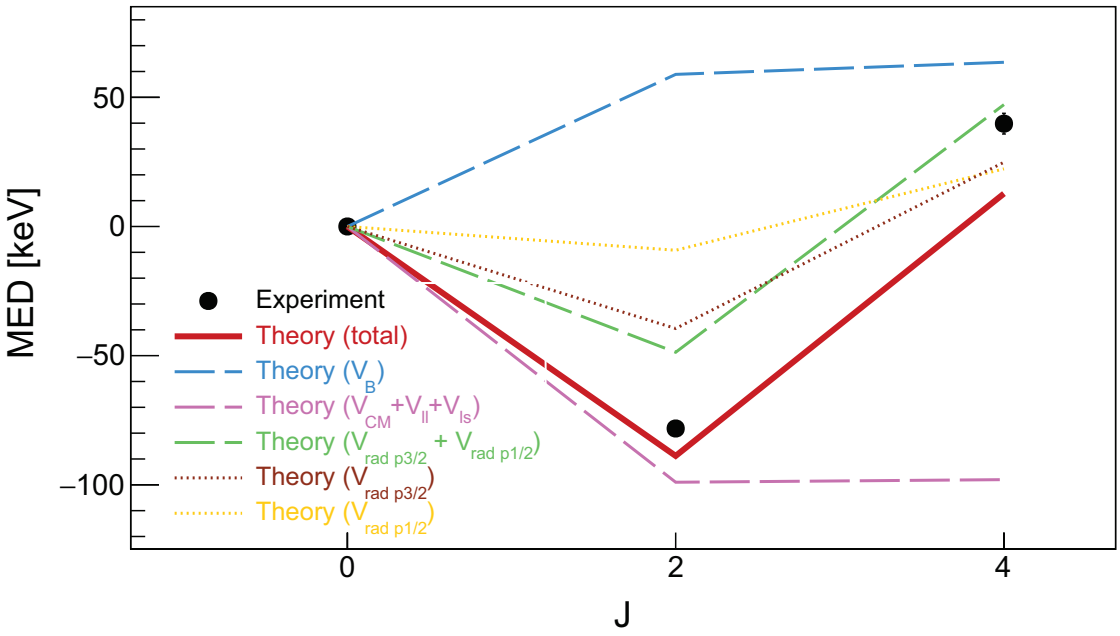

Figure 11.9: Comparison between experimental and calculated mirror energy differences in the $T_z = -1$, $A = 58$ pair.

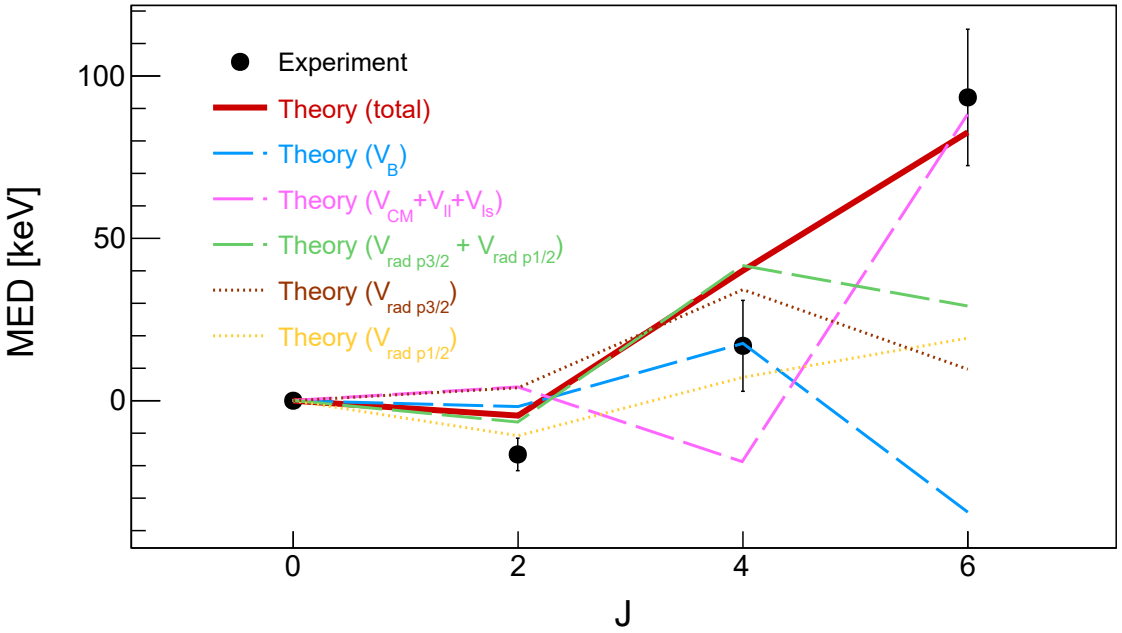

Figure 11.10: Comparison between experimental and calculated mirror energy differences in the $T_z = \pm 2$, $A = 56$ pair.

part of the upper fp shell can be solely attributed to the occupancy of p orbits with a much larger radius than the f ones and in this sense it is reasonable to associate the similar strength parameters $a_m(p_{3/2})$ and $a_m(p_{1/2})$ to the l dependence of the radii. The significance of these results may be better understood in connection with the data collected on isotope shifts and the analysis of nuclear radii[240] which suggest viewing the p orbits as halo orbits. Moreover, recent studies in the sd shell[241] have shown that the radius of a certain orbital is reduced when it is occupied by at least one nucleon. This is certainly the case of the $p_{3/2}$ orbital and much better agreement with the data can be found using e.g. $a_m(p_{3/2}) = 200\,\text{keV}$ and $a_m(p_{1/2}) = 400\,\text{keV}$, representing a possible change in the $p_{3/2}$ radius with respect to the $p_{1/2}$ one due to the increased occupancy of the former. More experimental data is needed to address these topics and establish the systematics of the different terms contributing to the MEDs around $A = 60$.

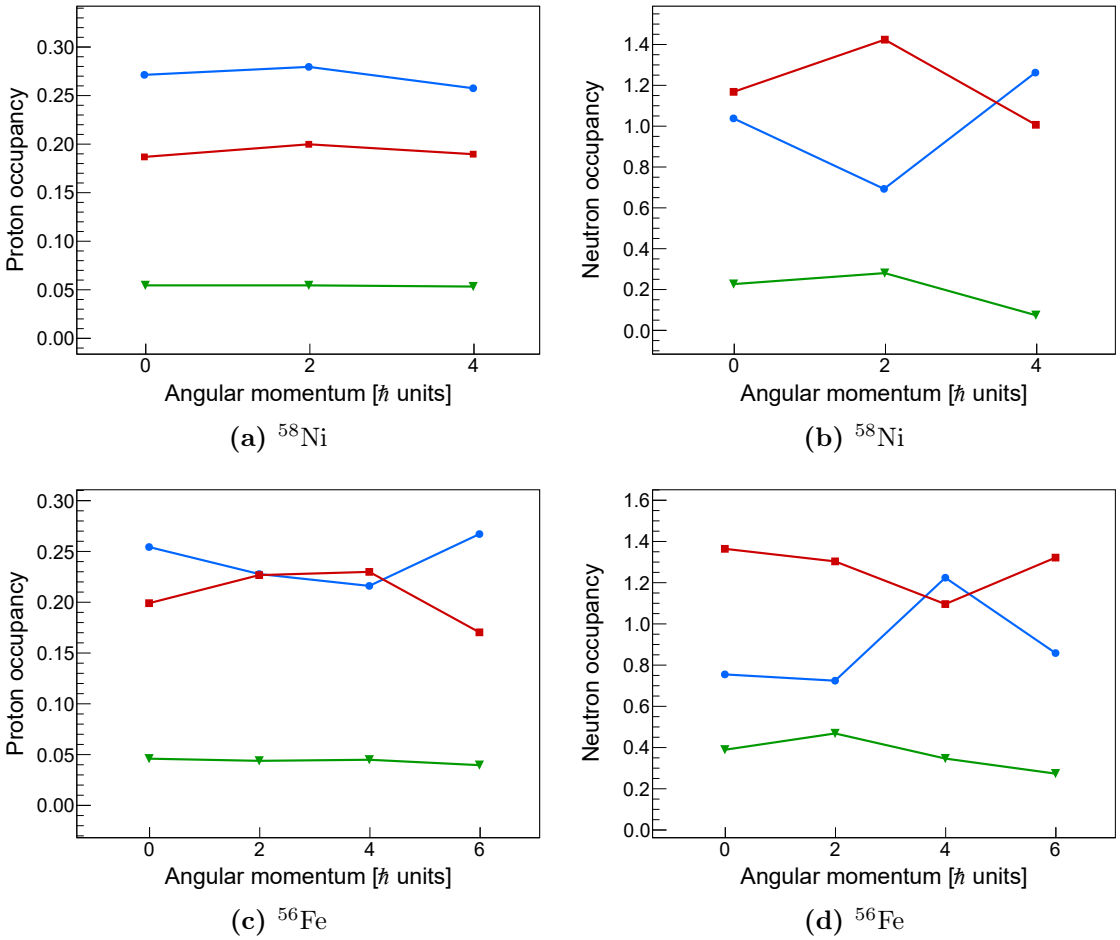

(a) ^{58}Ni **(b)** ^{58}Ni

(c) ^{56}Fe **(d)** ^{56}Fe

Figure 11.11: Proton and neutron occupation factors of the $p_{1/2}$ (green), $p_{3/2}$ (red) and $f_{5/2}$ (blue) orbitals for ^{56}Fe and ^{58}Ni. They were calculated using the KB3G interaction.

Chapter 12

Summary

In summary, the first spectroscopy of the ^{56}Zn nucleus has been presented. This nucleus has been populated in an RIB experiment that enabled the unambiguous identification of the produced ^{56}Zn nuclei while correlating them with the γ rays detected in the DALI2+ spectrometer. Three transitions have been observed and the level scheme has been constructed on the basis of temporal coincidences and γ-ray intensities. Mirror symmetry arguments have been invoked in order to assign the spin and parity to the excited states.

The ^{56}Zn nucleus is now the heaviest $T_z = -2$ nucleus in which excited states are known. Whereas there is a wealth of data on nuclei in the $f_{7/2}$ shell and also well above $A = 60$, where the $f_{7/2}$ shell is essentially closed, the information on MEDs for nuclei around and above ^{56}Ni is much more scarce. Thus the MED analysis of the ^{56}Fe/^{56}Zn pair has been performed and has been cross-validated with the $T_z = \pm 1$, $A = 58$ pair using the recently published data on ^{58}Zn[239]. The large occupancies above the $f_{7/2}$ shell amplify ISB effects in the p and $f_{5/2}$ orbitals and provide independent evidence for the presence of the isovector interaction V_B, different from the multipole Coulomb one, acting in all shells. This conclusion is in agreement with a previous work on the $T_z = \pm 1$ pairs in $A = 66$ and $A = 70$[203, 238].

Furthermore, the observed MEDs are extremely sensitive to the actual role of the p orbits in the observed MEDs via the monopole radial term: the occupancy of the p shells present significant variations among some of the excited states and these changes correlate with large MEDs of monopole origin. We find that a reasonable agreement between experimental and calculated MEDs is attained by extrapolating the description originally proposed for describing the MEDs in the $f_{7/2}$ shell. According to this ansatz, the occupancy of p orbits changes the Coulomb energy as a result of the larger radius in p orbits than in f orbits. The value of the a_m constant relating the p occupancy and the strength of the radial term is found to have a value around

300 keV, close to the value of 350 keV originally used by Zuker et al. below ^{56}Ni[187].

Contrary to the explanations invoking the Thomas-Ehrman shift[192] for interpreting the radial term in this mass region, these findings support its interpretation as a measure of p occupancy regardless of the degree of nuclear deformation. We have linked these results with the conclusions obtained by Bonnard et al. on nuclear radii from their study of isotope shifts near $A = 48$[240], in which the $p_{3/2}$ orbital is suggested to play a crucial role through a huge radius.

Appendices

Appendix A

DSAM simulations

The following figures show how the sensitivity to the lifetimes of interest in the experiment E693 depends on the target thickness. The simulations were performed with the software APCAD[60] and used as a guide for choosing the actual thicknesses of the DSAM targets used in the experiment. The lineshapes correspond to γ rays depopulating ^{212}Po nuclei produced in the reaction ^{12}C(^{208}Pb, ^{12}C)^{8}Be at a CM energy of 63.7 MeV. A 0.5 $^{mg}/_{cm^2}$ reaction layer made of graphite is assumed in the simulations. Doppler correction has been performed using $\theta_L \approx \theta_\gamma$ (see eq. (1.47)) and $\beta(^{212}\text{Po}) \approx 0.068$.

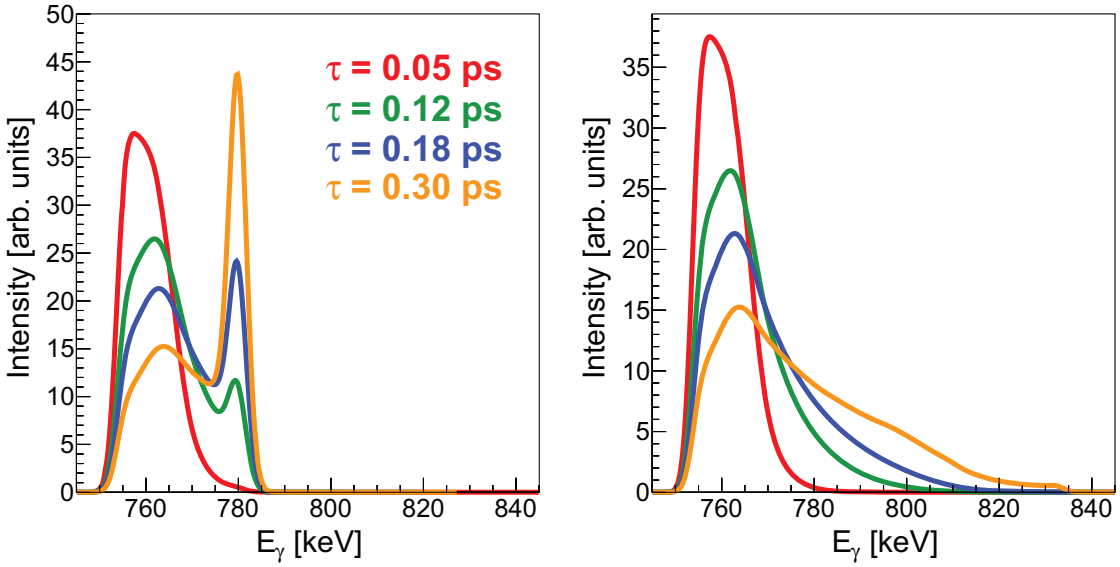

(a) 13.5 $^{mg}/_{cm^2}$-thick Au backing **(b)** 38.0 $^{mg}/_{cm^2}$-thick Au backing

Figure A.1: Integrated lineshapes in the range of polar angles between 120° and 170°. The energy of the transition is 780 keV.

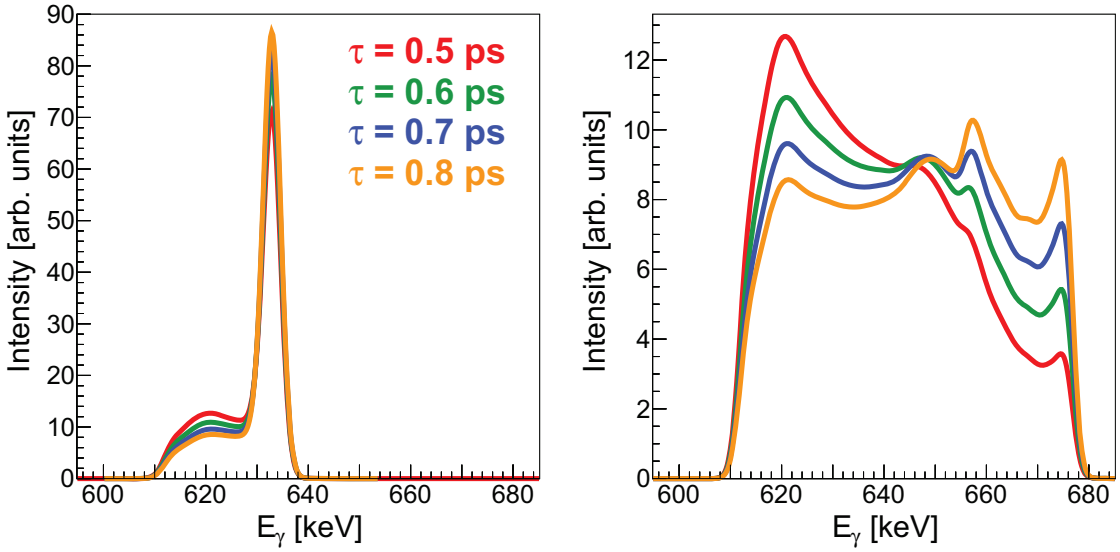

(a) 13.5 $^{mg}/_{cm^2}$-thick Au backing **(b)** 38.0 $^{mg}/_{cm^2}$-thick Au backing

Figure A.2: Integrated lineshapes in the range of polar angles between 120° and 170°. The energy of the transition is 633 keV.

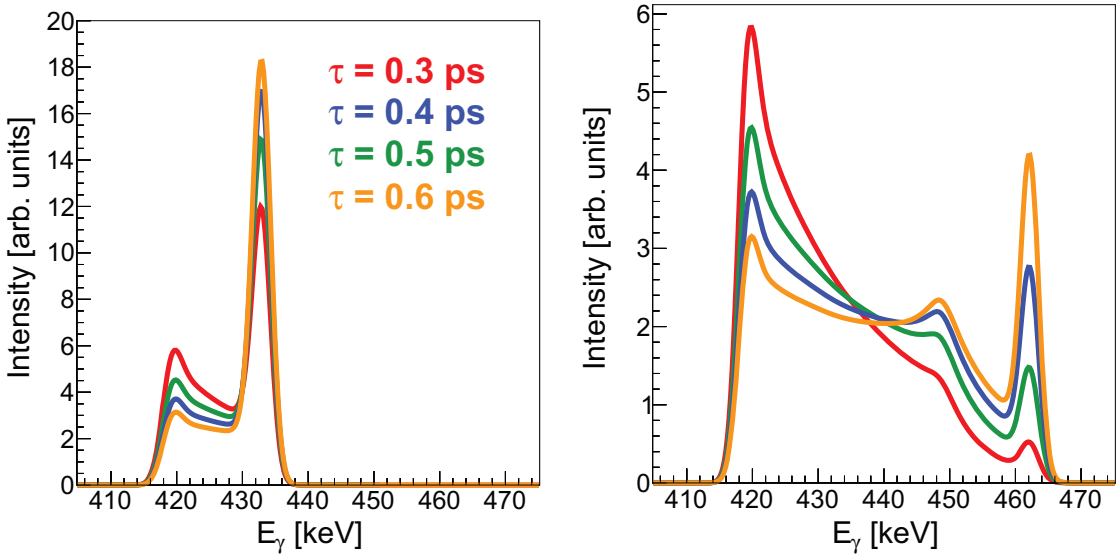

(a) 13.5 $^{mg}/_{cm^2}$-thick Au backing **(b)** 38.0 $^{mg}/_{cm^2}$-thick Au backing

Figure A.3: Simulated lineshapes for the angular slice 165°±5°. The energy of the transition is 433 keV.

Appendix B

Particle energy distributions

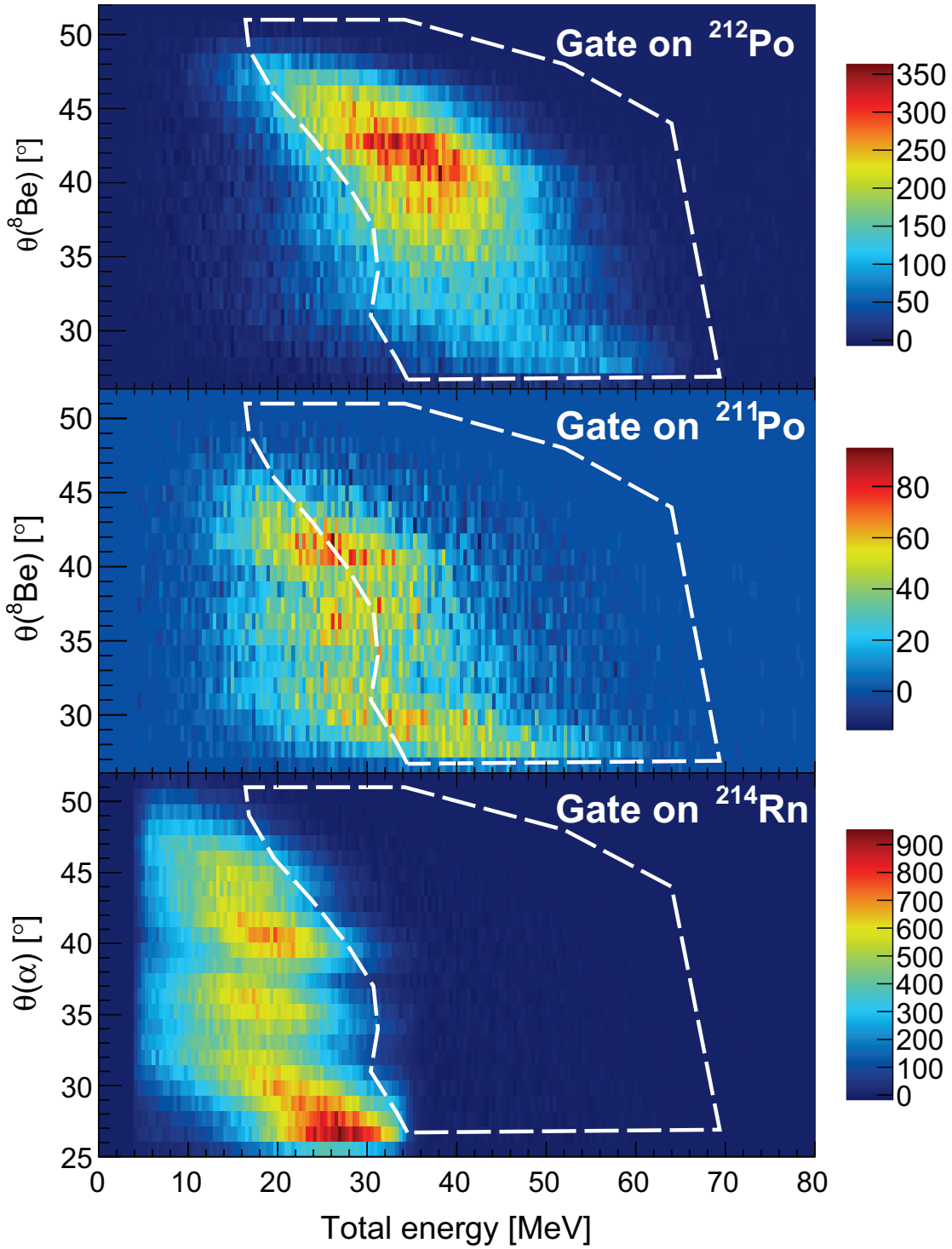

Figure B.1: Distributions of total DSSSD energies observed in coincidence with ^{214}Rn, ^{211}Po and ^{212}Po γ rays. Only energy depositions in 2 non-adjacent rings were considered to generate the ^{211}Po and ^{212}Po distributions. All the distributions are restricted to the regions $100° < \varphi < 150°$ and $300° < \varphi < 360°$ The region enclosed by the white, dashed line represents the selection used for recovering ^{212}Po events. Data was taken with the self-supporting target.

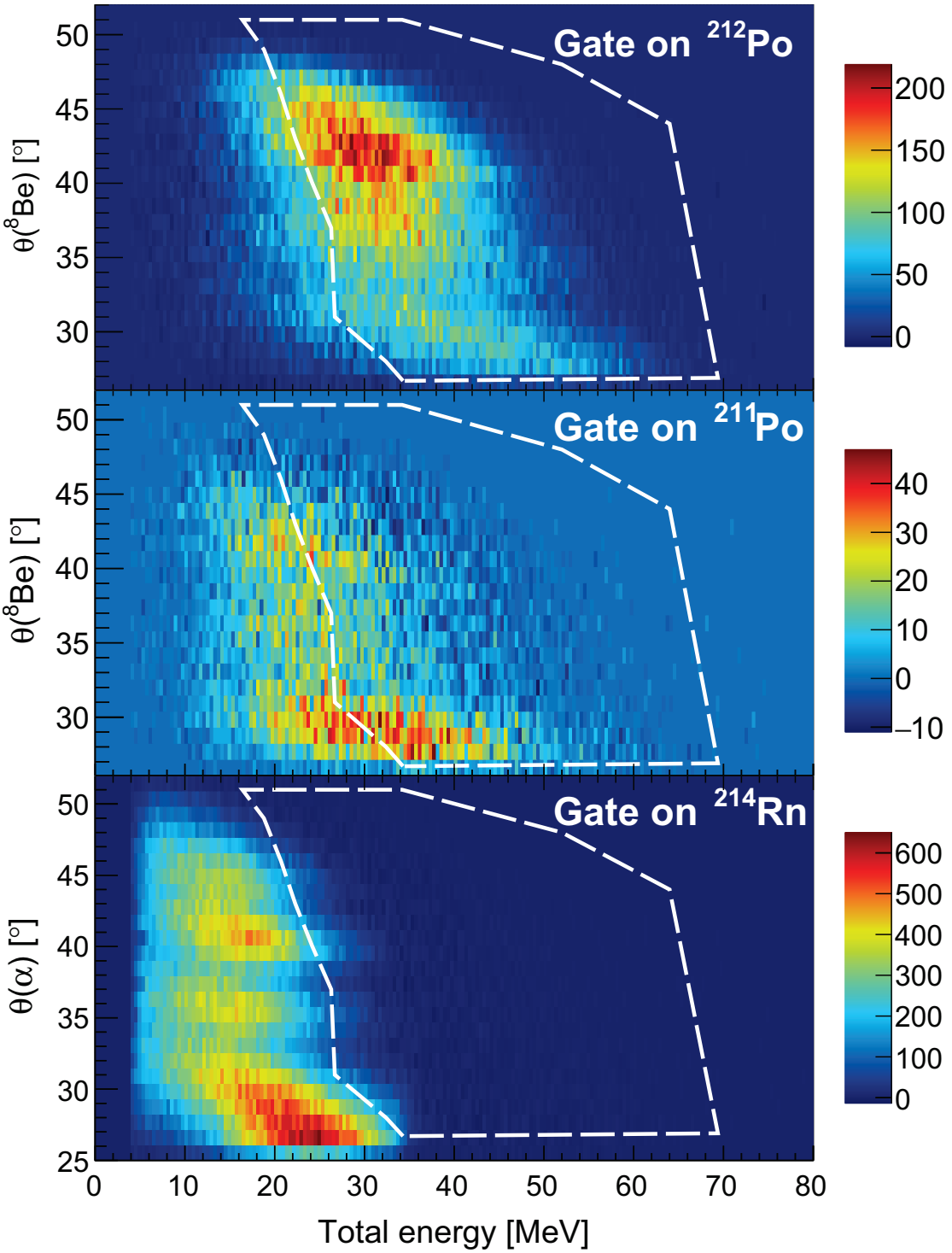

Figure B.2: Distributions of total DSSSD energies observed in coincidence with ^{214}Rn, ^{211}Po and ^{212}Po γ rays. Only energy depositions in 2 non-adjacent rings were considered to generate the ^{211}Po and ^{212}Po distributions. All the distributions are restricted to the region $0° < \varphi < 100°$. The region enclosed by the white, dashed line represents the selection used for recovering ^{212}Po events. Data was taken with the self-supporting target.

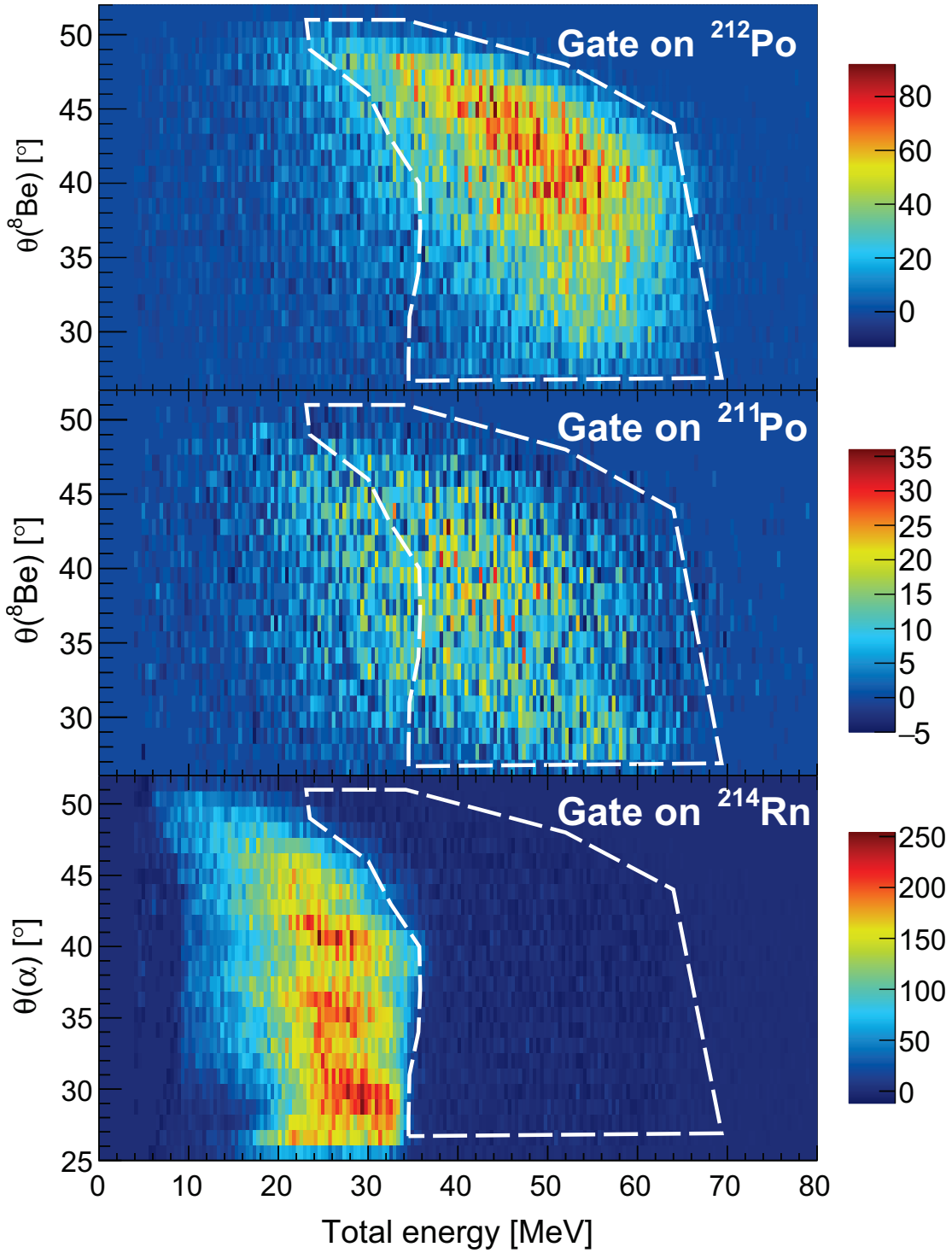

Figure B.3: Distributions of total DSSSD energies observed in coincidence with ^{214}Rn, ^{211}Po and ^{212}Po γ rays. Only energy depositions in 2 non-adjacent rings were considered to generate the ^{211}Po and ^{212}Po distributions. All the distributions are restricted to the region $150° < \varphi < 300°$. The region enclosed by the white, dashed line represents the selection used for recovering ^{212}Po events. Data was taken with the self-supporting target.

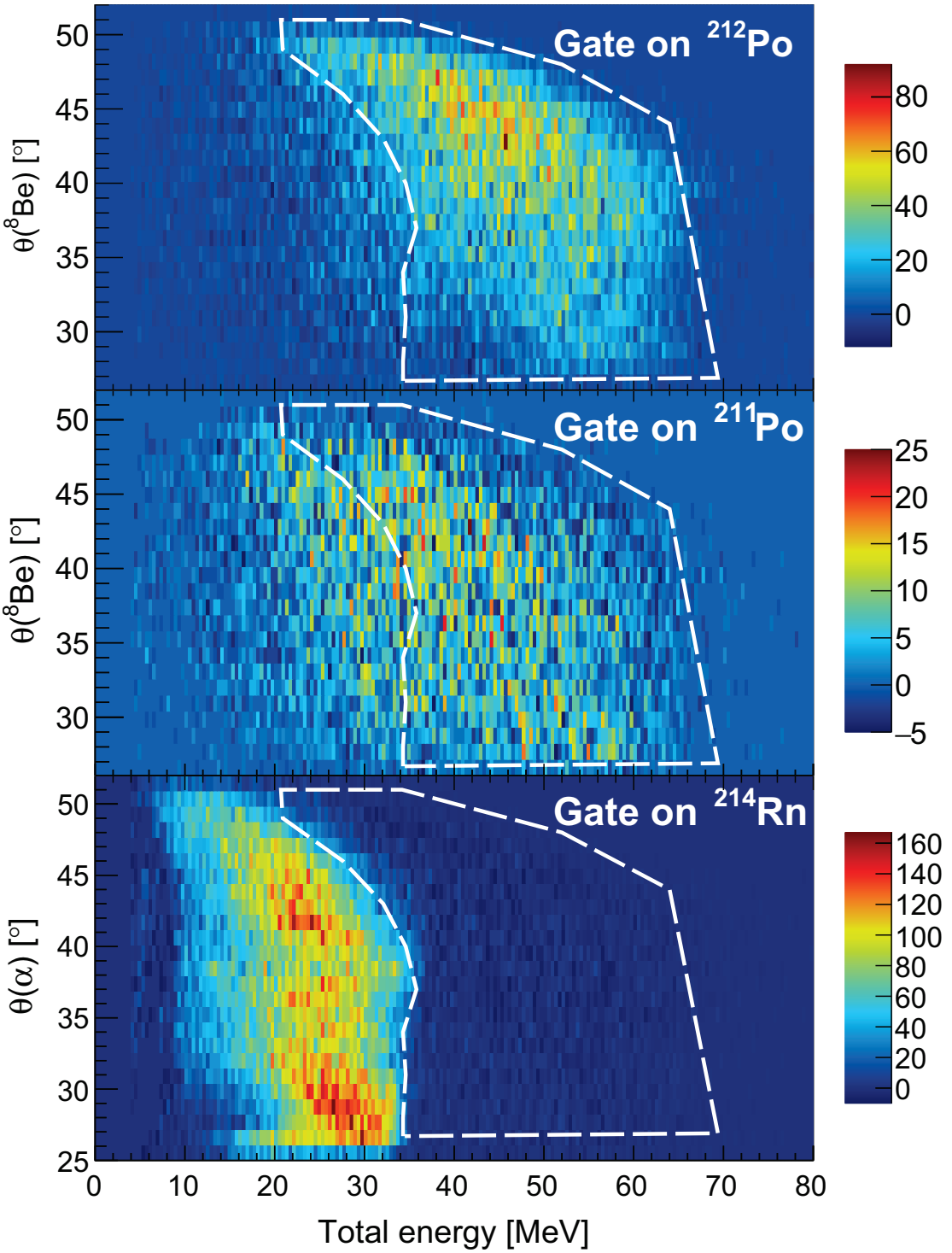

Figure B.4: Distributions of total DSSSD energies observed in coincidence with ^{214}Rn, ^{211}Po and ^{212}Po γ rays. Only energy depositions in 2 non-adjacent rings were considered to generate the ^{211}Po and ^{212}Po distributions. All the distributions are restricted to the regions $100^{\circ} < \varphi < 150^{\circ}$ and $300^{\circ} < \varphi < 360^{\circ}$. The region enclosed by the white, dashed line represents the selection used for recovering ^{212}Po events. Data was taken with the self-supporting target.

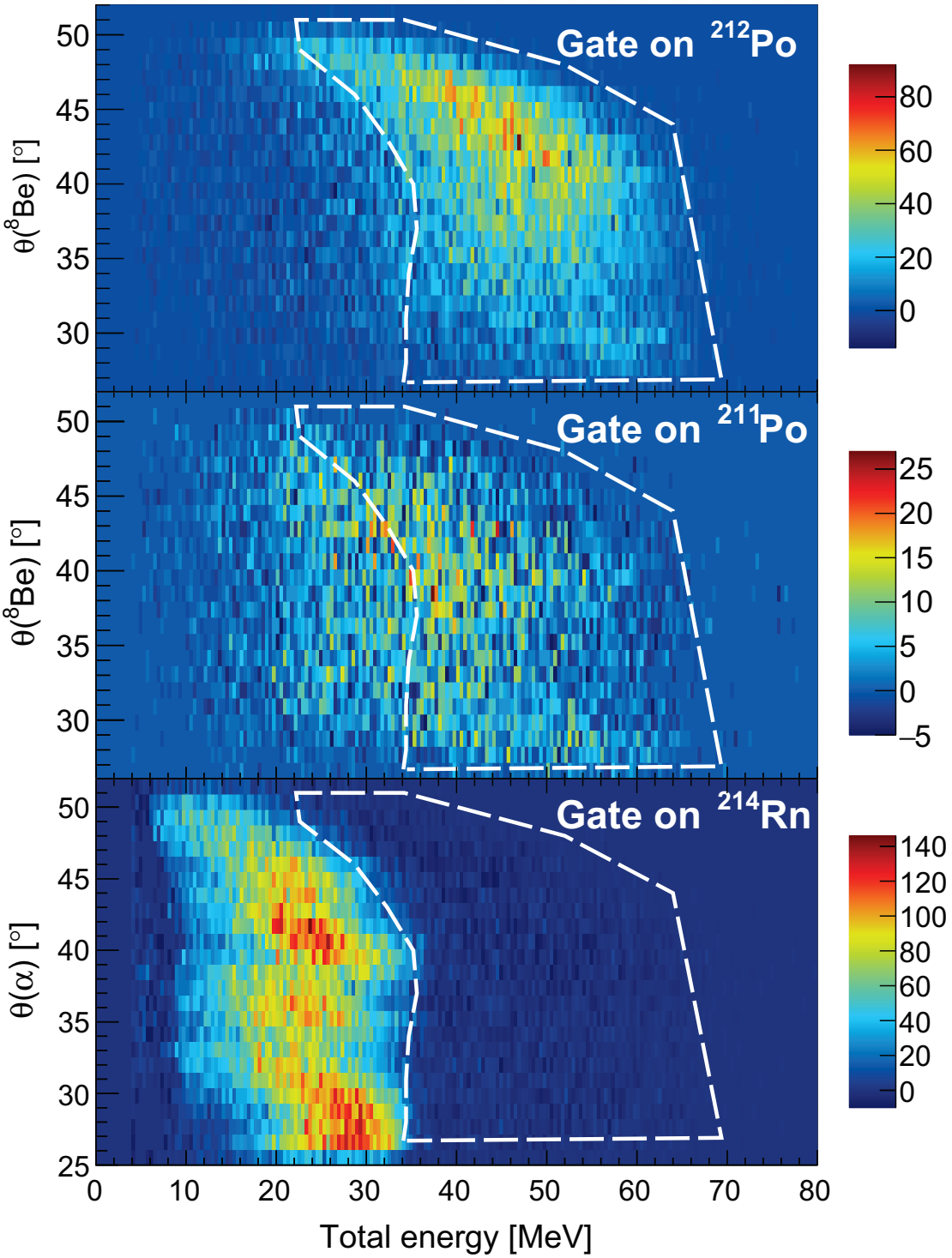

Figure B.5: Distributions of total DSSSD energies observed in coincidence with ^{214}Rn, ^{211}Po and ^{212}Po γ rays. Only energy depositions in 2 non-adjacent rings were considered to generate the ^{211}Po and ^{212}Po distributions. All the distributions are restricted to the region $0° < \varphi < 100°$. The region enclosed by the white, dashed line represents the selection used for recovering ^{212}Po events. Data was taken with the self-supporting target.

Appendix C

Resumen en castellano (parte I)

C.1 Introducción

La condensación de partículas α en el núcleo atómico es un efecto conocido de la interacción nuclear en núcleos ligeros[77, 78] y que coexiste con la existencia de capas nucleares que dan lugar a los números mágicos. En este tipo de núcleos la formación de estos clústers está asociada con grandes probabilidades de transición entre estados de una banda rotacional generada por una gran deformación nuclear.

Hoy en día se considera que el efecto de la interacción espín-órbita unido a la separación de los niveles de Fermi de protones y neutrones[93] impide la formación de clústers, tal y como ocurre en los núcleos ligeros, en núcleos con masas bien por encima del ^{56}Ni. Sin embargo, se han examinado a este respecto energías de ligadura, efectos de capas y probabilidades de decaimiento calculadas según el modelo de capas[94, 95, 98, 100]. En estos trabajos se encuentran deficiencias en las cantidades calculadas teóricamente que se atribuyen a la existencia de correlaciones 2p2n adicionales que posibilitarían la formación de clústers en regiones de masas más pesadas dentro de la carta de núcleos.

En este sentido, el núcleo ^{212}Po es el único caso en núcleos pesados en el que se ha propuesto la existencia de estados de naturaleza α-core sobre una evidencia experimental. De este núcleo se conocen probabilidades de transición entre estados de la banda fundamental que no se pueden reproducir dentro de los cálculos del modelo de capas[108]. La anchura de decaimiento α desde el estado fundamental ha sido objeto de numerosos estudios y tampoco se ha podido reproducir en este tipo de cálculos[103–106]. Se sabe que todas estas discrepancias se resuelven considerando una probabilidad de preformación adicional de la partícula alpha dentro de la función de onda, de manera tal que se ponen en igualdad de condiciones las correlaciones dentro del modelo de capas y las correlaciones adicionales que generan dicho clúster[107, 111,

112].

En un experimento de espectroscopía γ analizado por Astier y colaboradores[109, 113], se pobló el núcleo ^{212}Po mediante la reacción de transferencia ^{208}Pb(^{18}O, ^{14}C)^{212}Po. Se encontraron varios dobletes en torno a 2 MeV que decaen mediante transiciones electromagnéticas de multipolaridad 1 hacia el estado yrast con el mismo momento angular. En base a las vidas medias medidas de estas transiciones se propuso que dichos estados decaen mediante transiciones de tipo eléctrico muy colectivas, y que por lo tanto estos estados constituyen una evidencia de un movimiento oscilatorio α-core, siendo esta la primera evidencia experimental directa de estados de naturaleza α-core en núcleos tan pesados.

Se propusieron a continuación varios modelos para describir dichos estados[115, 114]. Las publicaciones que recogen estos modelos incluyen también las predicciones de los mismos que son contrastables desde un punto de vista experimental bajo condiciones de más sensitividad que en los experimentos previos con este núcleo. Con este fin y el de extraer nuevas vidas medias utilizando la técnica DSAM se planteó el experimento que se describe en la primera parte de esta memoria.

C.2 Técnica y montaje experimental

El experimento objeto de este trabajo se realizó en el laboratorio de GANIL y en él se puebla el núcleo ^{212}Po mediante la reacción de transferencia α en cinemática inversa ^{208}Pb(^{12}C, ^{8}Be)^{212}Po. La cinemática de esta reacción proporciona una sensibilidad excepcional para la medida de vidas medias mediante DSAM y al mismo tiempo permite mejorar la eficiencia de detección usando un trigger de partículas y detectando las dos partículas α procedentes del decaimiento α del ^{8}Be.

Como detector de partículas cargadas se usó un detector de Silicio circular[117] (DSSSD) de diámetro interno 32 mm y externo 85 mm. El DSSSD está segmentado en anillos concéntricos en el lado n y en sectores circulares en el lado p. Dicha segmentación permite identificar la marca experimental unívoca del ^{8}Be producido en el canal de transferencia, que es la detección de dos partículas α en píxeles separados menos de 5 mm. El posicionamiento del detector a 34 mm por detrás blanco y cubriendo ángulos polares entre 26° y 52° se escogió como un compromiso entre una energía del haz lo más baja posible por encima de la barrera coulombiana, la dependencia con la energía del máximo de la sección eficaz como función del ángulo polar, la necesidad de parar todos los núcleos ^{12}C dispersados elásticamente del blanco, permitir a los fragmentos de fisión abandonar la cámara de reacción y las restricciones introducidas por la propia geometría de la cámara. El DSSSD se protegió de los ^{12}C procedentes

de las reacciones elásticas colocando capas concéntricas de Ta que proveyeron de un espesor neto de Ta dependiente del ángulo polar. De esta forma se permite pasar a las partículas α frenando al mismo tiempo todos los núcleos de ^{12}C.

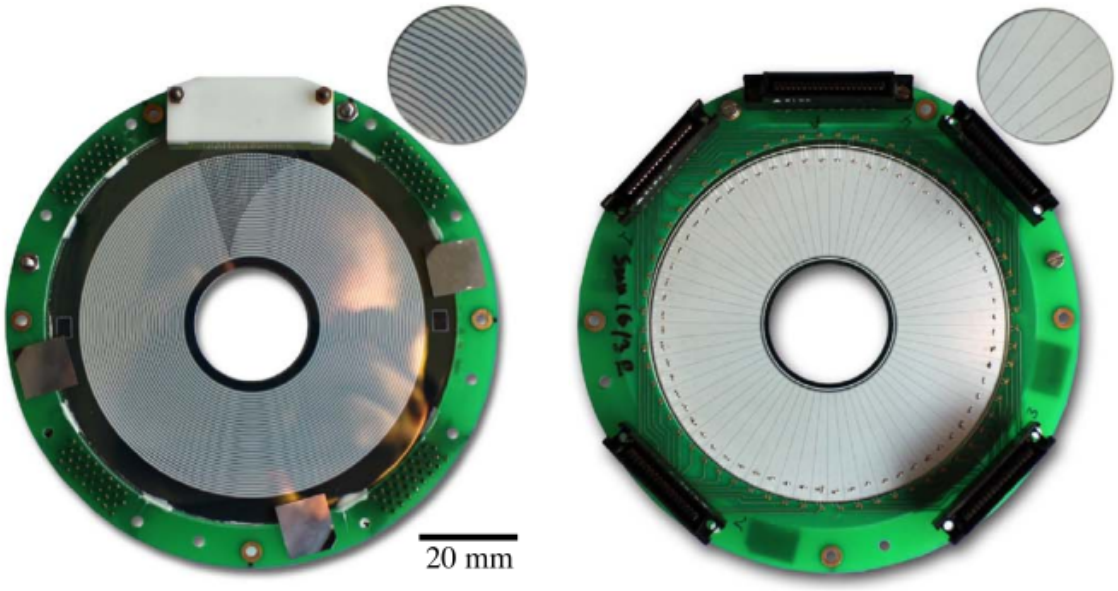

Figure C.1: Vista frontal (imagen de la izquierda) y trasera (imagen derecha) del modelo de DSSSD usado en el experimento. La figura ha sido adaptada de [117].

El espectrómetro γ AGATA[131] se usó para medir la energía de las transiciones entre estados excitados del ^{212}Po. Este espectrómetro es un proyecto internacional que representa una nueva generación de espectrómetros γ enfocados a conseguir una alta eficiencia en la detección de la energía total de la radiación incidente y una resolución espacial sin precedentes para poder corregir el efecto Doppler de manera precisa. Estas propiedades se consiguen mediante el uso de algoritmos de análisis de la forma del pulso (del inglés Pulse Shape Analysis, PSA) y algoritmos de tracking que permiten reconstruir el número de fotones y sus interacciones en el espectrómetro a partir de las posiciones en 3D obtenidas del PSA. Cada cristal HPGe que compone AGATA están segmentados eléctricamente en 36 porciones o segmentos. El espectrómetro se fijó en posición nominal, a una distancia de 235 mm por delante del blanco cubriendo ángulos polares del γ entre 120°-130° y 160°-170°.

La condición usada en el experimento para iniciar la escritura de los datos fue la detección de una partícula en el DSSSD en coincidencia con señales en al menos uno o dos cristales de AGATA dependiendo de la medida. Durante el experimento se tomaron medidas a una intensidad del haz de 1 pnA-2 pnA con un blanco de diamante de 0.56 $^{mg}/_{cm^2}$ durante 3 días y durante 2 días a una intensidad entre 0.3 pnA y 1 pnA con un blanco para medir vidas medias mediante DSAM y formado por una capa de

reacción de grafito de 0.49 $^{mg}/_{cm^2}$ y una capa de frenado de oro con un espesor de 13.5 $^{mg}/_{cm^2}$.

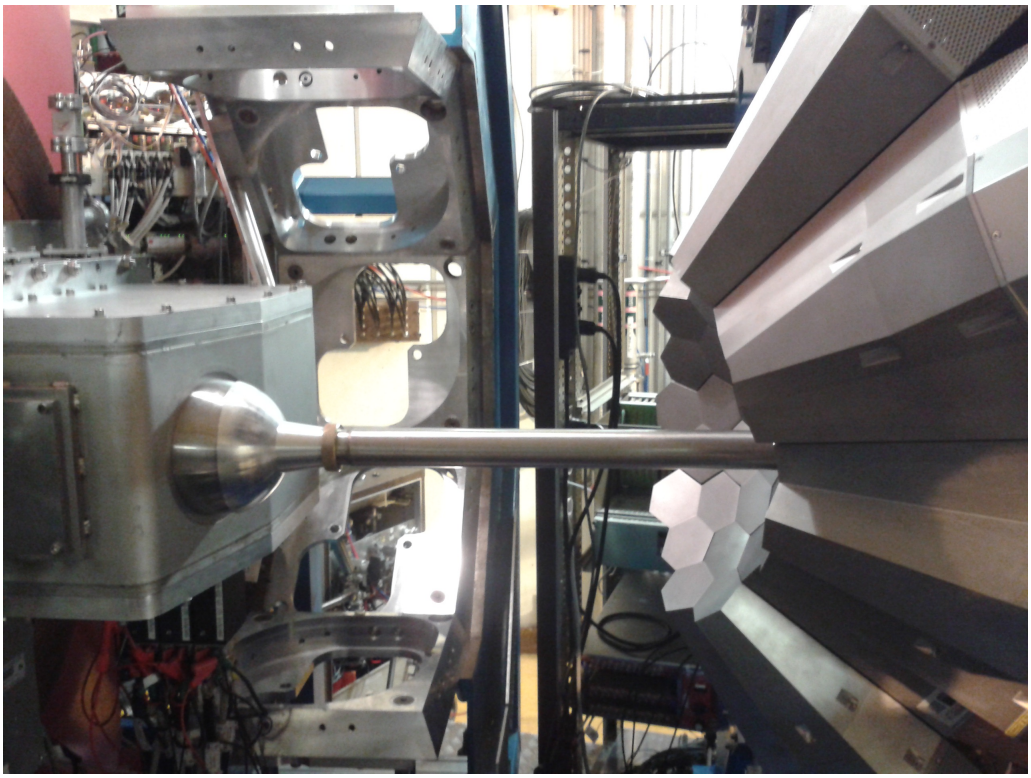

Figure C.2: Imagen de AGATA, el tubo del haz y la cámara de reacción. El haz viene por la derecha.

C.3 Análisis de los datos

Durante el preprocesamiento de los datos se calibraron los 1330 canales de energía procedentes de los segmentos y del contacto central de cada cristal de AGATA. También se introdujeron correcciones destinadas a optimizar la eficiencia del PSA y del tracking, mejorando la resolución temporal y energética de los datos. El DSSSD se calibró en energía usando una fuente triple α. El análisis de los espectros tomados durante el tiempo de haz se ha llevado a cabo usando las energías medidas por los contactos centrales de los cristales, donde la finalidad del tracking en este experimento con baja tasa de conteo por cristal es recuperar las energías depositadas por un fotón en cristales adyacentes usando la información de los segmentos junto con las posiciones extraídas del PSA para refinar la obtención de la posición de la primera interacción del γ.

En las etapas iniciales del análisis se extrajeron condiciones que permiten asociar una multiplicidad física de partículas con una determinada multiplicidad de eventos

en el DSSSD. En particular, se aplicó un algoritmo de add-back a los datos del DSSSD que permite recuperar la energía real depositada por una partícula en el detector y se introdujo un criterio para determinar de forma unívoca el píxel de detección de cada partícula en aquellos eventos con señal en más de un anillo y más de un sector. Este análisis permite hacer también una corrección Doppler precisa combinando únicamente las posiciones de detección en el DSSSD y las posiciones de la primera interacción del γ en AGATA. Para ello se reconstruyó la dirección del ^{8}Be en aquellos eventos con dos partículas α detectadas y se extrajeron mediante simulaciones de Montecarlo $\beta(^{212}\text{Po})$, $\theta(^{212}\text{Po})$ y $\phi(^{212}\text{Po})$ promedios como función de $\theta(^{8}\text{Be})$ y $\phi(^{8}\text{Be})$ permitiendo hacer una corrección Doppler para cada evento particular tras caracterizar los errores sistemáticos en las distancias relativas entre detectores.

Se identificaron cuatro canales de reacción en los datos: **1)** fusión-evaporación α2n con ^{214}Rn en el canal de salida, **2)** fusión-evaporación p2n produciendo ^{217}Fr, **3)** fusión incompleta produciendo ^{211}Po tras la ruptura del ^{12}C en ^{8}Be+α, la fusión de la partícula α con el projectil y la evaporación de 1 neutrón, **4)** reacción de transferencia $^{12}\text{C}(^{208}\text{Pb}, ^{212}\text{Po})^{8}\text{Be}$.

La selección de los eventos del ^{212}Po se llevó a cabo aplicando condiciones sobre la multiplicidad de eventos en el DSSSD junto con una selección basada en la energía total de las partículas en aquellos eventos con multiplicidad 1 de segmentos tras el add-back. Se estima que alrededor de un 5% de eventos originados por reacciones de transferencia con ambas partículas α detectadas no se han podido separar de aquellos con una única partícula detectada usando los criterios de selección expuestos en este trabajo. Estos eventos están dominados por el canal de fusión-evaporación α2n y por lo tanto no se han usado para extraer y discutir los resultados expuestos en esta memoria.

Tras separar el canal de transferencia del resto se encontró que, en una cantidad anormalmente alta de casos, γ's del ^{212}Po se encontraban en coincidencia con una única partícula α. Aunque parte de estos eventos se deben a un desalineamiento entre el DSSSD y el haz que hace que se pierda un 26% de los eventos con dos partículas en la porción del DSSSD más alejada del haz por la absorción en el filtro de tántalo de una o ambas, se observó también que hay una gran probabilidad de excitación del ^{8}Be al estado 2^{+} puesto que las desintegraciones α desde este estado dan lugar a una mayor separación espacial entre ambas partículas. Esto último hace que muchas de ellas también se paren en el filtro de tántalo. Comparando los espectros singles correspondientes del ^{212}Po no se encontró, sin embargo, una interferencia apreciable entre la población de estados del ^{212}Po y del ^{8}Be. Esta característica unida a la similitud entre el patrón de intensidades obtenido en este trabajo con el observado

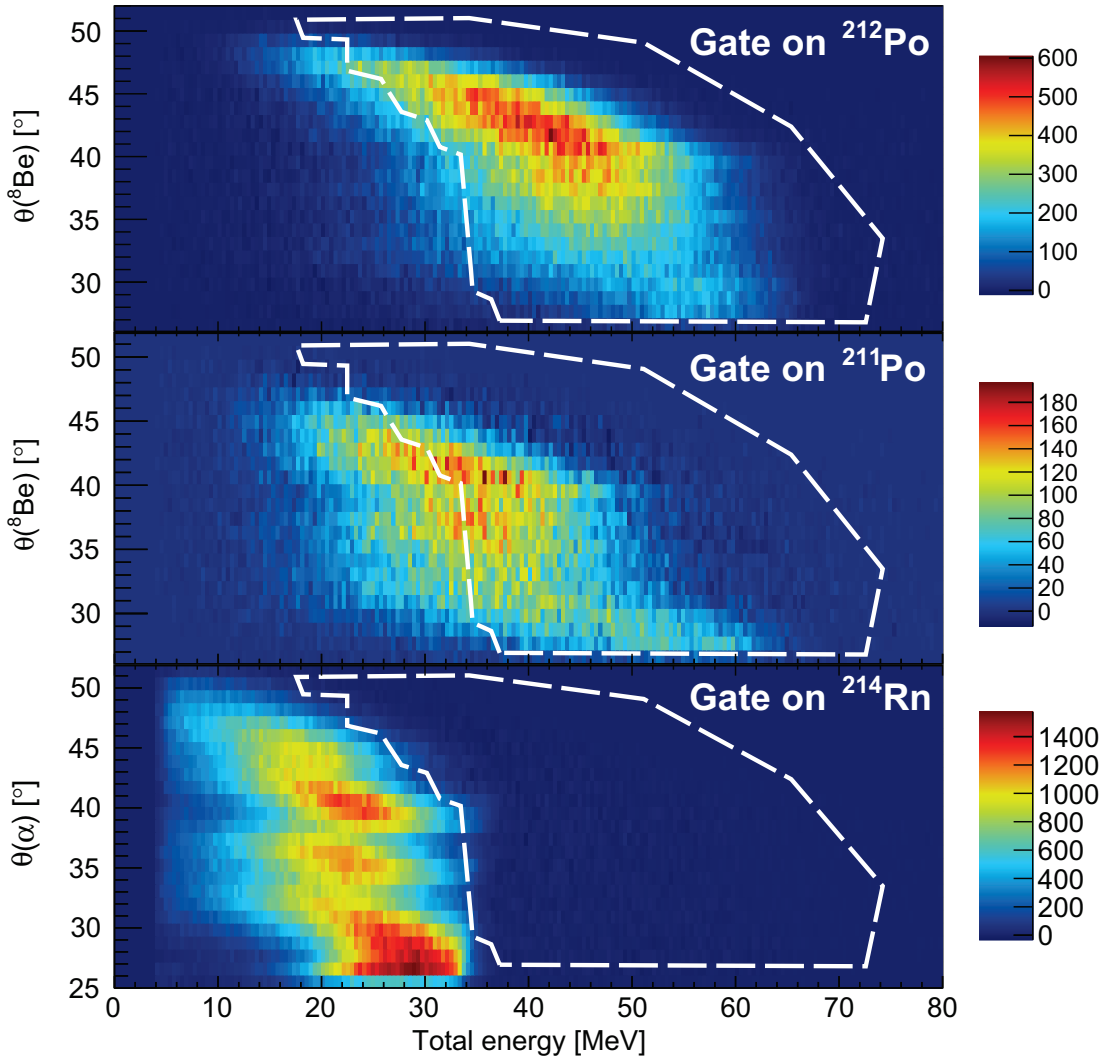

Figure C.3: Distribuciones de energía total depositada en el DSSSD observadas en coincidencia con γ's del ^{214}Rn, ^{211}Po y ^{212}Po y en los datos del blanco de diamante. Sólamente se han considerado deposiciones de energía en dos anillos no consecutivos para generar las distribuciones del ^{211,212}Po. Además, las distribuciones se han restringido a ángulos azimutales $150^\circ < \varphi < 300^\circ$. La línea discontinua delimita la región usada para seleccionar eventos del ^{212}Po en base a la energía total.

por Astier permite una discusión de los resultados del ^{212}Po con independencia de la estructura del núcleo ligero donante en la reacción.

Se estudió asimismo la dependencia del patrón de intensidades con la energía del haz, e igualmente que en un trabajo previo en el que se pobló el núcleo ^{140}Ba mediante la reacción ^{12}C(^{136}Xe,^{140}Ba)^{8}Be[165], se encontró que el mecanismo de la reacción no induce diferencias estadísticamente significativas en la población de estados del ^{212}Po a diferentes energías en torno a la barrera de Coulomb. Una energía del haz más baja sí que resulta, por el contrario, en una menor probabilidad de excitación del ^{8}Be.

La degradación del blanco de DSAM principal usado en la segunda parte del experimento impide una extracción rigurosa de vidas medias mediante la téncica DSAM. De este segundo conjunto de datos se han extraído únicamente cotas superiores a la vida media.

C.4 Resultados y discusión

C.4.1 Estructura de los estados colectivos en base al esquema de niveles y al patrón de intensidades.

El esquema de niveles del ^{212}Po se determinó a partir los datos tomados con el blanco de diamante de 0.56 $^{mg}/_{cm^2}$ y usando matrices de coincidencia $\gamma\gamma$. Las intensidades de las transiciones se determinaron usando espectros de coincidencia corregidos por la eficiencia de AGATA. Dichos espectros se obtuvieron aplicando la selección de los eventos procedentes de reacciones de transferencia α descrita en la sección anterior. Las transiciones que pueblan directamente el isómero 8^+_1 (cuya desexcitación ocurre lejos del blanco y no se observa en el experimento) así como el estado fundamental se identificaron a partir de los espectros singles comparando su intensidad con la de otras transiciones de energía similar presentes en los espectros de coincidencia. La tabla C.1 recoge la lista de intensidades y estados excitados observados en el experimento. El esquema de niveles se representa en las figuras C.4 y C.5.

E_i [keV]	E_f [keV]	E_γ [KeV]	I_γ	J^π_i	J^π_f
1355	1132	222.7(1)	15.3(3)	6^+	4^+
1751	1475	276.1*	6(2)	8^-	8^+
1832	1475	357.1*	7(3)	10^+	8^+
2103	1745	358.8(5)	0.4(2)	$5^{(-)}$	4^-
2376	2017	359.2(4)	0.5(2)	$7^{(-)}$	6^-
2781	2410	371.0(3)	0.7(3)	10	11^-
1132	727	405.0(1)	59.6(2)	4^+	2^+
1537	1132	405.1(2)	1.2(4)	$3^{(-)}$	4^+
1788	1355	432.7(1)	4.2(4)	6^-	6^+
2003	1537	466.3(1)	2.7(3)	$4^{(-)}$	3^-
1986	1475	510.9*	1.4(4)	8^-	8^+
2667	2103	564.2(5)	0.4(2)	$5^{(+)}$	5^-
2103	1537	565.7(4)	0.8(4)	$5^{(-)}$	3^-
2364	1788	575.5(2)	0.9(2)	6	6^-
2410	1832	577.5(2)	2.0(2)	11^-	10^+
2376	1788	588.2(2)	1.8(3)	$7^{(-)}$	6^-

Continúa en la página siguiente

Continuación de la página anterior

E_i [keV]	E_f [keV]	E_γ [KeV]	I_γ	J_i^π	J_f^π
2605	2003	601.6(4)	0.6(2)	5	$4^{(-)}$
1745	1132	612.7(2)	2.3(2)	4^-	4^+
2170	1537	632.5(6)	0.4(2)		3^-
2466	1832	633.4(3)	1.2(2)	10^-	10^+
2422	1788	634.4(4)	0.6(2)		6^-
2017	1355	661.8(2)	2.9(2)	6^-	6^+
2471	1751	719.2(4)	1.9(3)	$9^{(-)}$	8^-
727	0	727.2(1)	100.0(2)	2^+	0^+
2860	2103	756.9(4)	0.5(2)	$5^{(+)}$	5^-
2295	1537	758.4(4)	0.5(3)		3^-
3158	2376	780.9(2)	1.0(1)	$7^{(+)}$	7^-
1513	727	785.7(3)	2.2(3)	2^+	2^+
1537	727	809.6(1)	10.5(7)	$3^{(-)}$	2^+
1946	1132	813.7(1)	4.5(2)	4^-	4^+
2605	1751	853.2(2)	0.4(1)	8	8^-
2701	1832	868.4(4)	0.7(2)	12^+	10^+
2229	1355	873.5(3)	1.1(2)		6^+
2281	1355	926.0(2)	0.6(3)		6^+
1680	727	952.3(3)	3.8(3)	2^+	2^+
2085	1132	952.7(2)	1.8(2)	$(4^+)(\dagger)$	4^+
2103	1132	971.4(3)	4.2(3)	$5^{(-)}$	4^+
2838	1832	1005.8(4)	0.4(2)		10^+
2376	1355	1021.2(4)	0.3(1)	$7^{(-)}$	6^+
2882	1832	1049.4(4)	0.3(1)		10^+
1805	727	1078.4(2)	1.6(2)	2^+	2^+
2641	1537	1104.1(4)	0.4(2)		$3^{(-)}$
2487	1355	1131.6(7)	0.3(2)		6^+
1898	727	1171.2(6)	0.6(3)	$(3^+)(\dagger)$	2^+
2422	1132	1290.1(4)	0.7(2)		4^+
2085	727	1357.6(5)	0.4(2)	$(4^+)(\dagger)$	2^+
2753	1355	1398.1(6)	0.9(4)		6^+
2977	1537	1440.3(5)	0.3(1)		$3^{(-)}$
2175	727	1448.2(7)	1.1(4)		2^+
2592	1132	1459.5(5)	0.6(2)		4^+
2672	1132	1540.0(7)	0.9(3)		4^+
2303	727	1575.7(7)	0.7(3)		2^+
2328	727	1600.3(4)	1.2(3)		2^+
1621	0	1620.6(2)	1.6(3)	1^+	0^+
2976	1355	1621.0(7)	0.6(3)		6^+
2773	1132	1640.6(9)	0.5(2)		4^+
3024	1355	1669.2(8)	0.4(2)		6^+

Continúa en la página siguiente

Continuación de la página anterior					
E_i [keV]	E_f [keV]	E_γ [KeV]	I_γ	J_i^π	J_f^π
1680	0	1679.7(1)	1.2(2)	2^+	0^+
3253	1537	1715.8(5)	0.5(1)		$3^{(-)}$
2498	727	1770.3(4)	1.0(2)		2^+
3045	1132	1912.3(4)	1.6(2)		4^+
3000	727	2272.6(7)	0.9(2)		2^+
2574	0	2574.0(2)	1.0(2)	$(2^+)(\dagger)$	0^+

Table C.1: Lista de estados excitados del ^{212}Po y de las energías e intensidades de las transiciones que los desexcitan. Asignaciones indirectas de espín y paridad llevadas a cabo en este trabajo por comparación con cálculos del modelo de capas se indican con el símbolo (†). Los valores restantes de espín y paridad, así como las energías marcadas con un asterisco, han sido tomados de [109].

En las figuras C.6(a) y C.6(b) se demuestra que el mecanismo de reacción induce una dependencia suave con el momento angular en la sección eficaz exclusiva de los estados excitados que poseen una estructura microscópica similar según los trabajos previos. Esto es un efecto conocido de la selectividad cinemática del mecanismo de reacción, resultante del cambio en la energía potencial eléctrica entre el canal de entrada y el de salida y que en este experimento maximiza la sección eficaz de estados excitados con momento angular próximo a 0. Puesto que se observó en los datos que la excitación del núcleo ligero ^{8}Be no interfiere con la excitación del ^{212}Po y que el patrón de intensidades es independiente de la energía del haz en medidas próximas a la barrera de Coulomb, la reacción de transferencia constituye el mecanismo ideal para la observación de estados colectivos de espín 1^- y 2^- (cuya observación fue una de las motivaciones para proponer este experimento) predichos en los dos únicos cálculos teóricos previos[115, 114]. Estos cálculos tratan explicar la estructura de los llamados "estados α clúster", los dobletes colectivos de paridad negativa propuestos por Astier y colaboradores, en base a acoplamientos con el estado 3^- del ^{208}Pb con los que se tratan de reproducir, de forma simultánea, también los estados $(3, 5, 7, 9)^-$ identificados en ese experimento. A pesar de dicha selectividad, sólamente el estado excitado a 1898 keV es compatible en términos de energía con uno de los 2^-, pero su población directa es significativamente menor que la del resto y esto indica que dicho estado tiene estructura diferente. En base al mismo argumento tampoco se encuentran candidatos para los 2 estados 1^- predichos en los cálculos. Para explicar la ausencia de estados colectivos con momento angular menor que 3 a baja energía de excitación se realizaron cálculos

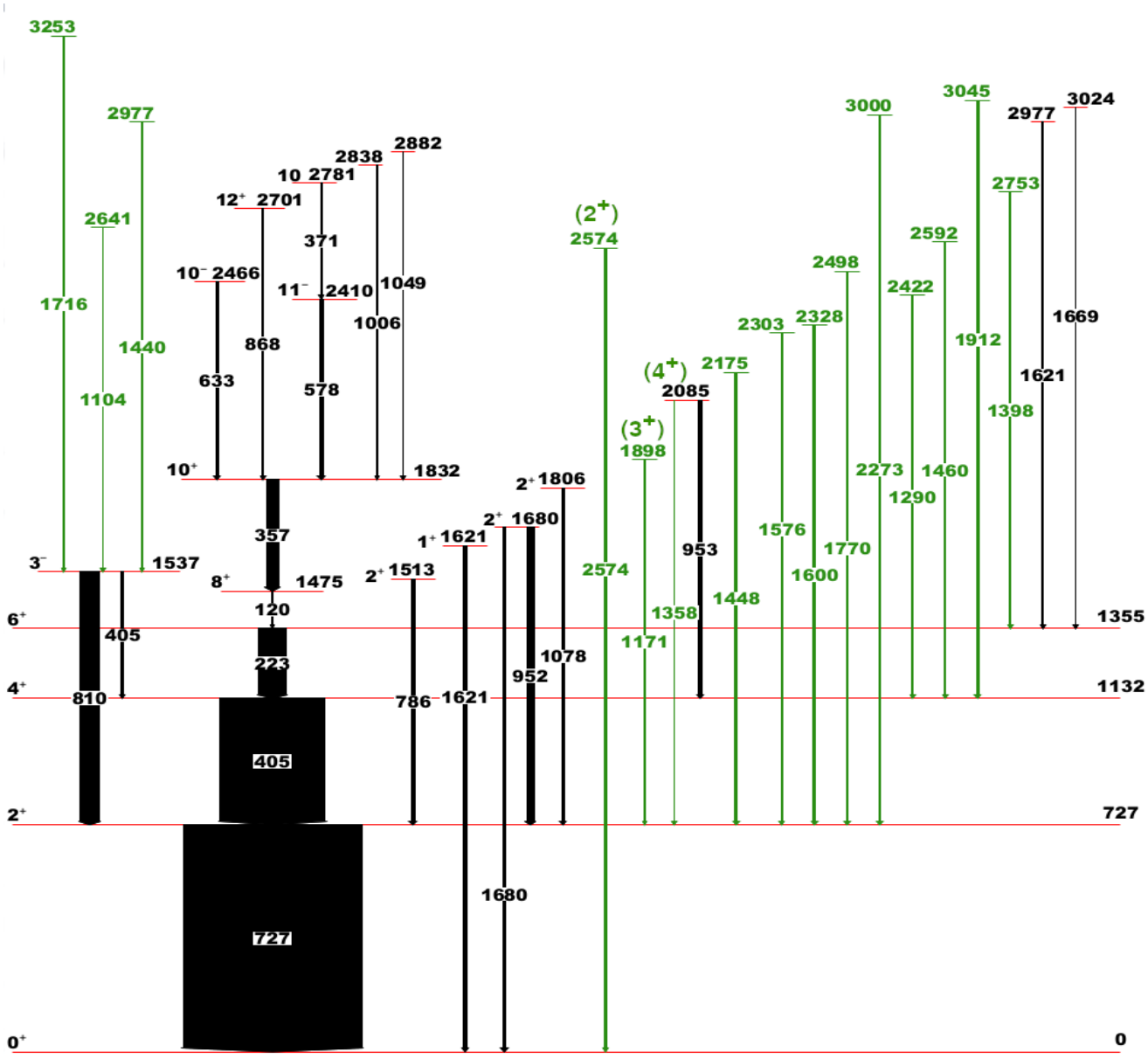

Figure C.4: Primera parte del esquema de niveles del ^{212}Po determinado en este trabajo. La anchura de las flechas es proporcional a la intensidad de la transición. Transiciones y estados excitados observados por primera vez en este trabajo se representan en color verde.

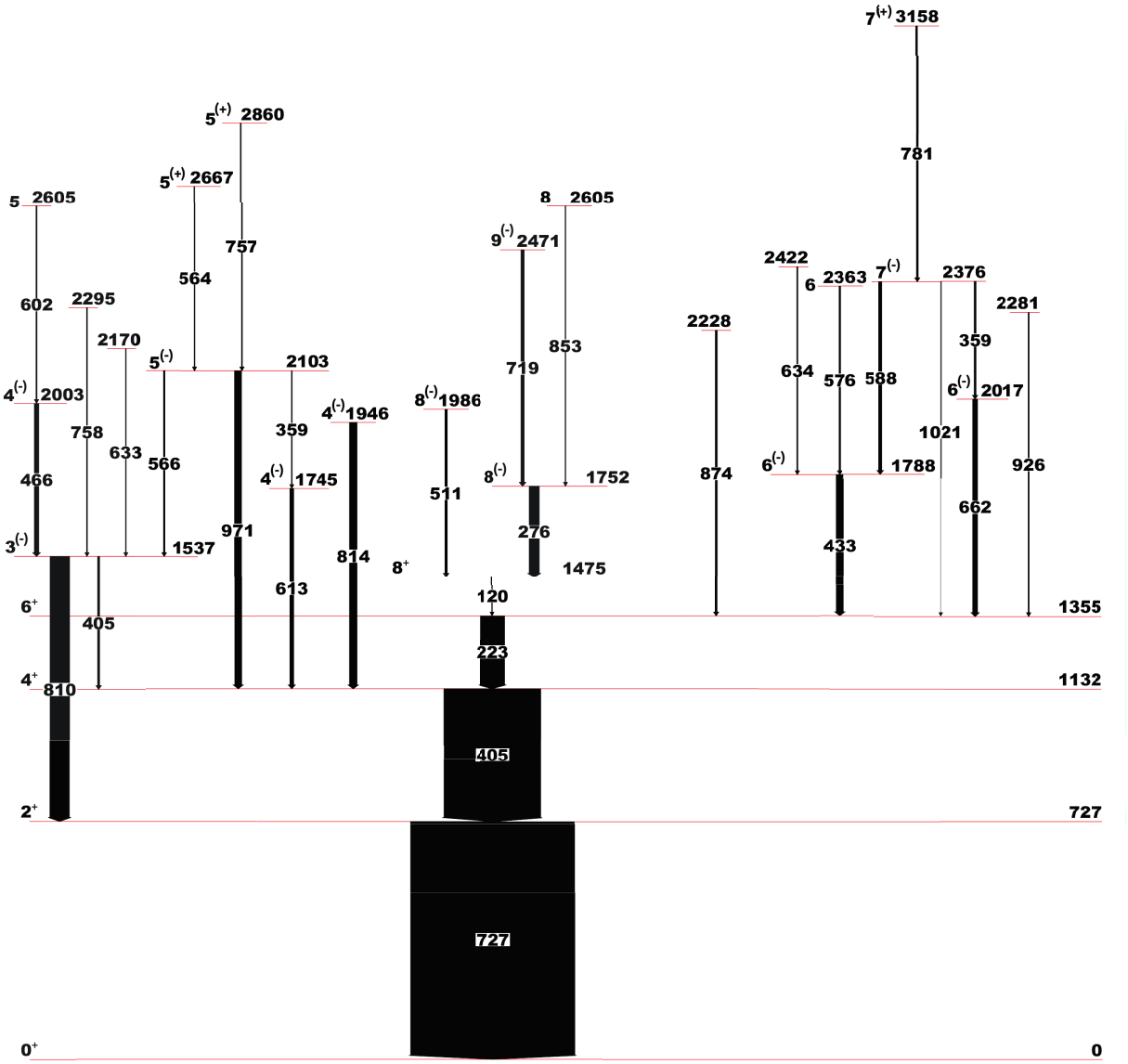

Figure C.5: Segunda parte del esquema de niveles del ^{212}Po determinado en este trabajo. La anchura de las flechas es proporcional a la intensidad de la transición. Todos los estados y transiciones mostrados en la figura ya han sido observados previamente.

del modelo de capas usando la interacción de Kuo-Herling[22, 24] para determinar la energía del multiplete $\pi(h^2_{9/2})_0\nu(g_{9/2}j_{15/2})_{I^-}$ en el ^{212}Po, encontrándose que estos estados están 200-400 keV por encima de los estados con espín impar y paridad negativa identificados por Astier tal y como se muestra en la figura C.7. Esta situación ya es conocida en el ^{209,210}Pb y por lo tanto se propone, de forma análoga, que los estados más bajos de paridad negativa surgen de mezclas entre el multiplete $\pi(h^2_{9/2})_0\nu(g_{9/2}j_{15/2})_{I^-}$

y las configuraciones ^{212}Po(2^+_1, 4^+_1, 6^+_1, 8^+_1)$\otimes^{208}$Pb(3^-) que estarían por encima de 3 MeV. Ningún estado 1^- ni 2^- se espera significativamente por debajo de 3 MeV en este modelo, en concordancia con los datos.

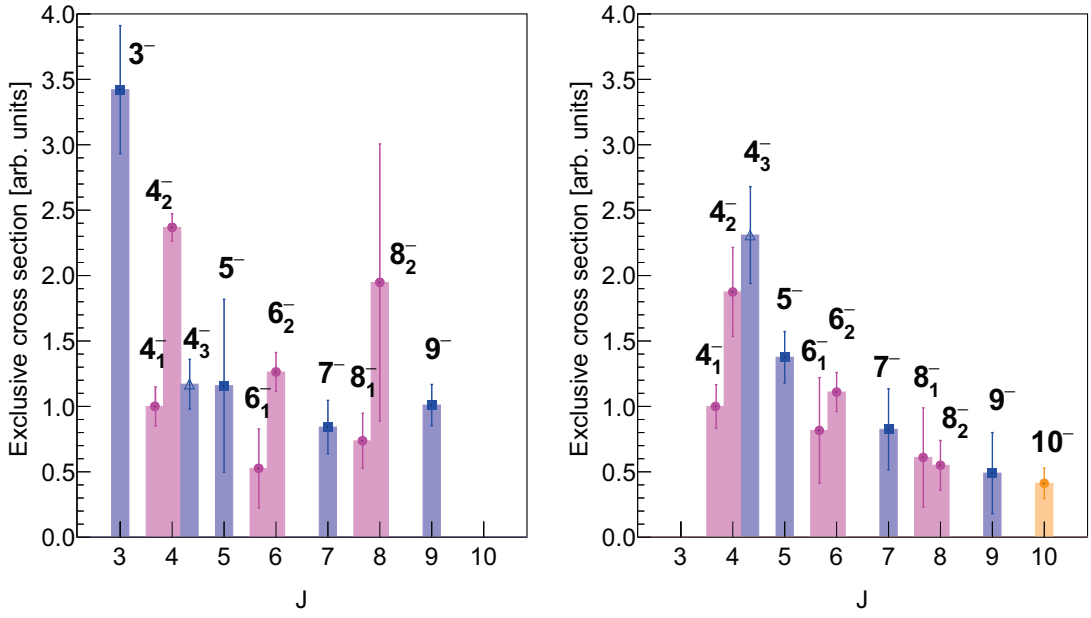

(a) ^{12}C(^{208}Pb, ^{212}Po)^{8}Be **(b)** ^{208}Pb(^{18}O, ^{14}C)^{212}Po

Figure C.6: Secciones eficaces exclusivas de población de los estados de paridad negativa más bajos, de acuerdo con las asignaciones en [109, 113], poblados con las reacciones ^{12}C(^{208}Pb, ^{212}Po)^{8}Be (en este trabajo) y ^{208}Pb(^{18}O, ^{14}C)^{212}Po (de [109]). Estas cantidades han sido normalizadas a la del estado (4^-) a 1745 keV.

C.4.2 Reinterpretación de los estados "α-cluster" a partir de la determinación directa de la paridad del estado a 1788 keV usando AGATA como un polarímetro Compton.

Siguiendo con este estudio de la colectividad octupolar en el ^{212}Po, se ha realizado la primera medida directa de la paridad del estado con $J = 6$ a 1788 keV, uno de los estados α-clúster. Esta medida parte de la observación por parte de Astier de un alto grado de alineamiento oblato inducido por el mecanismo de reacción, que permitió asignar el momento angular $J = 6$ en base al coeficiente $a_2 \approx 0.3$ positivo y a la vida media corta de la transición de 433 keV desde este nivel. Esto permite usar los espectros singles del ^{212}Po para este estudio de la asimetría en el ángulo azimuthal ϕ con respecto al plano de polarización en los procesos de dispersión Compton (técnica de *Compton polarimetry* en inglés). Con el fin de extraer el signo de la fase $(\pm)_{L_2=2}$ según la notación del artículo de Aoki[58], se extrajeron dos tipos de espectros singles:

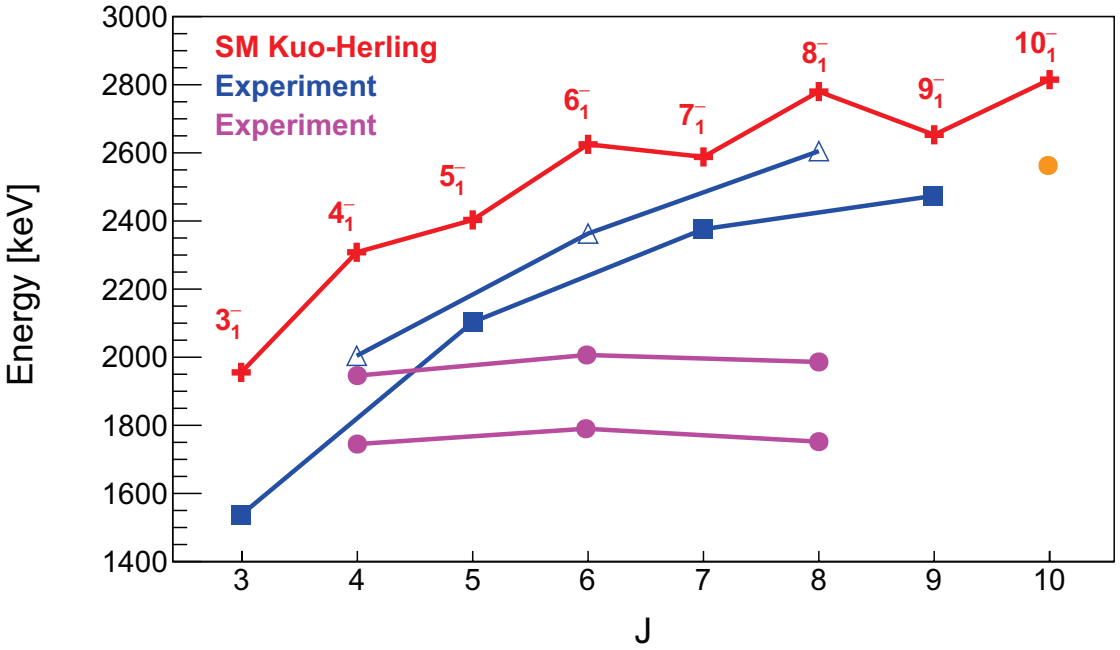

Figure C.7: Comparación entre los estados de paridad negativa según [109, 113] y las energías calculadas del multiplete $\pi(h^2_{11/2})_{0^+}\nu(g_{9/2}j_{15/2})_{I^-}$ (en rojo). Símbolos rellenos indican los estados que decaen con transiciones E1 hacia la banda del estado fundamental de acuerdo [109, 113].

1. Con selección de γ's detectados entre 120° y 140° y un ángulo polar de dispersión Compton θ_c entre 50° y 130°. La selección de ángulos próximos a 90° tanto en θ_c como en θ_γ tiene como objetivo maximizar las anisotropías como función del ángulo ϕ. Estos espectros han sido corregidos por la asimetría instrumental deducida de los datos tomados con la fuente de ^{152}Eu.

2. Con selección de γ's con un ángulo polar de dispersión Compton θ_c entre 50° y 130° y sin ninguna restricción en el ángulo polar θ_γ. Este espectro ofrece una mayor estadística a cambio de una menor sensitividad, y la anisotropía se estudia en relación a otras líneas próximas en energía, es decir, sin corregir la anisotropía instrumental usando la fuente de calibración.

Como verificación de la corrección de la anisotropía instrumental en los espectros obtenidos con la condición 1) se ha comparado el espectro integrado en $\phi \in [36°, 54°] + [216°, 234°]$ con el integrado en $\phi \in [126°, 144°] + [306°, 324°]$, no observándose entre ambos ninguna anisotropía de origen físico en concordancia con la dependencia con $\cos(2\phi)$ de dicho efecto. Ambos espectros se muestran en la figura C.8. En los restantes paneles de la figura C.8 se comparan los espectros integrados en $\phi \in [-20°, 20°] + [160°, 200°]$ y en $\phi \in [70°, 110°] + [250°, 290°]$. Tanto en 1) como en 2) se observa que la asimetría de la línea de 433 keV es en la misma dirección que para la línea de 405 keV

y es también de mayor magnitud, en concordancia con el coeficiente $a_2 \approx 0.3$ frente al $a_2 \approx 0.2$ dado en [109] para el γ de 405 keV. La asimetría $N(\phi = 0°)/N(\phi = 90°)$ que se obtiene de los espectros con la condición 1) es 0.8(2), un valor posible sólamente si la transición es de tipo magnético puesto que para la transición de tipo eléctrico habría de observarse $N(\phi = 0°)/N(\phi = 90°)$=1.3.

De acuerdo con los cálculos del modelo de capas, este estado se correspondería con el segundo 6^+ predicho a 1718 keV, generado principalmente por la configuración $\pi h^2_{9/2}\nu g^2_{9/2}$, y que decae mediante una transición M1 hacia el 6^+_1 el $\approx$ 100% de las veces con una B(M1) calculada de $0.72\,\mu^2_N$ si se usan factores g de nucleones no ligados. Usando el mismo argumento propuesto anteriormente acerca la selectividad cinemática y espectroscópica del mecanismo de reacción, se identifican los restantes estados que conforman los denominados dobletes "α-cluster" como estados de paridad positiva que decaen mediante transiciones M1 hacia la banda yrast. Según los cálculos, estos dobletes se corresponden con el segundo y el tercer estado excitado de un cierto momento angular par y paridad positiva, y todos ellos se desexcitan hacia el primer estado excitado del mismo momento angular en más del 93% de las veces y mediante una transición de vida media muy corta y de tipo M1 pura. Se interpretan estos estados de forma análoga al 2^+_2 y al 2^+_3, que presentan un patrón de decaimiento similar y han sido identificados como fragmentos de un estado con simetría mixta (del inglés mixed symmetry state, MSS) por Kocheva et. al.[17] en base a sus vidas medias. Este tipo de estados constituyen excitaciones de tipo isovector en las que la B(M1) tan grande surge como consecuencia de la antisimetría de la función de onda frente al intercambio de un par bosónico de protones y de neutrones, frente a la simetría ante dicho intercambio en el estado completamente simétrico (FSS) que es el estado yrast hacia el que decaen. Las propiedades calculadas de estos estados se comparan con las experimentales en la tabla C.2.

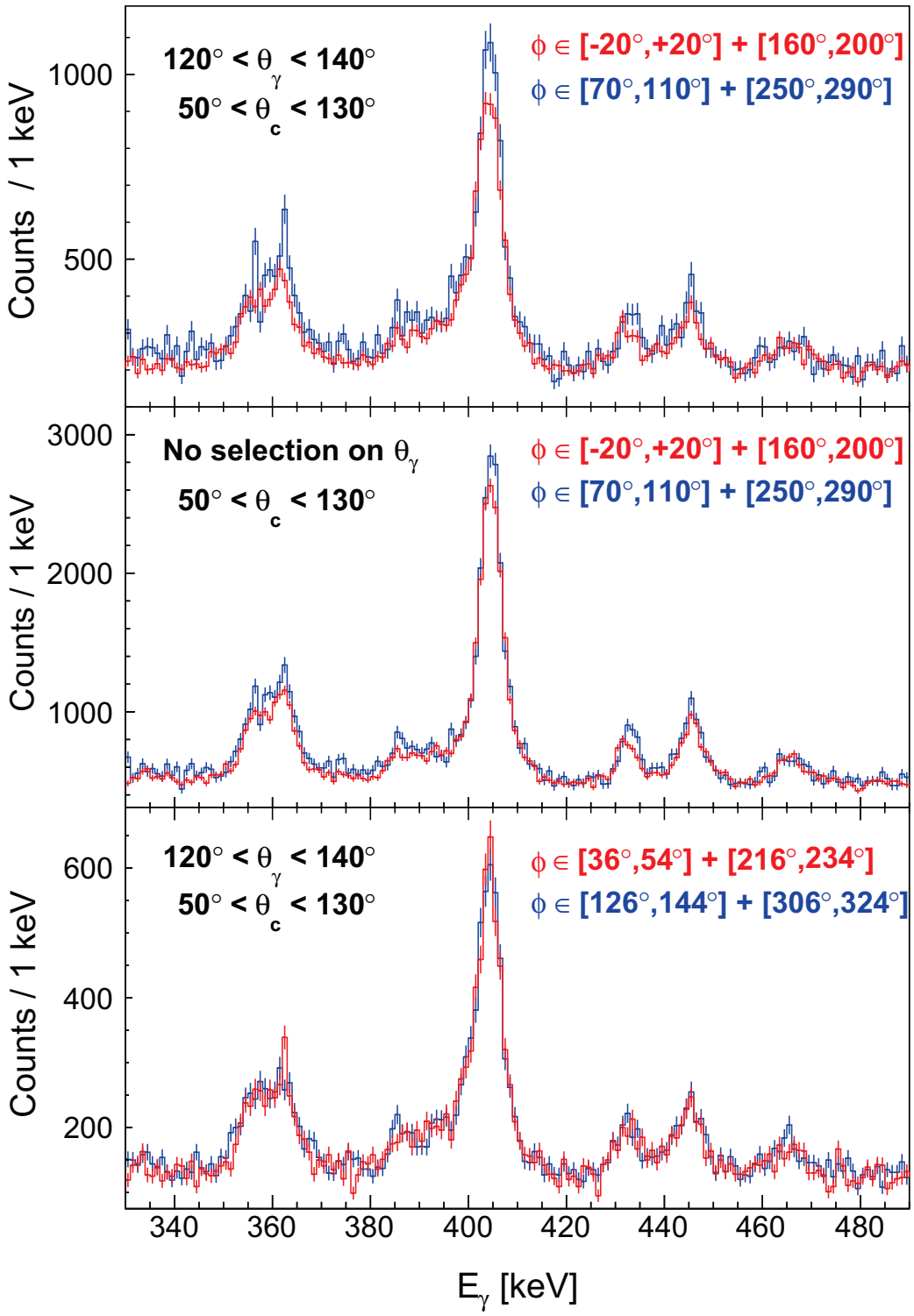

Figure C.8: Comparación de espectros γ singles entre 330 keV y 490 keV obtenidos con diferentes restricciones en el ángulo polar del γ y en el ángulo azimutal ϕ de la dispersión Compton.

J_n^+	E_x^{th} [keV]	E_x^{exp} [keV]	$B(M1; J_n^+ \to J_1^+)^{\text{th}}$ $[\mu_N^2]$	$B(M1; J_n^+ \to J_1^+)^{\text{exp}}$ $[\mu_N^2]$
2_2^+	1430	1513	0.293	0.126(16)
2_3^+	1714	1680	0.060	0.042(20)
4_2^+	1670	1745	0.564	0.52(16)
4_3^+	2005	1946	0.056	0.23(7)
6_2^+	1718	1788	0.723	1.56(12)
6_3^+	2081	2017	0.134	0.40(13)
8_2^+	1732	1752	0.933	5.6(2.3)
8_3^+	1908	1986	0.254	-

Table C.2: Energías y probabilidades de transición experimentales y calculadas del segundo y tercer estado excitado con momento angular par entre 2 y 8. Las B(M1) experimentales se han calculado usando las vidas medias dadas en [109] y en [17].

C.4.3 Cota superior a la vida media de 4 transiciones

El blanco de DSAM sufrió un deterioro significativo durante el experimento como consecuencia de la elevada intensidad del haz y por lo tanto únicamente se ha extraído información cualitativa en forma de cotas superiores a la vida media. Dichas cotas se dan en la tabla C.3 y se extrajeron comparando los espectros experimentales con simulaciones de DSAM usando el programa APCAD[60]. Se estima que el error sistemático en el espesor del blanco y en el factor de escala del poder de frenado calculado con SRIM[66] es inferior al 5% y no influye en los resultados. Por el contrario, una separación entre la capa de reacción y de frenado como una consecuencia probable del incremento de temperatura en el blanco, tal y como se ha indicado en trabajos previos[125], sí impactaría de forma significativa en las cotas a las vidas medias cortas. Dicha separación efectiva no se puede extraer de los datos debido al propio deterioro del blanco y por lo tanto para extraer las cotas se ha considerado una separación máxima en torno al 50% que daría lugar a una vida media de $\tau \approx 0.2\,\text{ps}$ para la transición de 781 keV, desexcitando el estado (7^+) a 3158 keV. Este valor de τ está en el límite del intervalo dado por Astier para la vida media de esta transición.

Este es el primer experimento en cinemática inversa orientado a la medida de vidas medias mediante DSAM en esta región. El interés principal de estas cotas es demostrar que el montaje experimental, que permite corregir el desplazamiento Doppler de forma muy precisa, combinado con la técnica de cinemática inversa, es el ideal para medir con una sensibilidad excelente usando espectros singles la vida media de transiciones

de alta energía ($E_\gamma \gtrsim 2\,\mathrm{MeV}$) y de vida media muy corta que se pueden observar con suficiente intensidad en esta región de núcleos cercanos al ^{208}Pb poblándolos mediante reacciones de transferencia.

E_x [keV]	2592	3045	3000	2574
E_γ [keV]	1462	1912	2273	2574
$\tau^\gamma_{\mathrm{max}}$ [ps]	0.7	0.3	0.3	0.4

Table C.3: Cotas superiores a la vida media extraídas de los datos tomados con el blanco de DSAM.

C.4.4 Asignación de momento angular y paridad a 3 estados excitados usando cálculos del modelo de capas

Se asignó el momento angular y la paridad de los estados a 1898 keV, 2085 keV y 2574 keV comparando su energía de excitación y propiedades de decaimiento con dichas cantidades calculadas según el modelo de capas.

Los estados excitados calculados con espín menor que 5 y paridad positiva hasta una energía de 2300 keV[1] se muestran en la figura C.9. Todos los estados 2^+ hasta el cuarto a 1881 keV ya se conocen experimentalmente, y tanto el quinto como el sexto, aunque decaerían principalmente hacia el 2^+_1, se predicen a una energía significativamente más alta (2197 keV y 2236 keV, respectivamente). Asimismo, el segundo 1^+ se predice a 2111 keV y decaería con intensidades comparables hacia el 2^+_1, el 1^+_1 y el 2^+_3. Únicamente el segundo y el tercer 0^+ se encontrarían por debajo de 2300 keV, y el segundo de ellos se correspondería con el estado ya conocido a 1801 keV[90]. Además, la rama principal de decaimiento de todos los estados 4^+ calculados por debajo de 2300 keV es hacia el 4^+_1, y en este trabajo ya se han propuesto candidatos para el 4^+_2 y el 4^+_3, calculándose el 4^+_4 en torno a 2223 keV.

De acuerdo con lo expuesto arriba, el estado a 1898 keV sólamente se puede identificar como el 3^+_1 calculado a 1858 keV y cuya probabilidad de decaimiento mayoritaria sería hacia el 2^+_1 el 61% de las veces. De forma similar, el estado a 2085 keV se correspondería con el 4^+_4 a 2223 keV ya que el 3^+_2 se desexcita principalmente hacia el 2^+_1 o hacia el 2^+_3 con una probabilidad cercana al 88%. La configuración principal de ambos estados sería $\pi h^2_{9/2}\nu g_{9/2} i_{11/2}$.

Se descarta una asignación $J^\pi = 3^-$ al estado a 2574 keV, que decae principalmente al estado fundamental, debido a su vida media corta en el rango de unas pocas décimas

[1] Únicamente se esperan dos de paridad negativa hasta 2300 keV, un 3^- a 1954 keV y un 2^- a 2288 keV.

de ps. Este estado sólo puede ser un 1^+ o un 2^+, y de acuerdo con las propiedades de los estados $(1,2)^+$ calculados hasta $\sim 3\,\mathrm{MeV}$, se correspondería con el 2_9^+ predicho a 2578 keV, el único estado con una rama de desexcitación de una intensidad apreciable y mayoritaria hacia el estado fundamental y que se calcula dentro de ± 200 keV del estado observado experimentalmente a 2574 keV.

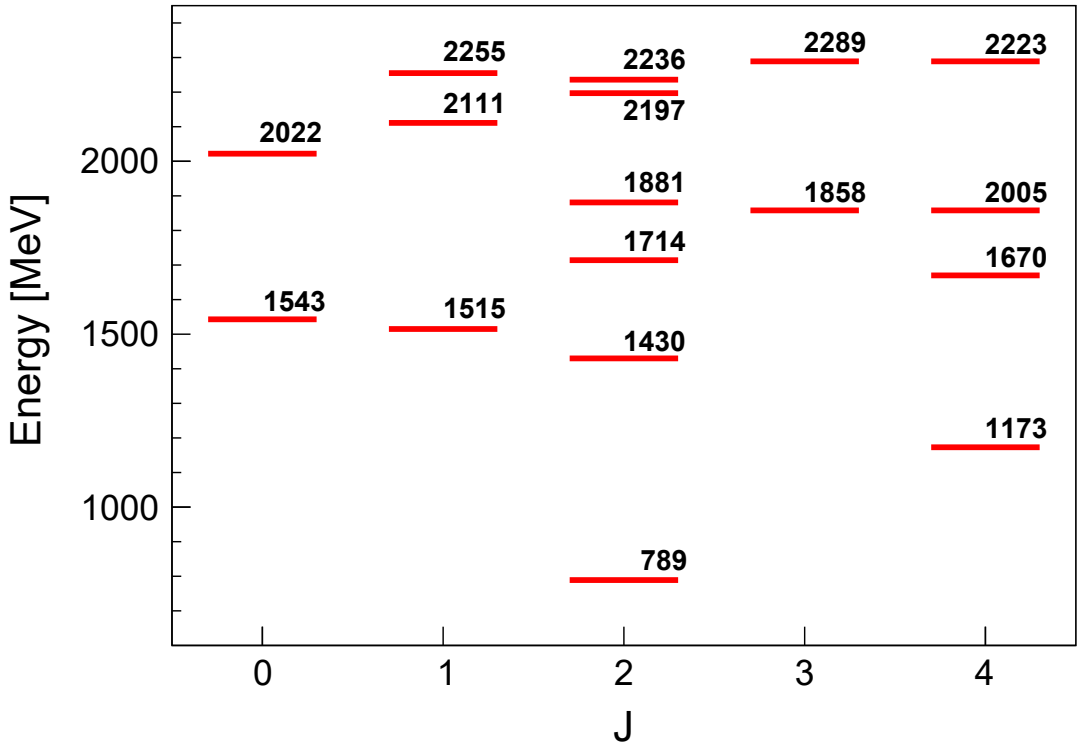

Figure C.9: Esquema de niveles calculado del ^{212}Po hasta una energía de 2300 keV. Sólamente se muestran estados de paridad positiva con momento angular J inferior a 5.

Appendix D

List of BigRIPS and ZeroDegree beam-line materials

Detector	Material	Thickness
F7PPAC1	$H_8C_{10}O_4$	45 µm
F7IC window	$C_{22}H_{10}N_2O_4$	125 µm
F7IC gas	H_8C_2 (10%) - Ar(90%)	586 mm
F7IC electrodes	$H_8C_{10}O_4$	100 µm
F7IC window	$C_{22}H_{10}N_2O_4$	125 µm
F7PPAC2	$H_8C_{10}O_4$	45 µm
F7PLscint	$H_{10}C_9$	500 µm
F8PPAC1	$H_8C_{10}O_4$	45 µm
F8PLscint	$H_{10}C_9$	500 µm
F8PPAC2	$H_8C_{10}O_4$	45 µm
2nd target	Be	5.94 mm
F8PPAC3	$H_8C_{10}O_4$	45 µm

Table D.1: Partial list of beam line detectors with their compositions and thicknesses. This table is used for calculating the velocity before the target as well as for calculating inclusive cross sections.

Appendix E

Resumen en castellano (parte II)

E.1 Introducción

Más allá del efecto de la interacción electromagnética, la interacción nucleón-nucleón es fundamentalmente independiente del par de nucleones que interaccionan. Esta invariancia se conoce como simetría de isospín y es la responsable de la similitud entre los espectros de estados excitados en núcleos espejo, núcleos que poseen el mismo número másico A pero cuyo número de protones y neutrones está intercambiado. Hoy en día se sabe que el isospín es únicamente una simetría aproximada que no sólo se rompe como consecuencia de la interacción electromagnética sino por la propia interacción fuerte entre los nucleones, aunque en un grado mucho menor. No se ha conseguido, sin embargo, reproducir de manera consistente ni precisa las masas en cadenas de isóbaros con interacciones efectivas obtenidas a partir de parametrizaciones de la interacción entre nucleones libres.

A este respecto, las diferencias de energía entre núcleos espejo y las diferencias de energía triples definidas como

$$\mathrm{MED}_J(T,T_z) = E_J(T,T_z=T) - E_J(T,T_z=-T) \tag{E.1}$$

$$\mathrm{TED}_{J,T=1} = E_J(T_z=1) + E_J(T_z=-1) - 2E_J(T_z=0) \tag{E.2}$$

se han usado en el pasado, fundamentalmente en núcleos de la capa $f_{7/2}$, para estudiar los mecanismos mediante los cuales las interacciones entre las partículas de valencia generan el momento angular. Se ha encontrado que la prescripción propuesta por Zuker[187] para la interacción efectiva que rompe la simetría de isospín es capaz de reproducir de forma sistemática las MEDs y TEDs en núcleos espejo de la capa $f_{7/2}$. En particular, se incluye un término radial que representa el cambio en la energía electrostática debido a variaciones en la ocupación de los orbitales p y una interacción V_B de origen desconocido y actuando con una intensidad significativa para pares de

nucleones acoplados a $J = 2$, en contraste con la interacción multipolar de origen electromagnético.

Estudios iniciales en la parte superior del espacio pf previos a este trabajo[192], en donde la capa $f_{7/2}$ permanece prácticamente cerrada y al mismo tiempo los orbitales $g_{9/2}$ no muestran todavía ocupaciones significativas, consideraron una descripción de las MEDs sin la interacción V_B y usando una formulación alternativa para el término radial, que surgiría únicamente como consecuencia del desplazamiento de Thomas-Ehrman[193, 194]. Un estudio más reciente[203], sin embargo, han concluido que la interacción V_B sí actuaría con la misma intensidad en todos los orbitales del espacio pf en experimentos donde no se ha encontrado necesidad de incluir un término radial de ningún tipo para describir las MEDs.

El experimento que se expone en la segunda parte de la memoria se planteó para complementar la información disponible en la capa pf y estudiar el papel del término radial en las MEDs de esta región mediante el estudio del par con $T_z = -2$ ^{56}Zn/^{56}Fe, un caso en el que se espera también la presencia de efectos significativos procedentes de la interacción V_B en las capas p y $f_{5/2}$ como consecuencia de la ocupación de estos orbitales por parte de los dos protones (neutrones) en el ^{56}Zn (^{56}Fe).

E.2 Experimento

El experimento se llevó a cabo en el laboratorio de RIKEN (Tokio). Se indujeron reacciones de fragmentación al incidir un haz primario de ^{78}Kr sobre un blanco de Be y los fragmentos resultantes, entre los cuales se encuentran núcleos de ^{57}Zn, se condujeron al separador BigRIPS[210, 212]. En este espectrómetro se purificó e identificó el haz secundario resultante mediante una medida conjunta de la $B\rho$ a partir de las posiciones, determinadas con 2 PPACs dobles[214, 215], en los planos focales F3, F5 y F7, del tiempo de vuelo usando un par de centelladores plásticos en los extremos del separador y de la energía depositada por los iones en una TEGIC[216], a partir de la cual se deduce su número atómico Z. Se usó un blanco secundario de Be de un espesor de 6 mm para inducir reacciones de separación de un neutrón (del inglés *knockout reactions*) sobre los núcleos de ^{57}Zn y producir así el núcleo de interés, ^{56}Zn.

La identificación de los productos de reacción en el blanco secundario se llevó a cabo en el espectrómetro ZeroDegree siguiendo la misma técnica que en BigRIPS, es decir, mediante una medida $B\rho$-ΔE-TOF conjunta midiendo la posición de los iones en F8, F9 y F11 así como la ΔE en una TEGIC situada en F11.

Las γ's procedentes de la desexcitación tras las reacciones en el blanco secundario se midieron en el espectrómetro γ DALI2+[218, 219]. Este dispositivo es un conjunto

de 226 cristales de NaI(Tl) dispuestos en 10 anillos a lo largo de la dirección del haz, que ofrece una alta eficiencia de detección y al mismo tiempo una alta granularidad para aumentar la precisión de la corrección del efecto Doppler en la energía de la radiación emitida en vuelo. El detector se posicionó con el blanco en su interior y situado en el plano del anillo 5.

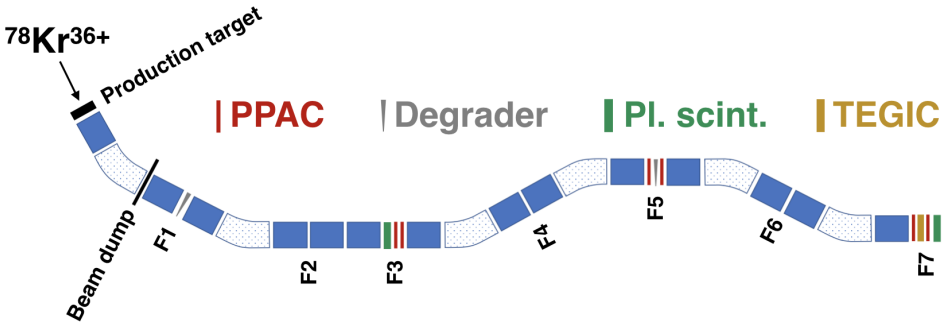

Figure E.1: Ilustración del separador BigRIPS. STQs y dipolos se representan en azul y punteados, respectivamente. Los detectores usados para la identificación de las partículas se indican en la figura.

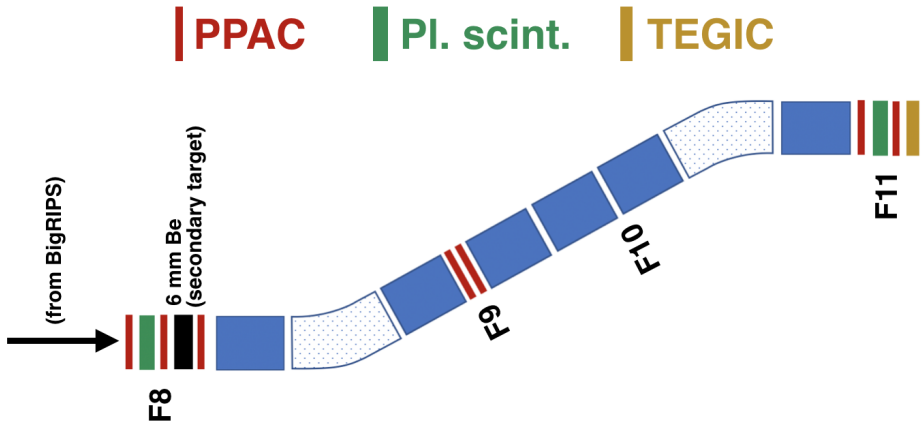

Figure E.2: Ilustración del separador ZeroDegree. STQs y dipolos se representan en azul y punteados, respectivamente. Los detectores usados para la identificación de las partículas se indican en la figura.

E.3 Análisis de los datos

El tiempo de vuelo del haz secundario se calculó en BigRIPS correlacionando al mismo tiempo las señales temporales de los dos fotomultiplicadores en de cada centellador plástico y las señales entre diferentes centelladores. La $B\rho$ se reconstruyó mediante transformaciones ópticas que relacionan la posición en el plano focal y la dispersión

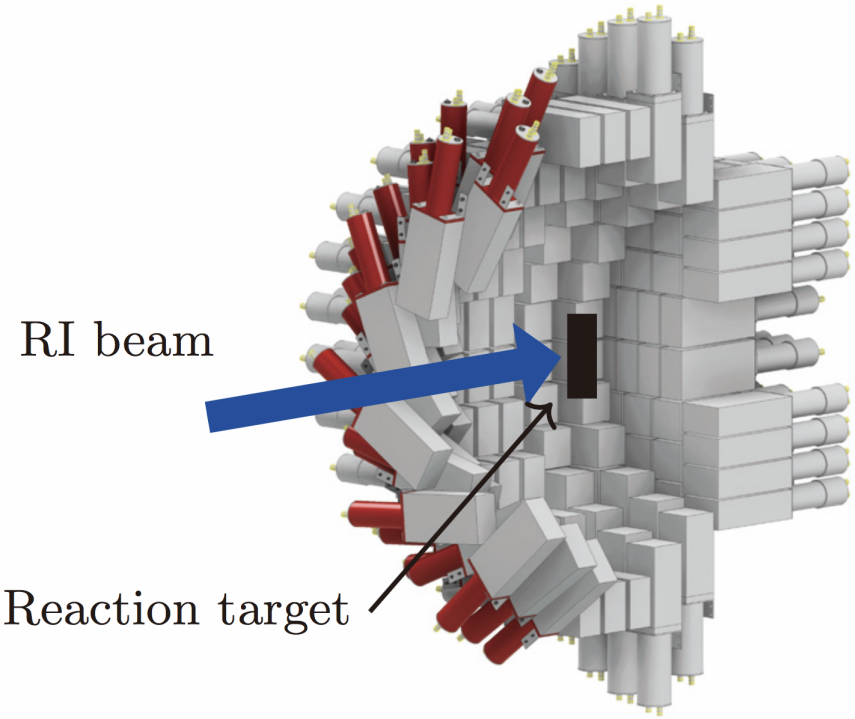

Figure E.3: Ilustración del espectrómetro γ DALI2+. Sólo se muestra una fracción de los cristales en cada capa. La imagen se ha tomado de [219].

del momento. En aquellos casos particulares en los cuales no se pudo reconstruir la posición en F3 a partir de las PPACs debido a su alta tasa de conteo, ésta se dedujo de la correlación entre la diferencia de tiempos y dicha posición[213] de acuerdo con el centellador en F3. Se introdujeron además correciones de segundo grado para eliminar las aberraciones ópticas en la reconstrucción del A/Q en ambos espectrómetros[213] y se corrigió la deriva de la ganancia en la TEGIC en F11 así como una dependencia residual de la Z con β en este detector.

Los cristales de DALI2+ se calibraron en energía usando polinominos de primer grado obtenidos a partir de la posición de los fotopicos observados con las fuentes de ^{137}Cs, ^{60}Co y ^{88}Y. La calibración se corrigió como función del tiempo en los datos tomados durante el tiempo de haz para cancelar los cambios en la respuesta energética de los cristales. Esta corrección se aplicó como un factor de escala sobre las energías y se determinó usando el pico de aniquilación a 511 keV. En este trabajo no se usó un algoritmo de add-back para deducir las energías de las transiciones porque introduce un error sistemático que es comparable en magnitud al estadístico en los casos presentados en esta tesis, y que está presente independientemente de la magnitud de las deposiciones de energía del γ.

La corrección Doppler se efectuó asumiendo que el núcleo se desexcita de manera

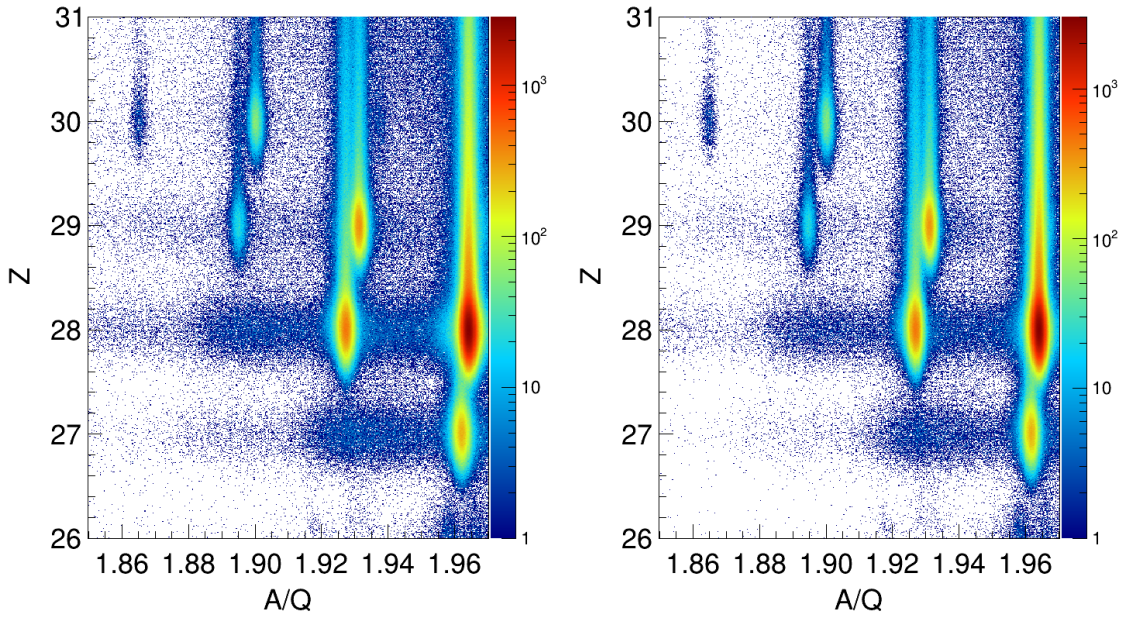

(a) BigRIPS, sin correcciones

(b) BigRIPS, con correcciones

(c) ZeroDegree, sin correcciones

(d) ZeroDegree, con correcciones

Figure E.4: Espectros de identificación de partículas en BigRIPS y ZeroDegree. Únicamente se ha usado un número limitado de eventos para generar las gráficas.

instantánea dentro del blanco. Se usó una velocidad a mitad del blanco calculada con LISE++[128] a partir de la β promedio del núcleo padre en BigRIPS y una tabla con las coordenadas promedio de la interacción del γ en el cristal para reconstruir el ángulo polar θ_L. Usando los espectros γ del ^{52}Fe producido en reacciones de separación de

un neutrón se encontró que asumiendo un desplazamiento de -2 cm del blanco y la β calculada con LISE++ se alinean los fotopicos en todos los cristales de DALI2+ si se usa una β y una tabla de ángulos calculada de acuerdo las vidas medias conocidas de las transiciones.

Los espectros corregidos Doppler se ajustaron a formas de línea simuladas con las librerías de GEANT4 junto con una exponencial doble que representa todo lo que no es fondo Compton. Como estimador se da el valor de los parámetros en el mínimo global del χ^2 y como incertidumbre estadística en las energías e intensidades se dan los extremos del contorno 1σ como función de todos los parámetros. El método de ajuste se validó usando productos de reacción con transiciones conocidas, adoptándose un error sistemático del 0.4% en las energías de las transiciones.

Asimismo, se calculó una sección eficaz exclusiva de $10(1)_{\text{stat}}(1)_{\text{sys}}$ para la reacción ^{57}Zn(Be,X)^{56}Zn.

E.4 Resultados y discusión

Se extrajeron espectros γ del ^{56}Zn bajo diferentes condiciones sobre la multiplicidad de cristales, con/sin add-back y con/sin selección del núcleo padre en BigRIPS con el fin de estudiar las incertidumbres estadísticas en situaciones de más estadística en detrimento del P/T y al revés. Se encontró que el espectro que resulta en las menores incertidumbres estadísticas es el que se obtuvo con una selección sobre el canal de separación de un neutrón y seleccionando únicamente aquellos eventos con multiplicidad de cristales inferior a 5. Las energías se extrajeron a partir de los espectros corregidos Doppler asumiendo desexcitación γ instantánea. Se encontraron tres transiciones cuyas energías son 830(5) keV, 1272(13) keV y 1380(16) keV y cuyas intensidades relativas son 100(5)%, 76(18)% y 58(13)%. Estas transiciones forman parte de una cascada con 3 γ's y despueblan estados excitados con energías de 830(5) keV, 2102(14) keV y 3482(21) keV. Se asignó de forma indirecta el espín y la paridad de dichos estados, que son identificados como el 2_1^+, el 4_1^+ y el 6_1^+, por comparación con el núcleo espejo ^{56}Fe. La información disponible previa a este trabajo viene fundamentalmente del análisis llevado a cabo por Ekman[192] y los trabajos posteriores de Kaneko con núcleos con masas por encima de $A = 60$[202, 195, 203]. Según Ekman, el desplazamiento de Thomas-Ehrman supone la contribución principal al término radial y no se consideran efectos en las MEDs que provengan de variaciones en la ocupación de los orbitales p. Este análisis se llevó a cabo sin necesidad de incorporar en el término multipolar la interacción V_B de origen desconocido. A su vez, se encuentra que ni las MED ni las TED en el par $A = 66$ y $A = 70$ son reproducibles, sin añadir

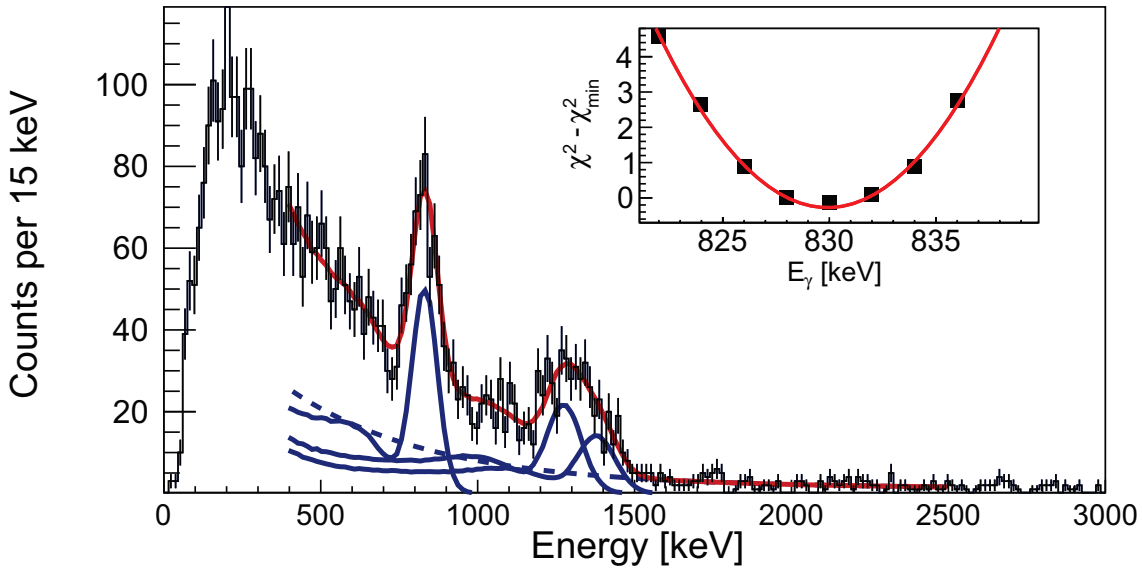

Figure E.5: Espectro γ sin add-back, en coincidencia con un núcleo de ^{57}Zn en BigRIPS y un núcleo de ^{56}Zn en ZeroDegree construido con eventos con una multiplicidad de cristales inferior a 5. El espectro se ajustó a formas de línea simuladas y una exponencial doble entre 400 keV y 2500 keV.

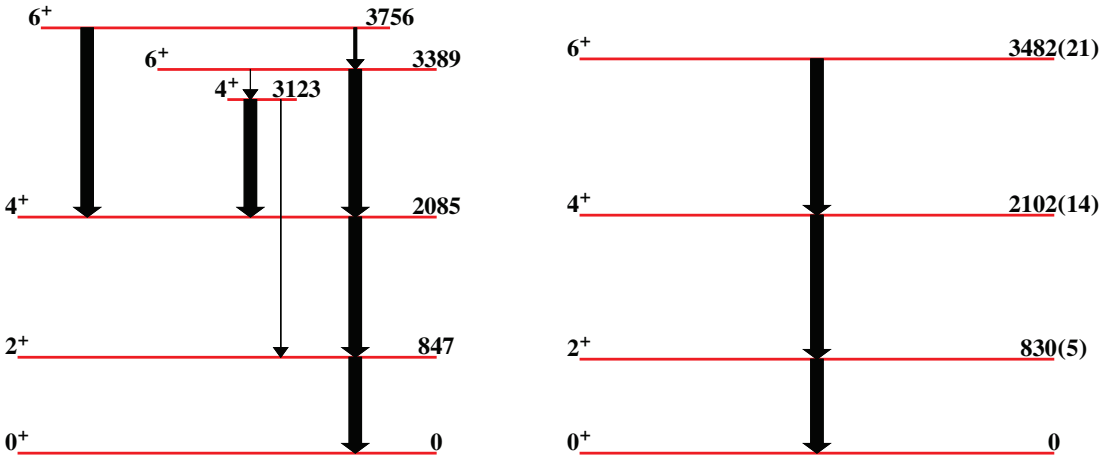

(a) ^{56}Fe (b) ^{56}Zn

Figure E.6: Comparación entre el esquema de niveles del ^{56}Zn, deducido en este trabajo, y el del núcleo espejo ^{56}Fe. De este último sólamente se muestran estados cuya desexcitación de lugar a cascadas con al menos 3γ's. La anchura de las flechas indica la probabilidad relativa entre las ramas de decaimiento. Las asignaciones de espín y paridad en el ^{56}Zn se han efectuado en base a la comparación entre ambos esquemas de niveles.

la interacción V_B actuando con la misma intensidad en todos los orbitales del espacio pf[203, 238], mientras que no se incluye ningún tipo de contribución procedente del término radial, siendo éste último insignificante.

En este trabajo se empezó estudiando el par $T_z = -1$ ^{58}Zn/^{58}Fe empleando la publicación reciente de dos estados excitados en el ^{58}Zn[239]. En el término multipolar que rompe la simetría de isospín se incluye el término de Coulomb y la interacción V_B actuando con una intensidad de -75 keV en todo el espacio de valencia. El término monopolar está compuesto por un término ll (corrección de Coulomb), la interacción espín-órbita de origen electromagnético y el término radial. Las MEDs se calculan a primer orden en teoría de perturbaciones usando las funciones de onda calculadas mediante el modelo de capas usando la interacción KB3G. Se encontró que la interacción multipolar da contribuciones idénticas a la MED tanto en el 2_1^+ como en el 4_1^+ para el par con $A = 58$, mientras que se observa un cambio de signo en la MED con un salto de más de 100 keV entre estos dos estados. Dicho cambio se correlaciona con una caída en la ocupación del $p_{3/2}$ (por parte de los protones/neutrones en el ^{58}Zn/^{58}Fe) en el estado 4^+ con respecto a dicha ocupación en el 2^+. Es posible reproducir la magnitud de dicho salto en las MEDs considerando un término radial proporcional a la ocupación de los orbitales $p_{3/2}$, donde el valor de la constante α_r es similar al empleado por Zuker en la capa $f_{7/2}$, $\alpha_r \approx 300$ keV.

A continuación se estudiaron las MEDs en el par ^{56}Zn/^{56}Fe empleando el mismo

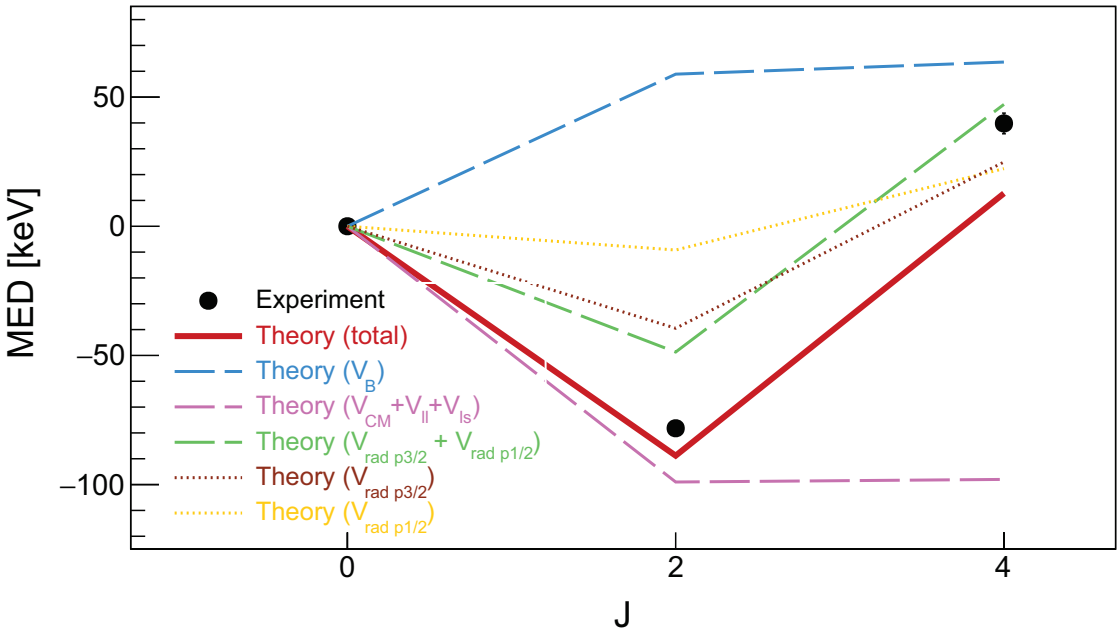

Figure E.7: Comparación entre las MEDs calculadas y experimentales en el par $T_z = -1$ de masa $A = 58$.

modelo para el término radial que en $A = 58$. Se encuentra que las MED en los estados 4^+ y 6^+ surgen principalmente del término radial. La ocupación de la capa $p_{3/2}$ por parte de los protones en el ^{56}Zn cae significativamente en el estado 4^+. A su vez, la caída de cerca del 50% en la ocupación del orbital $p_{1/2}$ por parte de los protones en el ^{56}Zn representa la contribución dominante al término radial en el 6^+. Se encuentra que, en ambos casos, las MEDs calculadas sin término radial subestiman en más de 30 keV el valor medido.

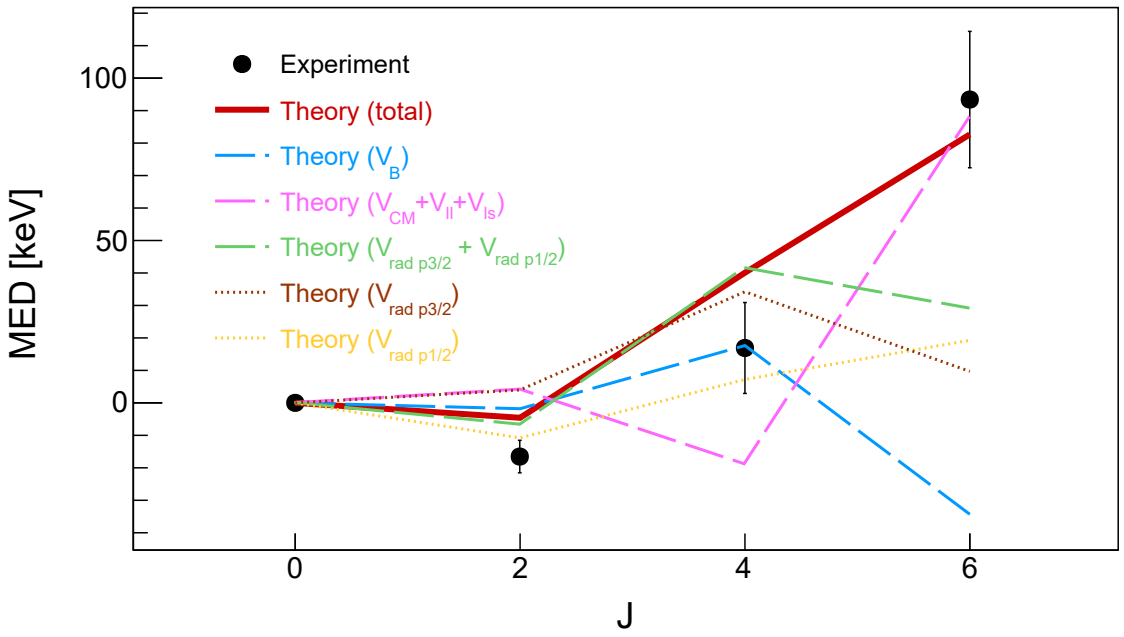

Figure E.8: Comparación entre las MEDs calculadas y experimentales en el par $T_z = -2$ de masa $A = 56$.

En resumen, este es el primer análisis de las MEDs en la parte superior del espacio pf bajo condiciones de alta sensibilidad tanto al término radial como a la interacción V_B. Se ha encontrado que es posible realizar una descripción simultánea de las MEDs en el par $T_z = -1$, $A = 58$ y en $T_z = -2$, $A = 56$ si la interacción V_B actúa con una intensidad de -75 keV en todos los orbitales, en concordancia con el análisis efectuado por Kaneko en $A = 66, 70$[203], y si se incluyen sendos términos radiales proporcionales a la ocupación del orbital $p_{3/2}$ y del $p_{1/2}$. Según ha sido señalado por Ekman[192], esta magnitud de la constante α_r se correspondería con un radio anormalmente alto de los orbitales p, mucho más de lo esperable incluso para órbitas por encima de la energía de separación de un nucleón. Los resultados de este análisis se han interpretado en relación con análisis previos de radios nucleares en base a desplazamientos isotópicos cerca de esta región de masas[240, 241], que sugieren interpretar los orbitales p como halos.

Bibliography

[1] E. Epelbaum, H. W. Hammer, and U. G. Meißner, Rev. Mod. Phys. **81**, 1773 (2009).

[2] S. Beane, W. Detmold, K. Orginos, and M. Savage, Prog. Part. Nucl. Phys. **66**, 1 (2011).

[3] P. Ring and P. Schuck, *The nuclear many-body problem* (Springer, 1980).

[4] J. Suhonen, *From nucleons to nucleus: concepts of microscopic nuclear theory* (Springer, 2007).

[5] M. G. Mayer, Phys. Rev. **74**, 235 (1948).

[6] M. G. Mayer, Phys. Rev. **75**, 1969 (1949).

[7] O. Haxel, J. H. D. Jensen, and H. E. Suess, Phys. Rev. **75**, 1766 (1949).

[8] K. L. G. Heyde, *The nuclear shell model* (Springer, 1994).

[9] S. Shen, H. Liang, W. H. Long, J. Meng, and P. Ring, Prog. Part. Nucl. Phys. **109**, 103713 (2019).

[10] M. Bender, P. H. Heenen, and P. G. Reinhard, Rev. Mod. Phys. **75**, 121 (2003).

[11] A. Bohr and B. R. Mottelson, *Nuclear structure*, vol. 2 (World Scientific, 1998).

[12] E. Caurier and F. Nowacki, Acta Phys. Pol. B **30**, 705 (1999).

[13] E. Caurier, G. Martínez-Pinedo, F. Nowacki, A. Poves, and A. P. Zuker, Rev. Mod. Phys. **77**, 427 (2005).

[14] B. Brown, Prog. Part. Nucl. Phys. **47**, 517 (2001).

[15] B. Brown and W. Rae, Nucl. Data Sheets **120**, 115 (2014).

[16] H. Grawe, *Shell Model from a Practitioner's Point of View* (Springer, 2004), vol. I of *The Euroschool Lectures on Physics with Exotic Beams*, pp. 33–75.

[17] D. Kocheva et al., Phys. Rev. C **93**, 011303 (2016).

[18] T. Kuo, E. Baranger, and M. Baranger, Nucl. Phys. **81**, 241 (1966).

[19] T. Kuo and G. Brown, Nucl. Phys. **85**, 40 (1966).

[20] T. Kuo and G. Brown, Nucl. Phys. A **114**, 241 (1968).

[21] T. T. S. Kuo and E. Osnes, *Folded-diagram theory of the effective interaction in nuclei, atoms and molecules* (Springer, 1990), vol. 364 of *Lecture Notes in Physics*, pp. 1–170.

[22] G. Herling and T. Kuo, Nucl. Phys. A **181**, 113 (1972).

[23] A. Poves, J. Sánchez-Solano, E. Caurier, and F. Nowacki, Nucl. Phys. A **694**, 157 (2001).

[24] E. K. Warburton and B. A. Brown, Phys. Rev. C **43**, 602 (1991).

[25] G. R. Satchler, *Introduction to nuclear reactions* (Palgrave Macmillan, 1990).

[26] P. G. Hansen and J. A. Tostevin, Annu. Rev. Nucl. Part. Sci. **53**, 219 (2003).

[27] M. Spieker et al., Phys. Rev. C **99**, 051304 (2019).

[28] A. Gade et al., Phys. Rev. C **77**, 044306 (2008).

[29] K. Alder and A. Winther, *Electromagnetic excitation: theory of Coulomb excitation with heavy ions* (North-Holland, 1975).

[30] L. Corradi, G. Pollarolo, and S. Szilner, J. Phys. G: Nucl. Part. Phys. **36**, 113101 (2009).

[31] J. H. Sorensen and A. Winther, J. Phys. G: Nucl. Part. Phys. **17**, 341 (1991).

[32] J. Quesada, G. Pollarolo, R. Broglia, and A. Winther, Nucl. Phys. A **442**, 381 (1985).

[33] B. F. Bayman and J. Chen, Phys. Rev. C **26**, 1509 (1982).

[34] D. C. Rafferty et al., Phys. Rev. C **94**, 024607 (2016).

[35] S. Saha, Y. K. Agarwal, and C. V. K. Baba, Phys. Rev. C **49**, 2578 (1994).

[36] W. R. Phillips, Rep. Prog. Phys. **40**, 345 (1977).

[37] A. G. Artukh et al., Nucl. Phys. A **160**, 511 (1971).

[38] J. S. Karp, S. G. Steadman, S. B. Gazes, R. Ledoux, and F. Videbæk, Phys. Rev. C **25**, 1838 (1982).

[39] S. B. Gazes, H. R. Schmidt, Y. Chan, E. Chavez, R. Kamermans, and R. G. Stokstad, Phys. Rev. C **38**, 712 (1988).

[40] P. J. Siemens, J. P. Bondorf, and D. H. E. Gross, Phys. Lett. B **36**, 24 (1971).

[41] D. Chattopadhyay et al., Phys. Rev. C **94**, 061602 (2016).

[42] C. Rodríguez-Tajes et al., Phys. Rev. C **89**, 1 (2014).

[43] R. A. Cunningham et al., Phys. Rev. C **51**, 173 (1995).

[44] D. M. Brink, Phys. Lett. B **40**, 37 (1972).

[45] P. von Neumann-Cosel, P. Schenk, U. Fister, T. K. Trelle, and R. Jahn, Phys. Rev. C **47**, 1027 (1993).

[46] R. Jahn, G. J. Wozniak, D. P. Stahel, and J. Cerny, Phys. Rev. Lett. **37**, 812 (1976).

[47] N. Anyas-Weiss et al., Phys. Rep. **12**, 201 (1974).

[48] W. D. Hamilton, ed., *The electromagnetic interaction in nuclear spectroscopy* (North-Holland, 1975).

[49] K. P. Lieb, *The Measurement of Nuclear Lifetimes* (De Gruyter, 1997), chap. 12, pp. 425 – 488, Experimental Techniques in Nuclear Physics.

[50] T. K. Alexander and J. S. Forster, *Lifetime Measurements of Excited Nuclear Levels by Doppler-Shift Methods* (Springer, 1978), vol. 10 of *Advances in Nuclear Physics*, pp. 197–331.

[51] P. J. Nolan and J. F. Sharpey-Schafer, Rep. Prog. Phys. **42**, 1 (1979).

[52] J. M. Blatt and V. F. Weisskopf, *Theoretical nuclear physics* (Courier Corporation, 1991).

[53] C. Stahl, N. Pietralla, G. Rainovski, and M. Reese, Nucl. Instrum. Meth. Phys. Res. A **770**, 123 (2015).

[54] P. Napiralla et al., Eur. Phys. J. A **56**, 147 (2020).

[55] T. Kibédi, T. W. Burrows, M. B. Trzhaskovskaya, P. M. Davidson, and C. W. Nestor Jr, Nucl. Instrum. Meth. Phys. Res. A **589**, 202 (2008).

[56] H. Olliver, T. Glasmacher, and A. E. Stuchbery, Phys. Rev. C **68**, 044312 (2003).

[57] T. Yamazaki, Nucl. Data Sheets **3**, 1 (1967).

[58] T. Aoki, K. Furuno, Y. Tagishi, S. Ohya, and J.-Z. Ruan, At. Data Nucl. Data Tables **23**, 349 (1979).

[59] A. Hennig et al., Nucl. Instrum. Meth. Phys. Res. A **794**, 171 (2015).

[60] C. Stahl, J. Leske, M. Lettmann, and N. Pietralla, Comput. Phys. Commun. **214**, 174 (2017).

[61] A. E. Blaugrund, Nucl. Phys. **88**, 501 (1966).

[62] J. Lindhard, M. Scharff, and H. E. Schiott, Mat. Fys. Medd. Dan. Vid. Selsk. **33**, 14 (1963).

[63] J. F. Ziegler and J. P. Biersack, *The Stopping and Range of Ions in Matter* (Springer, 1985), vol. 6 of *Treatise on Heavy-Ion Science*, pp. 93 – 129.

[64] H. E. Schiott, Mat. Fys. Medd. Dan. Vid. Selsk. **35**, 9 (1966).

[65] L. C. Northcliffe and R. F. Schilling, At. Data Nucl. Data Tables **7**, 233 (1970).

[66] J. F. Ziegler, M. Ziegler, and J. Biersack, Nucl. Instrum. Meth. Phys. Res. B **268**, 1818 (2010).

[67] L. R. Hafstad and E. Teller, Phys. Rev. **54**, 681 (1938).

[68] G. Gamow, Z. Phys. A **51**, 204 (1928).

[69] B. Al-Bataina and J. Jänecke, Phys. Rev. C **37**, 1667 (1988).

[70] P. J. Haigh et al., J. Phys. G: Nucl. Part. Phys. **37**, 035103 (2010).

[71] K. Ikeda, N. Takigawa, and H. Horiuchi, Prog. Theor. Phys. Supp. **E68**, 464 (1968).

[72] M. Freer and H. Fynbo, Prog. Part. Nucl. Phys. **78**, 1 (2014).

[73] R. B. Wiringa, S. C. Pieper, J. Carlson, and V. R. Pandharipande, Phys. Rev. C **62**, 014001 (2000).

[74] V. M. Datar et al., Phys. Rev. Lett. **94**, 122502 (2005).

[75] V. M. Datar et al., Phys. Rev. Lett. **111**, 062502 (2013).

[76] R. Bijker and F. Iachello, Ann. Phys. **298**, 334 (2002).

[77] C. Beck, *Clusters in nuclei*, vol. 1 (Springer, 2010).

[78] M. Freer, H. Horiuchi, Y. Kanada-En'yo, D. Lee, and U. G. Meißner, Rev. Mod. Phys. **90**, 035004 (2018).

[79] F. Hoyle, Astrophys. J. Suppl. Ser. **1**, 121 (1954).

[80] D. N. F. Dunbar, R. E. Pixley, W. A. Wenzel, and W. Whaling, Phys. Rev. **92**, 649 (1953).

[81] A. A. Ogloblin, T. L. Belyaeva, A. N. Danilov, A. S. Demyanova, and S. A. Goncharov, Eur. Phys. J. A **49**, 46 (2013).

[82] H. Horiuchi, Prog. Theor. Phys. **51**, 1266 (1974).

[83] H. Horiuchi, Prog. Theor. Phys. **53**, 447 (1975).

[84] P. Navrátil, J. P. Vary, and B. R. Barrett, Phys. Rev. Lett. **84**, 5728 (2000).

[85] A. Tohsaki, H. Horiuchi, P. Schuck, and G. Röpke, Phys. Rev. Lett. **87**, 192501 (2001).

[86] Y. Kanada-En'yo, Phys. Rev. Lett. **81**, 5291 (1998).

[87] Y. Kanada-En'yo, M. Kimura, and A. Ono, Prog. Theor. Exp. Phys. **2012**, 01A202 (2012).

[88] H. Horiuchi and K. Ikeda, Prog. Theor. Phys. **40**, 277 (1968).

[89] R. Bijker and F. Iachello, Phys. Rev. Lett. **112**, 152501 (2014).

[90] *Ensdf database*, https://www.nndc.bnl.gov/ensdf, accessed: 2020-10-10.

[91] A. Insolia, P. Curutchet, R. J. Liotta, and D. S. Delion, Phys. Rev. C **44**, 545 (1991).

[92] D. S. Delion, A. Insolia, and R. J. Liotta, Phys. Rev. C **46**, 1346 (1992).

[93] J. P. Ebran, E. Khan, T. Nikšić, and D. Vretenar, Nature **487**, 341 (2012).

[94] M. Hasegawa, Prog. Theor. Phys. Supp. **132**, 177 (1998).

[95] R. Zhong-zhou and X. Gong-ou, Phys. Rev. C **38**, 1078 (1988).

[96] F. D. Becchetti and J. Jänecke, Phys. Rev. Lett. **35**, 268 (1975).

[97] F. D. Becchetti, L. T. Chua, J. Jänecke, and A. M. VanderMolen, Phys. Rev. Lett. **34**, 225 (1975).

[98] R. Zhong-zhou and X. Gong-ou, Phys. Rev. C **36**, 456 (1987).

[99] A. N. Andreyev et al., Phys. Rev. Lett. **110**, 242502 (2013).

[100] D. S. Delion, A. Sandulescu, and W. Greiner, Phys. Rev. C **69**, 044318 (2004).

[101] S. M. S. Ahmed, R. Yahaya, S. Radiman, M. S. Yasir, H. A. Kassim, and M. U. Khandaker, Eur. Phys. J. A **51**, 13 (2015).

[102] Y. Qian and Z. Ren, Phys. Lett. B **777**, 298 (2018).

[103] H. J. Mang, Phys. Rev. **119**, 1069 (1960).

[104] I. Tonozuka and A. Arima, Nucl. Phys. A **323**, 45 (1979).

[105] G. Dodig-Crnkovič, F. A. Janouch, R. J. Liotta, and L. J. Sibanda, Nucl. Phys. A **444**, 419 (1985).

[106] G. Dodig-Crnkovič, F. A. Janouch, and R. J. Liotta, Nucl. Phys. A **501**, 533 (1989).

[107] K. Varga, R. G. Lovas, and R. J. Liotta, Phys. Rev. Lett. **69**, 37 (1992).

[108] A. R. Poletti, G. D. Dracoulis, A. P. Byrne, and A. E. Stuchbery, Nucl. Phys. A **473**, 595 (1987).

[109] A. Astier, P. Petkov, M. G. Porquet, D. S. Delion, and P. Schuck, Eur. Phys. J. A **46**, 165 (2010).

[110] D. Kocheva et al., Phys. Rev. C **96**, 044305 (2017).

[111] B. Buck, A. C. Merchant, and S. M. Perez, Phys. Rev. Lett. **72**, 1326 (1994).

[112] F. Hoyler, P. Mohr, and G. Staudt, Phys. Rev. C **50**, 2631 (1994).

[113] A. Astier, P. Petkov, M. G. Porquet, D. S. Delion, and P. Schuck, Phys. Rev. Lett. **104**, 042701 (2010).

[114] Y. Suzuki and S. Ohkubo, Phys. Rev. C **82**, 041303 (2010).

[115] D. S. Delion, R. J. Liotta, P. Schuck, A. Astier, and M.-G. Porquet, Phys. Rev. C **85**, 064306 (2012).

[116] https://www.ganil-spiral2.eu/.

[117] L. Kaya et al., Nucl. Instrum. Meth. Phys. Res. A **855**, 109 (2017).

[118] J. Benn, E. Dally, H. Muller, R. Pixley, H. Staub, and H. Winkler, Phys. Lett. **20**, 43 (1966).

[119] R. Bass, *Nuclear reactions with heavy ions* (Springer, NY, 1980).

[120] S. Santra, P. Singh, S. Kailas, A. Chatterjee, A. Shrivastava, and K. Mahata, Phys. Rev. C **64**, 024602 (2001).

[121] J. Wilczyński et al., Phys. Rev. Lett. **45**, 606 (1980).

[122] X. Derkx, Ph.D. thesis, Université de Caen (2010).

[123] D. C. Biswas, R. K. Choudhury, B. K. Nayak, D. M. Nadkarni, and V. S. Ramamurthy, Phys. Rev. C **56**, 1926 (1997).

[124] F. Videbæk, R. B. Goldstein, L. Grodzins, S. G. Steadman, T. A. Belote, and J. D. Garrett, Phys. Rev. C **15**, 954 (1977).

[125] C. Stahl, Ph.D. thesis, Technische Universität Darmstadt (2015).

[126] M. Wang et al., Chin. Phys. C **36**, 1603 (2012).

[127] E. Grusell and G. Rikner, Acta Radiol. Oncol. **23**, 465 (1984).

[128] O. Tarasov and D. Bazin, Nucl. Instrum. Meth. Phys. Res. B **266**, 4657 (2008).

[129] B. D. Wilkins, E. P. Steinberg, and R. R. Chasman, Phys. Rev. C **14**, 1832 (1976).

[130] P. Banerjee et al., Phys. Rev. C **92**, 024318 (2015).

[131] S. Akkoyun et al., Nucl. Instrum. Meth. Phys. Res. A **668**, 26 (2012).

[132] J. Simpson, Z. Phys. A **358**, 139 (1997).

[133] I. Y. Lee, in *Exotic Nuclear Spectroscopy* (Springer, 1990), pp. 245–258.

[134] W. Korten et al., Eur. Phys. J. A **56**, 1 (2020).

[135] A. Wiens et al., Nucl. Instrum. Meth. Phys. Res. A **618**, 223 (2010).

[136] D. W. Weißhaar, Ph.D. thesis, Universität zu Köln (2002).

[137] G. F. Knoll, *Radiation Detection and Measurement* (Wiley, NY, 2000).

[138] M. R. Dimmock et al., IEEE Trans. Nucl. Sci. **56**, 1593 (2009).

[139] N. Goel et al., Nucl. Instrum. Meth. Phys. Res. A **700**, 10 (2013).

[140] T. Ha et al., Nucl. Instrum. Meth. Phys. Res. A **697**, 123 (2013).

[141] B. Bruyneel, B. Birkenbach, and P. Reiter, Eur. Phys. J. A **52**, 70 (2016).

[142] J. Ljungvall et al., Nucl. Instrum. Meth. Phys. Res. A **955**, 163297 (2020).

[143] D. Bazzacco, Nucl. Phys. A **746**, 248 (2004).

[144] A. Lopez-Martens, K. Hauschild, A. Korichi, J. Roccaz, and J.-P. Thibaud, Nucl. Instrum. Meth. Phys. Res. A **533**, 454 (2004).

[145] A. Korichi et al., Nucl. Instrum. Meth. Phys. Res. A **872**, 80 (2017).

[146] C. Michelagnoli, Ph.D. thesis, Università degli Studi di Padova (2013).

[147] O. Stezowski and the AGATA Data Analysis Team, *Gammaware users's guide.*

[148] R. Brun and F. Rademakers, Nucl. Instrum. Meth. Phys. Res. A **389**, 81 (1997).

[149] E. Legay, R. Canedo, J. Clavelin, S. Du, and X. Grave, in *IEEE-NPSS Real Time Conference* (IEEE Computer Society, Los Alamitos, CA, USA, 2005), p. 65.

[150] N. Lalovic, Ph.D. thesis, Lund University (2017).

[151] B. Bruyneel et al., Nucl. Instrum. Meth. Phys. Res. A **608**, 99 (2009).

[152] D. Bazzacco and R. Venturelli, *Adaptive grid search as pulse shape analysis algorithm for γ-tracking and results*, LNL Annual Report (2004).

[153] D. Ralet, private communication.

[154] R. H. Pehl, N. W. Madden, J. H. Elliott, T. W. Raudorf, R. C. Trammell, and L. S. Darken, IEEE Trans. Nucl. Sci. **26**, 321 (1979).

[155] B. Bruyneel et al., Eur. Phys. J. A **49**, 61 (2013).

[156] M. Siciliano et al., *Lifetime measurement in $z = n = 50$ region: Optimization of oft parameters*, LNL Annual Report (2017).

[157] D. Radford, Nucl. Instrum. Meth. Phys. Res. A **361**, 297 (1995).

[158] N. Lalović et al., Nucl. Instrum. Meth. Phys. Res. A **806**, 258 (2016).

[159] E. Browne and J. K. Tuli, Nucl. Data Sheets **122**, 205 (2014).

[160] M. S. Basunia, Nucl. Data Sheets **107**, 2323 (2006).

[161] B. Singh and E. Browne, Nucl. Data Sheets **109**, 2439 (2008).

[162] P. R. John, Ph.D. thesis, Università degli Studi di Padova (2015).

[163] K. Siwek-Wilczynska, E. M. van Voorthuysen, J. van Popta, R. Siemssen, and J. Wilczynski, Nucl. Phys. A **330**, 150 (1979).

[164] T. Udagawa and T. Tamura, Phys. Rev. Lett. **45**, 1311 (1980).

[165] C. Stahl et al., Phys. Rev. C **92**, 044324 (2015).

[166] G. Bertolini, F. Cappellani, G. Restelli, and A. Rota, Nucl. Phys. **30**, 599 (1962).

[167] G. Schupp, H. Daniel, G. W. Eakins, and E. N. Jensen, Phys. Rev. **120**, 189 (1960).

[168] H. Daniel and G. Lührs, Z. Phys. A **176**, 30 (1963).

[169] B. Bengston, H. L. Nielsen, N. Rud, and WilskyK., Nucl. Phys. A **378**, 1 (1982).

[170] M. Giannini, D. Prospekt, and S. Sciuti, Nuovo Cim. **22**, 31 (1961).

[171] M. Sugawara, Y. Gono, Y. Ishikawa, M. Fukuda, and I. Fujiwara, Nucl. Phys. A **443**, 461 (1985).

[172] J. R. Cottle et al., Phys. Rev. C **95**, 064323 (2017).

[173] A. Winther, Nucl. Phys. A **572**, 191 (1994).

[174] H. Hasan and C. Warke, Nucl. Phys. A **318**, 523 (1979).

[175] E. Mathiak, K. Eberhard, J. Cramer, H. Rossner, J. Stettmeier, and A. Weidinger, Nucl. Phys. A **259**, 129 (1976).

[176] M. Rejmund et al., Eur. Phys. J. A **8**, 161 (2000).

[177] I. Hamamoto, Nucl. Phys. A **155**, 362 (1970).

[178] I. Hamamoto, Phys. Rep. **10**, 63 (1974).

[179] A. Stuchbery, G. Dracoulis, A. Byrne, S. Poletti, and A. Poletti, Nucl. Phys. A **482**, 692 (1988).

[180] C. Ellegaard, P. Barnes, E. Flynn, and G. Igo, Nucl. Phys. A **162**, 1 (1971).

[181] L. G. Mann et al., Phys. Rev. C **38**, 74 (1988).

[182] C. Ellegaard, P. Barnes, R. Eisenstein, E. Romberg, T. Bhatia, and T. Canada, Nucl. Phys. A **206**, 83 (1973).

[183] M. Piiparinen et al., Z. Phys. A **337**, 387 (1990).

[184] A. Gadea et al., Phys. Rev. Lett. **97**, 152501 (2006).

[185] W. E. Ormand, B. A. Brown, and M. Hjorth-Jensen, Phys. Rev. C **96**, 024323 (2017).

[186] M. Spieker et al., Phys. Rev. C **100**, 061303 (2019).

[187] A. P. Zuker, S. M. Lenzi, G. Martínez-Pinedo, and A. Poves, Phys. Rev. Lett. **89**, 142502 (2002).

[188] M. Bentley and S. Lenzi, Prog. Part. Nucl. Phys. **59**, 497 (2007).

[189] J. Duflo and A. P. Zuker, Phys. Rev. C **66**, 051304 (2002).

[190] J. Sheikh, P. Van Isacker, D. Warner, and J. Cameron, Phys. Lett. B **252**, 314 (1990).

[191] M. Bentley et al., Phys. Lett. B **437**, 243 (1998).

[192] J. Ekman, C. Fahlander, and C. Rudolph, Mod. Phys. Lett. A **20**, 2977 (2005).

[193] J. B. Ehrman, Phys. Rev. **81**, 412 (1951).

[194] R. G. Thomas, Phys. Rev. **88**, 1109 (1952).

[195] K. Kaneko, T. Mizusaki, Y. Sun, S. Tazaki, and G. de Angelis, Phys. Rev. Lett. **109**, 092504 (2012).

[196] B. S. Nara Singh et al., Phys. Rev. C **75**, 061301 (2007).

[197] S. J. Williams et al., Phys. Rev. C **68**, 011301 (2003).

[198] D. Rudolph et al., Phys. Rev. C **78**, 021301 (2008).

[199] P. J. Davies et al., Phys. Rev. Lett. **111**, 072501 (2013).

[200] S. M. Lenzi, M. A. Bentley, R. Lau, and C. A. Diget, Phys. Rev. C **98**, 054322 (2018).

[201] M. A. Bentley, S. M. Lenzi, S. A. Simpson, and C. A. Diget, Phys. Rev. C **92**, 024310 (2015).

[202] K. Kaneko, S. Tazaki, T. Mizusaki, Y. Sun, M. Hasegawa, and G. de Angelis, Phys. Rev. C **82**, 061301 (2010).

[203] K. Kaneko, Y. Sun, T. Mizusaki, and S. Tazaki, Phys. Rev. C **89**, 031302 (2014).

[204] D. J. Morrissey and B. M. Sherrill, *In-Flight Separation of Projectile Fragments* (Springer Berlin Heidelberg, Berlin, Heidelberg, 2004), pp. 113–135.

[205] J. J. Gaimard and K. H. Schmidt, Nucl. Phys. A **531**, 709 (1991).

[206] J. Gosset et al., Phys. Rev. C **16**, 629 (1977).

[207] A. Stolz et al., Phys. Rev. C **65**, 064603 (2002).

[208] K. Sümmerer, Phys. Rev. C **86**, 014601 (2012).

[209] Y. Yano, Nucl. Instrum. Meth. Phys. Res. B **261**, 1009 (2007).

[210] T. Kubo, Nucl. Instrum. Meth. Phys. Res. B **204**, 97 (2003).

[211] H. Okuno, N. Fukunishi, and O. Kamigaito, Prog. Theor. Exp. Phys. **2012**, 03C002 (2012).

[212] T. Kubo et al., Prog. Theor. Exp. Phys. **2012**, 03C003 (2012).

[213] N. Fukuda et al., Nucl. Instrum. Meth. Phys. Res. B **317**, 323 (2013).

[214] H. Kumagai, A. Ozawa, N. Fukuda, K. Sümmerer, and I. Tanihata, Nucl. Instrum. Meth. Phys. Res. A **470**, 562 (2001).

[215] H. Kumagai et al., Nucl. Instrum. Meth. Phys. Res. B **317**, 717 (2013).

[216] K. Kimura et al., Nucl. Instrum. Meth. Phys. Res. A **538**, 608 (2005).

[217] W. Christie et al., Nucl. Instrum. Meth. Phys. Res. A **255**, 466 (1987).

[218] S. Takeuchi et al., Nucl. Instrum. Meth. Phys. Res. A **763**, 596 (2014).

[219] I. Murray, F. Browne, S. Chen, M. L. Cortés, and P. Doornenbal, RIKEN Accel. Prog. Rep. **51**, 158 (2018).

[220] H. Baba et al., Nucl. Instrum. Meth. Phys. Res. A **616**, 65 (2010).

[221] T. Ohnishi et al., J. Phys. Soc. Jpn. **77**, 083201 (2008).

[222] C. M. Shand, Ph.D. thesis, University of Surrey (2017).

[223] P. Doornenbal, private communication.

[224] P. Doornenbal, *shogun-sim*, http://ribf.riken.jp/~pieter/shogun.

[225] H. Weick et al., Nucl. Instrum. Meth. Phys. Res. B **164-165**, 168 (2000).

[226] J. Huo, S. Huo, and C. Ma, Nucl. Data Sheets **108**, 773 (2007).

[227] G. Cowan, *Statistical Data Analysis* (Clarendon Press, Oxford, UK, 1998).

[228] S. R. Stroberg et al., Phys. Rev. C **90**, 034301 (2014).

[229] I. Murray et al., Phys. Rev. C **99**, 011302 (2019).

[230] S. Baker and R. D. Cousins, Nucl. Instrum. Methods **221**, 437 (1984).

[231] F. James and M. Roos, Comput. Phys. Commun. **10**, 343 (1975).

[232] D. Rogers, Nucl. Instrum. Methods **127**, 253 (1975).

[233] C. Dubi, A. Ocherashvilli, H. Ettegui, and B. Pedersen, Nucl. Instrum. Meth. Phys. Res. A **794**, 160 (2015).

[234] F. James, Comput. Phys. Commun. **20**, 29 (1980).

[235] Zielínska, M. et al., Eur. Phys. J. A **52**, 99 (2016).

[236] N. Paul et al., Phys. Rev. Lett. **122**, 162503 (2019).

[237] P. Ruotsalainen et al., Phys. Rev. C **88**, 041308 (2013).

[238] K. Wimmer et al., Phys. Lett. B **785**, 441 (2018).

[239] C. Langer et al., Phys. Rev. Lett. **113**, 032502 (2014).

[240] J. Bonnard, S. M. Lenzi, and A. P. Zuker, Phys. Rev. Lett. **116**, 212501 (2016).

[241] J. Bonnard and A. P. Zuker, J. Phys.: Conf. Ser. **1023**, 012016 (2018).